Evaluating Performance of Hybrid Geosynthetic-Reinforced Retaining Walls

By

Yan Jiang

Submitted to the graduate degree program in Civil, Environmental, and Architectural Engineering and the Graduate Faculty of the University of Kansas in partial fulfillment of the requirements for the degree of Doctor of Philosophy.

_____

Chairperson Dr. Jie Han

_____

Dr. Hongyi Cai

_____

Dr. Weizhang Huang

_____

Dr. Anil Misra

_____

Dr. Robert L. Parsons

Date Defended: 05/06/2016

The Dissertation Committee for Yan Jiang

certifies that this is the approved version of the following dissertation:

Evaluating Performance of Hybrid Geosynthetic-Reinforced Retaining Walls

_____

Chairperson Dr. Jie Han

Date approved: 05/09/2016

Abstracts

Geosynthetic-Reinforced Retaining (GRR) walls have been extensively used in highway projects. A novel GRR wall was proposed to mitigate the problems (e.g. high connection stress) resulting from the relatively large spacing of primary reinforcement. This new GRR wall has secondary reinforcement installed between primary reinforcement layers. This new GRR wall has a similarity in the structure of the GMSE wall and the GRS wall in terms of the vertical reinforcement spacing (i.e., it has the same vertical primary reinforcement spacing as the GMSE wall and the same vertical secondary reinforcement spacing as the GRS wall). In this study, it is named as a hybrid GRR wall. Since the hybrid GRR wall is an innovative retaining structure, few studies have been carried out on it and then its performance has not been well understood. Therefore, it is necessary to evaluate the performance of the hybrid GRR wall.

Three GRR wall sections were constructed and monitored in the field: (1) a hybrid GRR wall section with uniaxial geogrid layers as primary and secondary reinforcement, (2) a hybrid GRR wall section with uniaxial geogrid layers as primary reinforcement and with biaxial geogrid layers as secondary reinforcement, and (3) a GRR wall section with uniaxial geogrid layers as primary reinforcement only (i.e., the control section). Earth pressure cells, inclinometer casings and probes, and foil-type strain gauges were used in these three test wall sections to measure vertical and lateral earth pressures, accumulated lateral wall facing deflections, and strains of primary and secondary geogrid layers during construction, respectively. The results from monitoring of these three GRR wall sections were analyzed. The test results demonstrated the effects of secondary reinforcement on

the improved performance of GRR walls, including reduced accumulated wall facing deflections, a more uniform lateral earth pressure distribution, and reduced tensile strains in primary geogrid layers.

In addition to the field tests, the numerical study was performed to evaluate the performance of the instrumented GRR walls in the field tests. The wall facing and the foundation soil were modelled as a linearly elastic material and the retained soil was modelled as a linearly elastic perfectly plastic material with the Mohr Coulomb (MC) failure criterion. The behavior of the backfill soil in the reinforced soil zone was modelled using the Cap Yield (CY) model and the MC model. The behavior of the reinforcement was described by a strip element with a linearly elastic perfectly plastic behavior. An 8-kPa compaction stress was considered in the numerical model. The vertical and lateral earth pressures, wall facing deflections, and strains in primary and secondary geogrid layers during construction were calculated by the numerical simulation and also compared with the measured ones in the field tests. The calculated results from the numerical simulation agreed well with the measured one in the field tests. The calculated results from the numerical simulation also demonstrated that the secondary reinforcement could reduce wall facing deflections and tensile strains in primary geogrid layers.

A parametric study was also performed through varying one parameter in the baseline model to study its influence on the performance of the hybrid GRR wall, such as wall facing deflections, vertical earth pressures, lateral earth pressures, and stresses in reinforcement. The influence factors consisted of the length of primary reinforcement, the length of secondary reinforcement, the stiffness of primary reinforcement, the stiffness of secondary reinforcement, the backfill soil friction, the backfill soil dilation, the backfill soil

modulus, the compaction stress, and the foundation compressibility. The parametric study shows that the maximum wall facing deflection decreased with an increase in the primary reinforcement length, the secondary reinforcement length, the primary reinforcement stiffness, the secondary reinforcement stiffness, the backfill soil friction angle, the backfill soil dilation angle, the backfill soil modulus, and the foundation compressibility while increased with an increase in the compaction stress. The lateral earth pressure increased with an increase in the primary reinforcement stiffness, the secondary reinforcement stiffness, and the backfill soil friction angle because the wall facing deflections decreased with an increase in the primary reinforcement stiffness, the secondary reinforcement stiffness, and the backfill soil friction angle. The maximum tensile stress in the primary reinforcement increased with an increase in the primary reinforcement stiffness and the compaction stress, but decreased with an increase in the primary reinforcement length, the secondary reinforcement stiffness, and the backfill soil friction angle.

Acknowledgements

First, I would like to appreciate my advisor, Professor Jie Han, who provides me a great opportunity to pursue my Ph.D. degree at the University of Kansas. I am very fortunate to know him. He is a very kind person and always brought me warmth. In May 2013, I was very lucky to become his Ph.D. student and started my study journey in the U.S. I really enjoy my study life with his advice. He not only provides support for my research but also for my life. He is always selfless to share his personal experiences with me and prepares me to be ready for my future career. I really want to express my deepest gratitude to him again.

I would also like to acknowledge the financial support and field assistance from Kansas Department of Transportation and National Cooperative Highway Research Program for this research. Clarkson Construction Company provided great assistance and cooperation during wall instrumentation and monitoring. Tensar International provided geogrid for instrumentation. The Geosynthetic Institute (GSI) provided a GSI fellowship for my Ph.D. study.

In addition, our laboratory technologists, Matthew Maksimowicz, David Woody, Kent Dye, and Eric Nicholson, past and current graduate students, Dr. Xiaohui Sun, Dr. Deep Khatri, Jun Guo, Omar K. Ismael, Dr. Fei Wang, Wessam Mohammed, Jamal Ismael Kakrasul, Saif Mohammed Jawad, Ghaith M.Salih Abdulrasool, and Mehari Weldu, past undergraduate students, Zack Brady and Nick Andrus, and past and current visiting scholars, Mustapha Rahmaninezhad, Dan Chang, Dr. Fulin Li, Dr. Hongbo Zhang, Dr. Hongguang Zhang, and Meixiang Gu from the University of Kansas provided great

assistance in wall instrumentation and monitoring. All the above support and help are greatly appreciated.

I would like to thank my Ph.D. committee members, Professor Robert L. Parsons, Professor Anil Misra, Professor Hongyi Cai, and Professor Weizhang Huang for their guidance and help in reviewing this dissertation.

Finally, I would like to give my appreciation to my family, especially to my wife. Thank my wife for her understanding and supports. Without her understanding and supports, I would not be able to complete my Ph.D. dissertation on time.

Table of Contents

List of Figures

List of Tables

Chapter 1 Introduction

1.1. Problem statements

Geosynthetics have been extensively used to reinforce soil in geotechnical engineering for almost a half century. Their applications include geosynthetic reinforced roads, geosynthetic reinforced foundations, geosynthetic reinforced retaining (GRR) walls, geosynthetic reinforced slopes, etc. Among these applications, the GRR wall is one of the most commonly used geosynthetic reinforced soil structures worldwide.

A GRR wall usually consists of compacted backfill soil, geosynthetic reinforcement, and wall facing. The geosynthetic reinforcement usually uses geogrid or geotextile. During construction, the geogrid or geotextile is installed between layers of the backfill soil to provide confinement for the backfill soil. Frictional or mechanical connections are frequently used to connect the geosynthetic reinforcement and the wall facing. The wall facing could be concrete panel facing, shotcrete facing, timber facing, or modular-block facing. Among these wall facings, the modular-block facing is the most popular one. Figure 1 (a) and (b) shows the cross sections of two types of the GRR walls, which are a Geosynthetic-reinforced Mechanically Stabilized Earth (GMSE) wall and a Geosynthetic Reinforced Soil (GRS) wall.

Both GMSE and GRS walls have been extensively used in highway projects. A major difference between the GMSE wall and the GRS wall is vertical reinforcement spacing. The Federal Highway Administration (FHWA) has published design guidelines for GMSE and GRS walls. In the design guidelines, it is clearly stated that the vertical reinforcement spacing should not exceed 0.8 and 0.3 m for GMSE walls and GRS walls,

respectively. Typically, the vertical reinforcement spacing in the GRS wall and in the GMSE is 0.2 and 0.6 m, respectively. The relatively large vertical reinforcement spacing in the GMSE wall may result in a high connection force even bulging. In order to mitigate this problem, a concept of secondary reinforcement was proposed (Leschinsky 2001). The secondary reinforcement was installed between primary reinforcement layers in the GMSE wall, as shown in Figure 1 (c). The secondary reinforcement is shorter than the primary reinforcement. The inclusion of secondary reinforcement is able to (1) reduce the connection force of primary reinforcement, (2) improve the soil compaction near wall facing, (3) increase internal stability, and (4) reduce down-drag effect (Leschinsky 2001). This novel GRR wall has a similarity in the structure of the GMSE wall and the GRS wall in terms of the vertical reinforcement spacing (i.e., it has the same vertical primary reinforcement spacing as the GMSE wall and the same vertical secondary reinforcement spacing as the GRS wall). In this study, it is named as a hybrid GRR wall.

The GMSE wall and the GRS wall have different behavior and design methods of internal stability. In the GMSE wall, a failure surface is assumed to divide reinforced soil into a stable zone and an unstable zone. The unstable zone falls between a wall facing and the failure surface, and the stable zone is behind the failure surface (shown in Figure 1.1 (a)). The geosynthetic reinforcement functions as a tieback to hold the unstable zone. The design method of internal stability for GMSE walls can be seen in Elias and Christopher (2001). Compared with a GMSE wall, a GRS wall behaves as a composite mass due to its close vertical reinforcement spacing. Studies have been conducted to demonstrate this fact (Broms 1977, Ziegler et al., 2008, Elton and Patawaran, 2005, etc.). Therefore, in the design of internal stability for the GRS wall, the reinforced soil is treated as a composite

mass. The design method of internal stability for GRS walls can be seen in Adams et al. (2011).

Since the hybrid GRR wall is an innovative retaining structure, few studies have been carried out on it and then its performance has not been well understood. Therefore, it is necessary to evaluate the performance of the hybrid GRR wall.

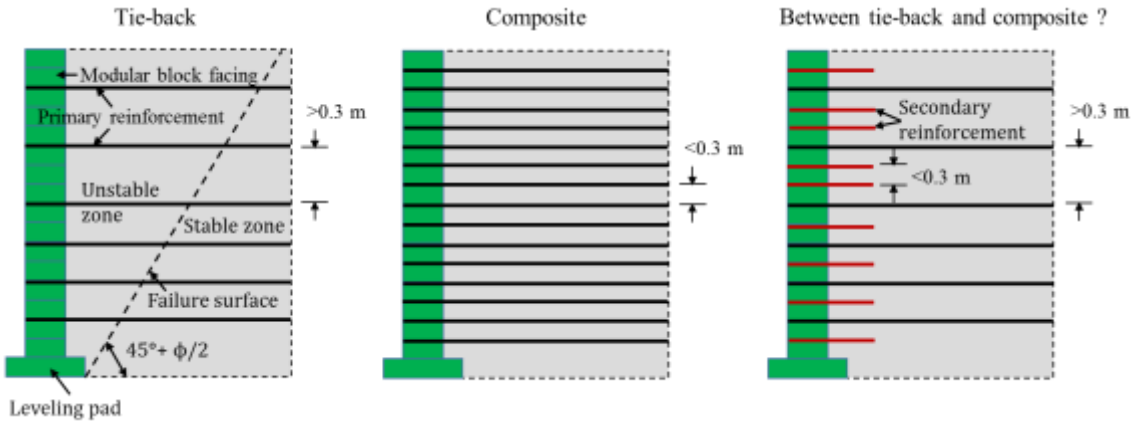

(a) GMSE wall (b) GRS wall (c) Hybrid GRR wall

Figure 1.1 Cross sections of GRR walls

1.2. Research objective and tasks

The objective of this study is to evaluate the performance of the hybrid GRR wall. The findings of this study will contribute to the development of the design for the hybrid GRR wall. To accomplish this research objective, field tests and numerical analyses were utilized. The main tasks in this study are listed as follows:

Firstly, three test wall sections (one GMSE wall and two hybrid GRR walls) were constructed and monitored in the field to investigate the performance of the hybrid GRR

walls. Wall facing deflections, vertical earth pressures, lateral earth pressures, and tensile strains in geogrid were measured during and after construction and analyzed.

Secondly, numerical models were developed to simulate the behavior of the hybrid GRR walls tested in the field. The results of the wall facing deflections, the vertical earth pressures, the lateral earth pressures, and the tensile strains in geogrid from numerical simulation and the field tests were compared.

Thirdly, a parametric study was performed based on the developed numerical models. The influence factors, such as the length of primary reinforcement, the length of secondary reinforcement, the stiffness of primary reinforcement, the stiffness of secondary reinforcement, the friction angle of backfill soil, the dilation angle of the backfill soil, the modulus of the backfill soil, compaction stress, and foundation compressibility on the performance of the hybrid GRR wall were investigated.

Finally, based on the results from the field tests and the numerical simulation, suggestions for the design of the hybrid GRR wall are given.

1.3. Dissertation organization

This dissertation consists of eight chapters. Following this chapter, a literature review of previous studies on GMSE walls and GRS walls is described in Chapter Two. Chapter Three presents the test results of the materials (e.g. reinforced soil, retained soil, geogrid) in the field tests. The measured results from the field tests during and after construction were analyzed and are discussed in Chapter Four. Chapter Five describes the preparation of numerical modeling for the field tests. The numerical results for the one GMSE wall and two hybrid GRS walls are compared and discussed in Chapter Six. Chapter Seven includes a parametric study to investigate the influence factors on the

performance of the hybrid GRR wall. Conclusions and recommendations are given in Chapter Eight.

Chapter 2 Literature Review

2.1. Overview

This chapter has three sections. The first section introduces the studies regarding GMSE walls. Research associated with GRS walls is summarized in the second section. In the third section, a literature review of the hybrid GRR wall is presented. In each section, the studies related to experimental tests and numerical simulation are described separately.

2.2. GMSE walls

2.2.1. Background of GMSE walls

The use of geosynthetics in GMSE walls has increased since last century and lasted until now. Schlosser (1978) reported a GMSE wall constructed in France in 1971. This GMSE wall used geotextile reinforcement with wraparound facing. Thereafter, geogrid was used in the GMSE walls as reinforcement. Compared with geotextile, geogrid has been more frequently utilized in the GMSE walls. In addition, approximate three-fourth of constructed GMSE walls had modular block facings (Koerner and Koerner 2011).

2.2.2. Field or experimental tests

Experimental tests were performed to understand the behavior of the GMSE walls. In the experimental tests, instrumentation was used to monitor the performance of these GMSE walls under a working condition or a limit state condition. Table 2.1 summarizes these experimental studies of the GMSE walls.

Fourteen experimental tests on the GMSE walls were reviewed in this study. These experimental tests were performed in several counties, such as the U.S., China, Korea and Canada. These GMSE walls had wraparound facing, concrete panel facing, or modular-block facing. Among them, most of GMSE walls had modular-block facing. The height of these GMSE walls varied from 3.6 to 17 m and the length of geosynthetic reinforcement changed from 2.5 to 12 m. The vertical reinforcement spacing was in the range from 0.3 to 1.0 m. Eight of fourteen GMSE walls had a 0.6-m vertical reinforcement spacing. Various types of geosynthetic reinforcement were used in these GMSE walls, such as high-density polyethylene (HDPE) geogrid, biaxial polypropylene geogrid, and polyester geogrid. Ten of fourteen GMSE walls utilized HDPE geogrid. Sand, aggregate, and lime-treated soil were employed to be the backfill soil in these walls. Most of these GMSE walls were constructed on strong foundations, such as bedrock, concrete, and sandy gravel. Numerous types of instrumentation were installed to monitor the performance of these GMSE walls. The instrumentation consisted of inclinometers, surveying targets, linear variable differential transformers (LVDTs), earth pressure cells, strain gauges, and extensometers. Inclinometers, earth pressure cells, and strain gauges are frequently used in the experimental tests. The performance of these GMSE walls, such as the wall facing deflections, vertical and lateral earth pressures, and strains in geosynthetic reinforcement, was of interest. Further discussion on these performance is provided below.

Allen et al. (1992) studied a 12.6 m high GMSE wall reinforced with geotextile. This GMSE wall was constructed in Seattle, Washington. Wall facing was wraparound. Woven geotextile was used to reinforce the wall. The length of geotextile reinforcement was 12 m and its vertical spacing was 0.38 m. A clean gravelly sand was selected as

backfill soil. Various types of instrumentation were utilized including an inclinometer, earth pressure cells, strain gauges, mechanical extensometers, settlement targets, and weather station. Wall facing deflections measured by the inclinometer increased with an increase in wall height during construction. The majority part of wall facing deflection occurred during the construction while the minority part of the wall facing deflection happened after the construction. The measured vertical pressure behind the back of wall facing at the toe of the wall was 20% higher than in the middle and the back of the wall. This result was because the outward rotation of the reinforced soil zone at the toe of the wall. Measured global strains in the geotextile were larger than their corresponding local strains. However, both measured strains were far smaller than the calculated strains from a design method. In addition, measured strain in soil was larger than the measured strain in geotextile, which meant that slippage occurred between the backfill soil and geotextile.

Similarly, Ling and Leshchinsky (1996) reported two instrumented GMSE walls with modular block facing constructed by Tensar Earth Technologies Inc., in Stockbridge, Georgia. These two walls were 6.84 m high and used HDPE geogrid as reinforcement. The length of geogrid reinforcement was 2 m and its vertical spacing varied from 0.4 to 0.8 m. Backfill soil was 98% sand and 2% silt and clay. Inclinometers, pressure transducers, and strain gauges were used to monitor lateral displacements, lateral earth pressures, and tensile strains in the geogrid. The lateral displacement between the back of wall facing and the end of geogrid was very small, indicating that a reinforced soil zone performed like a whole composite mass. The measured lateral pressures behind the back of wall facing were small as well. The measured strains in geogrid were between 0.1 %

and 0.4%. The corresponding tensile stresses were between 2 and 4 kN/m^2. The largest strain occurred at one-third of the wall height.

Bathurst et al. (2000) reported a series of experimental tests performed on GMSE walls with wraparound facing and modular block facing. The height of these GMSE walls was 3.6 m with 2.5 m long geosynthetic reinforcement. Vertical reinforcement spacing was 0.6 m and backfill soil was beach sand. The test results show that maximum tensile stresses in reinforcement occurred at the location of connection in these walls with the modular block facing. The stiffness of the wall facing had an influence on the tensile strains in the reinforcement. Relatively rigid facing reduced the tensile strains in reinforcement. Measured vertical earth pressures at the bottom of the wall facing was larger than the total weight of modular blocks because the geosynthetic reinforcement at the back of the wall facing also added down-drag force on the wall facing.

The field instrumentation and monitoring of the Founders/Meadows Bridges were reported in Abu-Hejleh et al. (2001). The bridges were seated on strip footings supported by GMSE wall abutments. The height of the GMSE walls varied from 4.5 to 4.9 m. The length of geosynthetic reinforcement was greater than 8 m and vertical reinforcement spacing was 0.6 m. Backfill soil was classified as CDOT (Colorado Department of Transportation) Class 1, which contained gravel, sand, and fine grained soil. Monitoring results show that the lowest vertical earth pressure happened at the location near a wall facing and the highest vertical earth pressure occurred in the middle of the bridge abutment. The distribution of the vertical earth pressures indicated no potential for the overturning of the GMSE wall abutments. The placement and compaction of the backfill soil had an influence on tensile strains in reinforcement. The wall facing deflection resulted from the

construction of the GMSE walls and the installation of the strip footings. The wall facing deflection was very small after the construction of the bridge.

Yang et al. (2009, 2010, 2012, and 2014) performed four field tests on the GMSE walls. They found that maximum vertical earth pressure happened in the middle of the reinforced soil zone. Measured lateral earth pressures were lower than active earth pressures due to soil arching effect. The measured lateral earth pressures slightly decreased after construction. Compaction had a great influence on wall facing deflections. Wall facing deflection after construction slightly developed and stopped approximately 9 months after construction. The wall facing deflection resulted from reinforcement creep and a slippage between reinforcement and backfill soil.

Allen and Bathurst (2013) studied the performance of a GMSE wall designed using the K-stiffness method. The GMSE wall had 6.3 m in height with well-graded silty graveled sand as backfill soil. HPDE geogrid was used in the GMSE wall as reinforcement. Field test results show that the maximum tensile strain occurred at the location near a wall facing and tensile strain in reinforcement dramatically decreased with an increase in a distance away from the wall facing. Measured wall facing deflections using a surveying method were less than 20 mm during construction and the wall facing deflection ceased after construction. No creep deflection was found after construction.

Table 2.1 Summary of the experimental tests of the GMSE walls

No.	1	2	3	4	5	7	6
Authors	Allen et al.	Ling and Leshchinsky	Bathurst et al.	Bathurst et al.	Abu-Hejleh et al.	Yoo	Yoo and Jung
Time	1992	1995	2000	2000	2001	2004	2008
Locations	Seattle, Washington, U.S.	Stockbridge, Georgia, U.S.	Royal Military College, Canada	Royal Military College, Canada	Founder/Meadows, Corolado, U.S.	Korea	Unavailable
Structure type	GMSE	GMSE	GMSE	GMSE	GMSE	GMSE	GMSE
Wall facing	Wrap-round	Modular block	Modular block	Wrap-round	Modular block	Modular block	Modular block
H (m)	12.6	6.84	3.6	3.6	4.5-5.9	8.4	5
L (m)	12	2	2.52	2.52	>8	6.3	3.5
S (m)	0.38	0.4-0.8	0.6	0.6	0.4	0.4-1.0	0.3-0.6
Geosynthetics type	Polyester and polypropylene geotextiles	HDPE geogrid	Biaxial polypropylene geogrid	HDPE geogrid	Geogrid	HDPE geogrid	Polyester geogrid
Backfill material	Gravelly sand	Sand	Beach sand	Beach sand	Gravel+sand+fine grained soil	Poorly-graded sand	Well-graded silty sand
Foundation	Unknown	Sand	Concrete	Concrete	Bedrock	Unknown	Unknown
Instrumentation	Inclinometers, earth pressure cells, strain gauges, mechanical extensometers, settlement targets, weather station	Inclinometers, earth pressure cells, and strain gauges	Facing potentiometers, earth pressure cells, and strain gauges, extensometers, settlement plates	Facing potentiometers, earth pressure cells, and strain gauges, extensometers, settlement plate	Inclinometers, survey targets, earth pressure cells, and strain gauges, moisture gages, and temperature gages	Surveying targets	LVDTs, and strain gauges
Monitored results	Wall deflections, vertical earth pressures, strains in soil, strains in geotextile, settlement	Lateral displacements, lateral earth pressures, and strains in geogrid	Wall deflections, lateral earth pressures, and strains in geogrid	Wall deflections, lateral earth pressures, and strains in geogrid	Wall deflections, stains in geogrid, temperatures, and vertical earth pressures	Wall deflections	Wall deflections, and stains in geogrid

Note: H: wall height; L: reinforcement length; S: reinforcement spacing; LVDT: linear variable differential transformer; HDPE: high density polyethylene.

Table 2.1 Summary of field or experimental test of GMSE walls (Continued)

No.	8	9	10	11	12	13	14
Authors	Desai and Hoseiny	Yang et al.	Yang et al.	Pierson	Yang et al.	Allen and Bathurst	Yang et al.
Time	2005	2009	2010	2011	2012	2013	2014
Locations	Tanque Verde, Arizona, U.S.	Fujian, China	Fujian, China	Kansas, U.S.	Heibei, China	Maple Valley, Washington, U.S.	Shangdong, China
Structure type	GMSE	GMSE	GMSE	GMSE	GMSE	GMSE	GMSE
Wall facing	Concrete panel	Geotextile gravel bag+Concrete	Geotextile gravel bag	Modular block	Modular block	Modular block	Modular block
H (m)	4.8	12.2	12.2	6	6	6.3	17
L (m)	3.7	7.5	7.5	4.2	5	7.9	2-14
S (m)	0.4-0.8	0.4-0.5	0.4-0.6	0.6	0.4-0.6	0.6	0.3-0.6
Geosynthetics type	HDPE geogrid	HDPE geogrid	HDPE geogrid	HDPE geogrid	HDPE geogrid	HDPE geogrid	HDPE geogrid
Backfill material	Unknown	Rammed clay+Reclaimed gravel soil	Rammed clay+Reclaimed gravel soil	Aggregate	Lime-treated soil	Well-graded silty gravelly sand	Soil-rock mixture
Foundation	Unknown	Gravel soil	Gravel soil	Bedrock	Sandy gravel	Dense silty sandy gravel	Bedrock
Instrumentation	Stain gauges, earth pressure cells, induction coils, and temperature gages	Inclinometers, surveying targets, earth pressure cells, and strain gauges	Inclinometers, surveying targets, earth pressure cells, and strain gauges	Inclinometers, earth pressure cells, and strain gauges	Inclinometers, earth pressure cells, and strain gauges	Stain gauges, extensometers, temperature gages	Surveying target, earth pressure cells, and strain gauges
Monitored results	Stains in geogrid, vertical earth pressures, and temperatures	Wall deflections, vertical and lateral earth pressures, and strains in geogrid	Wall deflections, vertical and lateral earth pressures, and strains in geogrid	Wall deflections, lateral earth pressures, and strains in geogrid	Wall deflections, lateral earth pressures, and strains in geogrid	Stains in geogrid, and temperatures	Wall deflections, lateral earth pressures, and strains in geogrid

Note: H: wall height; L: reinforcement length; S: reinforcement spacing; LVDT: linear variable differential transformer; HDPE: high density polyethylene.

2.2.3. Numerical methods

Numerical methods, finite element and finite difference methods, have been successfully used to simulate GMSE structures (e.g. Leshchinsky and Vulova 2001; Hatami and Bathurst 2005; and Huang et al. 2011 and 2013). Compared with the experimental tests, numerical methods have the following two major advantages: (1) obtaining more comprehensive results than the experimental tests; (2) investigating the effects of influence factors which are difficult and/or costly to achieve in the experimental tests. Literature review of experimental tests of the GMSE walls has been presented previously. This section will present a review on the numerical simulation of the GMSE walls. Table 2.2 summarizes the information of these numerical studies of the GMSE walls.

Numerous numerical studies have been conducted on the GMSE walls. Both the finite element method and the finite difference method have been used. For the finite element method, various programs have been used to model the GMSE walls, including CANDE, GEOFEM, AFENA, SSCOMP, M-CANDE, DACSAR, DSC-SST-2D, DYNA3D/LS-DYNA, and Plaxis. However, FLAC is the only finite difference software used to model the GMSE walls. Among 22 numerical studies reviewed, 19 studies used 2D models (i.e. plane strain) to simulate the GMSE walls, whereas only 3 studies (Huang et al. 2011, 2013, and 2014) adopted 3D models to simulate the GMSE walls. In the Huang et al. (2011, 2013, and 2014) studies, the 3D modeling was necessary because the lateral deformation of the wall resulted from a laterally-loaded pile. The GMSE walls analyzed had the following parameters: (1) wall height ranging from 2.6 to 12.6 m, (2) reinforcement length ranging from 0.6 to 12.0 m, (3) reinforcement spacing ranging from 0.2 to 1.5 m, (4) linearly elastic-perfectly plastic soil model with the Mohr-Coulomb failure criterion, or

stress-dependent nonlinear soil model (Duncan-Chang hyperbolic soil model, hardening soil model, or cap-yield soil model), (5) mostly linearly elastic cable, bar, or geosynthetic elements, (6) sliding or fully-bonded interface between geosynthetic and soil, (7) use of interface between facing blocks in most studies, and (8) compressible or incompressible foundation. Further discussion on these parameters is provided below.

Christopher et al. (1989a, 1989b), Ling et al. (1995), Ho and Rowe (1996), Holtz and Lee (2002), Helwany et al. (2003), Ling and Leshchinsky (2003), and Fakharian and Attar (2007) studied the effect of reinforcement length on the performance of the GMSE walls. Seven numerical studies (Ho and Rowe 1996, Ling and Leshchinsky 1996, Leshchinsky and Vulova 2001, Rowe and Skinner 2001, Holtz and Lee 2002, Ling and Leshchinsky 2003, and Guler et al. 2007) investigated the effect of reinforcement spacing on the performance of the GMSE walls and only Leshchinsky and Vulova (2001) reduced the reinforcement spacing to less than 0.3 m (1.0 ft.).

Most GMSE walls have been considered having modular blocks as facing. The facing modular blocks have been mostly modeled as elastic discrete blocks. Retained soil and foundation soil have been modeled as elastic materials or linearly elastic-perfectly plastic materials with the Mohr-Coulomb failure criterion. All researchers recognized the importance of properly modeling the backfill soil, the reinforcement, and the interface between backfill soil and reinforcement. The linearly elastic-perfectly plastic soil model with the Mohr-Coulomb failure criterion (commonly referred to as the Mohr-Coulomb model) or the stress dependent nonlinear soil model has been commonly adopted for the backfill soil. The stress-dependent nonlinear soil models include the Duncan-Chang hyperbolic soil model, the hardening soil model, and the cap yield model. Huang et al.

(2013 and 2014) found that the cap yield model not only could well describe the nonlinear elastic behavior but also could well capture the plasticity resulting from shear stress and compressive stress. Both the hardening soil model and the cap yield model can consider the dilation of soil between reinforcement layers. In the numerical modeling of GMSE walls, Hatami and Buthurst (2005) and Guler et al. (2007) modeled the compaction-induced stresses by applying an 8 kPa distribution pressure on the top of each lift. Mirmoradi and Ehrlich (2014) modeled the compaction-induced stresses by applying an 8-kPa distribution stress at the top and bottom of each soil layer. Huang et al. (2013 and 2014) simulated the effect of compaction-induced stress by applying additional lateral stress of 10 kPa to each lift if a heavy compactor is used or 8-kPa if a light compactor is used. The reinforcement has been modeled as linearly elastic structural elements (cable, bar, or geosynthetic elements) in most studies. Nonlinear structural elements were used for reinforcement in few studies. The interface between the backfill soil and reinforcement has been modeled as fully bonded with a tensile rupture strength, rigid plastic with the Mohr-Coulomb failure criterion, and linearly elastic-perfectly plastic with the Mohr-Coulomb failure criterion. Most numerical studies assumed incompressible foundations under GMSE walls but few studies (Christopher et al. 1989, Ling and Leshchinsky 1996, Rowe and Skinner 2001, Ling and Leshchinsky 2003, Skinner and Rowe 2005, Fakharian and Attar 2007) simulated compressible foundations under the GMSE walls. Among all the numerical studies on GMSE walls, two studies modeled real spread footings buried in the GMSE walls to support bridge girders while three studies modeled simple spread footings seated on the GMSE walls without any embedment to support simplified vertical and/or horizontal loads.

Table 2.2 Summary of numerical modeling of GMSE walls

No.	1	2	3	4	5	6	7
Authors	Christopher *et al*.	Adib et al.	Ling et al.	Karpurapu and Bathurst	Ho and Rowe	Ling and Leshchinsky	Leshchinsky and Vulova
Year	1989b	1990	1995	1995	1996	1996	2001
Type of structure	GMSE	GMSE	GMSE	GMSE	GMSE	GMSE	GMSE
NM	FEM	FEM	FEM	FEM	FEM	FEM	FDM
Software	SSCOMP	SSCOMP	CANDE	GEOFEM	AFENA	SSCOMP; M-CANDE	FLAC
2D or 3D	2D	2D	2D	2D	2D	2D	2D
H (ft.)	20-40	20.0	16.7	10.0	20.0	22.8	8.5-28.6
L (ft.)	5.5-20.0	14.0	2.0-11.7	10.0	6.0-25	6.7	5.0
S (ft.)	2.5	2.5	1.0	2.5	1.7-5	1.3-2.7	0.7-3.3
Load on wall top	Footing to support bridge	No load	Footing load	Uniform vertical load	No load	Uniform vertical load	No load
Backfill constitutive model	Stress dependent hyperbolic model with MC failure criterion	Stress dependent hyperbolic model with MC failure criterion	Stress dependent hyperbolic model with MC failure criterion	Stress dependent hyperbolic model with MC failure criterion	Nonlinearly elastic and perfectly plastic granular material with MC failure criterion	Stress dependent hyperbolic model with MC failure criterion	MC
RCM	Linearly elastic; bar element	Hyperbolic model	Linearly elastic; bar element	A nonlinear elastic material considering the creep effect	Linearly elastic; bar element	Non linearly elastic; fully bonded	Linearly elastic; cable element
BRI	Hyperbolic model	Hyperbolic model	Fully bonded with tensile rupture strength	Linearly elastic and perfectly plastic with MC failure criterion	Rigid plastic with MC failure criterion	Hyperbolic model with MC failure criterion	Sliding interface with MC failure criterion
BBI	Yes	Not described	No	Yes	Yes	Yes	Yes
BI	No	Not described	Yes	Yes	No	Yes	Yes
CIS	Yes	No	No	No	No	No	No
Foundation type	Incompressible and compressible	Compressible	Incompressible	Incompressible	Incompressible	Compressible	Incompressible
Stress conditions	Working stress	Working stress	Working stress and ultimate strength	Working stress and ultimate strength	Working stress	Working stress	Ultimate strength

Note: NM: Numerical method; FEM: finite element method; FDM: finite difference method; H: wall height; L: reinforcement length; S: reinforcement spacing; BCM: backfill constitutive model; RCM: reinforcement constitutive model; BRI: backfill/reinforcement interface; BBI: Backfill/Block interface; BI: block interface; CIS: compaction-induced stress; LR: long reinforcement; SR: short reinforcement; MC: Mohr-Coulomb.

Table 2.2 Summary of numerical modeling of GMSE walls (continued)

No.	8	9	10	11	12	13
Authors	Rowe and Skinner	Holtz and Lee	Helwany et al.	Ling and Leshchinsky	Desai and Hoseiny	Skinner and Rowe
Year	2001	2002	2003	2003	2005	2005
Type of structure	GMSE	GMSE	GMSE	GMSE	GMSE	GMSE
NM	FEM	FDM	FEM	FEM	FEM	FEM
Software	AFENA	FLAC	DACSAR	CANDE	DSC-SST-2D	AFENA
2D or 3D	2D	2D	2D	2D	2D	2D
H (ft.)	26.7	12.0-42	21.5	19.0	15.3	20.0
L (ft.)	20 (LR) and 3 (SR)	9.7-33.0	25-40	3.3-16	12.7	13.3
S (ft.)	1.7-3.3	1.3-2.5	1.3	0.5-3.4	1.0-2.0	2.0
Load on wall top	No load	No load	Footing to support bridge	No load	No load	Footing to support bridge
BCM	Nonlinearly elastic and perfectly plastic granular material with MC failure criterion	Stress dependent hyperbolic model with MC failure criterion	Stress dependent hyperbolic model with MC failure criterion	Stress dependent hyperbolic model with MC failure criterion	Disturbed state concept model	Nonlinearly elastic and perfectly plastic model with MC failure criterion
RCM	Linearly elastic; bar element	Linearly elastic; geogrid element	Linearly elastic	Linearly elastic; bar element	Linearly elastic	Linearly elastic; bar element
BRI	Rigid plastic with MC failure criterion	Sliding interface with MC failure criterion	Fully bonded	Fully bonded with tensile rupture strength	Not described	Rigid plastic with MC failure criterion
BBI	Yes	Yes	Yes	Yes	No	Yes
BI	Yes	Yes	Yes	Yes	No	Yes
CIS	No	Yes	No	No	No	No
Foundation type	Compressible	Incompressible	Incompressible	Compressible to incompressible	Incompressible	Compressible
Stress conditions	Working stress and ultimate strength	Working stress	Working stress	Working stress	Working stress	Working stress and ultimate strength

Note: NM: Numerical method; FEM: finite element method; FDM: finite difference method; H: wall height; L: reinforcement length; S: reinforcement spacing; BCM: backfill constitutive model; RCM: reinforcement constitutive model; BRI: backfill/reinforcement interface; BBI: Backfill/Block interface; BI: block interface; CIS: compaction-induced stress; LR: long reinforcement; SR: short reinforcement; MC: Mohr-Coulomb.

Table 2.2 Summary of numerical modeling of GMSE walls (continued)

No.	14	15	16	17	18
Authors	Hatami and Bathurst	Hatami and Bathurst	Fakharian and Attar	Guler et al.	Huang et al.
Year	2005	2006	2007	2007	2009
Type of structure	GMSE	GMSE	GMSE	GMSE	GMSE
NM	FDM	FDM	FDM	FEM	FDM
Software	FLAC	FLAC	FLAC	Plaxis	FLAC
2D or 3D	2D	2D	2D	2D	2D
H (ft.)	12.0	12.0	19.3	12.0	12.0
L (ft.)	8.4	8.4	24.0-40.0	8.4	8.4
S (ft.)	2.0	2.0	1.3	2.0-3.0	2.0
Load on wall top	No load	Uniform vertical load	Footing to support bridge	No load	Uniform vertical load
BCM	Stress dependent hyperbolic model with MC failure criterion	Stress dependent hyperbolic model with MC failure criterion	Stress dependent hyperbolic model with MC failure criterion	Hardening soil model	MC, Modified Duncan-Chang hyperbolic model, and Lade's Model
RCM	Hyperbolic model considering load-strain-time for PP geogrid; cable element	Hyperbolic model with load-strain-time for PP geogrid; and linearly elastic-perfectly plastic for PET geogrid cable element	Elastic-plastic; cable elements	Linearly elastic; geosynthetic element	Hyperbolic model with load-strain-time for PP geogrid; cable element
BRI	Fully bonded	Fully bonded	Not described	Not described	Sliding interface with MC failure criterion
BBI	Yes	Yes	Yes	Yes	Yes
BI	Yes	Yes	Yes	Yes	Yes
CIS	Yes	Yes	No	Yes	Yes
Foundation type	Incompressible	Incompressible	Compressible	Incompressible	Incompressible
Stress conditions	Working stress	Working stress	Working stress	Working stress	Working stress

Note: NM: Numerical method; FEM: finite element method; FDM: finite difference method; H: wall height; L: reinforcement length; S: reinforcement spacing; BCM: backfill constitutive model; RCM: reinforcement constitutive model; BRI: backfill/reinforcement interface; BBI: Backfill/Block interface; BI: block interface; CIS: compaction-induced stress; LR: long reinforcement; SR: short reinforcement; MC: Mohr-Coulomb.

Table 2.2 Summary of numerical modeling of GMSE walls (continued)

No.	19	20	21	22
Authors	Huang et al.	Huang et al.	Mirmoradi and Ehrlich	Huang et al.
Year	2011	2013	2014	2014
Type of structure	GMSE	GMSE	GMSE	GMSE
NM	FDM	FDM	FEM	FDM
Software	FLAC	FLAC	Plaxis	FLAC
2D or 3D	3D	3D	2D	3D
H (ft.)	20.0	20.0	13.3	20.0
L (ft.)	14.0	14.0	9.3	14.0
S (ft.)	2.0	2.0	1.3	2.0
Load on wall top	Lateral load	Lateral load	No load	Lateral load
BCM	MC	Cap yield model	Hardening soil model	Cap yield soil model
RCM	Linearly elastic; geogrid element	Linearly elastic; geogrid element	Linearly elastic; geosynthetic element	Linearly elastic; geogrid element
BRI	Sliding interface with MC failure criterion	Sliding interface with MC failure criterion	Fully bonded	Sliding interface with MC failure criterion
BBI	No	No	Yes	No
BI	No	Yes	Yes	Yes
CIS	No	Yes	Yes	Yes
Foundation type	Incompressible	Incompressible	Incompressible	Incompressible
Stress conditions	Working stress	Working stress	Working stress	Working stress

Note: NM: Numerical method; FEM: finite element method; FDM: finite difference method; H: wall height; L: reinforcement length; S: reinforcement spacing; BCM: backfill constitutive model; RCM: reinforcement constitutive model; BRI: backfill/reinforcement interface; BBI: Backfill/Block interface; BI: block interface; CIS: compaction-induced stress; LR: long reinforcement; SR: short reinforcement; MC: Mohr-Coulomb.

2.3. GRS walls

2.3.1. Background of GRS walls

The GRS walls are often constructed as abutments to support small and medium-size bridges. Wu et al. (2006) reported and summarized the existing in-service GRS walls with flexible facing to support bridges. Adams et al. (2011) published a manual to design a GRS wall supporting an integrated bridge system. This system is referred to as a GRS-integrated bridge systems (IBS) or GRS-IBS. Figure 2.1 presents a typical cross section of the GRS-IBS. This new system includes a GRS wall and an integrated bridge system above the GRS wall. A maximum vertical spacing of geosynthetic reinforcement at less than 0.3 m in GRS walls is recommended. Wu (2013) stated that the benefit of geosynthetic reinforcement was significantly enhanced with vertical spacing of reinforcement less than 0.3 m. Up to 2015, there are more than 200 bridges that were built using GRS abutments in the United States.

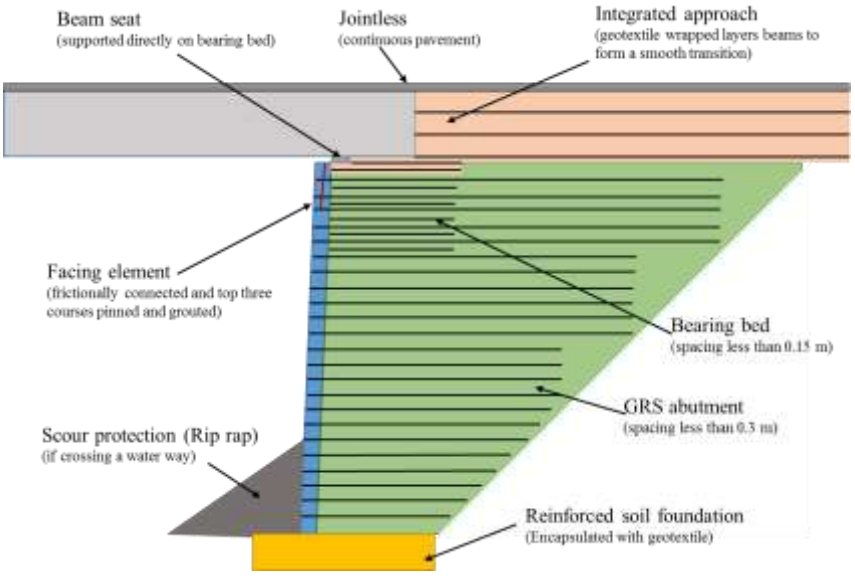

Figure 2.1 Cross section of the GRS-IBS system (re-drawn from Adams et al., 2011)

2.3.2. Experimental tests

Experimental tests have been conducted on GRS structures including GRS piers, GRS abutments, and GRS-IBS. Table 2.3 summarizes the information of these experimental studies of the GRS structures. Most of these GRS structures used modular-block facing while few used wraparound facing. GRS wall heights varied from 1.14 to 6.81 m and geotextile was the most commonly used reinforcement except one structure using geogrid as reinforcement (Budge et al. 2014). Various types of the backfill soil were used to construct the GRS walls, including well-graded gravel, silty sand with clay, and coarse aggregate. A reinforced foundation was also commonly adopted in these GRS structures. In these field tests, instrumentation, including inclinometer casings, earth pressure cells, strain gauges, and surveying, was employed to monitor the behavior of these GRS structures, such as settlement, lateral deformation, and vertical and lateral earth pressures. Further discussion on these parameters is provided below.

Wu et al. (2001) reported a field test of a GRS pier in Turner Fairbank, Virginia in the United States. The pier was constructed on a three-layer geogrid-reinforced foundation. A footing load seated on the top of the pier was loaded up to 900 kPa with seven stages. The measured vertical deformation of the pier approximately linearly increased with an increase of applied footing pressure up to 825 kPa and dramatically increased after 825 kPa, which indicated the ultimate bearing capacity of this pier. The lateral deformation of the wall facing also increased with the applied footing load. The maximum lateral deformation of the wall facing first happened in the upper part of the wall and then moved to the middle of the wall height with an increase of the footing load. A clear bulge was found in the middle area of the wall facing when the footing load reached to the ultimate

bearing capacity. In addition, the measured strains in reinforcement increased with the applied footing load to 2.3% when the applied footing load was 900 kPa. The measured strains in each instrumented geotextile were uniformly distributed because the footing load was evenly applied over the entire area of the pier. The maximum strains in the geotextiles occurred in the area near the middle of the wall facing.

Wu et al. (2006) performed another study on two GRS abutments in Turner-Fairbank, Virginia. One of the abutments used strong geotextile reinforcement with an ultimate tensile strength of 70 kN/m and the second abutment used weak geotextile reinforcement with an ultimate tensile strength of 21 kN/m. After the construction of these abutments, a series of vertical loads with a 50-kPa increment were applied on a 0.91-m wide rigid sill seated near the wall facing on the top of abutments. The vertical and lateral deformations and strains in reinforcement were measured during the loading. Similar to the findings from Wu et al. (2001), the vertical and lateral deformations and strains in the reinforcement increased with the applied load. Figure 8 shows the load-vertical deformation relationship of the GRS abutments under stage loading. It can be seen that the bearing capacity of the abutment using the strong reinforcement was beyond 900 kPa while the bearing capacity of the abutment using the weak reinforcement barely reached 400 kPa. Under the same load, the abutment using the weak reinforcement produced about twice the vertical deformation than the one using the strong reinforcement. This phenomenon was also found in the lateral deformation. The maximum strains in the strong and weak reinforcement were about 2.0% and 1.7% at 200-kPa applied load, respectively. These measured results indicate that the stiffness of reinforcement had a significant effect on vertical and lateral deformations but a minimal effect on the strains in the reinforcement.

In addition, the measured vertical earth pressures at the bottom of the abutments linearly decreased with the distance away from the facing. The method based on the 2(H):1(V) load distribution recommended could roughly estimate the vertical pressures at the bottom of the abutment.

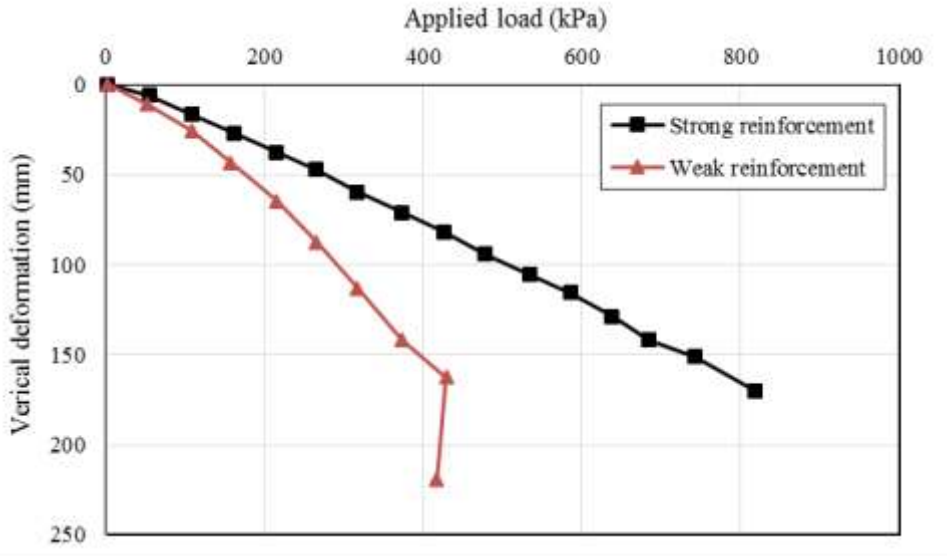

Figure 2.2 Vertical deformation of the GRS abutments (after Wu et al., 2006)

Adams and Saunders (2007) conducted a field test of GRS-IBS. The GRS-IBS used a wrapped-around facing and had a 1.5 m wall height. Settlement and lateral deformation were measured using magnetic extensometers and an inclinometer, respectively. The measured settlement of the bridge footing was smaller than 37.5 mm and the differential settlement between the bridge and its neighboring road was about 13 mm, which implied that no bump developed at connection.

In addition to the field tests, Adams et al. (2011) introduced the basic principles of GRS structures and proposed the methods to calculate the ultimate bearing capacity of the

footing on the GRS system and the required reinforcement strength in the reinforcement. The analytical solution was developed based on the concept of passive failure of a confined composite soil column with an apparent cohesion. The confinement by the wall facing, the geosynthetic vertical spacing, the geosynthetic tensile strength, the maximum particle size of backfill, and the friction angle of backfill contribute to the ultimate bearing capacity of the footing. The required tensile strength of the geosynthetic reinforcement depends on the lateral earth pressure, the geosynthetic vertical spacing, the maximum particle size of backfill, and the friction angle of backfill. In addition, Adams et al. (2011) proposed a method to estimate the lateral deformation of the wall facing based on the assumption that the volume change in the GRS composite is zero. This assumption led to a relationship that the lateral strain is half of the vertical strain.

Table 2.3 Summary of field or experimental test of GRS walls

No.	1	2	3	4	5	6	7	8
Authors	Wu	Wu	Wu	Wu	Wu et al.	Adams and Saunders	Adams et al.	Adams et al.
Years	2001	2001	2001	2001	2006	2007	2011	2011
Locations	Havana Yard	Havana Yard	Turner Fairbank	Black Hawk	Turner Fairbank	Cecil Creek	Vine Street	Glenburg Road
Structure type	GRS pier	GRS abutment	GRS pier	GRS abutment	GRS abutment	GRS-IBS	GRS-IBS	GRS-IBS
Wall facing	Modular blocks	Modular blocks	Modular blocks	Modular blocks	Modular blocks	Wraparound	Modular blocks	Modular blocks
H (m)	7.62	7.62	5.3	7.62	4.7	1.5	3.7 (3.1)	3.4
S (m)	0.2	0.2	0.2	0.2	0.2	0.2	N/A	N/A
Geosynthetic type	Woven geotextile	Woven geotextile	Woven geotextile	Woven geotextile	Woven geotextile	Woven geotextile	N/A	N/A
Backfill material	Road base material with 13% fine particle	Road base material with 13% fine particle	Well graded gravel (crushed diabase)	Silty sand with clay (12% fine particle)	Non-plastic Silty Sand (SP-SM)	Base coarse aggregate	N/A	N/A
Foundation	Reinforced soil foundation	Reinforced soil foundation	Reinforced soil foundation	Reinforced soil foundation	Reinforced concrete foundation	N/A	N/A	N/A
Instrumen-tation	Leveling rod, elastic springs, and strain gauges	Leveling rod, elastic springs, and strain gauges	Potentiometers, LVDTs, dial gauges and strain gauges	Surveying targets, digimatic indicators, and strain gauges	Potentiometers, LVDTs, strain gauges and contact pressure cells	Magnetic extensometer, inclinometer and surveying targets	Standard Survey level & rod system	Standard Survey level & rod system
Measured results	Vertical and lateral deformations, stains in reinforcement	Vertical and lateral deformations, stains in reinforcement	Vertical and lateral deformations, stains in reinforcement	Vertical and lateral deformations, stains in reinforcement	Lateral deformation, settlement and strains	Lateral deformation, settlement and calculated angular distortion	Total and differential settlement	Total and differential settlement

Note: H represents wall height, S represents vertical reinforcement spacing, and EDM represents Electronic Distance Measurement

Table 2.3 Summary of field or experimental test of GRS walls (continued)

No.	9	10	11	12	13	14	15	16
Authors	Adams et al.	Adams et al.	Vennapusa et al.	Vennapusa et al.	Bloser et al.	Alzamora	Budge et al.	Warren et al.
Years	2011	2011	2012	2012	2012	2013	2014	2014
Locations	Huber Road	Bowman Road	Olympic Avenue, Buchanan County, Iowa	250th Street, Buchanan County, Iowa	Mt. Pleasant Road Bridge, Pennsylvania	Massachusetts	Rock County Highway 55, Minnesota	Tiffin River
Structure type	GRS-IBS	GRS-IBS	GRS-IBS	GRS-IBS	GRS-IBS	GRS-IBS	GRS-IBS	GRS-IBS
Wall facing	Modular blocks	Modular blocks	Wraparound	Wraparound	Modular blocks	Modular blocks	Modular blocks	Modular blocks
H (m)	3.9	5.0	1.14	1.14	N/A	N/A	6.81	5.0
S (m)	N/A	N/A	0.2	0.2	0.2	0.2	0.2	0.2
Geosynthetic type	N/A	N/A	Woven geotextile	Woven geotextile	Geotextile	N/A	Geogrid	Woven geotextile
Backfill material	N/A	N/A	Well graded Gravel with sand	Well graded Gravel with sand	AASHTO No. 8 coarse aggregate	N/A	Crushed granite material	N/A
Foundation	N/A	N/A	Reinforced soil foundation	Reinforced soil foundation	Reinforced soil foundation	Reinforced soil foundation	Reinforced soil foundation	Reinforced concrete foundation
Instrumen-tation	Standard Survey level and rod system	EDM and total station system	Piezometers, earth pressure cells and inclinometer	Piezometers, earth pressure cells and inclinometer	Survey pole	Survey targets, earth pressure cells, inclinometer and inertial profilometer	Earth pressure cells and weather station	EDM, total station system and earth pressure cells
Measured results	Total and differential settlement	Total and differential settlement	Settlement and lateral deformations, vertical and lateral earth pressure	Settlement and lateral deformations, vertical stresses and lateral earth pressure	Settlement	N/A	Vertical and horizontal deformations, earth pressure and thermal cycle effects	Settlement and horizontal deformations, vertical and lateral earth pressure

Note: H represents wall height, S represents vertical reinforcement spacing, and EDM represents Electronic Distance Measurement.

2.3.3. Numerical methods

Similar to the GMSE walls, numerical methods have also been successfully used to simulate GRS walls (e.g. Wu et al. 2006; Pham 2009). Literature review of experimental studies and field instrumentation of GRS structures has been presented in the preceding section. This section will present a review on numerical simulation of the GRS structures. Table 2.4 summarizes the information of these numerical studies of the GRS structures.

Limited numerical studies have been done so far on the GRS structures. All these studies used the finite element method. Most of the numerical analyses were done in 2D under working or ultimate strength conditions. The GRS structures analyzed had the following parameters: (1) wall height ranging from 1.9 m (6.2 ft.) to 6.7 m (22.0 ft.), (2) reinforcement length ranging from 1.4 m (4.6 ft.) to 5.0 m (16.7 ft.), (3) reinforcement spacing ranging from 0.2 m (0.7 ft.) to 0.4 m (1.3 ft.), (4) geologic cap or hardening soil model, (5) mostly linearly elastic geosynthetic elements, (6) fully-bonded interface between geosynthetic and soil, (7) use of interface between backfill soil and facing block, and interface between facing blocks, and (8) compressible or incompressible foundation. In all the reviewed GRS-IBS studies, no seismic condition was considered. A brief description of each study is presented below.

The early numerical simulation of GRS-IBS was conducted by Wu et al. (2006). In their study, a finite element code DYNA3D/LS-DYNA was employed to estimate the allowable bearing pressure a bridge can convey to GRS abutments with flexible facing under static conditions. The numerical analysis used a geologic cap model to capture the dilation and time dependency of the backfill material. The geosynthetic reinforcement was

modeled as an elastic material. The bearing capacities based on two criteria were compared . Moreover, Wu et al. (2006b) recommended a bearing capacity for preliminary design.

Helwany et al. (2007) used the same finite element code and the same geologic cap soil model as Wu et al. (2006) did to study the performance of GRS bridge abutments. Helwany et al. (2007) used an isotropic elastic-plastic model to describe the response of the geosynthetic reinforcement. The vertical and horizontal displacements under different surcharge loading from the numerical modeling were compared with those from the two experimental tests. Additionally, a parametric study was conducted to evaluate the effects of the geosynthetic spacing, the backfill friction angle, and the geosynthetic stiffness on the performance of the GRS bridge abutments including the vertical displacement and horizontal displacements at the beam seat, the maximum facing displacement, and the footing distortion. The parametric results showed that the geosynthetic stiffness at 2% strain had a significant effect on the performance of the GRS bridge abutment, the geosynthetic spacing had a moderate effect, and the fill friction angle had the least effect.

Pham (2009) utilized a 2D finite element software, Plaxis2D, to study the composite behavior of GRS considering the effect of compaction induced stress. In his analysis, the backfill soil was modeled by a hardening soil model that is a hyperbolic model considering elastic-plastic and dilative behavior of soil. A special tension element provided by Plaxis2D was used to simulate the geotextile reinforcement. The interface between geotextile reinforcement and backfill material was assumed fully bonded. Pham's study reached the following key conclusions: (1) the numerical method can simulate the behavior of soil-geosynthetic composites; (2) the soil-geosynthetic composites become strong when

the dilation of backfill is restrained by geosynthetic reinforcement; and (3) the numerical model verified the derived analytical solution for the compaction induced stress.

Table 2.4 Summary of numerical modeling of GRS walls

No.	1	2	3	4
Authors	Wu et al.	Helwany et al.	Pham	Wu et al.
Year	2006	2007	2009	2013
Type of structure	GRS-IBS	GRS-IBS	GRS-IBS	GRS-IBS
NM	FEM	FEM	FEM	FEM
Software	DYNA3D/LS-DYNA	DYNA3D/LS-DYNA	Plaxis	Plaxis
2D or 3D	2D	2D and 3D	2D	2D
H (ft.)	15.6	15.5	6.5	6.5
L (ft.)	16.7	10.5	4.6	4.6
S (ft.)	0.7	0.7	0.7-1.3	0.7-1.3
Load on wall top	Footing to support bridge	Footing to support bridge	Uniform vertical load (Pier)	Uniform vertical load (Pier)
BCM	Geologic cap model	Geologic cap model	Hardening soil model	Hardening soil model
RCM	Linearly elastic	Isotropic elastic-plastic considering linear strain hardening and material failure	Linearly elastic; geosynthetic element	Linearly elastic; geosynthetic element
BRI	Not described	Fully bonded	Fully bonded	Fully bonded
BBI	Not described	Yes	Not described	Not described
BI	Not described	Yes	Yes	Yes
CIS	No	No	Yes	Yes
Foundation type	Compressible	Compressible	Incompressible	Incompressible
Stress conditions	Working stress and ultimate strength	Working stress and ultimate strength	Working stress	Working stress

Note: H: wall height; L: reinforcement length; S: reinforcement spacing.

2.4. Hybrid GRR walls

Hybrid GRR walls are a wall type between typical GMSE walls and GRS walls. In this new wall system, there are long and strong primary reinforcement and short and weak secondary reinforcement. Leshchinsky (2000) stated that the use of secondary reinforcement between primary reinforcement layers could mitigate the problems resulting from the large vertical spacing of primary reinforcement in GRR walls. Leshchinsky (2000) indicated that the inclusion of secondary reinforcement can result in the following benefits: (1) a reduction in connection load for primary reinforcement, (2) an increase in internal stability from lower layers of secondary reinforcement, (3) an improved compaction near the wall facing, and (4) an alleviation of down-drag behind the wall facing. Leshchinsky and Vulova (2001) employed a numerical method to investigate the influence of secondary reinforcement on the performance of hybrid walls. Their study illustrated that the inclusion of secondary reinforcement could reduce the connection load in the primary reinforcement, increase wall internal stability, and change the failure mode from connection failure to compound failure. Han and Leshchinsky (2006) and Leshchinsky et al. (2014) used a limit equilibrium method to investigate the effect of secondary reinforcement on the behavior of GRR walls. In addition to these theoretical and numerical analyses of the hybrid GRR wall, Jiang et al. (2015) performed field tests to investigate the effect of the secondary reinforcement on the performance of hybrid GRR walls. The results from the field tests confirmed that the secondary reinforcement could reduce the lateral deformation of wall facing, reduce the connection load, and the tensile force in the primary reinforcement. Jiang et al. (2015) also found that the secondary reinforcement changed the lateral earth pressure distribution to a more uniform one.

Chapter 3 Material Properties

In this chapter, tests were performed to obtain the physical and mechanical properties of the materials used in the test walls. The tested materials included backfill soil, retained soil, and geogrid. The test results are not only used to evaluate the performance of GRR walls in field test, but also used to determine related material parameters in numerical modeling.

3.1. Backfill soil

The backfill soil used in the field MSE wall was aggregates. The aggregates were produced by a local quarry in Bonner Springs in Kansas. Representative aggregates were taken from the test site. The tests conducted in the laboratory and field were sieve analysis tests, standard Proctor tests, sand cone tests, plate loading tests, and triaxial shear tests.

3.1.1. Sieve tests

Sieve analysis tests were performed in the laboratory to determine the particle size distribution of the aggregate for the backfill soil. These sieve analysis tests followed the ASTM C136 standard. Figure 3.1 shows the particle size distribution of this aggregate. The particle size distributions of the aggregate were within the upper and lower bounds.

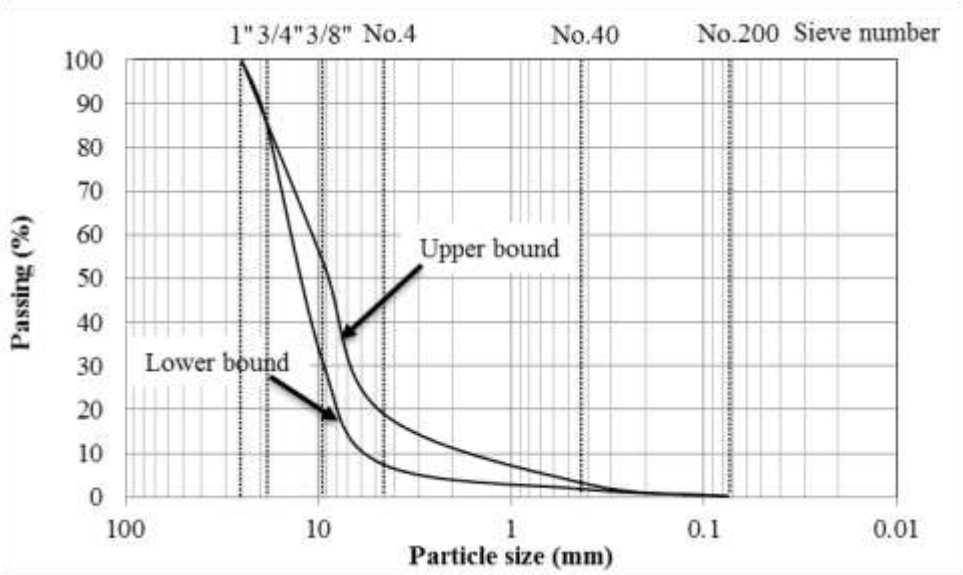

Figure 3.1 Particle size distribution of the backfill soil

3.1.2. Standard Proctor tests

Standard Proctor tests were performed to obtain the maximum dry unit weight and its corresponding optimum moisture content of the aggregate. According to the particle size distribution of the aggregate, less than 30% particles of the aggregate was retained on the 19 mm sieve. Therefore, Method C in the ASTM D698 standard was adopted. Figure 3.2 shows the compaction curve of this aggregate. The maximum dry unit weight of the aggregate was 16.8 kN/m^3 and its corresponding optimum water content was 2.65%.

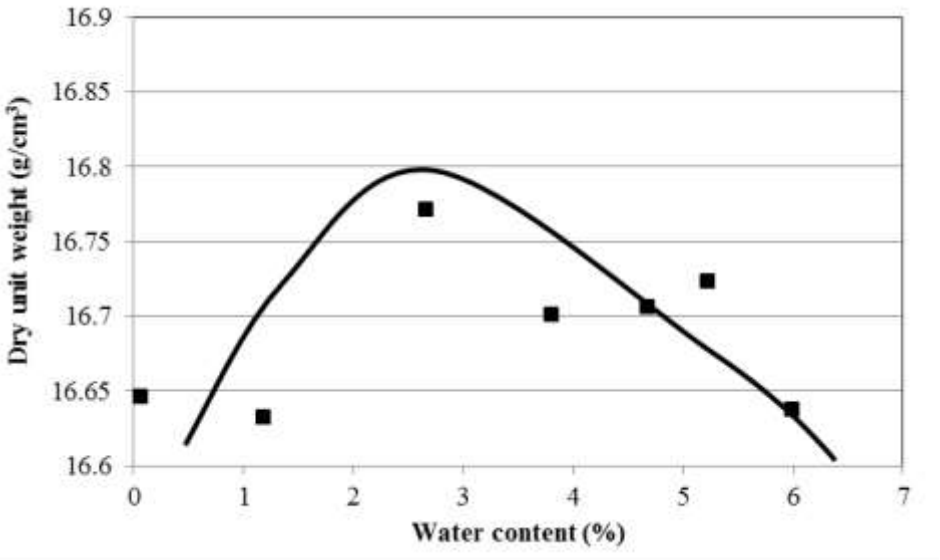

Figure 3.2 Results of standard Proctor tests

3.1.3. Sand cone tests

During construction, two types of equipment were used to compact the aggregate. One was a roller compactor and the other one was a light-weight plate compactor, as shown in Figure 3.3. The light-weight plate compactor was used to compact the aggregate within 1 m behind the back of wall facing; while the roller compactor was used to compact the aggregate of 1 m away from the back of wall facing.

Sand cone tests were performed at selected locations in these two areas. The procedures of sand cone tests followed the ASTM D1556 standard. Additionally, in each sand cone test, a piece of thin plastic wrap was placed and fully in contact with the top surface of aggregates. This piece of thin plastic wrap was used to prevent loss of sand into aggregates. Four sand cone tests were conducted in the area within 1 m behind the back of wall facing; while eight sand cone tests were conducted in the area of 1 m away from the back of wall facing. Figure 3.4 shows the operation of sand cone tests at two different

compaction areas in the field. The average moist unit weight of the compacted aggregate was 18.1 kN/m^3 and its corresponding average moisture content was 3.1%; therefore, the average unit weight of the aggregate was 17.5 kN/m^3. In addition, the relative compaction of aggregate was more than 100%.

Figure 3.3 Roller compactor and light-weight plate compactor

(a) The location within 1 m behind the back of wall facing

(b) The location away from 1 m behind the back of wall facing

Figure 3.4 Sand cone tests in the field

3.1.4. Plate loading tests

Plate loading tests were conducted in the laboratory to obtain the load-displacement curves of the aggregate, which would be used to estimate the elastic modulus of the aggregate in the numerical study. Figure 3.5 shows the setup of one plate loading test. The equipment of the plate loading test included a wood box, a reaction frame, an air cylinder, and a circular loading plate. The dimension of the wood box was 0.6 m in length, 0.6 m in width, and 0.5 m in height. The diameter of the loading plate was 0.15 m. In addition, the thickness of the compacted aggregate underneath the loading plate in the wood box was 0.4 m. The length and width of the wood box were four times larger than the diameter of the loading plate; while the thickness of the aggregate was four times larger than the diameter of the loading plate. As a result, the boundary effect was minimized.

In order to find the relationship between the unit weight and the modulus of the aggregate, three plate loading tests were performed on the aggregate at three different unit weights. The aggregate was compacted in the wood box with three lifts. Each lift did not exceed 0.2 m. An air hammer compactor was employed to compact the aggregate to the desired density with a level surface. A less than 1.3 cm layer of sand was placed on the top surface of the aggregate underneath the loading plate. After that, loads were applied in increments on the aggregate until the aggregate failed or the 723-kPa loading capacity of the air cylinder was reached. At each load increment, a stable settlement and its corresponding load were recorded for the load-displacement curve. The detailed procedures of the plate loading test followed the ASTM D1196 standard.

Figure 3.6 shows the load-displacement curves of the aggregate at three unit weights. The aggregate at a higher unit weight had less settlement at the same load. In other words, the aggregate at a higher unit weight had a higher elastic modulus. Equation (3.1) was used to calculate the elastic modulus of the aggregate based on the linear portion of the load-displacement relationship:

$$E = \frac{qB\left(1-\upsilon^2\right)}{s} I_f \tag{3.1}$$

where E = elastic modulus, q = applied pressure on the aggregate, B = width of the loading plate, υ = Poisson's ratio, s = displacement, and I_f = influence factor for the circular loading plate. Figure 3.7 shows that the modulus of the aggregate had a good linear relationship with the density.

Figure 3.5 Setup of a plate loading test

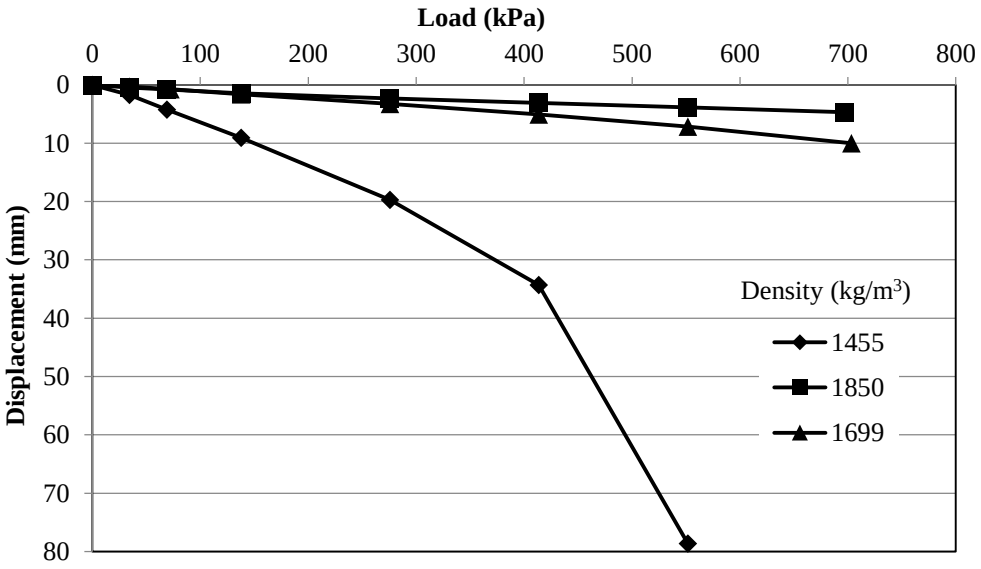

Figure 3.6 Load-displacement relationship of the aggregate at three compaction unit weights

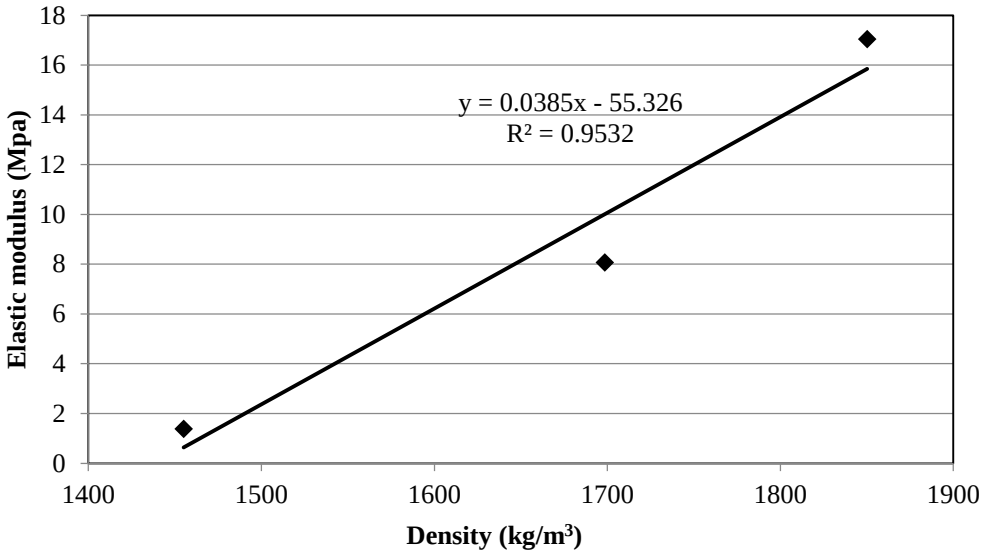

Figure 3.7 Relationship between modulus and unit weight of the aggregate

3.1.5. Triaxial tests

Triaxial shear tests were performed to obtain stress-strain relationships and shear strength of the aggregate. According to the maximum particle size of the aggregate, the aggregate samples with a diameter of 10 cm and a height of 20 cm were prepared in the tests to minimize the boundary effect. Figure 3.8 shows the setup of a triaxial shear test. The tests were conducted at three confining stresses to obtain a Mohr-Coulomb envelope. The confining stresses of 50, 100, and 200 kPa were selected and applied to the samples to simulate the overburden stresses of the aggregate at three depths in the field. The confining stress was applied after the sample was saturated. Each sample was tested under a drained condition. In addition to the strain and stress measured in the test, the volume change of the sample was measured. The procedures for triaxial shear tests were in accordance with the ASTM D7181 standard.

Figures 3.9 (a) and (b) show the stress-strain relationships and the axial-volumetric strain relationships of the aggregate at three confining stresses, respectively. Figure 3.9 (a) shows that the strains at three confining stresses gradually increased with an increase of the deviatoric stresses until the sample reached the critical state. The peak friction angle of the aggregate, ϕ_{peak} = 47° was obtained. In addition, the aggregate had the dilative behavior under the confining stresses of 50 and 100 kPa.

Figure 3.8 Setup of a triaxial shear test

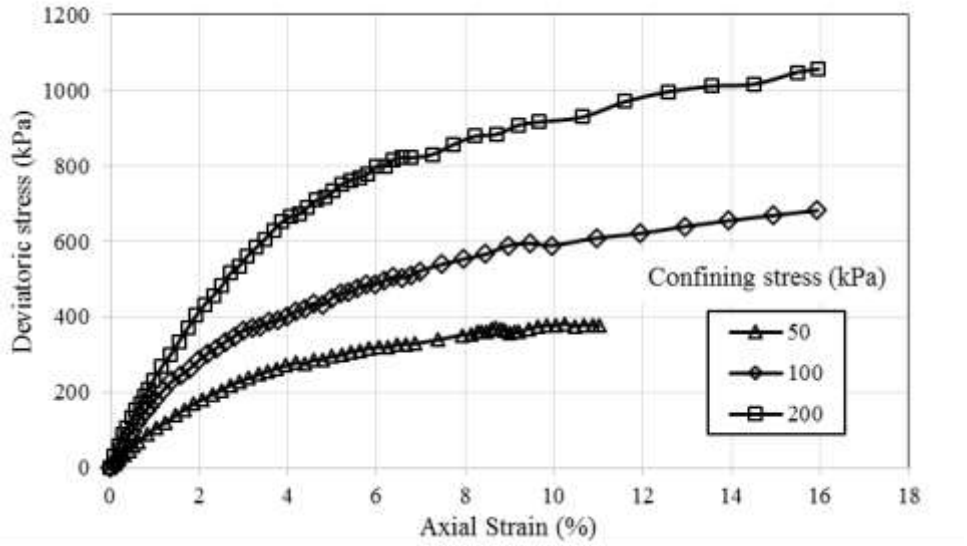

(a) Stress-strain relationships

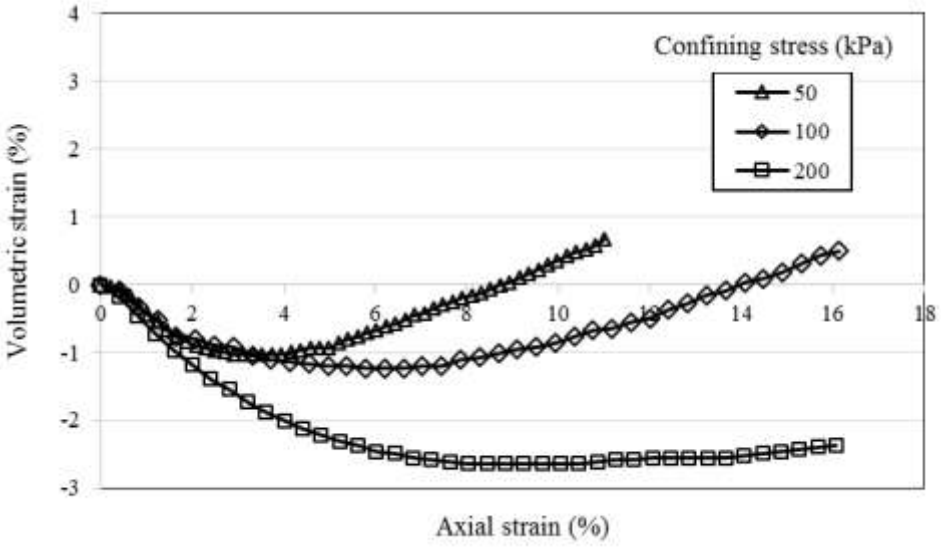

(b) Axial-volumetric strain relationships

Figure 3.9 Triaxial shear test results of the aggregate

3.2. Retained soil

The retained soil in the field test was a borrow soil. This soil was obtained from a site nearby the field test site. Atterberg limit and sand cone tests were conducted in the laboratory and in the field, respectively, to obtain the physical properties of the retained soil.

3.2.1. Atterberg limits tests

Atterberg limit tests were conducted to obtain plastic limit (PL) and liquid limit (LL) of the retained soil. The retained soil was first dried in an oven at 110° for 24 hours. The dry soil was smashed and ground. This ground soil that passed No. 40 sieve was kept to carry out the Atterberg limit tests. The test procedures for PL and LL followed the ASTM D4318 standard. The measured LL and PL of the retained soil were 42 and 20, respectively. The plastic index was calculated to be 22 based on Equation (3.2):

$$PI = LL - PL \tag{3.2}$$

According to the plasticity chart (shown in Figure 3.10), the retained soil is classified as CL. Furthermore, the shrinkage limit of the retained soil was 15 according to Holtz and Kovacs (1981).

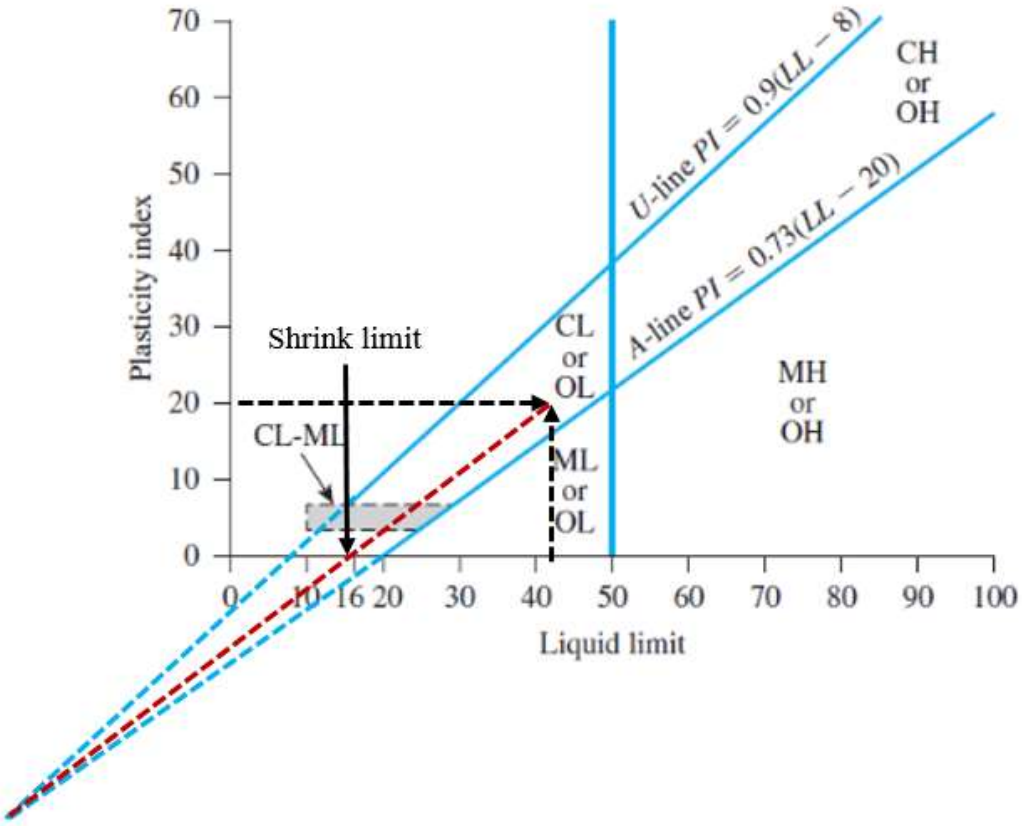

Figure 3.10 Plasticity chart (modified from ASTM D2487 standard)

3.2.2. Sand cone tests

The retained soil was compacted by a sheep foot roller in the field. Sand cone tests were carried out to measure the unit weight of the compacted retained soil. The procedures of the sand cone tests were consistent with the ASTM D1556 standard. The moist unit weight of the retained soil was 20.3 kN/m^3 and its corresponding moisture content was 21%. The dry density of the retained soil was 16.8 kN/m^3.

3.3. Geogrid

Five types of geogrid were used in the field test as reinforcement. Four of them were uniaxial (UX) HDPE geogrid and one of them was biaxial (BX) polyethylene geogrid. The pictures of UX and BX geogrid are shown in Figures 3.11 (a) and (b), respectively. The physical and mechanical properties of the geogrid provided by the manufacturer are shown in Table 3.1. The following properties of BX geogrid are presented in the cross-machine direction (XMD): initial modulus = 400 kN/m, tensile strength at 2% strain = 6.6 kN/m, and junction efficiency = 93%.

(a) Uniaxial geogrid

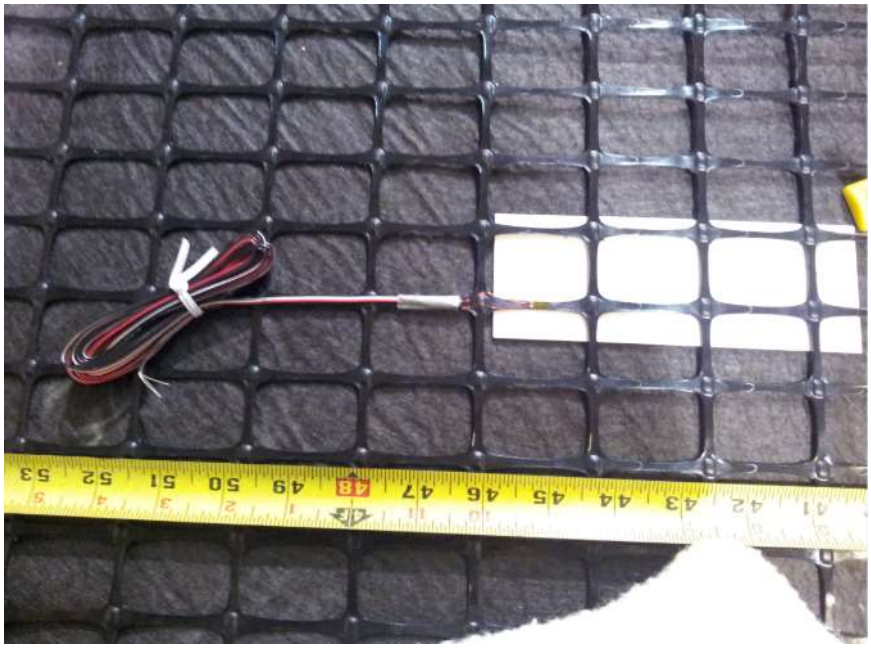

(b) Biaxial geogrid

Figure 3.11 Two types of geogrid

Table 3.1 Properties of geogrid (provided by manufacturer)

Property	UX1	UX2	UX3	UX4
Ultimate tensile strength (kN/m)	58	70	114	144
Maximum allowable (design) strength for 120-year design life (kN/m)	21.2	25.6	41.8	52.7
Reduction factor for installation damage RF_{ID}	1.05			
Reduction factor for creep RF_{CR}	2.6			
Reduction factor for durability RF_{D}	1.0			

Note: The relevant BX properties are in the cross-machine direction (XMD); true initial modulus of BX in use is 400 kN/m; tensile strength at 2% strain of BX is 6.6 kN/m; junction efficiency of BX is 93%.

3.3.1. Tests for global strain and local strain

In the field test, strain gauges were attached on the geogrid to measure strains of geogrid. Perkins et al. (1997) and Bathurst et al. (2002) found that the measured local

strains on a geogrid by strain gauges might be different from the global strains of the geogrid because of the geogrid apertures. The difference between local and global strains depends on geogrid type.

Laboratory tests were conducted to establish the relationships between local and global strains of the geogrid used in this study. Figure 3.12 shows the setup of the test. The procedures of the ASTM D6637 standard that are used to measure the tensile strength of geogrid were adopted to conduct this test. Figure 3.13 shows the relationships of the local and global strains of the geogrid. A calibration factor (CF) was used to describe the relationship, which is defined as the ratio of global strain to local strain. The global strains linearly increased with the local strains at the beginning. However, the global strains increased dramatically when the local strains approached to 2%, because the attached strain gauges were debonded from the geogrid. Therefore, the CF was computed based on the linear portion, which was prior to the debonding of strain gauges from the geogrid. The CFs for primary and secondary geogrid ranged from 1.00 to 1.29. In addition, Figure 3.14 shows the tensile stress-strain relationships of all the geogrid used in this study. The global strains of the geogrid increased nonlinearly with the tensile stresses. Under the same tensile stress, the induced global strains of the geogrid from the maximum to the minimum were BX, UX1, UX2, UX3, and UX4. These results are consistent with the properties of the geogrid provided by the manufacturer.

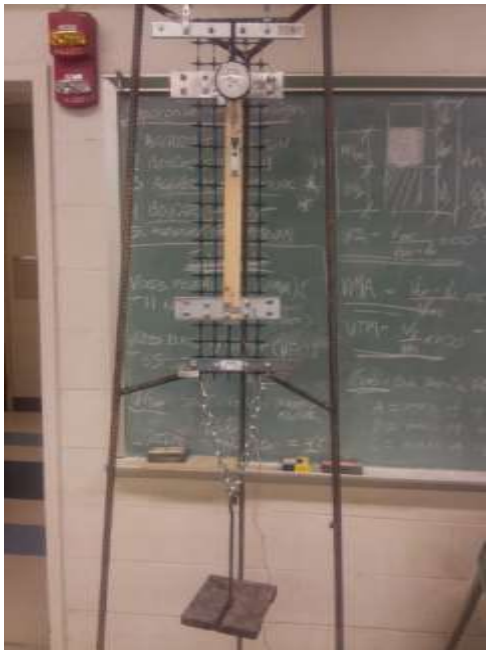

Figure 3.12 Test setup for local and global strains of geogrid

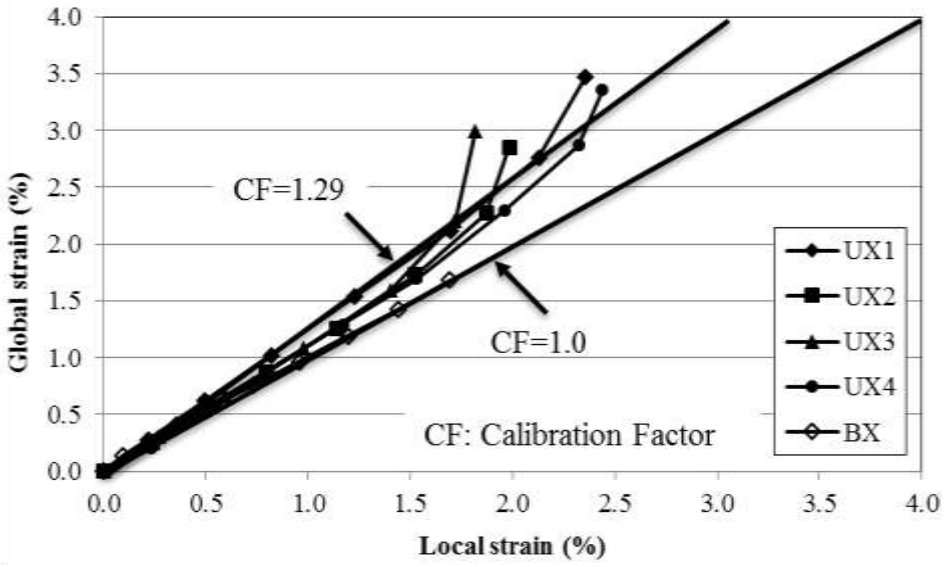

Figure 3.13 Relationships of local and global strains of geogrid

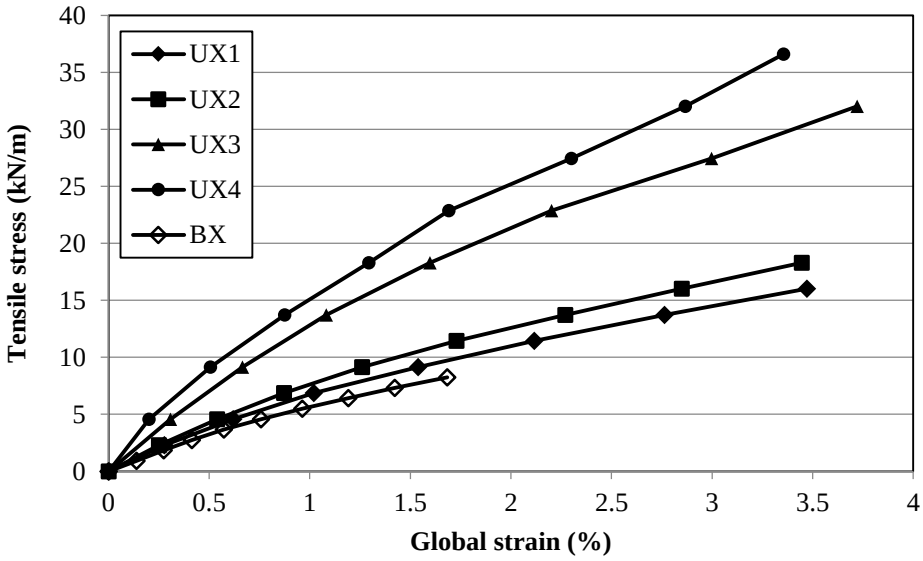

Figure 3.14 Tensile stress-strain relationships of geogrid

3.3.2. Pullout tests

A pullout testing system designed at the University of Kansas was utilized to run the pullout test for geogrid. Figure 3.3.4 shows the pictures of the pullout testing system. This new pullout testing system mainly includes a steel box with 1.5 m in length, 0.6 m in width, and 0.6 m in height, double actions hydraulic jack, hydraulic oil pump, and a clamp. The normal pressure is applied by an air bag placed on the top of soil in the sealed box. Earth pressure cells were buried underneath the geogrid to measure the actual overburden stress. A load cell and four linear variable differential transformers (LVDTs) were installed to measured pullout force and displacements of geogrid at four locations, respectively.

The procedures of the pullout tests followed the ASTM D6706 standard. Three types of geogrid were used to run the pullout tests. Each type of geogrid had three pullout tests with different normal pressures applied. Figure 3.16 show the results of the pullout tests. As shown in Figure 3.16, the pullout force increased with displacement until reached

pullout resistance. For each type of geogrid, the pullout resistance also increased with the normal pressure. A high normal pressure resulted in a high pullout resistance.

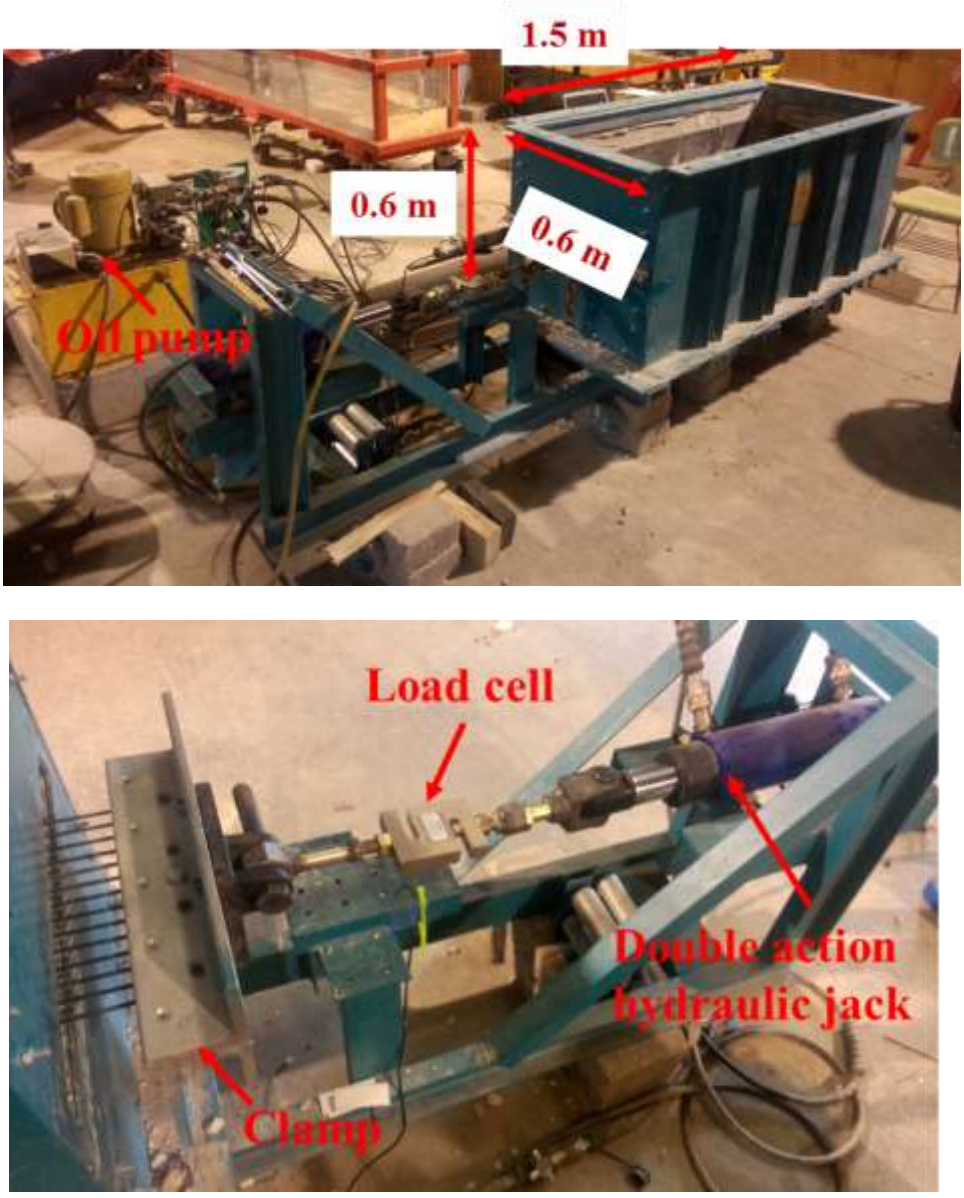

Figure 3.15 Pictures of the pullout testing system

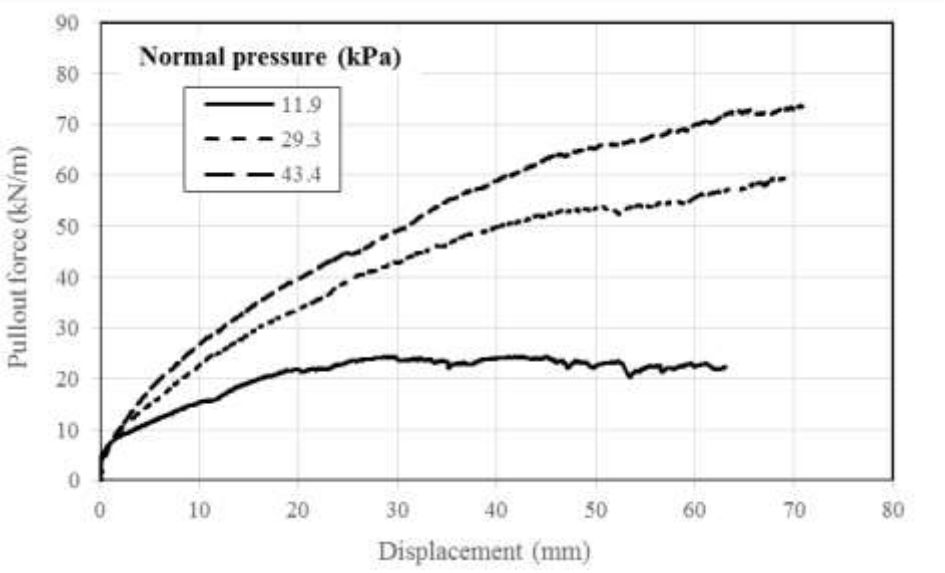
Normal pressure (kPa)
11.9
29.3
43.4
Pullout force (kN/m)
Displacement (mm)
0
10
20
30
40
50
60
70
80
90

(a) UX4

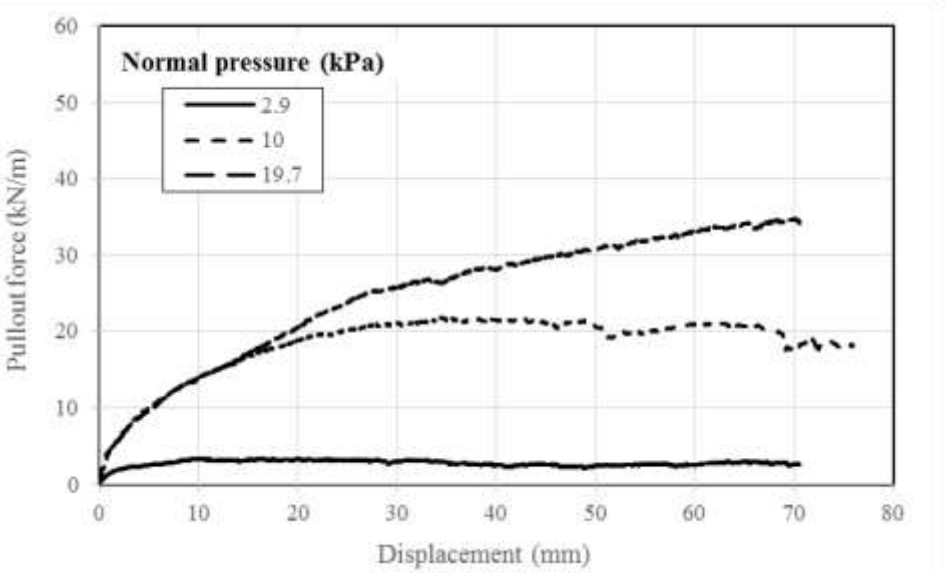
Normal pressure (kPa)
2.9
10
19.7
Pullout force (kN/m)
Displacement (mm)
0
10
20
30
40
50
60
70
80

(b) UX1

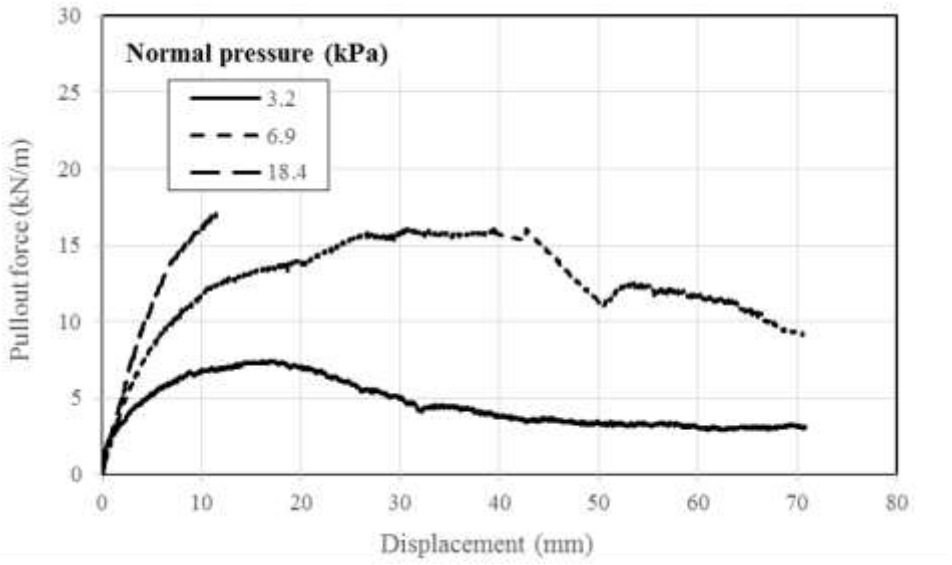

(c) BX

Figure 3.16 Results of pullout test for three types of geogrid

Chapter 4 Field Tests of GRR Wall and Hybrid GRR Walls

4.1. Project background

The GRR wall is located at Bonner Springs, Wyandotte County, Kansas. This GRR wall was constructed to support a new ramp in the Kansas DOT I-70/K-7 interchange project, as shown in Figure 4.1.

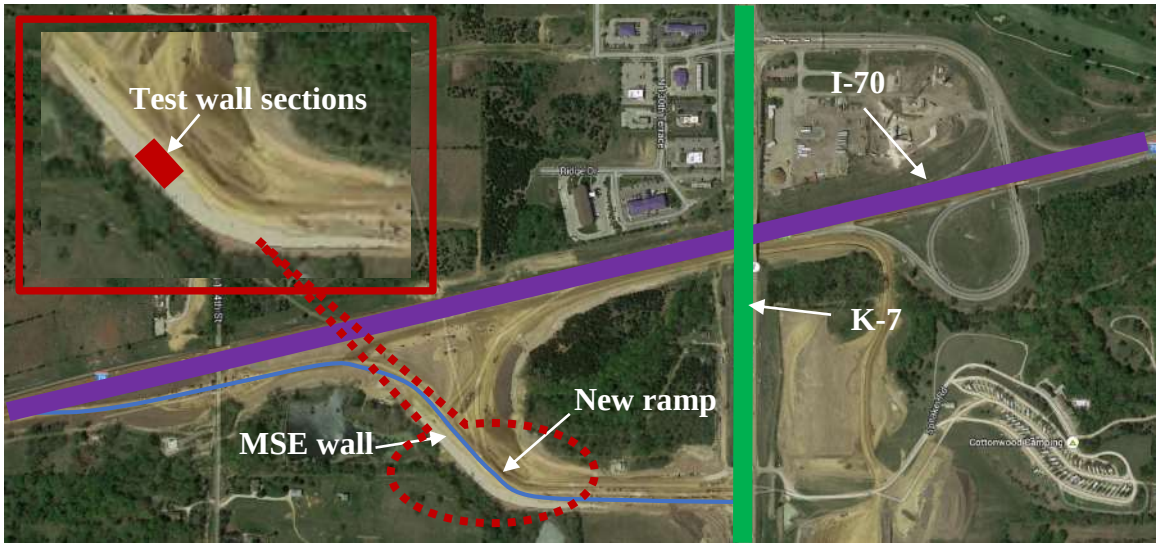

Figure 4.1 Location of three test wall sections (from Google Earth)

4.2. Wall layout

In this GRR wall, three test wall sections were selected to be monitored. Vertical separation planes were included within the wall to isolate test wall sections between each other. The vertical separations were created by inserting a slip material, which is made of a drainage composite with a 250 mil thick plastic core covered by a non-woven geotextile on each side, between facing blocks to minimize the interaction between two test wall sections next to each other. At the vertical separation, the modular blocks were cut if

needed and a slip material was inserted, which helped reduce the friction between two blocks. Figure 4.2 presents the front view of these test wall sections. The three test wall sections had a width ranging from 10.2 to 11.3 m, and had a height ranging from 11.3 to 11.9m.

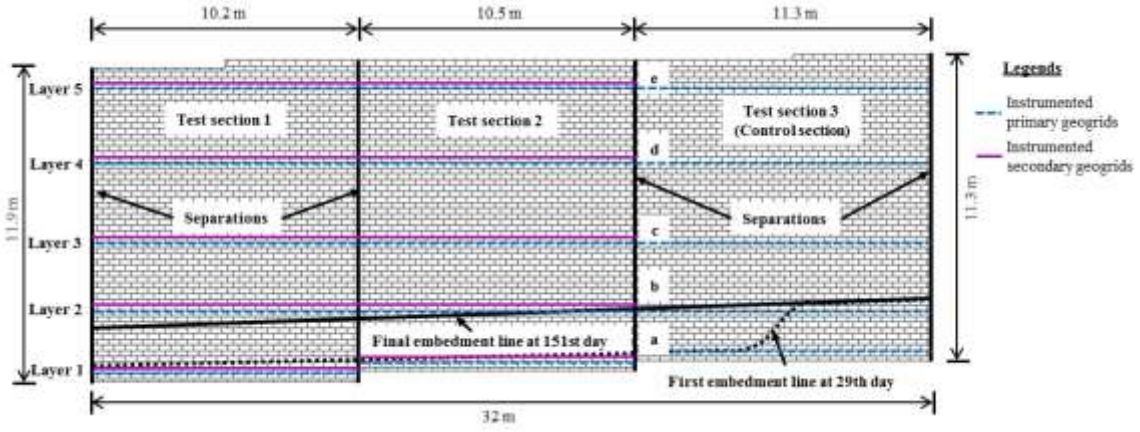

Figure 4.2 Front view of three test wall sections (not to scale)

Figure 4.3 shows the cross sections and the layout of primary reinforcement and secondary reinforcement of the test wall sections. These wall sections had 3 (H): 1 (V) toe slopes and 4:1 top slopes. The primary reinforcement lengths of TS1, TS2, and TS3 were 18.9, 18.6, and 18 m, respectively. The ratios of the primary reinforcement length to the wall height for all three test wall sections was approximately 1.6. This ratio was about two times greater than the recommended ratio of 0.7 by Elias et al. (2001), indicating that the primary reinforcement was conservatively designed by designers. The reasons for the use of such long reinforcement are that there are top and toe slopes and inaccurate information on the depth of bedrock. However, the effect of secondary reinforcement on the wall performance were not influenced by excessive long primary reinforcement. The primary reinforcement

was placed every two blocks (i.e., 0.4 m) in the lower one-third part of test wall sections and placed every three blocks (i.e., 0.6 m) in the upper two-third part of test wall sections. The secondary reinforcement in TS1 was 1.4 m long (without including tails) and placed between two primary reinforcement layers. Similarly, the secondary reinforcement in TS2 was 1.3 m long and placed between two primary reinforcement layers. The coverage ratio of both primary and secondary reinforcement in three test wall sections was 100 percent. The main difference among these test sections is the secondary reinforcement and the objective of this study was to investigate the effect of secondary reinforcement. The ratio of the section width to the secondary reinforcement length is about 7 to 8, which is typically required for a plane strain condition.

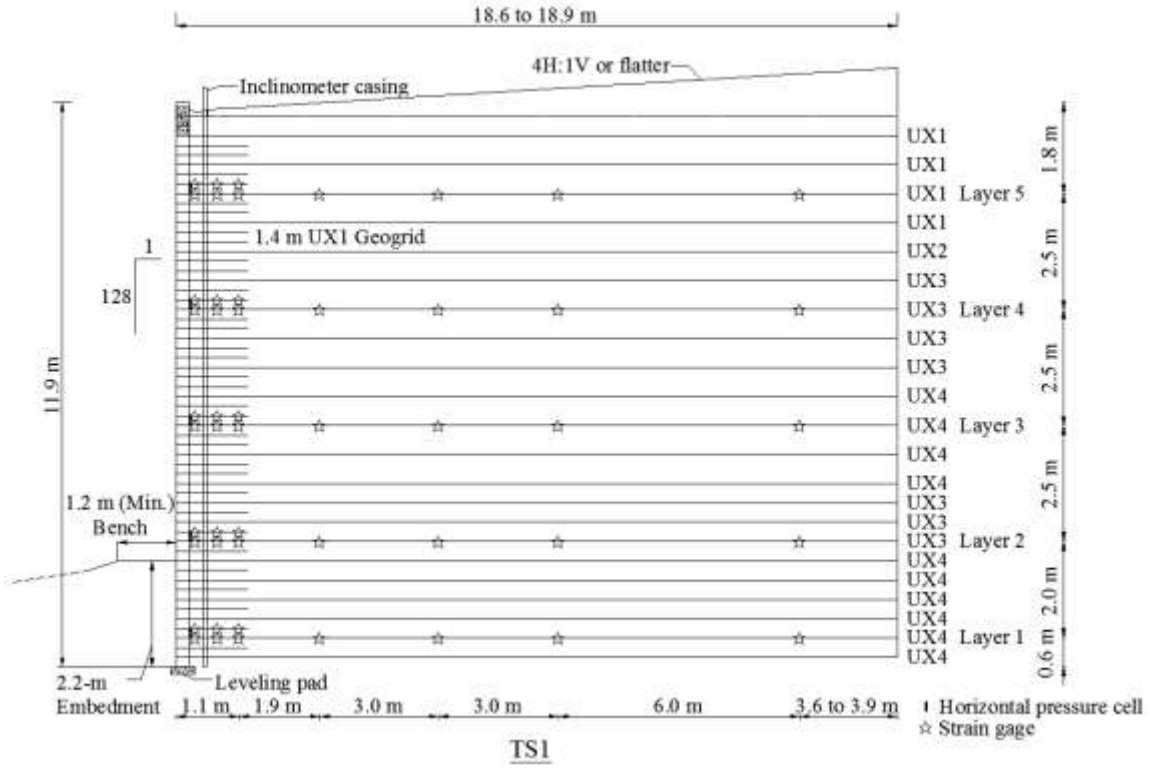

(a) TS1

Fig. 4.3 Cross sections of three test wall sections with instrumentation (not to scale)

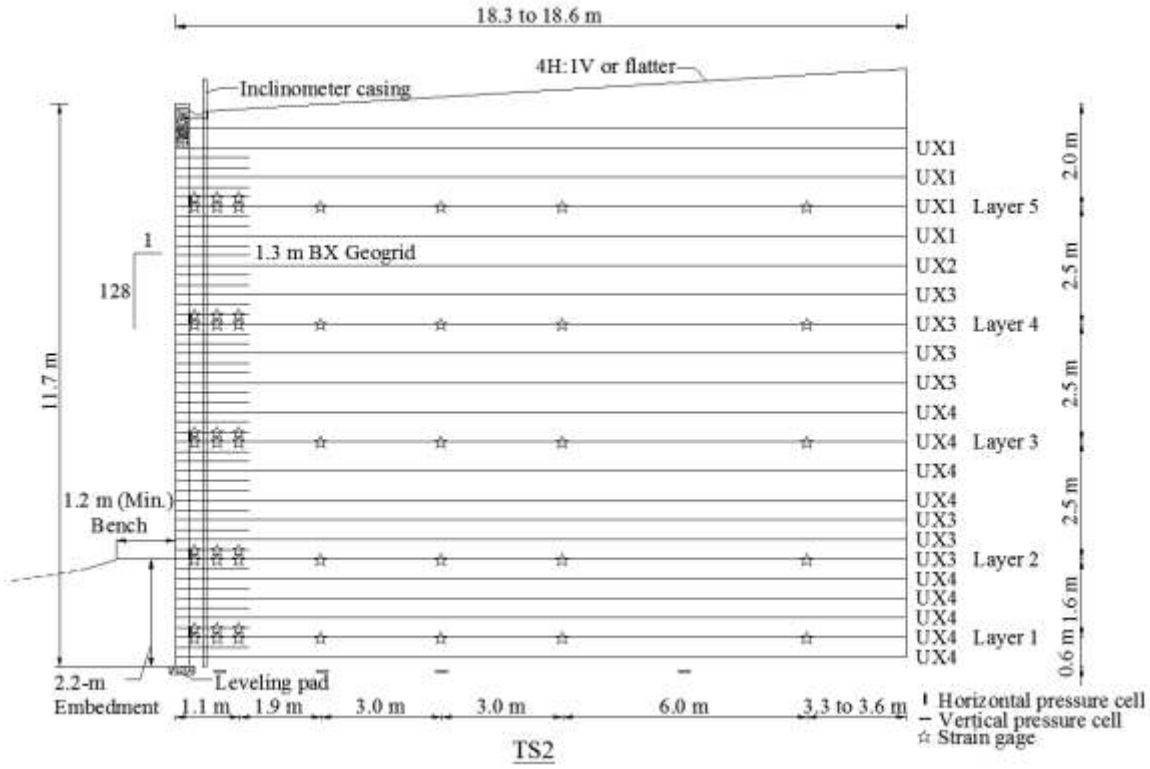

(b) TS2

Fig. 4.3 Cross sections of three test wall sections with instrumentation (not to scale)

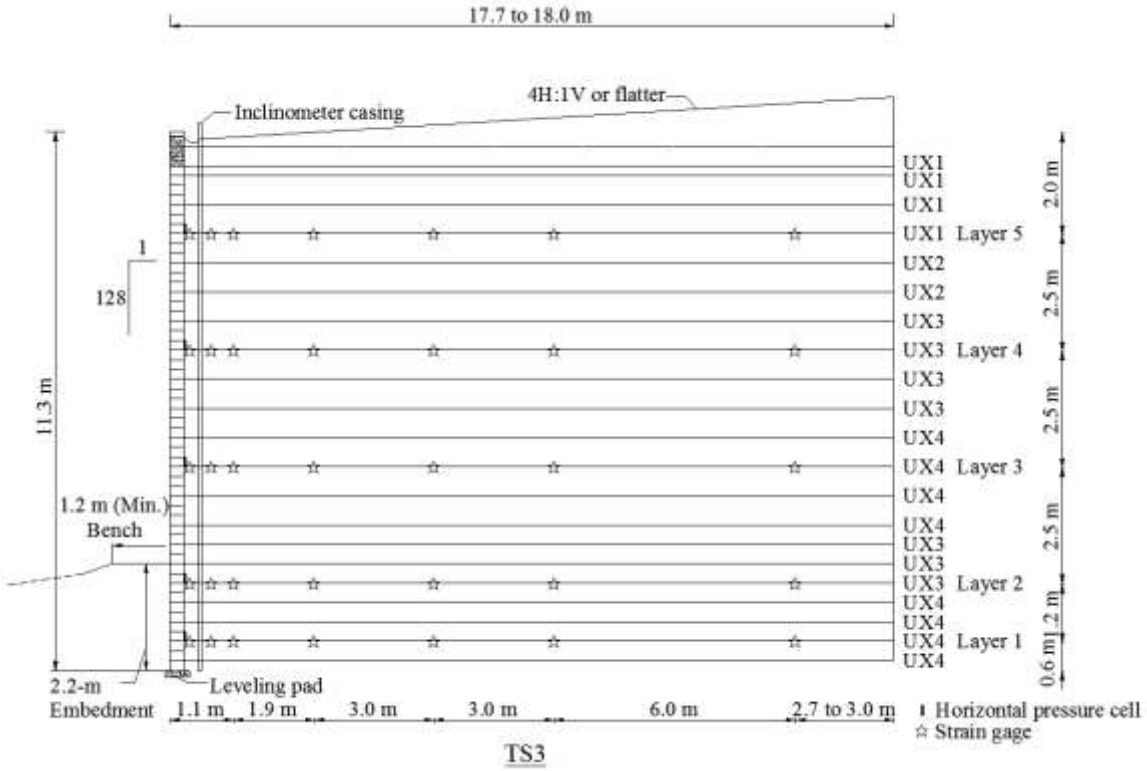

(c) TS3

Figure 4.3 Cross sections of three test wall sections with instrumentation (not to scale)

4.3. Wall design

The test wall sections were designed by the supplier and verified by the authors for the GRR wall reinforced with primary reinforcement only. The Load and Resistance Factor Design (LRFD) method included in AASHTO (2007) was used to design the test wall sections with primary reinforcement only. In this study, a software of MSEW 3.0 was employed to examine the design of the test wall sections. The MSEW 3.0 was an updated version of MSEW 1.0 that was developed for the Federal Highway Administration (FHWA) and widely used for design of MSE walls in the North America. A Capacity Demanding

Ratio (CDR) was introduced in the MSEW 3.0 for the design of MSE walls in 2006 and later was adopted by Berg et al. (2009).

The parameters used in the original analysis of three test wall sections were determined before the construction. The selection of these parameters was in accordance with AASHTO (2007). After the construction of the test wall sections, lab tests were performed on the reinforced fill to determine the parameters used in the updated analysis. Table 4.1 summarizes the soil parameters used in the wall analyses. The settlement of foundations of test wall sections were ignored because they were built on bedrock. The capacity demanding ratios (CDRs) for external and internal stability in the original and updated analyses are summarized in Table 4.2. The design of a test wall section meets the AASHTO requirements for an MSE wall. The CDRs for external stability in the updated analysis were the same as those in the original analysis because the friction angle of the retained soil used in the updated analysis was the same as that in the original analysis. The CDRs for internal stability in the updated analysis were much larger than those in the original analysis because the friction angle of the reinforced fill used in the updated analysis was larger than that in the original analysis, which dramatically reduced the lateral earth pressure.

Table 4.1 Summary of the soil parameters in the design of test wall sections

Properties	Original analysis			Updated analysis		
	Unit weight (kN/m^3)	Friction angle (degrees)	Cohesion (kPa)	Unit weight (kN/m^3)	Friction angle (degrees)	Cohesion (kPa)
Reinforced soil	18.9	34	0	18.1	47	0
Retained soil	20.3	25	0	20	25	0
Foundation soil	20.4	0	1000	20.4	0	1000

Note: The foundation of the test wall sections during the construction was confirmed to be limestone and sandstone, and the cohesion of the foundation soil were assumed to be 1000 kPa in the design.

Table 4.2 Summary of capacity demanding ratio (CDR) in the design of test wall sections

Stability		Loading factor	Resistance factor	CDR (Original analysis)			CDR (Updated analysis)		
				TS1	TS2	TS3	TS1	TS2	TS3
External stability	Base sliding	1	1	1.6	1.6	1.3	1.6	1.6	1.3
	Overturning	N/A	N/A	5.3	5.3	5.4	5.3	5.3	5.4
	Bearing capacity	1.35	0.65	8.3	8.4	8.8	8.3	8.4	8.8
	Eccentricity e/L[2]	1	1	0.04	0.04	0.04	0.04	0.04	0.04
Internal stability[1]	Rupture	1.35	0.9	1	1	1.1	1.9	1.7	1.9
	Pullout	1.35	0.9	49	45	53	166	140	158
	Connection	1.35	0.9	1	1	1	1.7	1.6	1.9

Note: [1]only minimum CDRs were shown in the table; [2] the requirement for eccentricity is e/L<0.25 (e is eccentricity and L is the length of the geogrid).

4.4. Wall construction

The construction of the test wall sections started in October 2013 and was completed by September 2014, lasting about 11 months. The test wall sections consisted of leveling pads, modular blocks, geogrid reinforcement, geotextile drainage and filter layers, reinforced backfill, and retained soil. Figure 4.4 illustrates the main construction steps of the test walls. The concrete leveling pad was cast in situ on the foundation to meet the grade and elevation requirements. Modular blocks were placed, spaced, and leveled accurately. Horizontal and vertical alignments of wall facing were examined about every 15 m and 1.2 m, respectively. The connections between primary reinforcement and wall facing, and secondary reinforcement and wall facing were mechanical connectors. Pre-tensioning by hand was performed on primary geogrid and secondary geogrid to reduce the slack before aggregates were placed on the top of them. The aggregate was placed at an uncompacted lift thickness of approximately 0.25 m. A roller compactor was used to compact the aggregate at 1 m away from the back of wall facing with four to six passes while a vibratory plate compactor was used to compact the aggregate within 1 m of the

back of wall facing. An approximately 0.1-m high concrete cap block was installed on the top as a protective course. Slip joints were set between test wall sections to reduce the interaction between two test wall sections. Blocks and geogrid were cut at each slip joint location; however, reinforced fill was not separated between two adjacent sections. The aggregate interlock became the major medium of force transmission between two MSE wall sections. The embedment of the test wall sections was constructed at two different times as shown in Figure 4.2. The control section (i.e., TS3) had more embedment compared with the other two test sections after the first completion of embedment. It resulted in more passive resistance effect in the control section as compared with TS1 and TS2. The three test wall sections had an approximate 2.2-m embedment depth after the final completion of embedment.

(a) Leveling pad

(b) Installation of primary geogrid

(c) Installation of secondary geogrid

(d) Backfill material

(e) Compaction

(f) Wall capping

Figure 4.4 Construction steps of the MSE walls

4.5. Instrumentation preparation and installation

Instrumentation, such as survey targets, inclinometer casings and probes, earth pressures cells, extensometers, telltales, and strain gauges, has been commonly employed to monitor performance of MSE walls in many studies. A detailed review of 14 instrumented MSE walls can be found in Jiang et al. (2015). Wall facing deflection, lateral earth pressure distribution, and tensile strain distribution in reinforcement are three commonly measured parameters to evaluate performance of MSE walls. In this study,

inclinometer casings, earth pressure cells, and strain gauges were employed to monitor wall facing deflections, distributions of lateral earth pressures, and distributions of tensile strains in geogrid layers during construction. Figure 4.3 presents the layout of instrumentation in the test sections in this study.

An inclinometer casing with a diameter of 85 mm was installed in each test section to measure wall facing deflections. The location of the inclinometer casing for each test wall section was approximately 0.18 to 0.35 m behind the back of wall facing. Figure 4.5 shows the installation of an inclinometer casing. The bottom of the casing was fixed into the bedrock. The inclinometer casing was spliced for extension according to wall height during construction. The wall facing deflections were measured during the construction for approximately every three blocks, and measured every two weeks if there was no construction activity. Two inclinometer readings were taken at each elevation to guarantee the accuracy and reliability of data.

(a) Drilling a borehole (b) Casing installation

Figure 4.5 Inclinometer casing installation

The pressure cells were calibrated in the soil in laboratory before they were installed in the field. The calibration results of earth pressure cells can be found in Jiang et al. (2015). The calibration results were used to calculate the measured earth pressures from pressure cells. Four vertical pressure cells were installed on the top of the foundation of TS2 to measure vertical earth pressures. The vertical pressure cells were placed close to the middle of the test wall section at four locations away from the wall facing. However, vertical pressure cells were not installed in TS1 and TS3 sections. Therefore the comparison between the three test wall sections were not made regarding the effect of the secondary reinforcement on the vertical earth pressures. Fifteen lateral pressure cells were installed in three test wall sections to measure lateral earth pressures; each test wall section had five lateral pressure cells instrumented along the wall height. The locations of the installed vertical and lateral pressure cells in three test wall sections can be seen in Figure 4.3. Figure 4.6 provides the photographs of the installation of the vertical and lateral pressure cells.

(a) Vertical pressure cell

(b) Lateral pressure cells

Figure 4.6 Installation of Vertical and lateral pressure cells

Five layers of primary geogrid were selected as instrumented layers in each test wall section. Each layer of primary geogrid was instrumented with eight strain gages at seven locations from the back of wall facing. All the strain gages were installed in the middle point of the longitudinal rib between two transverse bars. Strain gages were mounted to the top side and the bottom side of the geogrid at the first location close to the wall facing with the purpose of eliminating the bending effect of the geogrid. Five layers of UX1 secondary geogrid and five layers of BX secondary geogrid were selected and instrumented with strain gages in TS1 and TS2, respectively. Each layer of secondary geogrid had four strain gages attached at the three locations from the wall facing. Two strain gages were bonded on the top side and bottom side of the geogrid at the first location close to the wall facing with the purpose of eliminating the bending effect of the geogrid. Initial readings for strains of geogrid were taken datum readings after the first lift of aggregate was placed and compacted. The measured strain for each strain gauge was determined using the current reading minus the datum reading. The photographs of the installation of primary and secondary geogrid layers are provided in Figure 4.7.

(a) Primary geogrid

Fig. 4.7 Installation of geogrid.

(b) Secondary uniaxial geogrid

(c) Secondary biaxial geogrid

Figure 4.7 Installation of geogrid

4.6. Instrumentation results and discussion

4.6.1. Wall facing deflections

The profiles of measured accumulated wall facing deflections with wall height before and after the construction of the backslope are shown in Fig. 4.8. Since the inclinometer casing was keyed into the bedrock, the casing portion inside the bedrock was fixed and used as a reference for zero displacement. The accumulated wall facing deflection at each location shown in Fig. 4.8 was calculated by adding the deflection at the current location since the block was installed to the wall facing deflection below this

location. Figure 4.8 shows that the measured accumulated lateral wall facing deflections in the three test wall sections increased with the wall height. The maximum deflections occurred at the top of the wall. As shown in Fig. 4.8, the accumulated facing deflections increased with the construction of the backslope because additional lateral earth pressure due to the weight of the backslope was applied on the wall facing. In addition, the measured accumulated wall facing deflections within the top part of the wall section in TS1 and TS2 were lower than those in TS3 (i.e. the control section) indicating that the inclusion of secondary reinforcement reduced the accumulated wall facing deflections. In addition, the accumulated wall facing deflections in the three test wall sections after the construction of the backslope were calculated by integrating the measured strains along the length of the geogrid at each instrumented layer as shown in Fig. 4.8 (b). In this calculation, the end of each geogrid at the interface between the reinforced fill and the retained soil was taken as a reference position of zero displacement. The displacement was accumulated from the reference position towards the wall facing. The details of the measured strains will be presented in the "Global strains of geogrid" section later. Figure 4.8 (b) shows that the accumulated wall facing deflections estimated based on the measured strains of the geogrid and those from the inclinometers had similar trends and magnitudes. In addition, the maximum accumulated wall facing deflections calculated from the geogrid strains in TS3 were larger than those in TS1 and TS2. This result is consistent with that measured by the inclinometers.

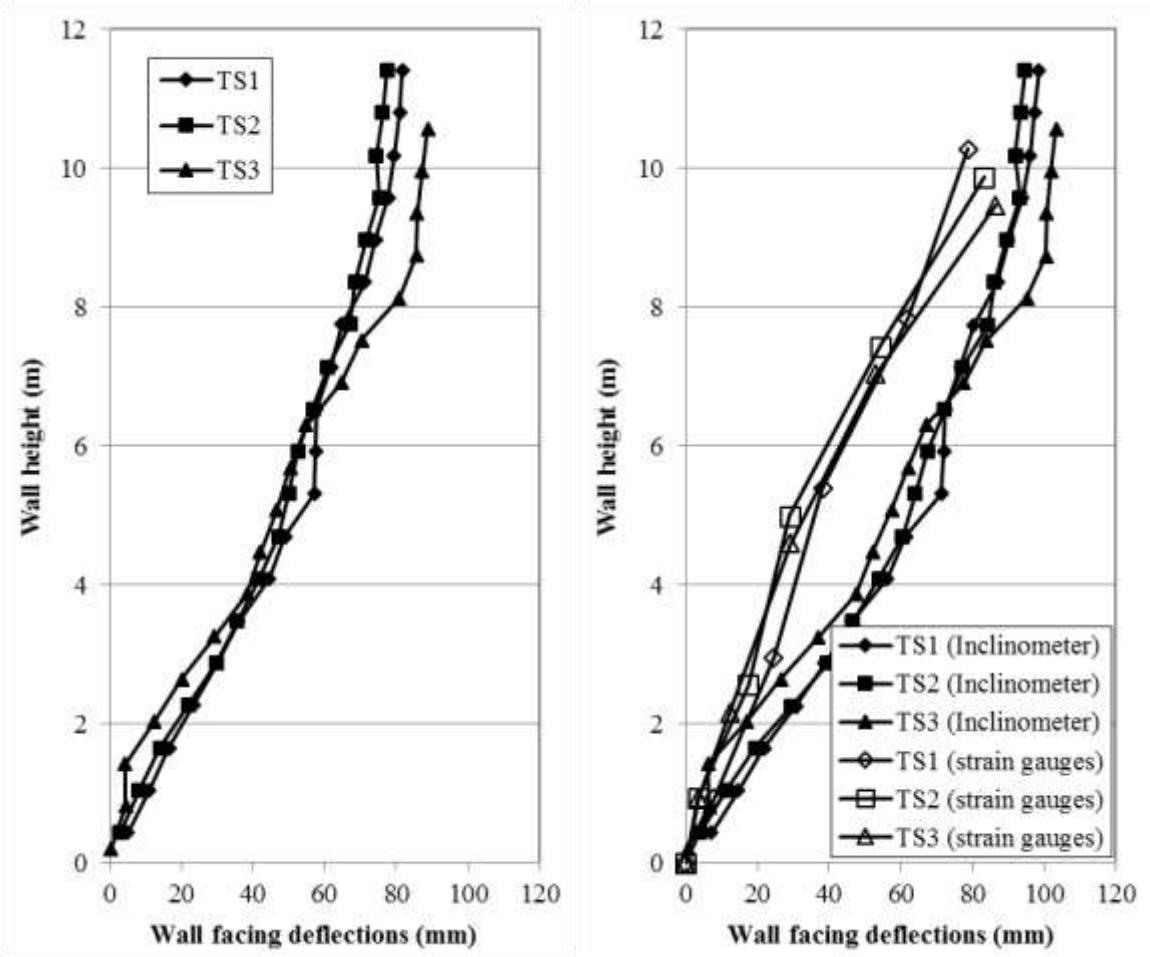

(a) before the construction of the backslope (b) after the construction of the backslope

Figure 4.8 Profiles of wall deflections with full wall height

Figure 4.8 also presents that at the bottom part of the wall, the wall facing deflection in TS3 was smaller than those in TS1 and TS2. This phenomenon can be explained by the fact that TS3 had more embedment than TS1 and TS2 during the construction, which means that more passive resistance reduced the wall facing deflection in TS3. In order to eliminate the influence of passive resistance, the accumulated wall facing deflections at the location of the top of embedment were set to be zero and then the profiles of wall facing deflection with free wall height (i.e. full wall height minus embedment depth) were obtained and are

compared among three test wall sections as illustrated in Fig. 4.9. For the lower parts of the walls, the accumulated wall facing deflections were almost the same for the three test wall sections due to close primary reinforcement spacing; while for the top portions of the walls, the inclusion of the secondary reinforcement appeared to reduce the accumulated wall facing deflections in TS1 and TS2.

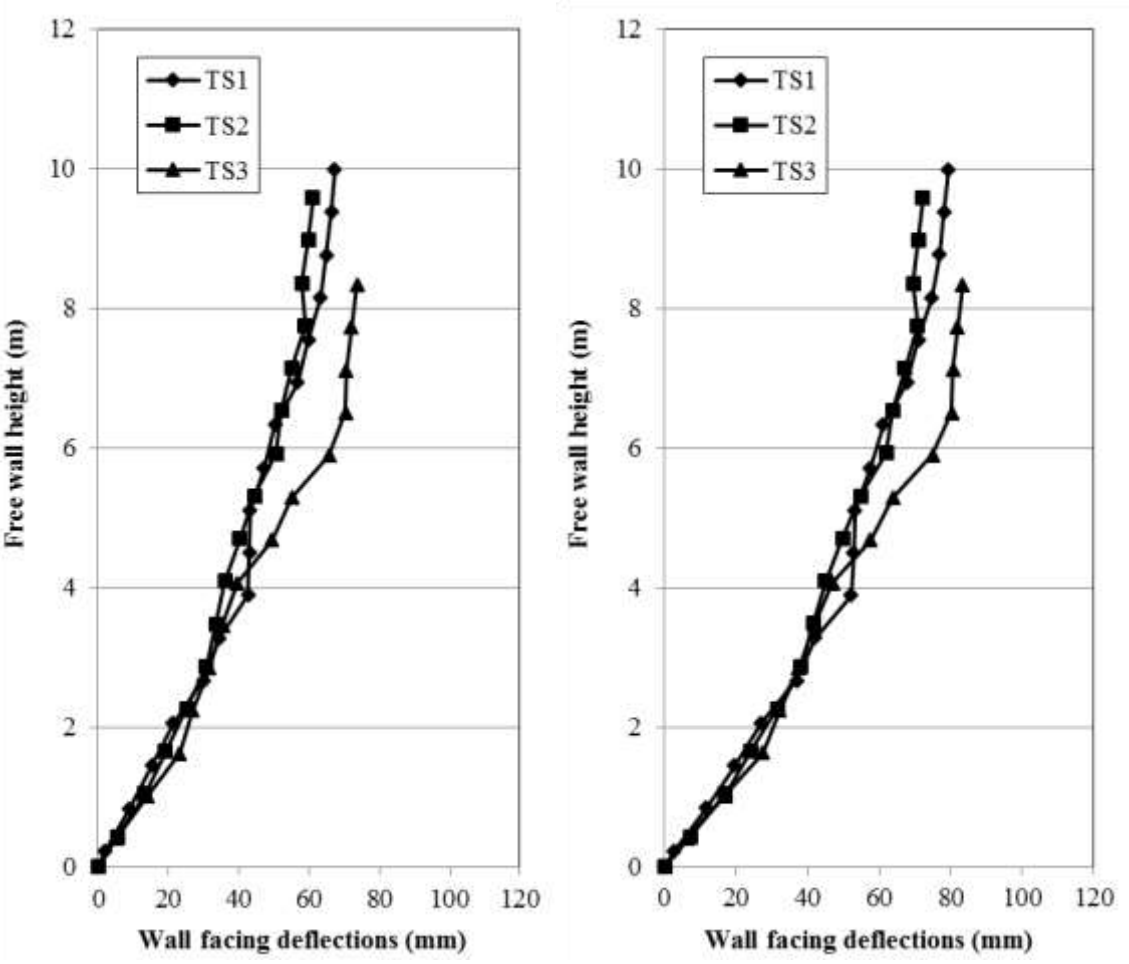

(a) before the construction of the backslope (b) after the construction of the backslope

Figure 4.9 Profiles of wall deflections with free wall height

Figure 4.10 shows the development of the maximum wall facing deflection with the wall height during the construction. The maximum wall facing deflection increased with the increase of the wall height in the three test wall sections. Christopher et al. (1989) developed an empirical relationship between the reinforcement length and the maximum wall facing deflection based on the results from eight field tests and a numerical study. They found that the maximum wall facing deflection decreased dramatically with the length of reinforcement when it was less than the wall height and a further increase of the reinforcement length did not result in much reduction in the maximum wall facing deflection. In this study, the normalized accumulated wall facing deflections at the end of the construction ($\Delta x/H$, where Δx = the maximum accumulated wall facing deflection), were calculated for the three test wall sections at 0.82%, 0.8%, and 0.91%, respectively, for TS1, TS2, and TS3. Using a numerical method, Rowe and Ho (1998) investigated other influence factors on the maximum wall facing deflections, such as wall facing stiffness, friction angle of backfill, and reinforcement stiffness. Rowe and Ho's study indicated that wall facing stiffness had a limited effect on the maximum wall facing deflection but an increase of reinforcement stiffness or friction angle of backfill significantly reduced the maximum wall facing deflection. In this study, the measured maximum accumulated wall facing deflection was small because of the long geogrid reinforcement and the high friction angle of backfill material.

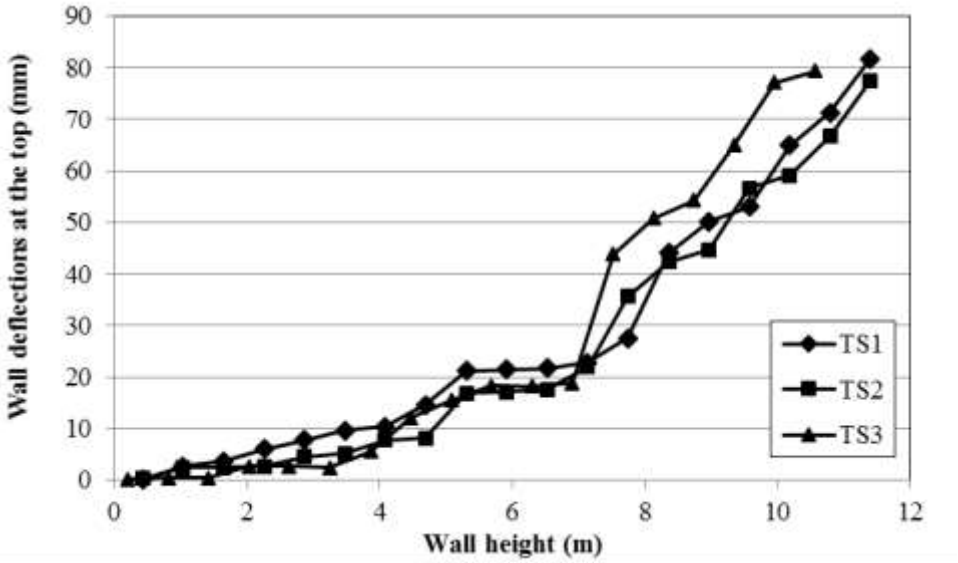

Figure 4.10 Development of the maximum wall facing deflection with the wall height

4.6.2. Vertical earth pressures

Figure 4.11 shows an increase of the measured vertical earth pressures with wall construction at different locations in TS2. The overburden stress at Location of 4 was calculated to compare with the corresponding measured vertical earth pressure and is shown in Fig. 4.11. Overall, the calculated overburden stress matched well with measured vertical earth pressure. In addition, a backslope was constructed on the top of the wall within a short time at the end of the wall construction. The measured vertical earth pressure and calculated overburden stress at Location 4 captured the rapid growth in vertical earth pressure induced by the weight of the backslope. However, the measured vertical earth pressure at Location 2 was unexpectedly small during the construction. The high vertical pressure at Location 1 might result from the trapezoidal stress distribution, especially with the top slope. The secondary reinforcement extended the wall facing to the end of the secondary reinforcement zone so that the effect of the down-drag load increased the

pressure at Location 1 but reduced the pressure at Location 2. The result of such a low value of earth pressure may also be explained due to a malfunctioning earth pressure cell. A numerical study was conducted to investigate the possible reason for this low pressure and will be presented later.

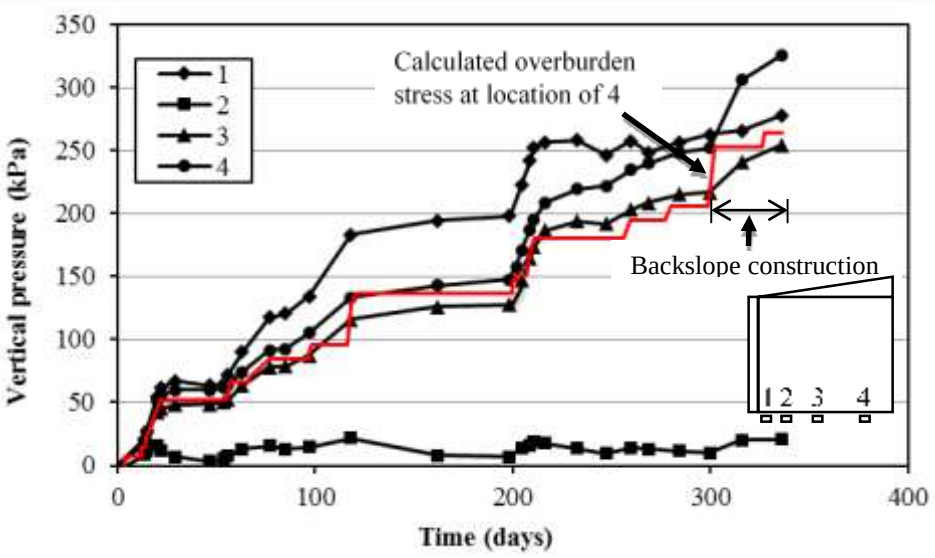

Figure 4.11 Development of measured vertical earth pressures with the wall construction

Figure 4.12 presents the distributions of the measured vertical earth pressures and the calculated overburden stresses under the wall before the construction of the backslope and after the construction of the backslope. Before the construction of the backslope, the measured vertical earth pressures were slightly higher than the calculated overburden stresses and equivalent trapezoidal stresses considering external lateral earth pressure as shown in Fig. 4.12(a). The measured vertical stress close to the wall facing was higher than that away from the wall facing because the external lateral earth pressure from the retained soil increased the eccentricity of the reinforced soil towards the toe of the wall facing and

an increase in the bearing stress close to the wall facing. This feature was well captured by the calculated trapezoidal stresses. However, the distribution of calculated overburden stresses of the wall was uniform because the calculation of the overburden stress did not consider the lateral earth pressure from the retained soil.

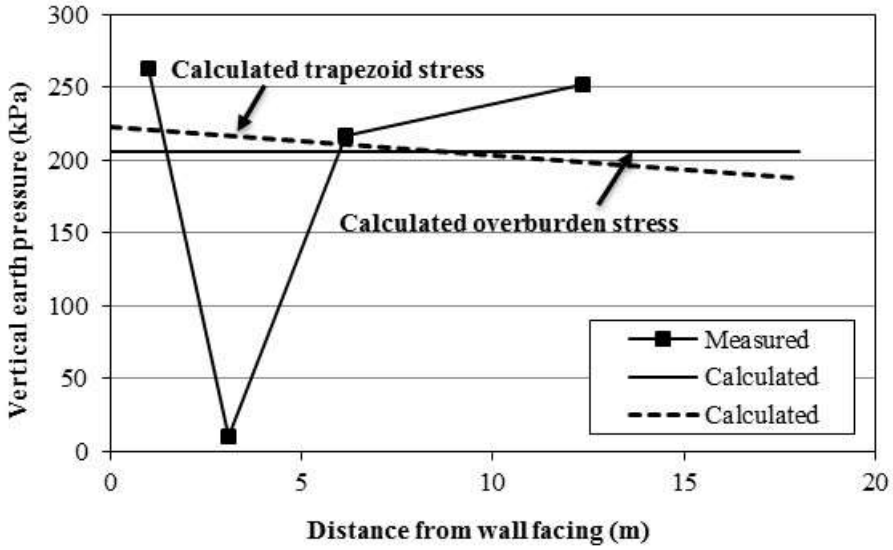

(a) Before the construction of the backslope

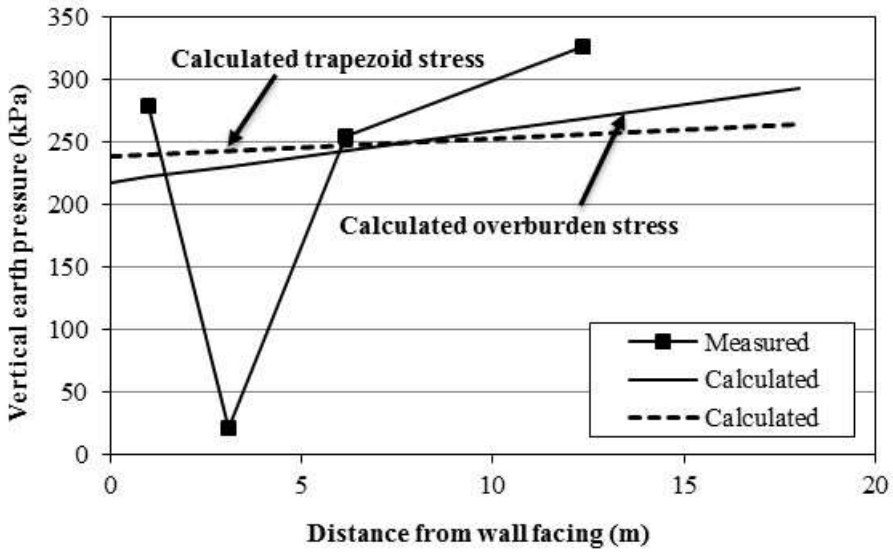

(b) After the construction of the backslope

Figure 4.12 Distributions of measured vertical earth pressures under the wall

After the construction of the backslope, the measured vertical earth pressures continued increasing due to the construction load. In addition, the measured vertical earth pressures were slightly higher than the calculated overburden stresses as well. However, the pattern of the distribution of the measured vertical earth pressures after the construction of the backslope changed as compared with that before the construction of the backslope. The measured vertical earth pressures close to the wall facing were lower than those away from the wall facing because the backslope added more overburden stress and as an eccentric load led to a potential rotation away from the toe of the wall. This pattern was captured by both the calculated overburden stresses and trapezoidal stresses. In addition, the calculated overburden stresses were lower than the calculated trapezoidal stresses at the locations close to the wall facing while the calculated overburden stresses became higher than the calculated trapezoidal stresses at the locations away from the wall facing. This phenomenon can be attributed to the backslope acting as an eccentric load.

4.6.3. Horizontal earth pressures

Figure 4.13 presents the profiles of the measured lateral earth pressures for the three test wall sections at the end of the construction. For comparison purposes, the profiles of calculated active earth pressure using two friction angles (34°, a friction angle used in the original analysis; 47°, a peak friction angle of aggregate obtained from triaxial tests and also used in the updated analysis) and the profile of at-rest earth pressure using the peak friction angle of aggregate from triaxial tests are plotted as well. The active earth pressures

were calculated based on the coefficient of active earth pressure using Rankine's theory considering the backslope on the top of the wall as follows:

$$K_a = \cos\beta \left[\frac{\cos\beta - \sqrt{\cos^2\beta - \cos^2\phi}}{\cos\beta + \sqrt{\cos^2\beta - \cos^2\phi}} \right] \tag{4.2}$$

where ϕ is the friction angle of the aggregate and β is the angle of the backslope. The lateral earth pressures at rest were calculated based on the coefficient of earth pressure at rest proposed by Jaky (1948):

$$K_0 = 1 - sin\,\phi \tag{4.3}$$

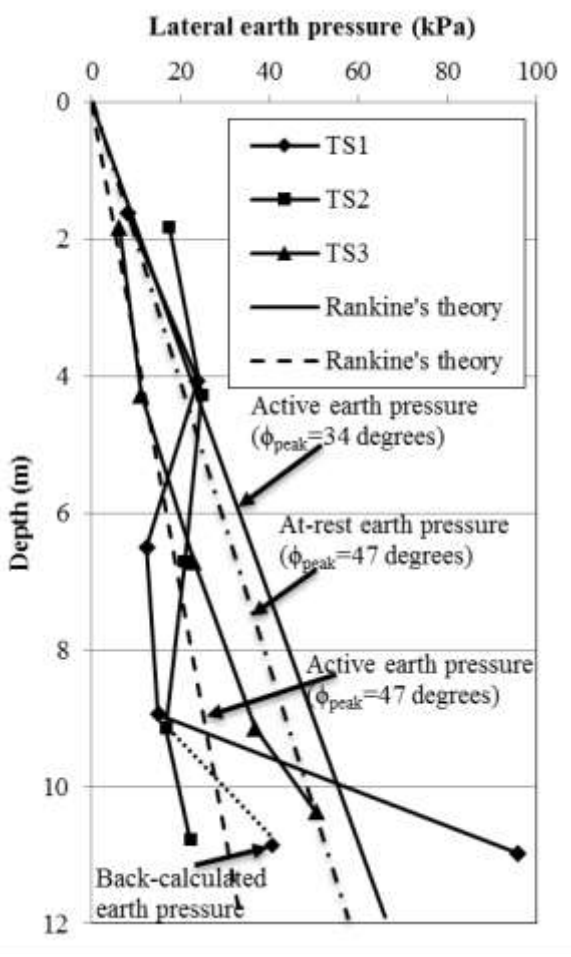

Figure 4.13 Profiles of measured lateral earth pressures

Figure 2.13 shows that the calculated active earth pressures using the design friction angle of 34° were mostly higher than the measured earth pressures. In TS3 (i.e. the control section), the measured lateral earth pressures increased approximately linearly with depth and were between the calculated active earth pressures and at-rest earth pressures using the actual friction angle of 47°. The measured earth pressures at the bottom part of the wall were close to the at-rest earth pressure because the existence of the embedment limited the wall deflection at the bottom of the wall. However, the measured earth pressures within the upper portion of the wall were close to the active earth pressure because the wall

deflection was sufficient to allow the fill to be in an active state within the upper portion of the wall.

Compared with the linear distribution of the measured lateral earth pressures in TS3, the distribution of the measured lateral earth pressures in TS1 and TS2 (i.e. test wall sections reinforced by secondary geogrid) were approximately uniform. The active earth pressures within the upper portion of the wall were close to and even higher than the at-rest earth pressures. This result is likely because the inclusion of secondary reinforcement reduced the wall deflection within the upper portion of the wall and the total earth pressure was re-distributed.

The total lateral thrust forces applied on the back of wall facing for the three test sections at the end of the construction were calculated by integrating the measured lateral earth pressure along the wall height as 324.1, 220.9, and 241.3 kN for TS1, TS2, and TS3, respectively. TS2 and TS3 had similar thrust forces; however, TS1 had a much larger thrust force than TS2 and TS3 because TS1 had a much higher measured lateral earth pressure at the depth of 11.3 m. Since the three wall sections had similar dimensions, it is expected that they should have similar total lateral thrust forces. Therefore, the much higher lateral earth pressure at the depth of 11.3 m was unreasonable. Because TS1 and TS2 had similar geogrid layouts and wall heights, the total lateral thrust forces on the back of wall facing in TS1 and TS2 could be assumed to be equal. Then the lateral earth pressure at the depth of 11.3 m in TS1 could be back-calculated as 42.6 kPa. Figure 14 shows that the back-calculated lateral earth pressure at the depth of 11.3 fitted the profile well.

Coefficient of lateral earth pressure behind the wall can be estimated in two ways: (1) using the measured lateral earth pressure behind the wall facing as

$$K_r = \frac{\sigma_h}{\sigma_v} \tag{4.4}$$

where σ_h = measured lateral earth pressure behind the wall facing and σ_v = vertical overburden stress and (2) using the measured maximum tension in the reinforcement as

$$K_r = \frac{T_{max}}{S_v \cdot R_c \cdot \sigma_v} \tag{4.5}$$

where T_{max} = measured maximum tension in the reinforcement (can be estimated using the global strain of a geogrid multiplied by its tensile stiffness), S_v = vertical spacing of geogrid, and R_c = coverage ratio of geogrid. A normalized coefficient of lateral earth pressure is defined as K_r / K_a, where $K_a = tan^2\left(45^o - \phi/2\right)$. The method for calculating the coefficient of lateral earth pressure based on the measured maximum tension in the reinforcement was adopted by AASHTO to develop the profile of K_r / K_a with depth included in AASHTO (2007) and AASHTO (2014).

Figure 4.14 shows that the profile of the normalized coefficient of lateral earth pressure with the depth when $\phi = 47°$ was used. Figure 4.14(a) presents the profile back-calculated based on the measured lateral earth pressures behind the wall facing. It is shown that TS3 had the K_r / K_a ratio close to 1.0. However, for TS1 and TS2, the K_r / K_a ratio was greater than 1.0 when the depth was less than 6.0 m, while the ratio was less than 1.0 when the depth was greater than 6.0 m. Overall, TS1 and TS2 had similar K_r / K_a ratios width depth. Figure 4.14(b) presents the profile back-calculated based on the measured maximum tension in the reinforcement, which is the method adopted by AASHTO. It is shown that the K_r / K_a ratios at the top three layers of the instrumented geogrid were

between 0.56 and 0.69, 0.41 and 0.63, and 0.89 and 1.27, in TS1, TS2, and TS3, respectively. The average ratio at the top three layers of the instrumented geogrid in TS3 was greater than those in TS1 and TS2. This result can be explained that the secondary reinforcement shared part of the required tension and reduced the maximum tension in the primary reinforcement. The K_r / K_a ratios at the bottom two layers of the instrumented geogrid in TS3 were less than those in TS1 and TS2 due to the effect of the embedment. Figure 4.14 also shows that the K_r / K_a ratios back-calculated based on the measured lateral earth pressures were greater than those back-calculated based on the measured maximum tension in the reinforcement. This is because the measured maximum tension in the reinforcement was reduced by the toe resistance of the wall due to embedment and shear resistance of block facing, which are often ignored in practice but were clearly illustrated by Leshchinsky and Vahedifard (2012) and Leshchinsky et al. (2014).

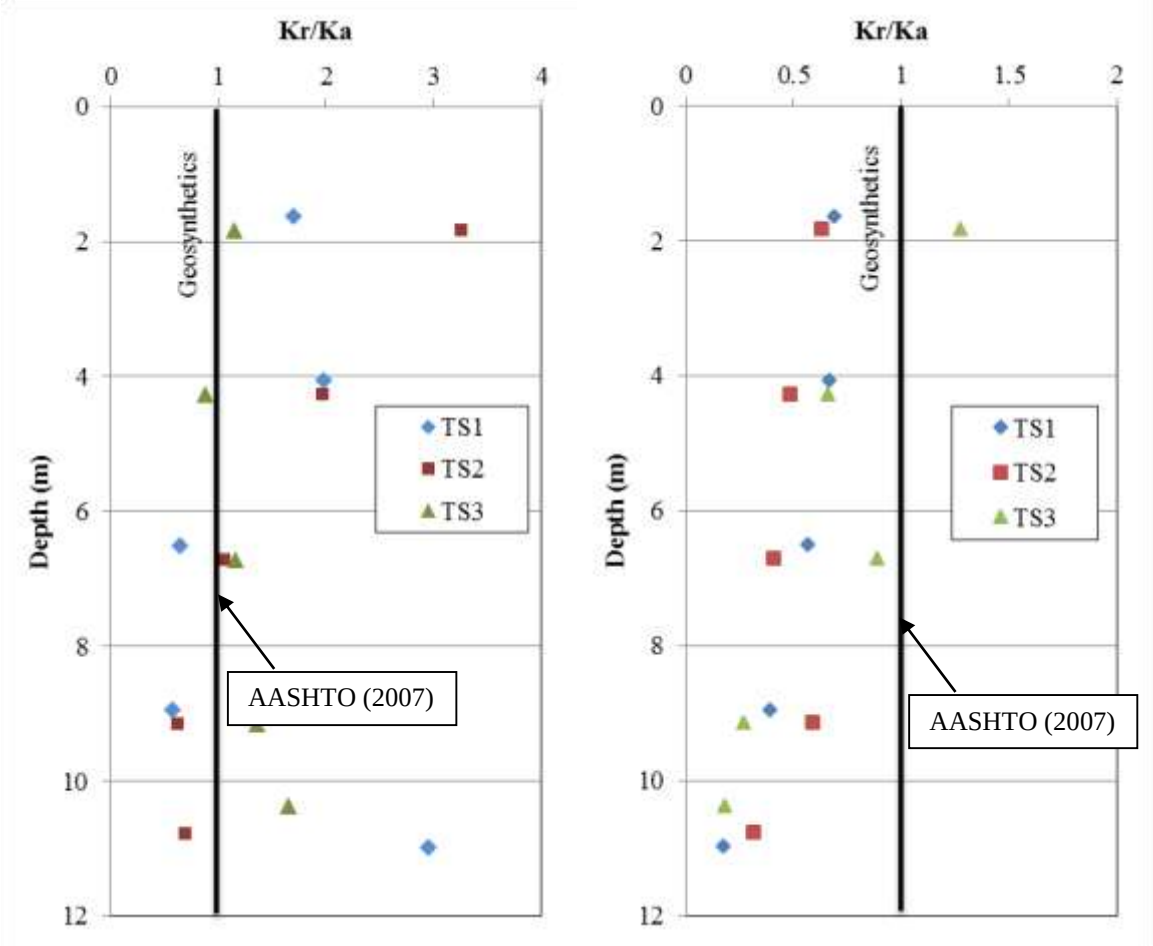

(a) From measured lateral earth pressures (b) From maximum tensile forces

Figure 4.14 Distribution of coefficient of lateral earth pressure with depth

4.6.4. Strains in geogrid

Figure 4.15 shows the global strains of primary and secondary geogrid layers at five instrumented elevations (see Fig. 4.3) in the three test wall sections at the end of the construction. The global strains were calculated from the measured local strains multiplied by the calibration factors between local strains and global strains in Fig. 3.13.

Figure 4.15(a) shows that for each instrumented layer, the strains of primary geogrid increased along the geogrid to a maximum value and then decreased to zero at a

distance away from the wall facing, which is called a tension mobilization distance in this dissertation. Figure 4.15(a) shows that the tension mobilization distance increased with the wall height. A similar result was presented in Leshchinsky et al. (2014). Figure 4.15(b) presents the strains of secondary geogrid in TS1 and TS2 at the end of the construction, indicating that secondary geogrid carried tensile loads. If the total required tensile load to maintain the stability of the wall was constant, the secondary geogrid carrying part of the tensile load would reduce the tensile load carried by the primary geogrid in the area close to the wall facing. In other words, the secondary geogrid could reduce the tensile loads in the primary geogrid.

Figure 4.15 also shows some negative strains in the geogrid. These negative strains may be caused by the bending moment of geogrid at the instrumented locations. Additionally, the measured global strains of geogrid at the connections were very low. Since initial readings of strains of geogrid were taken after the one lift of aggregate was placed and compacted, the strains of geogrid occurred during the compaction of the aggregate were not included. In addition, all the strain gauges were placed on the longitudinal ribs along the centerline of the wall facing block. Since the middle portion of the connector might not be in tight contact with the block, the longitudinal ribs within this portion were not stressed within the first geogrid aperture so that the measured strains at this location were very low or close to zero. Therefore, the measured strains at this location were not representative and not included. It is expected that the longitudinal ribs corresponding to the connector teeth, which were in tight contact with the block, carried higher loads. The longitudinal ribs in the apertures farther away from the wall facing carried more uniform loads due to the load re-distribution through the transverse bars.

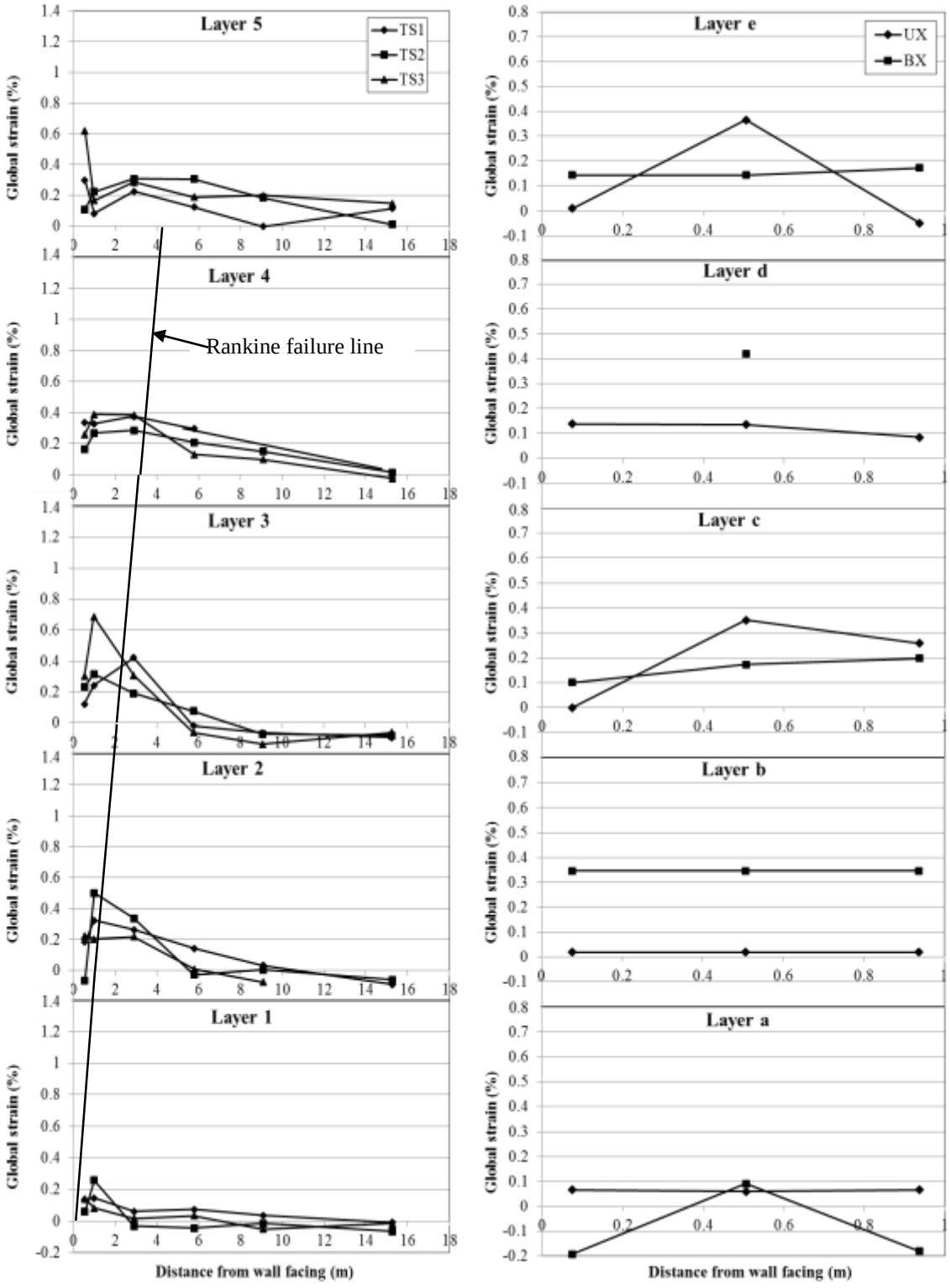

(a) Primary geogrid (b) Secondary geogrid

Figure 4.15 Strains in geogrid

Figure 4.16 presents the profile of the maximum strains with depth for all three test wall sections, respectively, which shows the maximum strains for all three test wall section occurring at the location close to the wall facing within the reinforced backfill zone. The maximum strains were in the range of 0.15%-0.43%, 0.26%-0.5%, and 0.14%-0.69%, for TS1, TS2, and TS3, respectively. Similar magnitudes of strains were obtained by Allen and Bathurst (2014a and 2014b) in their instrumented MSE walls, in which the measured maximum strains of geogrid were less than 1%. The maximum strains of primary geogrid at the instrumented layers above the embedment (instrumented Layers 3, 4, and 5) in TS3 in this study were larger than those in TS1 and TS2. This result can be explained that the secondary reinforcement in TS1 and TS2 carried a portion of the tensile force from lateral earth pressures and reduced the maximum tensile force in the primary geogrid.

However, the maximum strains of the primary geogrid at the first two instrumented layers (i.e., Layers 1 and 2) in TS3 were smaller than those in TS1 and TS2. This result can be attributed to the influence of the embedment. Huang et al. (2010) and Ehrich and Mirmoradi (2013) also showed that an increase of the toe resistance reduced the tensile strains of the geosynthetic reinforcement. TS3 had more embedment than TS1 and TS2 at the first embedment level (i.e., the 29th day of the construction as shown in Figure 4.2), which resulted in the reduction in the strains of the lower geogrid in TS3. At the second embedment level (i.e., the 151st day of the construction), the three test wall sections had the same embedment; therefore, the influence of the toe resistance on the geogrid strains installed after reaching the second embedment level was minimal.

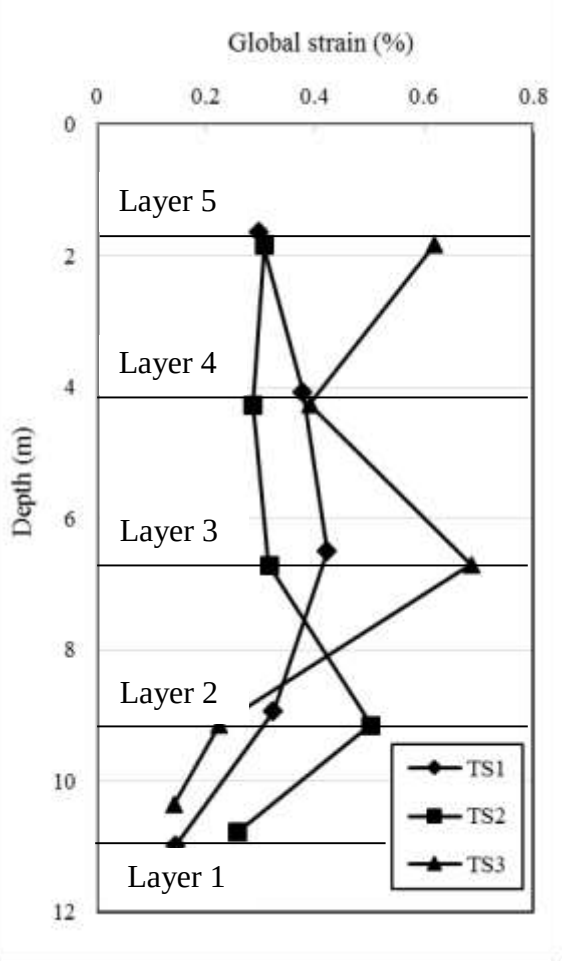

Figure 4.16 Profiles of the maximum global strains of primary geogrid

Chapter 5 Constitutive Models and Parameters for Numerical Analysis

This chapter describes the software, the constitutive models, and the determination, calibration, or validation of the parameters for the numerical analysis in this study. The parameters include the material properties (e.g. backfill soil, retained soil, foundation soil, modular block facing, geosynthetic reinforcement, etc.) in the numerical models as well as the interfaces properties (e.g. an interface between modular block and modular block, an interface between modular block and backfill soil, and interface between backfill soil and geosynthetic reinforcement).

5.1. Numerical software

This study used the Fast Lagrangian Analysis of Continua (FLAC) software for the numerical modeling. FLAC is numerical software using a finite differential method to solve boundary value problems. FLAC has been extensively and successfully employed to model many geotechnical problems, such as column-supported embankments, slope stability, pit excavation, pile foundations, and earth retaining structures. A geosynthetic reinforced retaining (GRR) wall is a complex structure since it has many interactions between materials. Due to its complexity, numerical modelling of GRR walls requires the numerical software having the following features:

(1) Comprehensive soil constitutive models

Compared with other commercial software, such as ABAQUS and PLAXIS, FLAC provides more selections for soil constitutive models to simulate behavior of soils. Table 5.1 summarizes soil constitutive models in ABAQUS, PLAXIS, and FLAC. In this study,

two soil constitutive models, the Mohr-Coulomb (MC) model and the Cap-Yield (CY) model were chosen to simulate the behavior of the backfill soil in FLAC.

Table 5.1 Soil constitutive models in ABAQUS, PLAXIS, and FLAC

Software	ABAQUS	PLAXIS	FLAC
Mohr-Coulomb Model	x	x	x
Drucker-Prager	x		x
Modified Cam-Clay model	x		x
Strain-Hardening/Softening model			x
Double-Yield model			x
Cap-Yield model			x
Simplified Cap-Yield model			x
Hardening Soil model		x	
Soft Soil model		x	

(2) Various interface models

In addition to comprehensive soil constitutive models, FLAC provides various interface models to simulate the interaction between two different materials. These interface models were able to describe interface features, such as an interface slip or opening, interface strength, and interface tension. So the interface models in FLAC are able to simulate complex interaction behavior in the GRR walls with modular block facing (e.g. an interface between geosynthetic and backfill material, an interface between wall facing and backfill material, and an interface between modular block and modular block).

(3) Extensive boundary and initial conditions

FLAC also provides extensive boundary and initial conditions in numerical modeling. The boundary condition can be applied to a numerical model using a stress boundary condition, a displacement boundary condition, and/or an interior boundary condition. Similar to the boundary condition, various types of the initial condition, such

as a gradient stress and a velocity, can be applied in a numerical model as the initial condition. These boundary and initial conditions and their combinations in FLAC are sufficient to capture most of the features in GRR walls.

In addition to the above three major features, FLAC is capable to model a staged construction. In this study, a 2D version of FLAC was employed to model GRR walls as they were under a plane-strain condition.

5.2. Constitutive models

5.2.1. Linearly elastic model

In the numerical modelling, the modular block was modelled as a linearly elastic material. A linearly elastic model has a linear relationship between deviatoric stress and axial strain as illustrated in Figure 5.1. FLAC has incorporated this linearly elastic model, which requires parameters, such as Young's modulus, E and Poisson's ratio, ν.

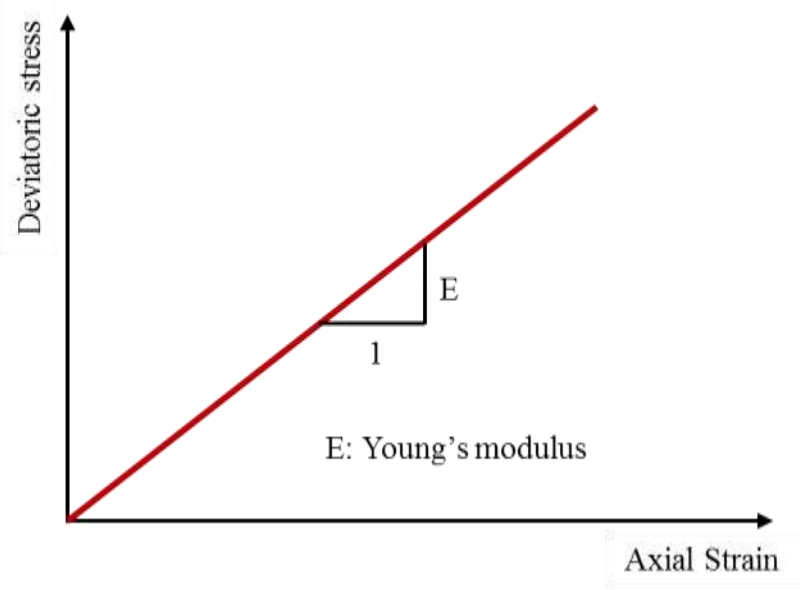

Figure 5.1 Stress-strain relationship for a linearly elastic material

5.2.2. Mohr-Coulomb model

The Mohr-Coulomb (MC) model used in the numerical modeling is linearly elastic and perfectly plastic with an MC failure criterion. The MC model has been extensively used in numerical modeling of earth retaining structures and studies have demonstrated that Mohr-Coulomb model had capabilities to simulate the behavior of backfill soil in GRR walls. The stress-strain relationship of the MC model is illustrated in Figure 5.2. It is shown that the stress linearly increases with strain and failure occurred when the stress reaches a yield stress, σ_y. The yield stress is determined using the MC failure criterion as shown in Figure 5.3, which can be determined based on Equation (5.1):

$$\sigma_y = c + \sigma_c' \tan\phi' \tag{5.1}$$

where

σ_y - yield stress

c - cohesion

σ_c' - effective confining stress

ϕ' - effective friction angle

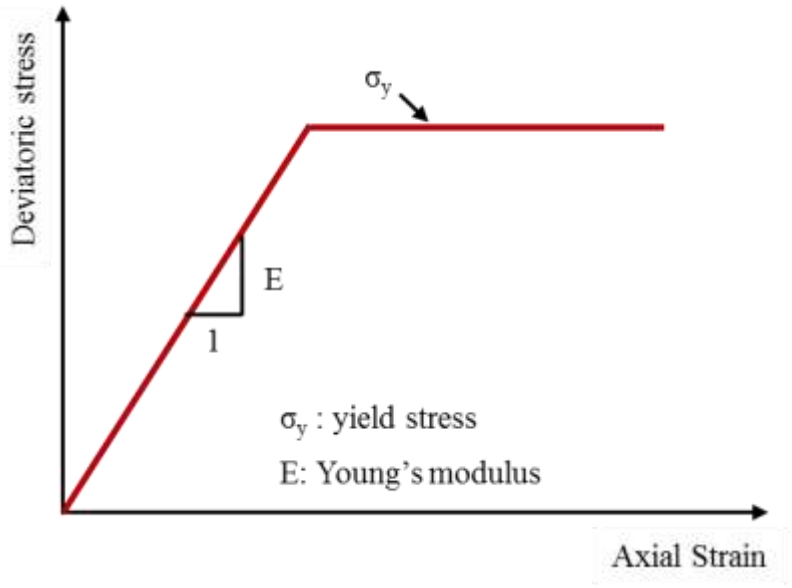

Figure 5.2 Stress-strain relationship for Mohr-Coulomb model

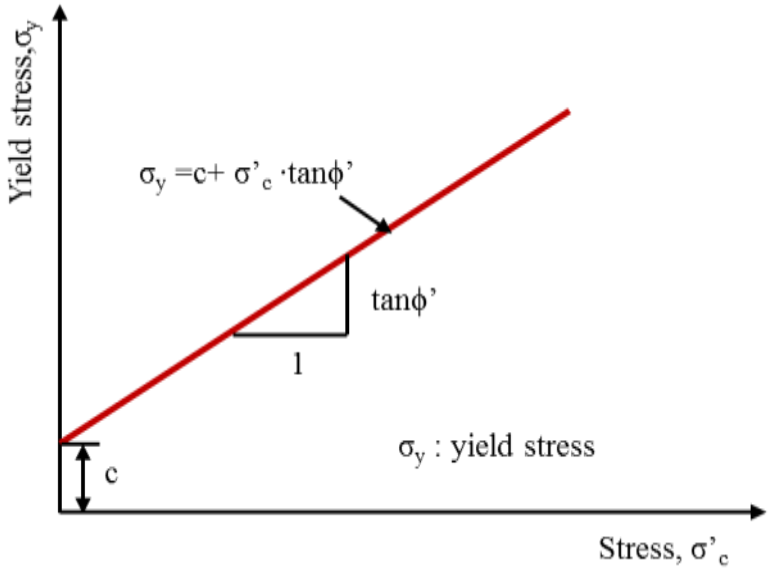

Figure 5.3 Mohr-Coulomb failure criterion

In the numerical model, the backfill soil, retained soil, foundation soil, embedment soil, and backslope soil were modeled using the MC model.

5.2.3. Cap-Yield model

Although being capable to capture basic features of the soil with fewer parameters in the numerical model, the MC model has some drawbacks. An obvious drawback is that the MC model cannot reflect the feature of the stress dependent modulus for the backfill soil. In addition to this drawback, the MC model is unable to capture the hardening behavior of volumetric strain under isotropic compression. In order to overcome the drawbacks, an advanced soil constitutive model, the Cap-Yield (CY) model, was employed in the numerical model to simulate the behavior of the backfill soil. The CY model had capabilities to model hardening behavior of volumetric strain under isotropic compression, to present soil stiffness decrease and plastic deformation subjected to shear loading, and to exhibit dilative characteristics. These features are shown through Figures 5.4 to 5.6.

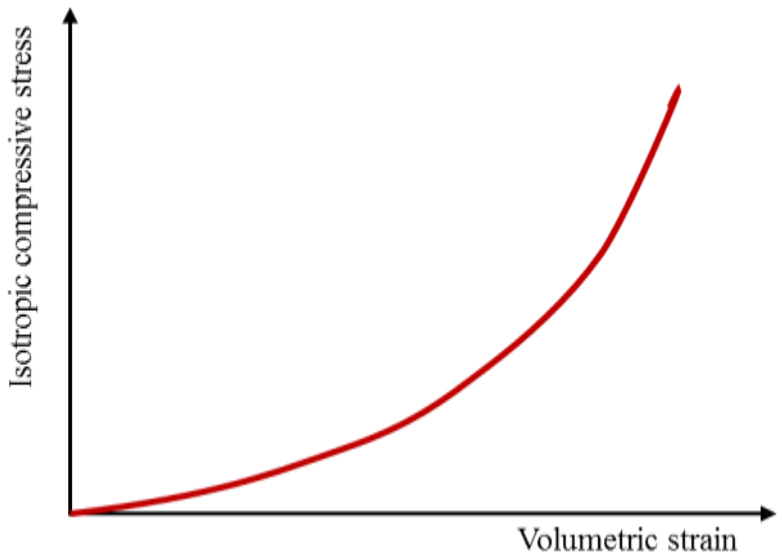

Figure 5.4 Nonlinear isotropic compressive stress-volumetric strain relationship

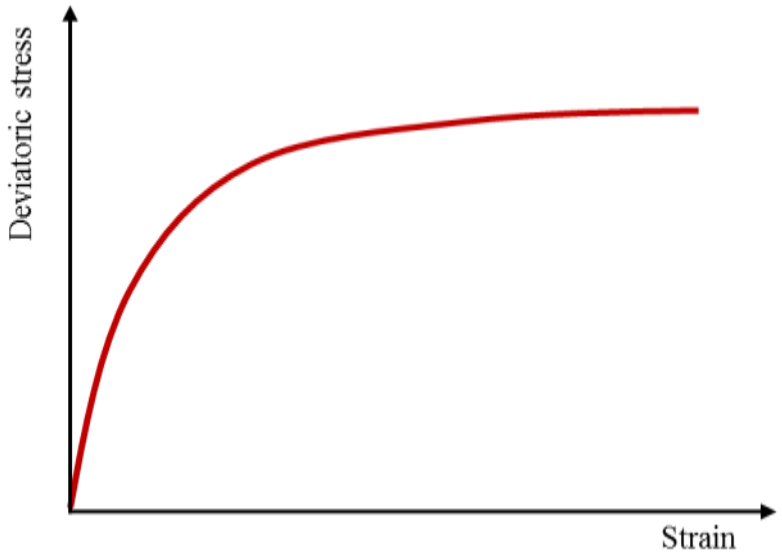

Figure 5.5 Hyperbolic stress-strain relationship

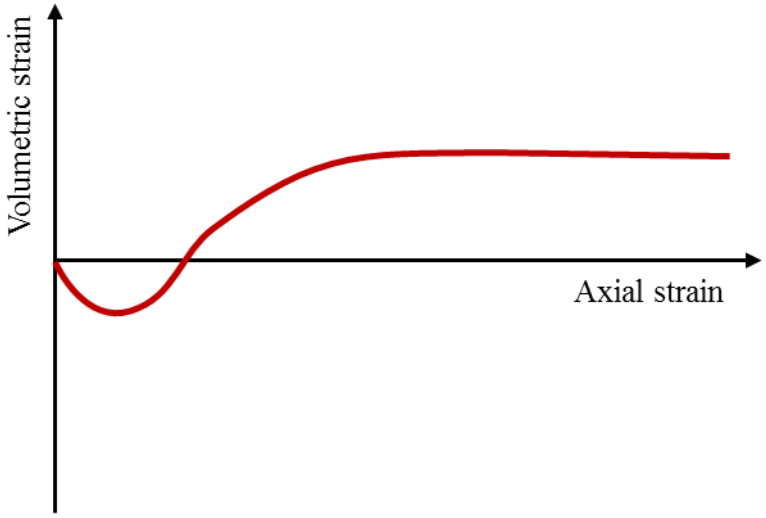

Figure 5.6 Volumetric strain-axial strain relationship

The CY model has two major yield surfaces: (1) cap yield surface, and (2) shear yield surface. An associated flow rule is used for the cap yield surface while a non-associated flow rule is adopted for the shear yield surface. Figure 5.7 shows these two major yield surfaces in p'-q space.

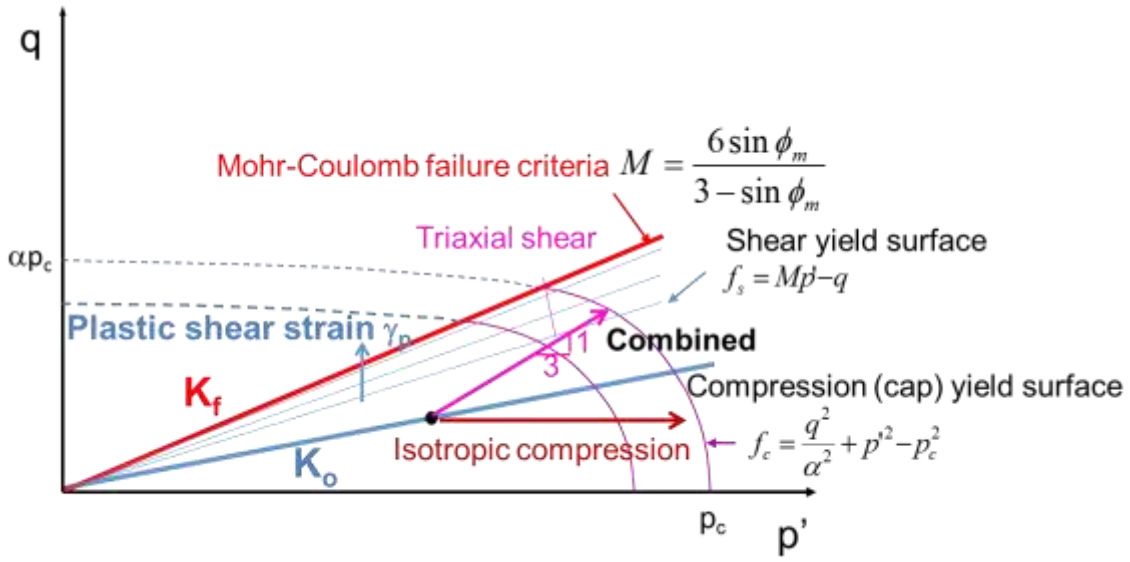

Figure 5.7 Yield surfaces of the CY model in p'-q space

(1) Cap yield surface

Equation (5.2) is the function of the cap-yield surface in p'-q space.

$$f_c = \frac{q^2}{\alpha^2} + p'^2 - p_c^2 \tag{5.2}$$

where

α - dimensionless parameter to determine the shape of elliptical cap yield surface;

p_c - cap pressure;

p' - mean effective stress (compression is positive), $p' = \frac{\sigma_1' + \sigma_2' + \sigma_3'}{3}$, where σ_1', σ_2', and σ_3' are principal effective stress;

q - measure of shear stress, $q = \left[\sigma_1' + \frac{3+\sin\phi_m}{3-\sin\phi_m} \cdot (\sigma_2' + \sigma_3') - \sigma_2'\right]$, where ϕ_m is the mobilized friction angle.

(2) Shear yield surface

The function of shear yield surface is expressed by Equation (5.3):

$$f_s = Mp' - q \tag{5.3}$$

where

M - slope ratio of the failure line in p'-q space, $M = \frac{6\sin\phi_m}{3-\sin\phi_m}$;

The potential function corresponding to the shear yield surface is described by Equation (5.4):

$$g_s = M^* p' - q^* \tag{5.4}$$

where

M^* - $M^* = \frac{6\sin\psi_m}{3-\sin\psi_m}$, where ψ_m is a mobilized dilation angle;

q^* - $q^* = \left[\sigma_1' + \frac{3+\sin\psi_m}{3-\sin\psi_m}\cdot(\sigma_2' + \sigma_3') - \sigma_2'\right]$.

There are three hardening laws in the CY model: (1) a cap hardening law, (2) a friction hardening law, and (3) a dilation law.

(1) Cap hardening law

The cap hardening law is to describe nonlinear behavior between isotropic compressive stresses and volumetric strains in isotropic compression tests. Equation (5.5) describes the relationship between cap pressure and plastic volumetric strain:

$$p_c = p_{ref}\left[(1-m)\frac{1+R}{R}\cdot\frac{K_{ref}^{iso}}{p_{ref}}e^p\right]^{\frac{1}{1-m}} \tag{5.5}$$

where

p_{ref} - reference effective pressure;

m - power exponent;

K_{ref}^{iso} - bulk modulus of reference effective pressure divides volumetric strain;

e^p - plastic volumetric strain;

R - ratio of elastic and plastic volumetric strain;

(2) Friction hardening law

The friction hardening law is to describe the hyperbolic stress-strain relationship observed in triaxial shear tests. Equation (5.6) describes the relationship between a mobilized friction angle and a plastic shear strain:

$$\gamma^p = \frac{1}{\beta}\frac{p_{ref}}{G_{ref}^e}\left(\frac{p'}{p_{ref}}\right)^{1-m}\frac{\sin\phi}{R_f}\left[\frac{1}{1-\frac{\sin\phi_m}{\sin\phi}R_f}-1\right] \tag{5.6}$$

where

p_{ref} - reference effective pressure;

m - power exponent;

G_{ref}^e - elastic tangent shear modulus at reference effective pressure;

ϕ_m - mobilized friction angle;

ϕ - friction angle;

R_f - failure ratio.

(3) Dilation law

The dilation law is to describe the soil volume dilation (a volumetric strain increase) subjected to shear loading. Equation (5.7) expresses a relationship between a plastic shear strain rate and a plastic volumetric strain rate:

$$\dot{e}^p = \dot{\gamma}^p \sin\psi_m \tag{5.7}$$

where

$\dot{e}^p$ - plastic volumetric strain rate;

$\dot{\gamma}^p$ - plastic shear strain rate;

ψ_m - mobilized dilation angle, $\sin\psi_m = \frac{\sin\phi_m - \sin\phi_{cv}}{1-\sin\phi_m \sin\phi_{cv}}$, where $\sin\phi_{cv} = \frac{\sin\phi - \sin\psi}{1-\sin\phi\sin\phi}$.

5.2.4. Linearly elastic and perfectly plastic model for geosynthetic

In the numerical modelling, geosynthetic was modelled as a linearly elastic and perfectly plastic material. Its stress-strain relationship refers to Figure 5.2 while its yield stress has nothing to do with the confining stress. The yield stress was assigned to the ultimate tensile strength provided by the manufacturer.

5.3. Material properties

5.3.1. Backfill soil

Two constitutive models were used to simulate behavior of the backfill soil: the MC model and the CY model.

5.3.1.1. Parameters for the Mohr-Coulomb model

The MC model in FLAC requires five parameters, which are unit weight, γ_{rs}, Young's modulus, E_{rs}, Poisson's ratio, ν_{rs}, cohesion, c_{rs}, friction angle, ϕ_{rs}, and dilation angle, ψ_{rs}. The parameters used in the MC model for the backfill soil is summarized in

Table 5.2. The unit weight was determined from the average unit weight measured from the sand cone tests performed in the field. Young's modulus was assumed to be the secant elastic modulus corresponding to 50% of yield strength at the confining stress of 200 kPa (see Figure 5.8). Poisson's ratio was assumed to be 0.2, which is a typical value for backfill soil (i.e., aggregates). The cohesion was assumed to be zero since the backfill material was a granular material. The friction angle was obtained from the Mohr circles at the three confining stresses of 50, 100, and 200 kPa. Since the numerical simulation is in a plain strain condition, the friction angle in a plane strain condition was considered using a relationship recommended by Kulhway and Mayne (1990) for cohesionless soils: $\phi_s = 1.12\phi_{tc}$, where ϕ_s is the friction angle from plane strain compression tests and ϕ_{tc} is the friction angle from triaxial compression tests. The determination of the dilation angle was referred to a method suggested by the FLAC manual, which is based on the idealized relationship for the dilation angle given by Vermeer and de Borst (1984).

Table 5.2 Parameters of the Mohr-Coulomb model for the backfill soil

Parameters	unit	value
Unit weight, γ_{rs}	kN/m^3	18.1
Young's modulus, E_{rs}	MPa	20
Poisson's ratio, ν_{rs}	-	0.2
Cohesion, c_{rs}	kPa	0
Friction angle, ϕ_{rs}[1]	degrees	52
Dilation angle, ψ_{rs}	degrees	8

Note: $\phi_{rs} = 1.12 \times 47 = 52$

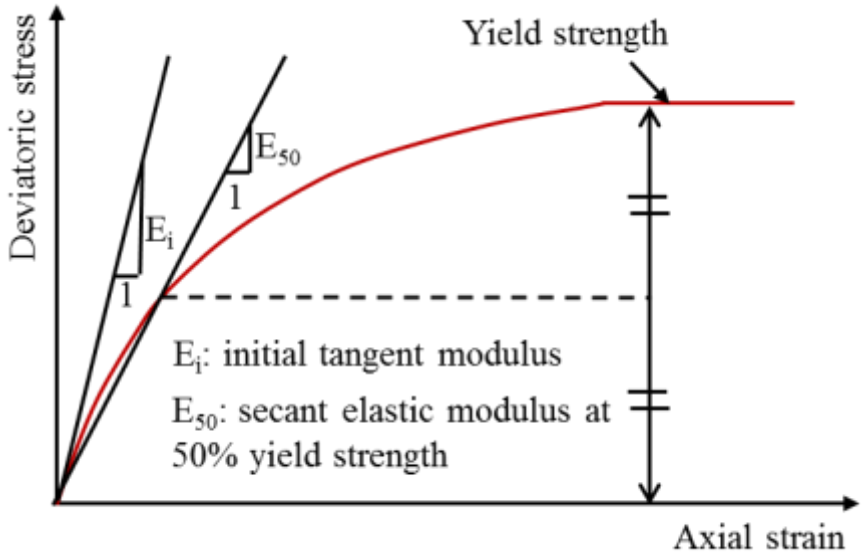

Figure 5.8 Selection of elastic modulus (modified from Plaxis v8.2)

Triaxial shear tests at the confining stresses of 50, 100, and 200 kPa were simulated. Figures 5.9 (a) and (b) show the comparison of results between the tests and the numerical simulation. The results from the tests and the numerical simulation shows that the deviatoric stress increased with the axial strain and the higher confining stress resulted in a higher deviatoric stress at the same strain. The test results also show that the rate of deviatoric stress decreased with an increase in the axial strain. In other words, the soil modulus decreased with an increase in the axial strain. The numerical results cannot capture the behavior of the soil modulus decrease because the MC model only has a constant elastic modulus. In Figure 5.9 (b), although there was a deviation between numerical and test results, the MC model exhibits a capability to simulate the dilation of the backfill soil.

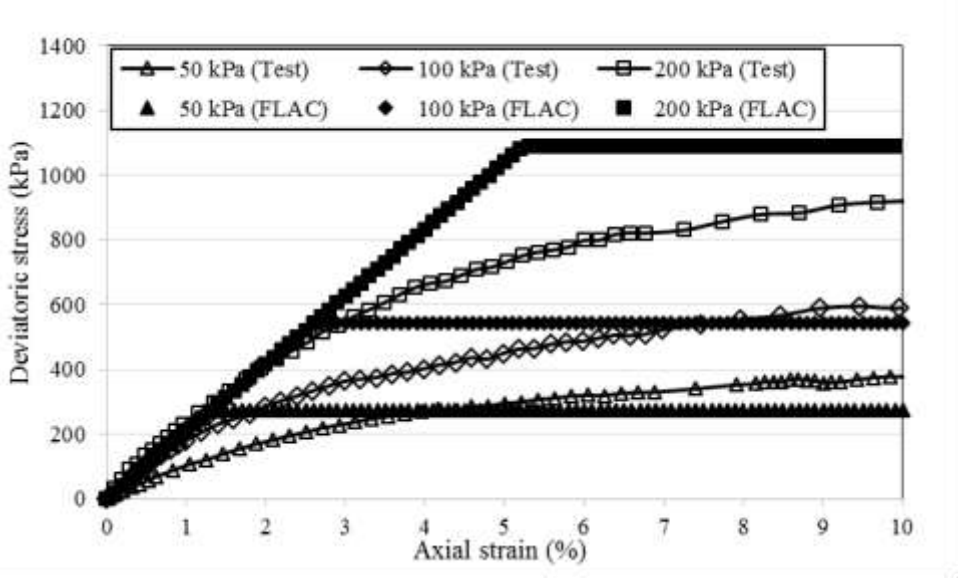

(a) Stress-strain relationship

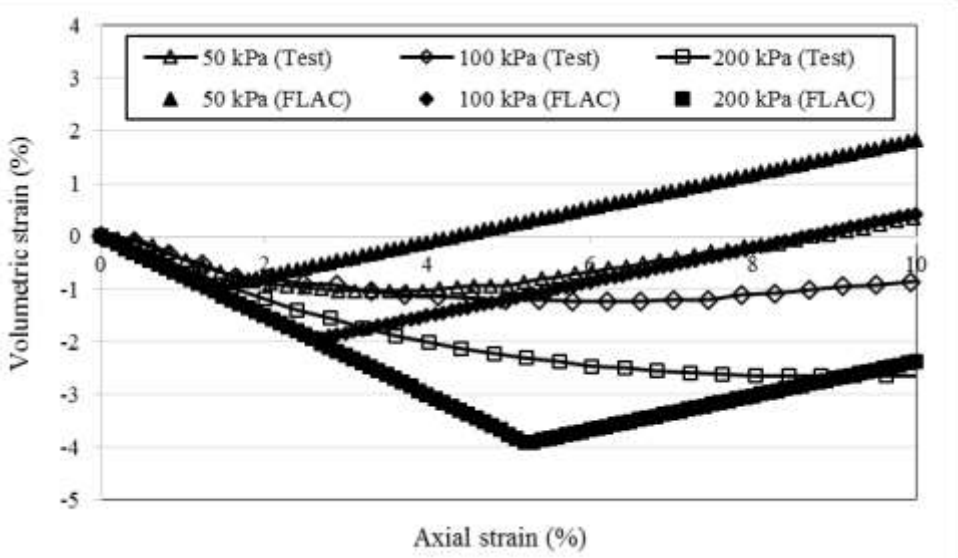

(b) Volumetric strain-axial strain relationship

Figure 5.9 Numerical simulation of triaxial shear tests for the backfill soil using the MC model

In addition to the simulation of the triaxial shear tests, the isotropic compression test was simulated using the MC model (see Figure 5.10). The isotropic compression test

shows that the isotropic stress increased with an increase in the volumetric strain but the rate of the isotropic stress increased with an increase in the volumetric strain. This behavior means that the backfill soil exhibits the feature of volumetric hardening. The test result shows a nonlinear relationship between isotropic stress and volumetric strain while the numerical results present a linear relationship. This difference between the test result and the numerical results is because the MC model has a limitation of describing the feature of volumetric hardening for the backfill soil.

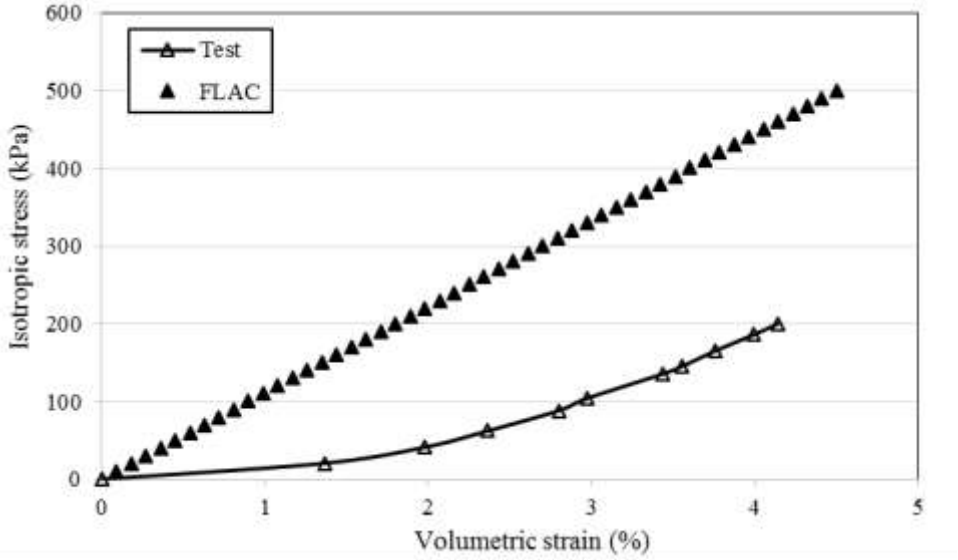

Figure 5.10 Numerical simulation of isotropic compression test for the backfill soil using the MC model

5.3.1.2. Parameters for the Cap-Yield model

The CY model requires nearly twenty parameters. Fourteen of them have to be determined or calibrated from the isotropic test and traxial shear tests of the backfill soil. Some of these parameters, such as the unit weight, γ_{rs}, Poisson's ratio, ν_{ur}, the cohesion, c_{rs}, the friction angle, ϕ_{rs}, and the dilation angle, ψ_{rs}, are the same as those in the MC model. The other parameters, such as the cap-yield surface parameter, α, multiplier, R, plastic

strain coefficient, β, bulk modulus at reference effective pressure, K^{iso}_{ref}, reference effective pressure, P_{ref}, and failure ratio, R_f, have to be determined or calibrated.

In the CY model, the reference effective pressure was set to be 100 kPa and the failure ratio was assigned to be a typical value of 0.9. According to the isotropic compression test, the bulk modulus at the reference effective pressure could be determined. The relationship between the isotropic compressive stress and the volumetric strain could be expressed by a power function in Eq. (5.8):

$$\frac{dp'}{de} = K_{ref}^{iso}\left(\frac{p'}{p_{ref}}\right)^{m} \tag{5.8}$$

where

p' - mean effective stress;

e - volumetric strain;

K_{ref}^{iso} - bulk modulus at reference effective pressure;

m - power exponent.

Equation (5.9) was the solution of Eq. (5.8) with the condition of $e = 0$ at $p' = 0$:

$$p' = \left[(1-m)\frac{K_{ref}^{iso}}{p_{ref}^{m}}\right]^{\frac{1}{1-m}} e^{\frac{1}{1-m}} \tag{5.9}$$

Equation (5.9) is a power function, used to fit the test data points from the isotropic test as shown in Figure 5.11. The fitted power function and its R-square value are also shown in Figure 5.11. Compared with the fitted power function, the power exponent and

the bulk modulus at the reference effective pressure in Equation (5.9) could be determined as $m = 0.52$ and $K_{ref}^{iso} = 6971$.

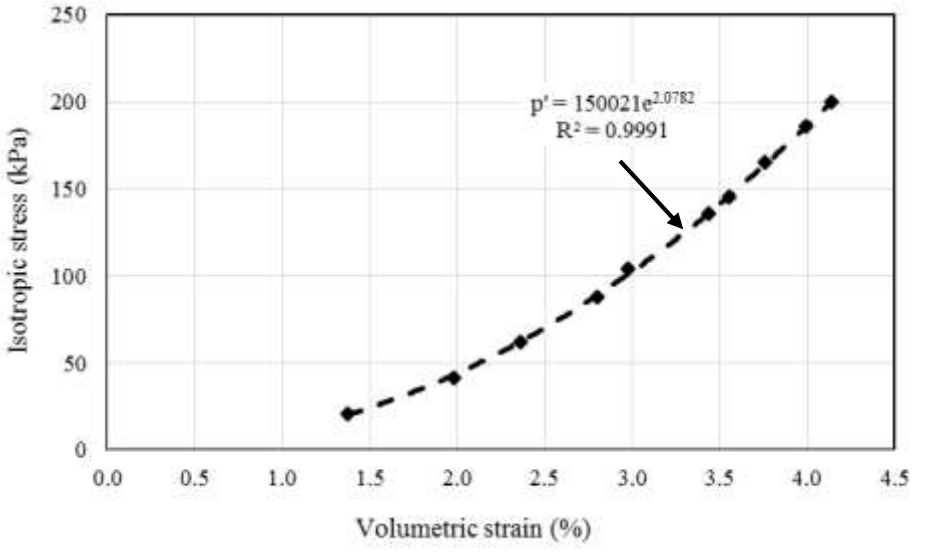

Figure 5.11 Power function for the relationship between volumetric strain and isotropic compression stress

Itasca (2011) recommended a formula to determinate the elastic tangent shear modulus at the reference effective pressure and the multiplier, which are expressed in Eq. (5.10) and Eq. (5.11). In these two equations, the elastic tangent shear modulus at the reference effective pressure and the multiplier could be calculated using an unloading and reloading modulus at the reference effective pressure, E_{ur}^{ref} and a bulk modulus at the reference effective pressure, K_{ref}^{iso}. The determination of the unloading and reloading modulus at the reference effective pressure is illustrated in Figure 5.12.

$$G_{ref}^{e} = \frac{E_{ur}^{ref}}{2(1+\upsilon_{ur})} \tag{5.10}$$

where

E_{ur}^{ref} - unloading and reloading modulus at the reference effective pressure,

$E_{ur}^{ref} = 5 \cdot E_{50}^{ref}$;

υ_{ur} - Poisson's ratio, $\upsilon_{ur} = 0.2$.

$$R = \frac{E_{ur}^{ref}}{3(1-2\upsilon_{ur})K_{ref}^{iso}} - 1 \tag{5.11}$$

where

K_{ref}^{iso} - bulk modulus at the reference effective pressure.

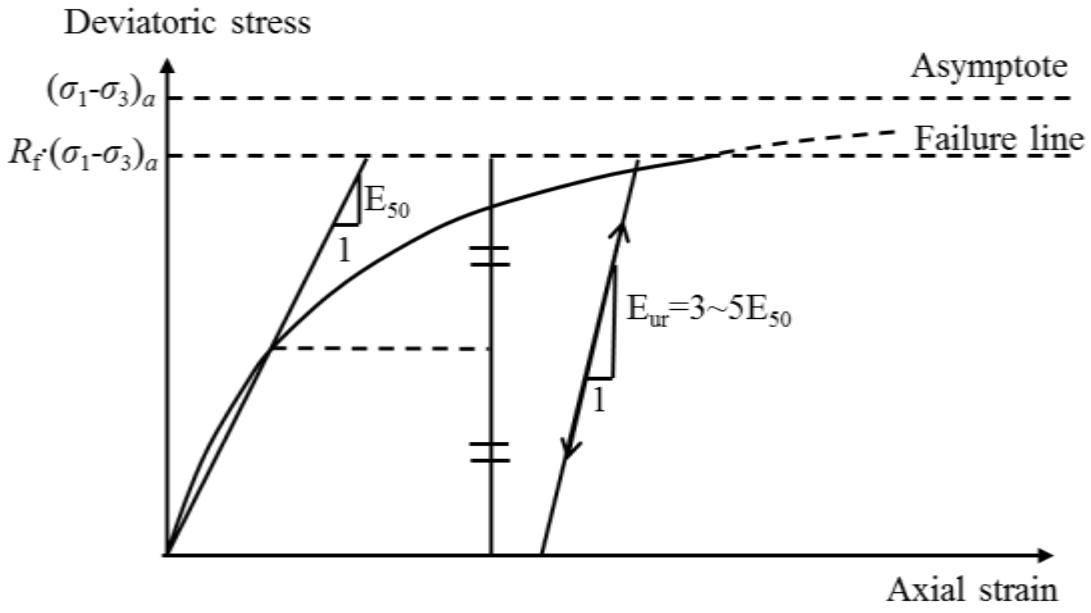

Figure 5.12 Determination of unloading and reloading modulus in the Hardening Soil model (after Plaxis v8.2)

Except for the parameters determined by the test results or estimated using typical values, two remaining parameters, cap-yield surface parameter, α, and plastic strain

coefficient, β, needed to be calibrated through a trial and error method. These two parameters were adjusted in a numerical model simulating the triaxial shear test at the confining stress of 200 kPa to generate a stress-strain curve matching that from the test. Table 5.3 summarizes the parameters of the CY model for the backfill material.

Table 5.3 Parameters of the CY model for the backfill soil

Parameters	unit	value
Unit weight, γ_{rs}	kN/m^3	18.1
Cap-yield surface parameter, α	-	1.5
Ultimate friction angle, ϕ_{rs}	degrees	52
Ultimate dilation angle, ψ_{rs}	degrees	8
Multiplier, R	-	6.2
Plastic strain coefficient, β	-	0.5
Reference elastic tangent shear modulus, G^{e}_{ref}	kPa	32500
Reference bulk modulus, K^{iso}_{ref}	kPa	6971
Reference pressure, P_{ref}	kPa	100
Poisson's ratio, ν_{ur}	-	0.2
Cohesion, c_{rs}	kPa	0
Power, m	-	0.52
Failure ratio, R_f	-	0.9

The results from the numerical simulation using the CY model under the confining stresses of 50 and 100 kPa were compared with those from the triaxial tests as presented in Figure 5.13 (a) and (b). Figure 5.13 (a) presents a satisfactory calculation in the stress-strain relationship using the CY model in the numerical simulation. Similarly, as shown in Figure 5.13 (b), the numerical simulation reasonably calculated the volumetric-axial strain relationship of triaxial tests at confining stresses of 50, 100, and 200 kPa. The dilation behavior of the backfill soil was well captured by the numerical simulation. In addition, the isotropic compression test was numerically simulated. Figure 5.14 shows the comparison between the test results and the numerical results. The comparison shows that

the numerical simulation well captured the behavior of volumetric hardening of the backfill soil.

Compared with the test results in the triaxial tests and the isotropic compression test, the numerical results show a satisfactory calculation which demonstrated the validity of determined, estimated, and calibrated parameters. Additionally, compared with the MC model, the CY model shows the capability to simulate the decrease in soil stiffness during the shear loading. Overall, the numerical simulation using the CY model resulted in a better calculation in the behavior of the backfill soil than the MC model.

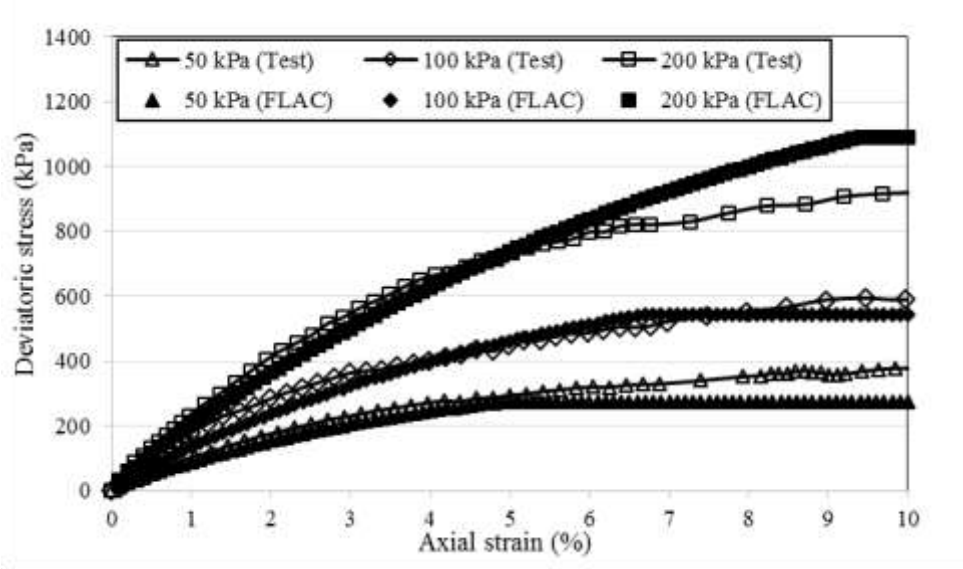

(a) Stress-strain relationship

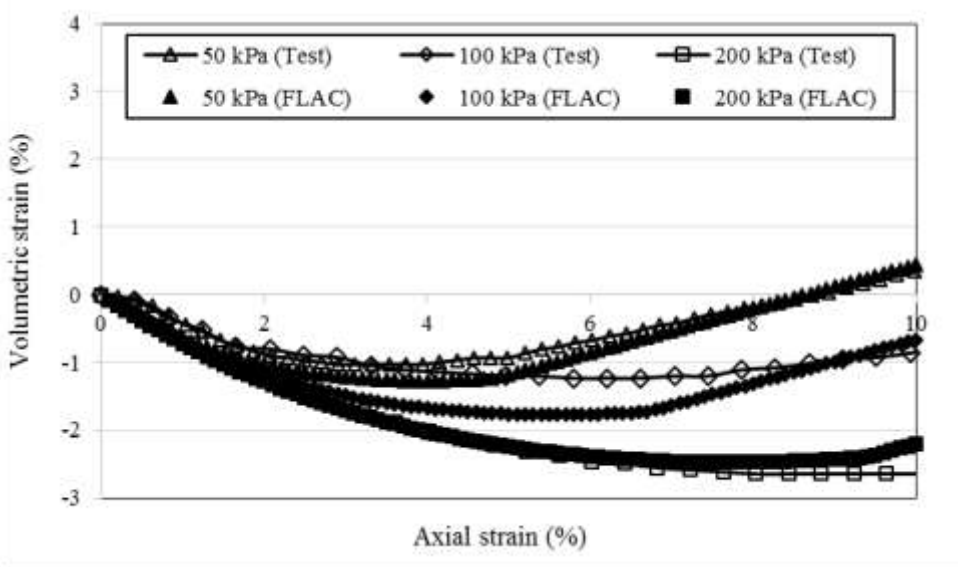

(b) Volumetric and axial strain relationship

Figure 5.13 Numerical simulation of triaxial tests for the backfill soil using the CY model

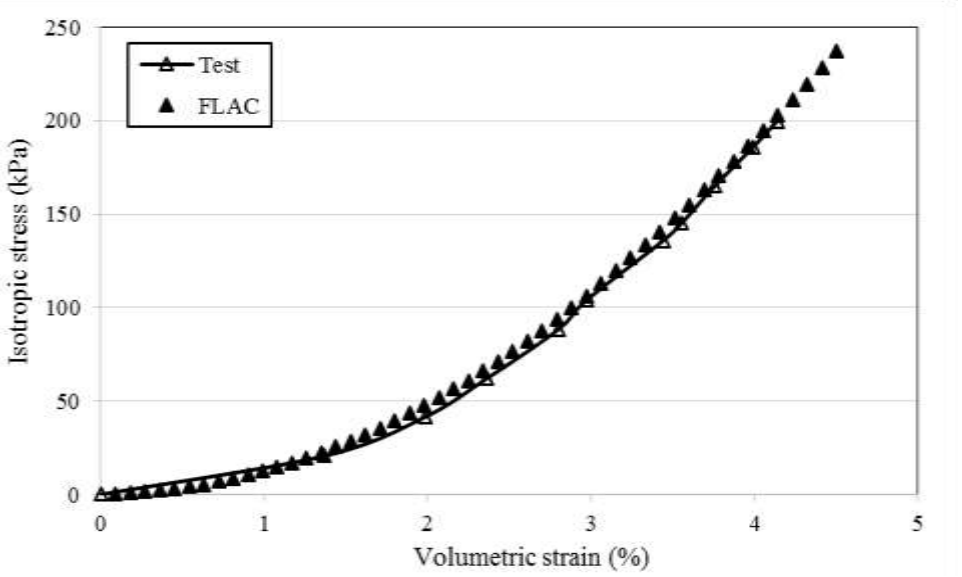

Figure 5.14 Numerical simulation of isotropic compression test for the backfill soil using the CY model

5.3.2. Retained soil

The MC model was used to simulate the behavior of the retained soil, which was a borrow soil. The parameters of the MC model for the retained soil was referred to those used in Huang et al. (2011) because the retained soil in this study came from the same area where the retained soil in Huang et al. (2011) came from. The parameters of the MC model are tabulated in Table 5.4.

Table 5.4 Parameters of the MC model for the retained soil

Parameters	Unit	value
Unit weight, γ_s[1]	kN/m^3	20.3
Young's modulus, E_s	MPa	20
Poisson's ratio, ν_s	-	0.3
Cohesion, c_s	kPa	1
Friction angle, ϕ_s	degrees	34
Dilation angle, ψ_s	degrees	0

Note: [1]The unit weight for the backslope and embankment was 16.8 kN/m^3.

5.3.3. Embedment soil and backslope soil

The embedment soil and the backslope soil were simulated using the MC model as well. Since the embedment and the backslope used the same soil as the retained soil, the parameters of the MC model for the embedment soil and the backslope soil were the same as those in the retained soil (see Table 5.4).

5.3.4. Foundation soil

The foundation soil was bedrock, which was simulated using the linearly elastic model. The unit weight of 20 kN/m^3 was used because this unit weight was used in the design of the wall. The other parameters in the linearly elastic model, such as Young's

modulus and Poisson's ratio, were estimated based on the typical values for bedrock. Table 5.5 summarizes the parameters of the linearly elastic for the foundation soil.

Table 5.5 Parameters of the linearly elastic model for the foundation soil

Parameters	Unit	Value
Unit weight, γ_f	kN/m^3	20
Young's modulus, E_f	MPa	2000
Poisson's ratio, ν_f	-	0.25

5.3.5. Geosynthetic reinforcement

Five types of geogrid were used as reinforcement including four types of uniaxial geogrid and one type of biaxial geogrid. A strip element incorporated in FLAC was used in the numerical simulation. The strip element was developed to simulate the behavior of reinforcement in earth retaining structures. The strip element was modelled as a linearly elastic and perfectly plastic material. Figure 5.14 illustrates a stress-strain relationship for the strip element. Since the tensile stiffness of geogrid decreases with the strain, the relationships between the stiffness at different strains for five types of geogrid are shown in Figure 5.15. As shown in Figure 5.15, the stiffness of geogrid dropped quickly when the strain was less than 1% and the decrease rate became smaller with an increase of strain. In addition, the time has an influence on the stiffness of geogrid. Typically, the stiffness of geogrid decreases with time. The average strain rate in the test was about 0.1%, the time effect on the stiffness was minimal such that its effect was not considered for the stiffness of geogrid. In the numerical model, the stiffness at 2% strain were selected for the geogrid, which is summarized in Table 5.6. Table 5.6 also provides the yield strengths of the

geogrid that are the same as those given by the manufacturer. Tensile failure strains were determined to be 10%.

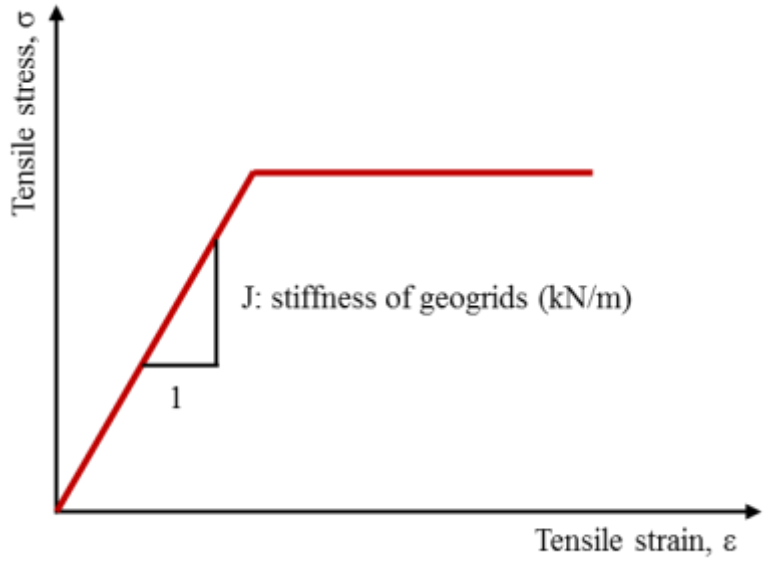

Figure 5.15 Tensile stress and strain relationship for the strip element

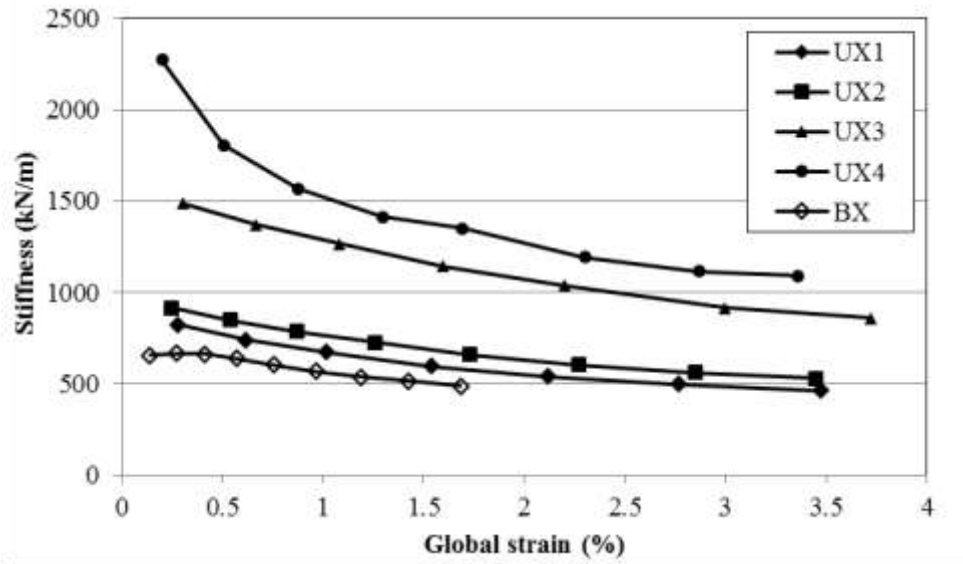

Figure 5.16 Tensile stiffness-strain relationship

Table 5.6 Parameters of geogrid in numerical modelling

Materials	Structure element type	Constitutive model	Secant stiffness@2%, J (kN/m)	Yield strength (kN/m)	Tensile failure strain (%)
UX1600	Strip	Linearly elastic and perfectly plastic	1271	144	10
UX1500			1074	114	10
UX1400			632	70	10
UX1100			551	58	10
BX1120			478*	19	10

Note: * stiffness in the cross machine direction

5.3.6. Modular block facing

The wall facing was comprised of stacked modular blocks and an interface was created to simulate the interaction between the modular block and the modular block. The modular block was modelled as a linearly elastic material. Young's modulus and Poisson's ratio in the constitutive model were estimated to be 2000 MPa and 0.2, respectively, which are typical properties of cement masonry. The unit weight of modular block was determined to be 15 kN/m^3, which was based on the weight of one block divided by its volume.

5.4. Interface properties

Three types of interfaces were considered in the numerical simulation for the GRR walls with modular block facings, which are an interface between the geogrid and the backfill soil, an interface between modular blocks and the backfill soil, and an interface between the modular block and the modular block. These interfaces play important roles

for the performance of the GRR walls. Attention was paid to the determination of the properties of these interfaces in the numerical models using test results or typical values.

5.4.1. Interfaces in FLAC

Itasca (2011) provides several interfaces for users to model an interaction between materials. The interface behavior is modelled using a combination of springs and sliders. Figure 5.17 illustrates the schematic diagram of an interface. The interface behavior in the normal direction is modelled using a vertical spring with a tensile strength while the interface in the tangent direction is modelled using a horizontal spring and a horizontal slider.

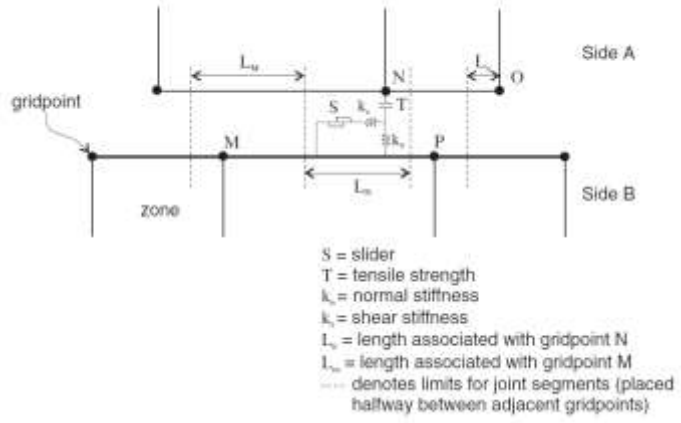

Figure 5.17 Implementation of the interface (Itasca, 2011)

In the numerical model, the interface between the geogrid and the backfill soil, the interface between the modular block and the modular block, and the interface between the modular block and the backfill soil are modelled as a linearly elastic and perfectly plastic material with the MC failure criterion. Figure 5.18 presents a shear stress-relative displacement relationship of the interface. The shear stress linearly increases with an

increase in the relative displacement until the maximum shear stress reaches. The interface starts to fail at the maximum shear stress. The calculation of the maximum shear stress is illustrated in Figure 5.19. The maximum shear stress depends on the interface cohesion, the effective normal stress, and the friction angle of the interface. Equation (5.12) gives the formula to calculate the maximum shear stress:

$$\tau_{\max} = c_{inter} + \sigma'_n \cdot \tan\phi'_{inter} \tag{5.12}$$

wher

c_{inter} - interface cohesion

σ'_n - effective normal stress

ϕ'_{inter} - friction angle of interface

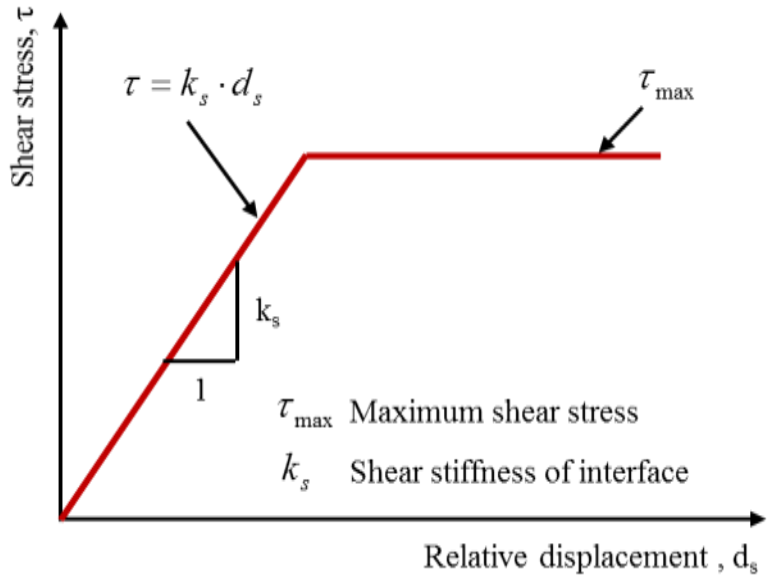

Figure 5.18 Shear stress-relative displacement relationship of interface

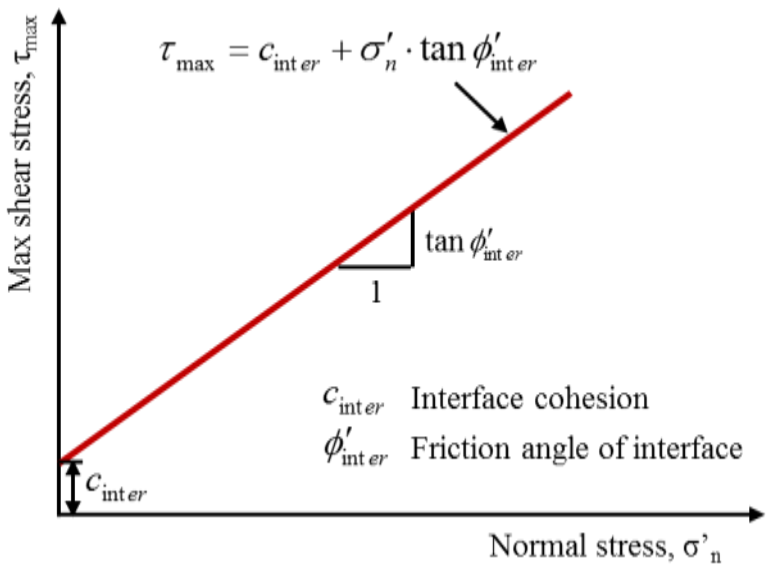

Figure 5.19 Relationship between maximum shear stress and confining stress

According to Equation (5.12), the maximum shear stress is the function of the interface cohesion, the effective normal stress, and the friction angle of the interface. Among these variables, the interface cohesion and the friction angle of interface are determined based on the properties of the interface. The friction angle of the interface could be determined according to Equation (5.13):

$$\tan\phi'_{inter} = c_{rf} \cdot \tan\phi' \tag{5.13}$$

c_{rf} - reduction factor

ϕ' - friction angle

5.4.2. Interface between geogrid and backfill material

The interface between the geogrid and the backfill soil influences the load transfer between them. Two load transfer mechanisms were found in previous studies (as shown in Figure 5.20): friction mechanism and passive-resistance mechanism.

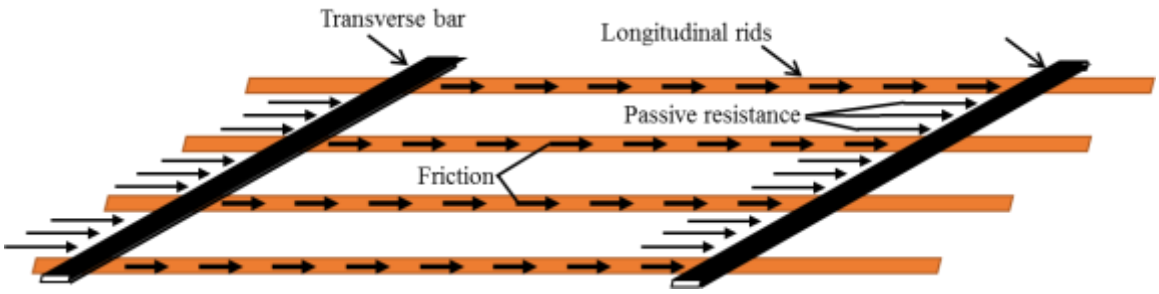

Figure 5.20 Interaction between geogrid and backfill materials

The determination of the interface properties is significant to study the behavior of the GRR walls. Direct shear test and pullout tests are two test methods to determine the properties of the interface between the geogrid and the backfill soil. Direct shear tests can only measure one-side interface friction between the geogrid and the backfill soil while pullout tests can measure the both sides interface friction between the geogrid and the backfill soil. In addition to the interface friction, the pullout test can measure a passive resistance resulting from the interaction between the transverse bar and the backfill soil.

(1) Numerical modelling of pullout tests

A two-dimensional numerical model was developed to simulate the pullout tests and determine and calibrate the interface properties between the geogrid and the backfill soil. As described in Chapter 3, nine pullout tests were performed with three types of geogrid, which included two types of uniaxial geogrid and one type of biaxial geogrid. Each type of geogrid was used to perform pullout tests at the three different normal pressures.

Figure 5.21 presents the numerical model for the pullout tests. The numerical model included a 1.5 m (length) by 0.3 m (thickness) backfill soil and a 1.2 m long geogrid placed in the middle of the backfill. The bottom of numerical model was fixed in vertical and horizontal directions and the left and right sides of the numerical model were fixed in the horizontal direction and moved freely in the vertical direction. A uniform normal pressure was applied on top of the numerical model to simulate the confining stress. A displacement load was applied to the front of the geogrid with a control displacement rate. The geogrid was modelled as a linearly elastic and perfectly plastic material. The properties of the geogrid are summarized in Table 5.7. A strip element was used to simulate the geogrid. The interface properties between the geogrid and the backfill soil were incorporated in the strip element. Table 5.8 gives the interface properties between the geogrid and the backfill soil. Among the interface properties, the interface cohesion was assumed to zero because the backfill soil is an angular material without cohesion. The determination of friction coefficient was referred to Eq. (5.13). The reduction factor was assumed to be 0.67 for uniaxial geogrid and 0.84 for biaxial geogrid. The friction angle of the backfill soil was used for the friction angle of interface. The shear stiffness of geogrid was calibrated using one pullout test with the UX1600 geogrid under the normal pressure of 43.4 kPa.

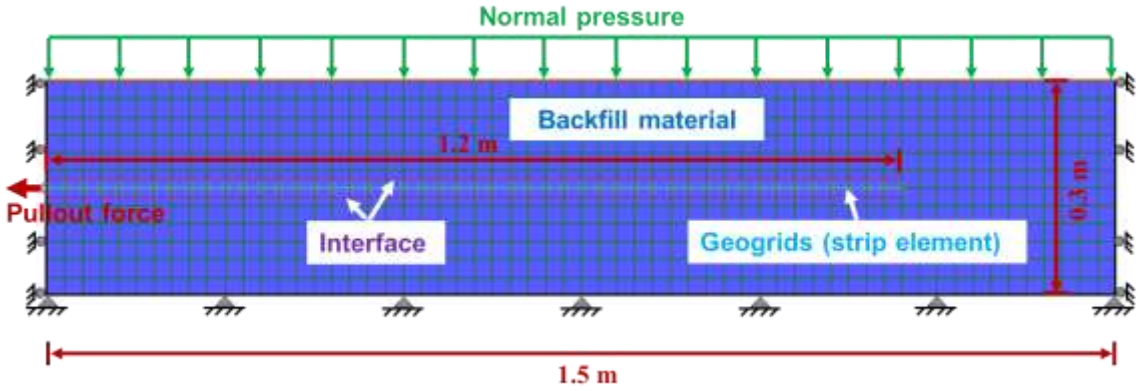

Figure 5.21 Numerical model of pullout tests

Table 5.7 Parameters of the geogrid in the numerical model for pullout tests

Parameters	unit	UX1600	UX1100	BX1120
Secant stiffness, J	kN/m	990	450	435
Yield strength	kN/m	144	58	19*
Tensile failure strain	%	20	20	20

Note: * cross machine direction

Table 5.8 Interface properties between the geogrid and the backfill soil

Parameters	unit	UX1600	UX1100	BX1120
Interface cohesion, c_{inter}	kN/m	0	0	0
Friction angle of interface, ϕ	°	40	40	47
Shear stiffness, k_s	kN/m/m	6500	6500	6500

(2) Results of the numerical simulation of pullout tests

Figure 5.22 presented the relationships between pullout forces and displacements calculated by the numerical simulation for UX1100, UX1600, and biaxial geogrid, respectively. In the numerical simulation, the backfill soil was modelled as a linearly elastic and perfectly plastic material with the MC failure criterion. The properties of the

backfill soil in this model can be seen in Table 5.2. The results from pullout tests are presented as well for the comparison purpose. Solid lines in the figures represent the test results while dash lines represent the numerical results. As can be seen in Figure 5.22, the pullout forces calculated by the numerical simulation increased with an increase in displacements and then gradually approached to a maximum pullout force, indicating that the geogrid with a full length was pulled out after the maximum pullout force. The test results and the numerical results show that the pullout force increased with an increase in normal pressure. Overall, the results from pullout tests and numerical simulation agree well with each other.

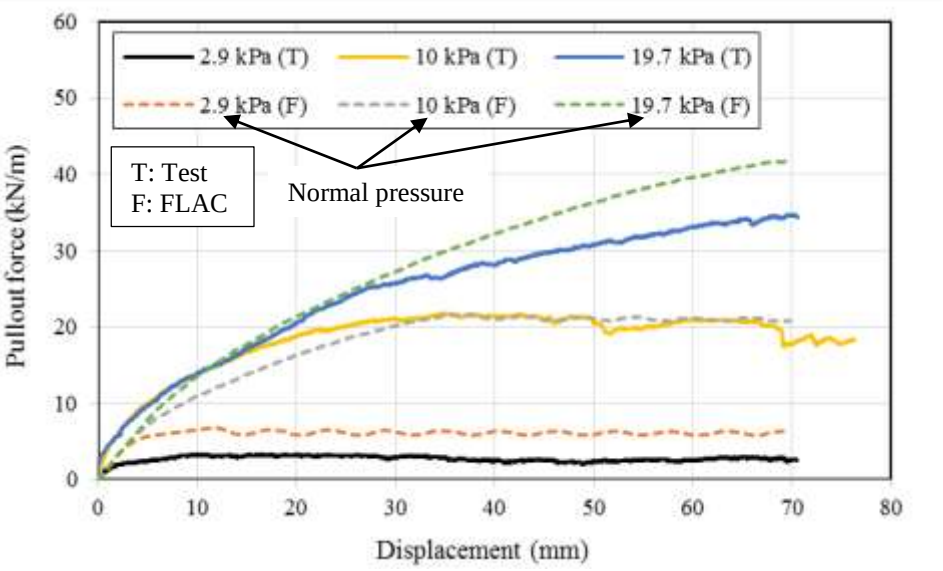

(a) UX 1100

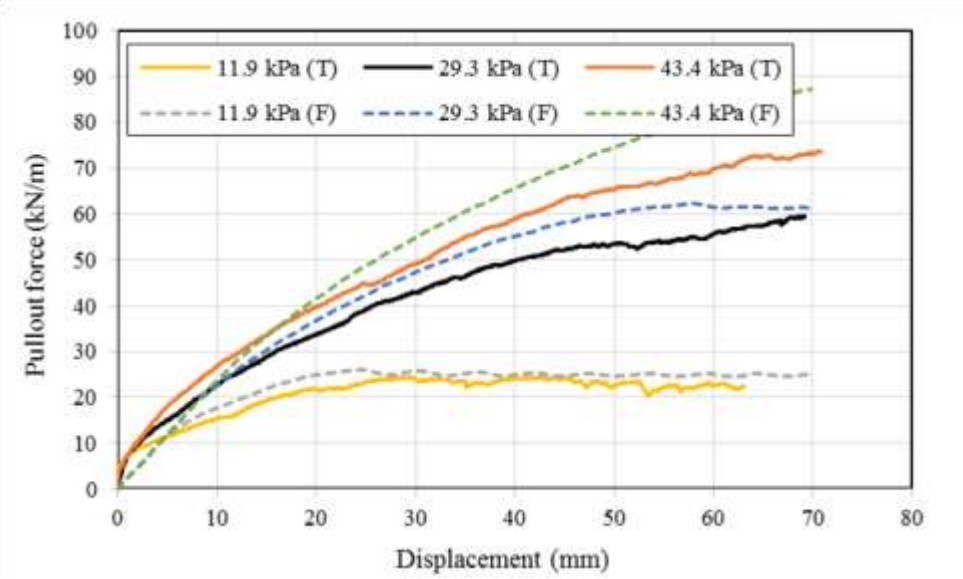

(b) UX 1600

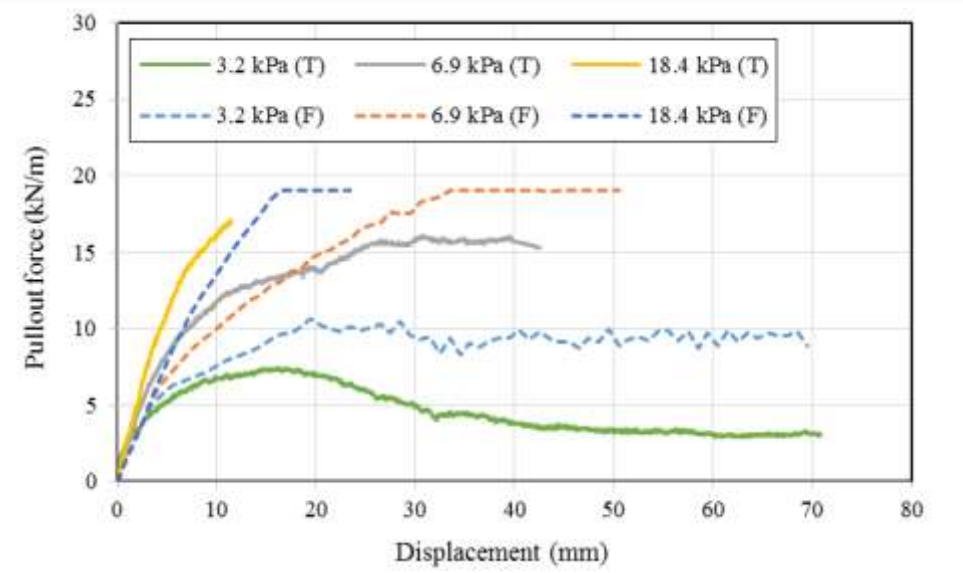

(c) Biaxial

Figure 5.22 Numerical simulation of the pullout tests using the MC model

Similar to Figure 5.22, Figure 5.23 presents the relationships between the pullout forces and the displacements calculated by the numerical simulation for UX1100, UX1600, and biaxial geogrid. In the numerical simulation, the backfill soil was modelled using the

CY model. The properties of the backfill soil using the CY model can be found in Table 5.3. The relationships of pullout force and displacement measured from pullout tests are presented as well for the comparison purpose. Solid lines in the figures represent the test results while dash lines represent the numerical results. As can be seen in Figure 5.23, the pullout forces calculated by the numerical simulation increased with an increase in displacements and then gradually approached to a maximum pullout force, indicating that the geogrid with a full length was pulled out after the maximum pullout force. The test results and the numerical results show that the pullout force increased with an increase in normal pressure. Overall, the results from pullout tests and numerical simulation agree well with each other.

Compared with the MC model, the numerical simulation using the CY model computed the results better. Therefore, the numerical modeling of GRR walls in this study mainly used the CY model to simulate the behavior of the backfill soil.

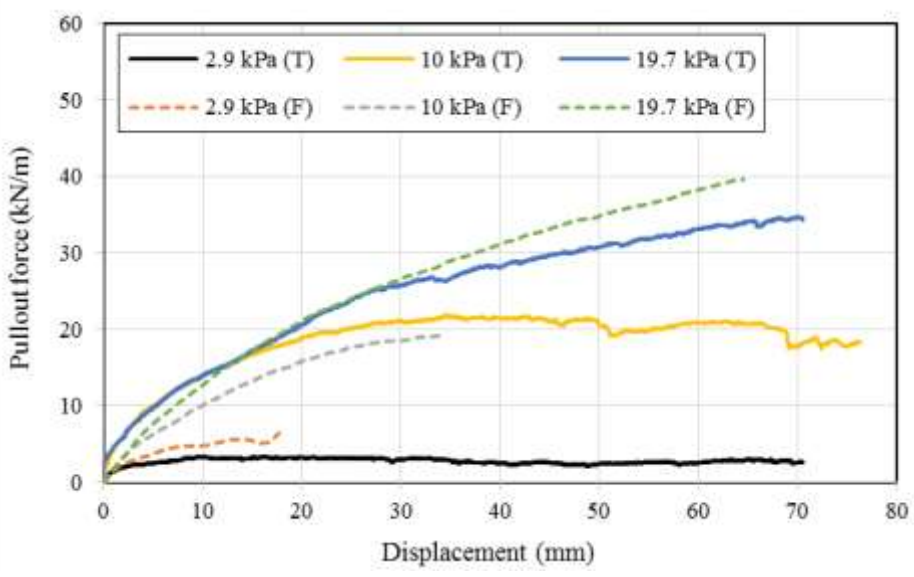

(a) UX 1100

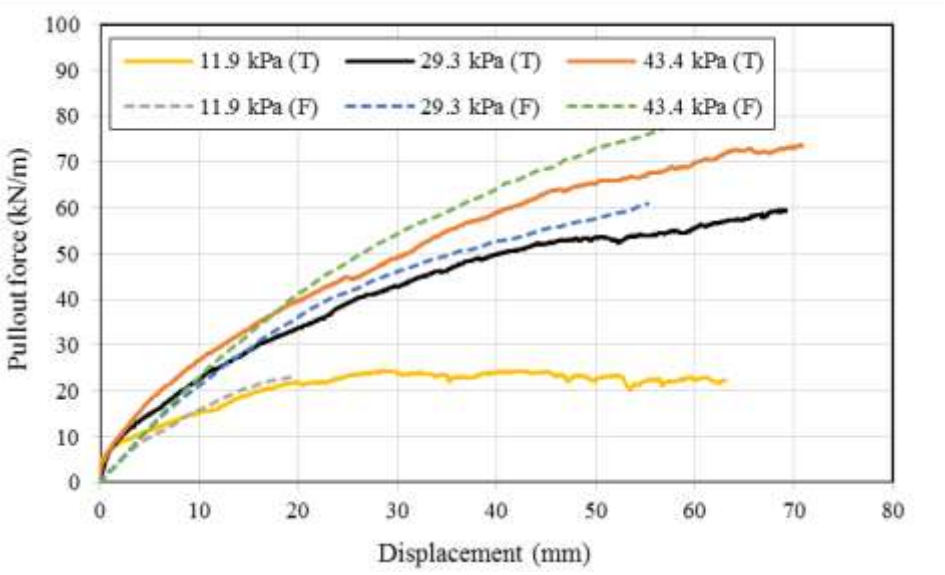

(b) UX 1600

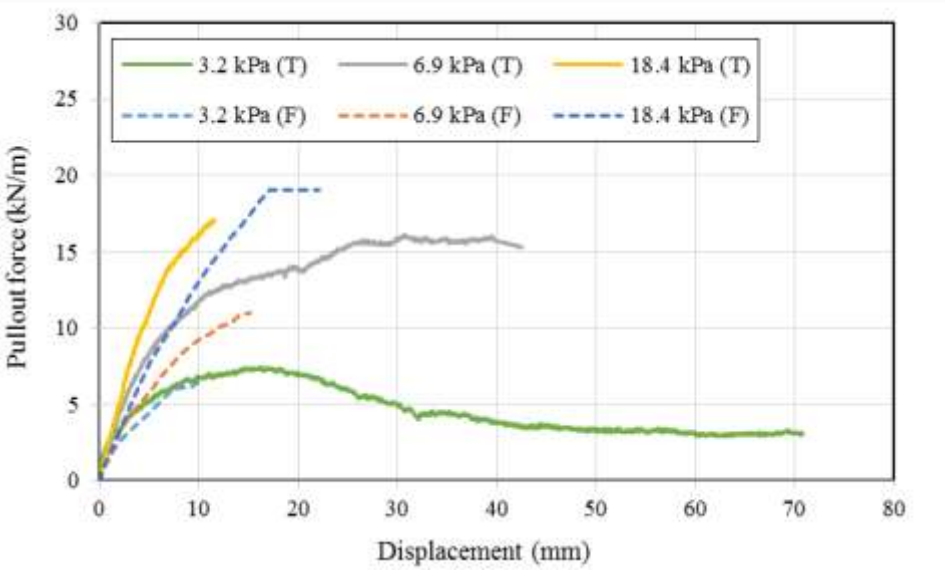

(c) BX

Figure 5.23 Numerical simulation of the pullout tests using the CY model

5.4.3. Interface between modular block and modular block

The interface was considered to simulate the interaction between the modular block and the modular block. The dimension of the modular block is illustrated in Figure 5.24.

The cross section of the modular block had 20 cm in height and 30 cm (nominal) in width. In a plane strain condition, only the interface between the top face of the modular block and the bottom face of another one was considered. The effect of interaction between side faces of modular blocks was neglected.

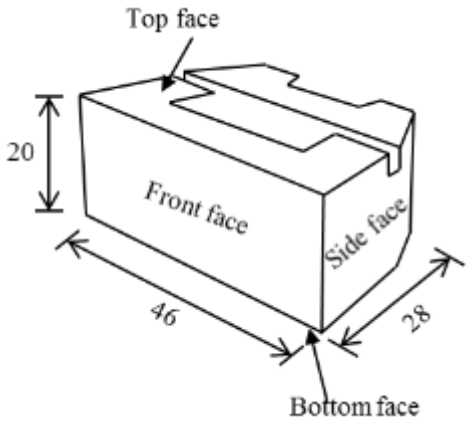

Figure 5.24 Dimensions of a modular block (unit: cm)

The interaction between the modular blocks depends on the configuration of the contact surface between modular blocks. The interaction of two modular blocks is shown in Figure 5.25. Figure 5.25 presents the normal stress and the shear stress of an interface between two modular blocks. The normal stress results from the weights of modular blocks above the upper one, the friction between modular blocks and backfill material, and the down drag force of reinforcement. The shear stress consists of two parts: (1) a friction due to relative displacement between modular blocks, and (2) a cohesion due to a shear key between modular blocks.

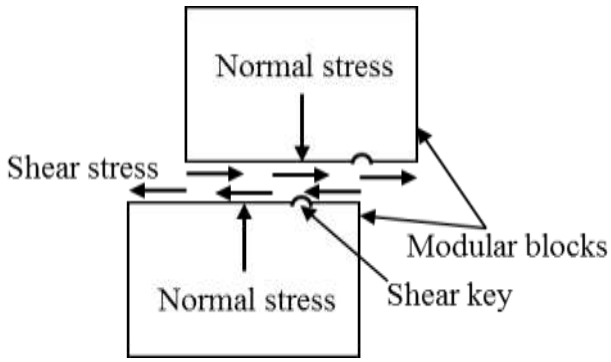

Figure 5.25 Free body diagram of modular blocks (cross section)

Hatami and Bathurst (2006) reported the tests of interface between modular blocks. The properties of the interface between modular blocks used in their study was employed in this study. Table 5.9 summarizes the properties of interface between the modular block and the modular block.

Table 5.9 Interface properties between modular block and modular block

Interface	Friction angle,φ_i (degree)	Dilation angle,ψ_i (degree)	Interface cohesion (kPa)	Normal stiffness, kn (MN/m/m)	Shear stiffness, ks (MN/m/m)
Block-block	57	-	46	1000	40

5.4.4. Interfaces between modular block and backfill soil

Similar to the interaction between the modular blocks, the interaction between the modular block and the backfill soil has two major stresses, which are normal stress and shear stress. The normal stress results from weights of backfill material, which is lateral earth pressure. The shear stress comes from a friction due to the relative displacement between modular blocks and backfill materials.

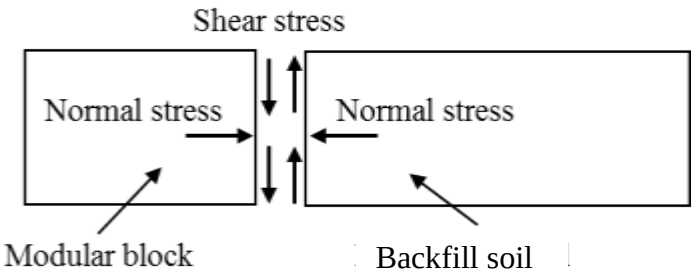

Figure 5.26 Interface between the modular block and the backfill soil

Table 5.10 summarizes the properties of the interface between the modular block and the backfill soil. The friction angle of interface was determined based on Eq. (5.13), where a typical value of 0.67 was assigned to the reduction factor and the friction angle of backfill soil was taken. The dilation angle of interface was assumed to be the same as that of backfill soil. The normal and shear stiffness were the same as the values used in Hatami and Bathurst (2006).

Table 5.10 Interface properties between modular block and backfill material

Interface	Friction angle of interface, ϕ_{inter} (degree)	Dilation angle of interface, ψ_{inter} (degree)	Interface cohesion (kPa)	Normal stiffness, kn (MN/m/m)	Shear stiffness, ks (MN/m/m)
Soil-block	40/24[1]	8/0	0	100	1

Note: [1]means properties between embedment and wall facing;

5.4.5. Connection between modular block and geosynthetic

Mechanical connectors were used to connect the geogrid and the modular blocks. In the numerical model, a pin connection was used to connect the geogrid and the modular block as shown in Figure 5.27. The front of the geogrid was pinned to the top right corner

of the lower block. The geogrid had the same movement as the top right corner of the lower block but had a free rotation.

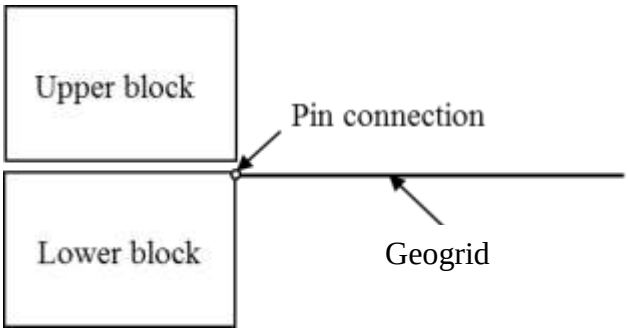

Figure 5.27 Connection between the modular block and the geogrid

Chapter 6 Numerical Modeling of Hybrid GRR Walls

6.1. Introduction of numerical modeling of GRR walls

In this chapter, FLAC was used to evaluate the performance of one GRR wall and two hybrid GRR walls in the field. The properties of materials and interfaces were determined, calibrated, and verified in Chapter 5 while the geometry, the boundary condition, and the construction stage will be introduced in this chapter. Calculated results from the numerical simulation are analyzed, discussed, and compared with those from the field tests.

6.2. Numerical modeling

6.2.1. Model geometry

A two-dimensional numerical model was used to investigate the behavior of earth walls instead of a three-dimensional numerical model because the dimension of the simulated walls in longitudinal direction was much larger than that in transverse direction so that the field test section was close to a plane-strain condition.

Figure 6.1 shows the representative geometry of the numerical model for the three tests sections. The model consisted of six zones, a foundation zone, an embedment zone, a wall facing zone, a reinforced soil zone, a retained soil zone, and a backslope zone. The foundation zone was 20 m high and 72 m long. The foundation zone below the wall facing zone, the reinforced soil zone and the retained soil zone was 36 m in length. The length of the foundation zone in front of wall facing zone was 36m as well, which was used to minimize the boundary effect.

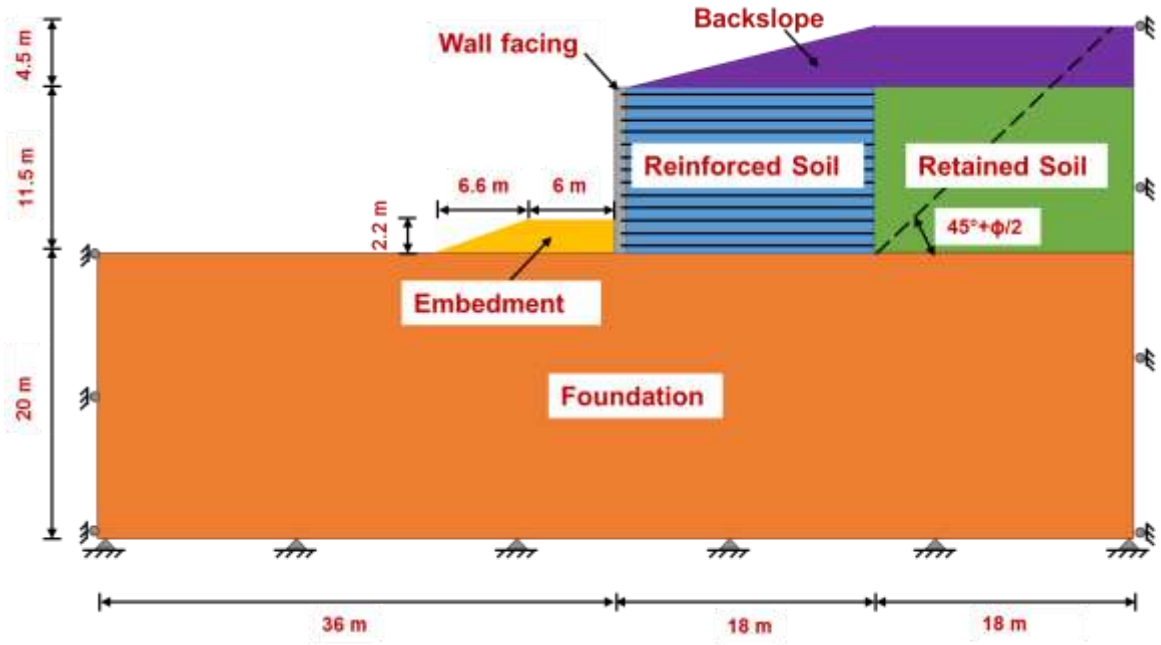

Figure 6.1 Geometry of numerical model

The height of the wall facing zone was 11.5 m, which was an average height of the three test GRR wall sections. The wall height had 57 stacked modular blocks and one wall cap above them. The width of wall facing was 0.3 m, which was the nominal width of the modular blocks. The reinforced soil zone was behind the wall facing zone. The width and the height of the reinforced soil zone were 18 and 11.5 m, respectively. The geogrid layers were installed in the reinforced soil zone as reinforcement. The length of reinforcement was the same as the width of the reinforced soil zone. The vertical spacing of the reinforcement layers was the same those in the field tests (as shown in Figure 4.3). The retained soil zone was behind the reinforcement soil zone. The width and the height of retained soil zone were 18 and 11.3 m, respectively. The width of the retained soil zone was extended to 18 m to minimize the boundary effect. The embedment was constructed in front of the wall facing. The embedment zone in the numerical model was a right angle

trapezoid. The height and top width of the embedment zone were 2.2 and 6 m, respectively. A side slope of the embedment zone started from the top of the embedment and extended down to the top of the foundation zone, which had a side slope ratio of 3(h): 1 (v). The backslope zone was constructed on the top of the reinforced soil zone and the retained soil zone. The height of the backslope was 4.5 m. There was a side slope of the backslope zone, which started from 1 m away from the back of the wall facing and went up to the top of backslope with an approximate slope angle of 11.5°.

6.2.2. Boundary conditions

Boundary conditions of the numerical model are presented in Figure 6.2. The bottom of the model was fixed in vertical and horizontal directions. The left and right sides of the model were fixed in the horizontal direction but were set free in the vertical direction. Three types of interfaces were considered in the numerical model, which are the interface between the geogrid and the backfill soil, the interface between the modular block and the modular block, and the interface between the modular block and the backfill soil. These three types of interfaces were introduced in Chapter 5 and are presented in Figure 6.2. Figure 6.2 also shows the mesh of the numerical model.

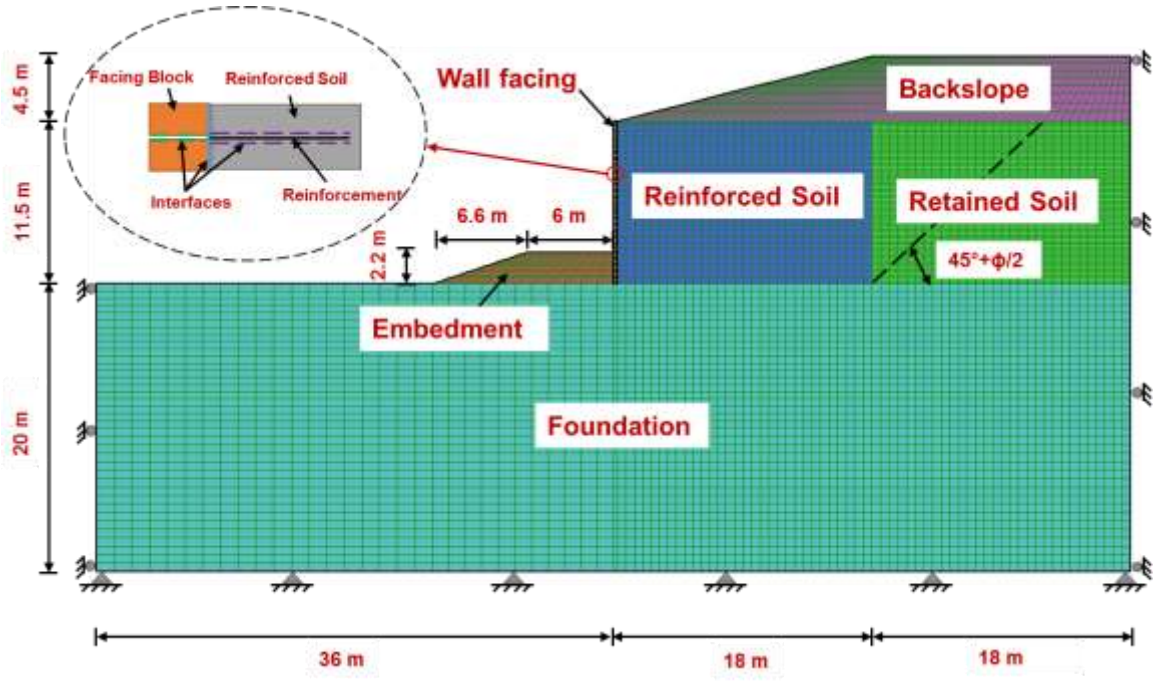

Figure 6.2 Mesh of the numerical model

6.3. Construction stage

The one GRR wall and two hybrid GRR walls were constructed by stages in the field and these construction stages were simulated in the numerical modeling. The construction stages are described as follows:

(1) Before the wall construction, the foundation soil reached an equilibrium under gravity.

(2) A layer of the wall facing, the backfill soil, the retained soil, and the geogrid was installed in the numerical model.

(3) Corresponding interfaces and connection were assigned.

(4) A horizontal 8 kPa vertical compaction stress was applied on the top of the reinforced soil because Hatami and Bathurst (2005 and 2006) have successfully used the 8

kPa vertical compaction stress in their numerical models to study the behavior of GRR walls.

(5) The numerical model was solved to reach a new equilibrium.

(6) Repeat Stages (2) to (5) till the top of the wall.

(7) Install the backslope on the top of the wall.

6.4. Numerical results of the GRR wall control section

6.4.1. Wall facing deflections

The wall facing deflections from the numerical simulation were the displacements occurring after the placement of the facing block. In other words, the displacement at the wall height started at the moment when the wall construction reached that wall height. This fact has been discussed in other studies, such as Hatami and Bathurst (2005) and Yu et al. (2016). In addition, it is inconvenient to convert the wall facing deflection to an accumulated wall facing deflection from the numerical simulation. In the following sections, the wall facing deflections are used for the convenience of presentation.

Wall facing deflections along the wall height before and after the construction of the backslope were calculated by the numerical simulation. Figure 6.3 shows the wall facing deflections calculated by the numerical simulation. For the comparison purpose, the wall facing deflections measured from the field tests are added in Figure 6.3 as well. Figure 6.3 (a) and (b) presents the wall facing deflections before and after the construction of the backslope, respectively. As shown in Figure 6.3, the wall facing deflections calculated by the numerical simulation increased to the maximum and then decreased along wall height. The wall facing deflections approached to the maximum value approximately

in the middle of the wall height. The wall facing deflections calculated by the numerical simulation agreed well with those from the field test before the construction of the backslope while the wall facing deflections calculated by the numerical simulation were slightly larger than those from the field test after the construction of the backslope. After the construction of the backslope, the wall facing deflections increased both in the field tests and the numerical simulation. The maximum wall facing deflection calculated by the numerical simulation using the CY model increased from around 29 mm before the construction of the backslope to 43 mm after the construction of the backslope. The increase in the wall facing deflections resulted from the weight of the backslope and the lateral earth pressure induced by the backslope.

In addition, the wall facing deflection calculated by the numerical simulation using the MC model and the CY model are compared as shown in Figure 6.3. The wall facing deflections calculated by the numerical simulation using the CY model are slightly larger than those using the MC model. This result is because the soil modulus in the CY model was lower than that in the MC model. The difference in the wall facing deflection became greater after the construction of the backslope because the soil modulus in the CY model decreased under shear loading while the soil modulus in the MC model was constant.

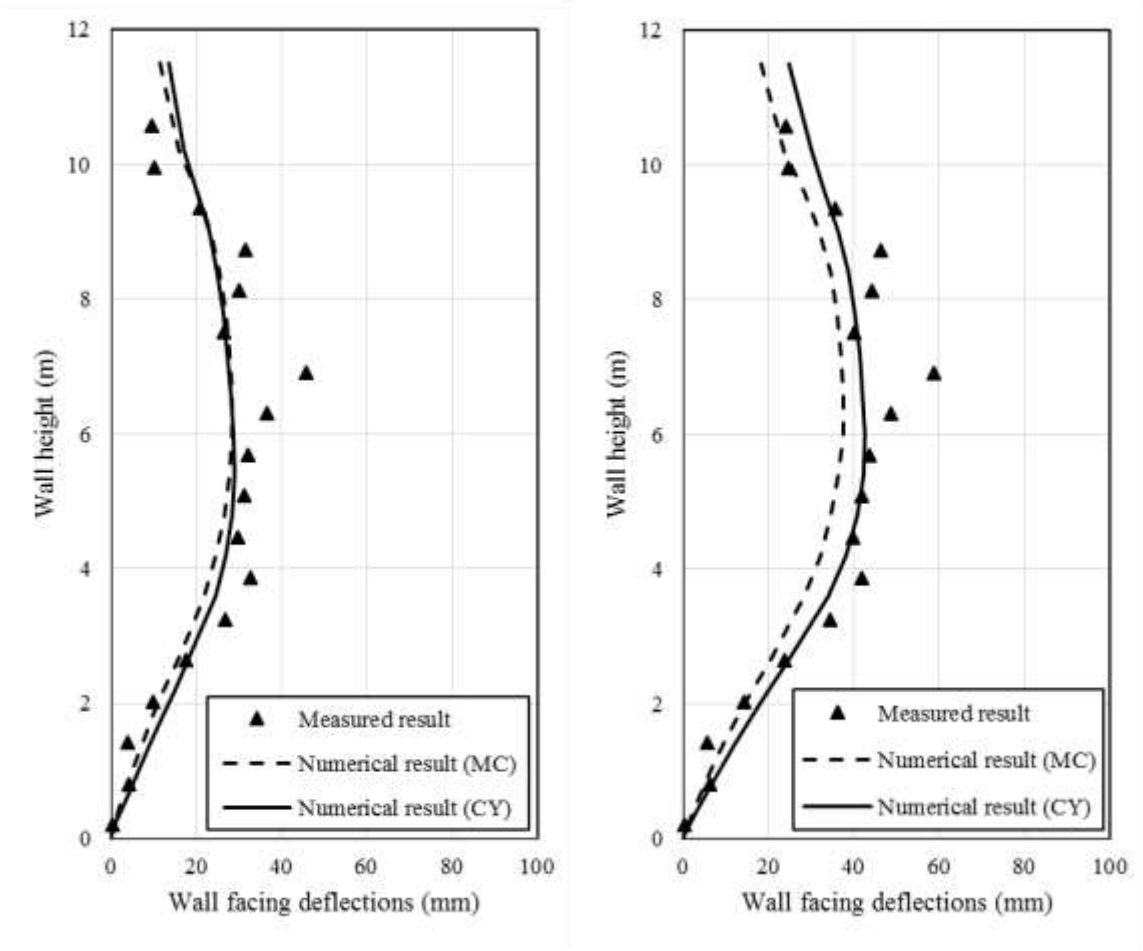

(a) Before the construction of the backslope (b) After the construction of the backslope

Figure 6.3 Wall facing deflections

6.4.2. Vertical earth pressures

The vertical earth pressures calculated by the numerical simulation are shown in Figure 6.4. Figure 6.4 (a) and (b) shows the distributions of vertical earth pressure calculated by the numerical simulation before and after the construction of the backslope, respectively. For the comparison purpose, the vertical earth pressures measured from the field tests are presented in Figure 6.4 as well as the calculated vertical earth pressures using the simplified methods. As shown in Figure 6.4, the vertical pressures calculated by the numerical simulation quickly decreased within a distance around 1.5 m from the back of

wall facing before and after the construction of the backslope. A similar drop was also found in the results from the field tests. This phenomenon could be attributed to the effect of the interaction between the wall facing and the backfill soil. An upward friction due to the relative displacement between soil and wall facing was applied to the backfill soil behind the back of wall facing, which reduced the vertical earth pressure at the bottom of the wall. However, the effect of friction was not considered in the simplified methods to calculate the trapezoid stress and the overburden stress. After the rapid drop, the vertical earth pressure reached a constant value before the construction of the backslope and then gradually increased after the construction of the backslope. Although the vertical earth pressure calculated by the numerical simulation slightly underestimated the one measured in the field test, the calculated vertical pressures reasonably matched the measured ones as well as the calculated trapezoid stress.

The vertical earth pressures calculated by the numerical simulation using the MC model and the CY model are compared as well (see Figure 6.4). The numerical simulation using the CY model calculated slightly larger vertical earth pressures than those using the MC model. From practical viewpoint, there is not much difference between using the MC model and CY model in terms of the vertical earth pressures.

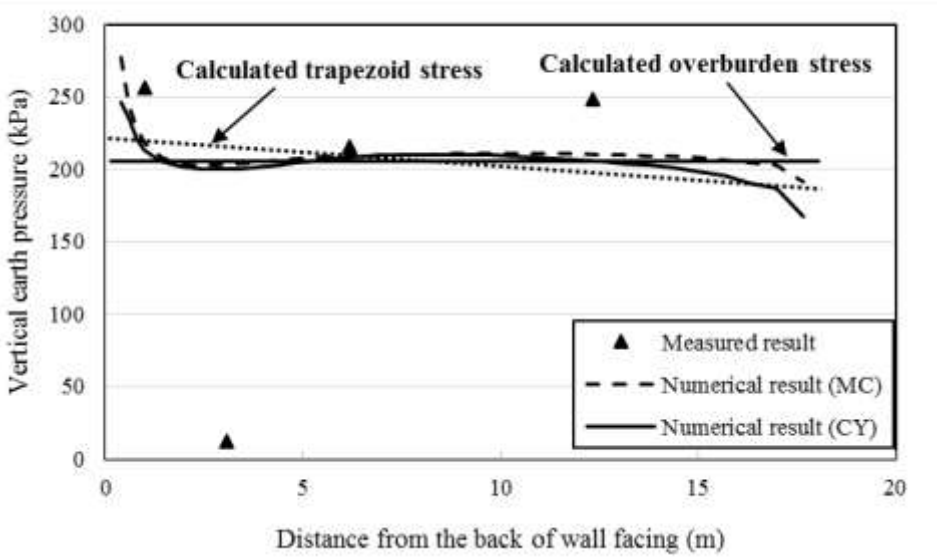

(a) Before the construction of the backslope

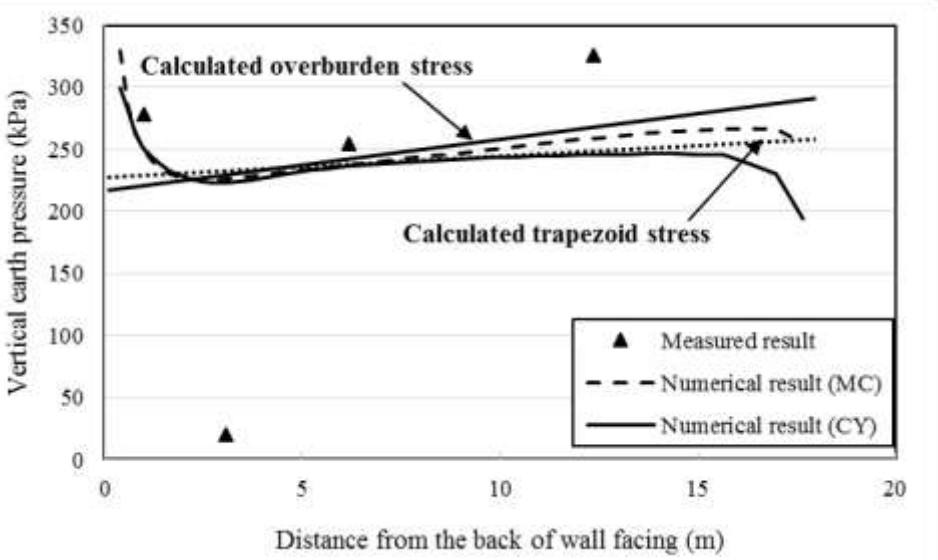

(b) After the construction of the backslope

Figure 6.4 Distribution of vertical earth pressures

6.4.3. Lateral earth pressures

Lateral earth pressures along depth before and after the construction of the backslope were calculated by the numerical simulation. Figure 6.5 shows the lateral earth pressures calculated by the numerical simulation. For the comparison purpose, the lateral

earth pressures measured in the field tests are shown in Figure 6.5 as well as the Rankine active earth pressure and the at-rest earth pressure. Figure 6.5 (a) and (b) presents the lateral earth pressure before and after the construction of the backslope, respectively. As shown in Figure 6.5, the lateral earth pressures calculated by the numerical simulation above the embedment zone approximately linearly increased with depth, which are close to the Rankine active earth pressures. The lateral earth pressure calculated by the numerical simulation below the top of the embedment zone rapidly increased till the bottom of the wall. The calculated lateral earth pressures were close to the at-rest earth pressure at the bottom of the wall. This result is because the lateral wall facing deflections below the top of the embedment zone were restricted so that the lateral earth pressure within the zone of embedment was close to the at-rest earth pressure. The lateral earth pressures calculated by the numerical simulation agreed well with those from the field tests. The lateral earth pressures from the field tests and the numerical simulation increased with the construction of the backslope. The increase in the lateral earth pressure resulted from the weight of the backslope.

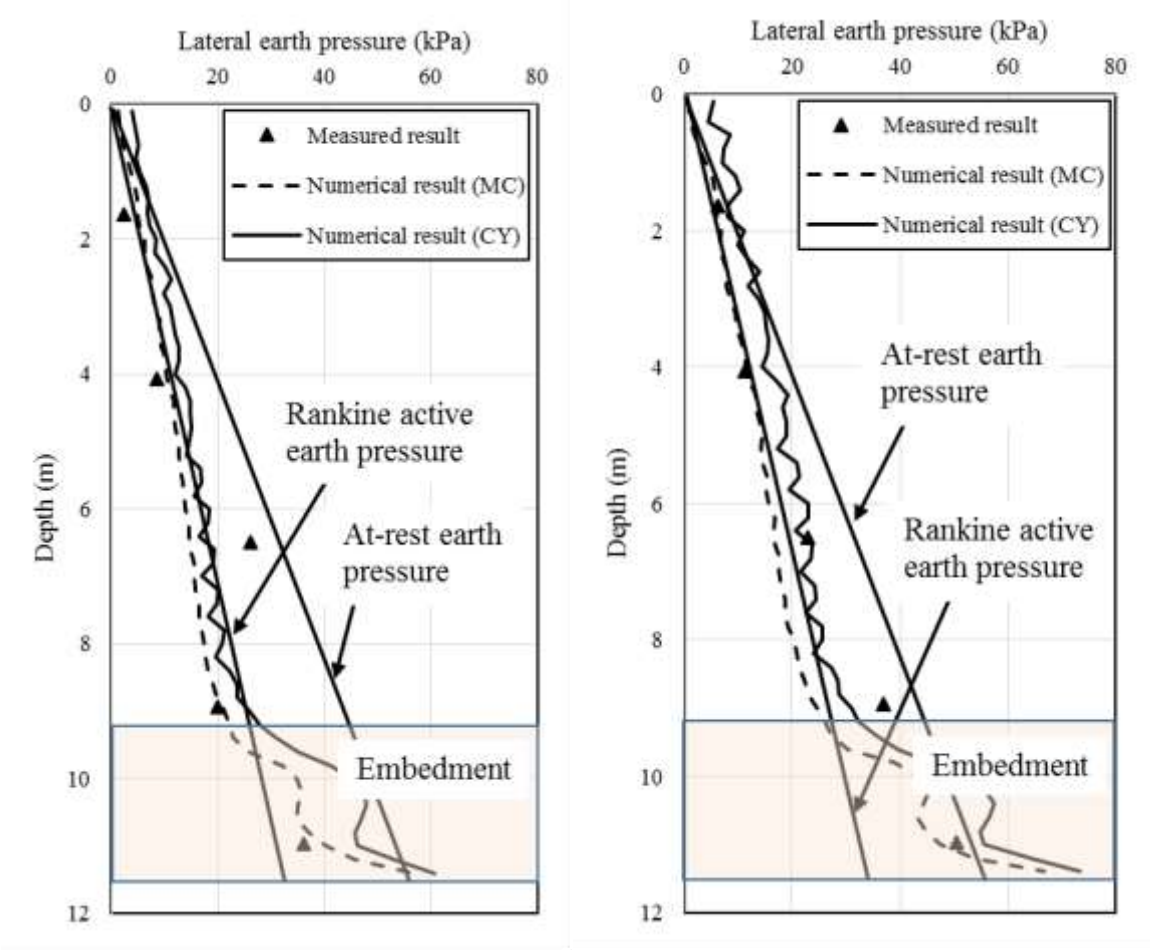

(a) Before the construction of backslope (b) After the construction of backslope

Figure 6.5 Distribution of lateral earth pressures

6.4.4. Strains in geogrid

Figure 6.6 presents the distribution of strains in the geogrid layers calculated by the numerical simulation at five instrumented layers at the end of construction. For the comparison purpose, the measured strains in the geogrid at these instrumented layers are added in Figure 6.6 as well. The calculated strains at each instrumented layer decreased quickly within a distance behind the back of wall facing and gradually approached to zero. This rapid decrease was found in the measured strains as well. The maximum strains in the

geogrid calculated by the numerical simulation happened at the connection. Overall, the strains calculated by the numerical simulation reasonably agreed with those measured in the field test. The numerical simulation also had negative strains at the rear end of the geogrid, which means that the geogrid was compressed at the rear end of the reinforced soil.

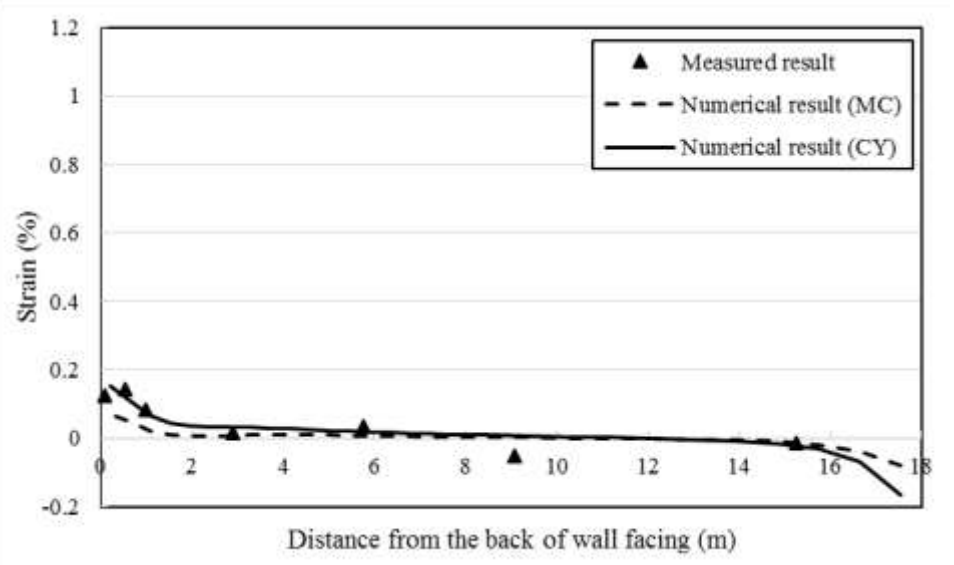

(a) Layer 1

Figure 6.6 Distribution of strains in the geogrid

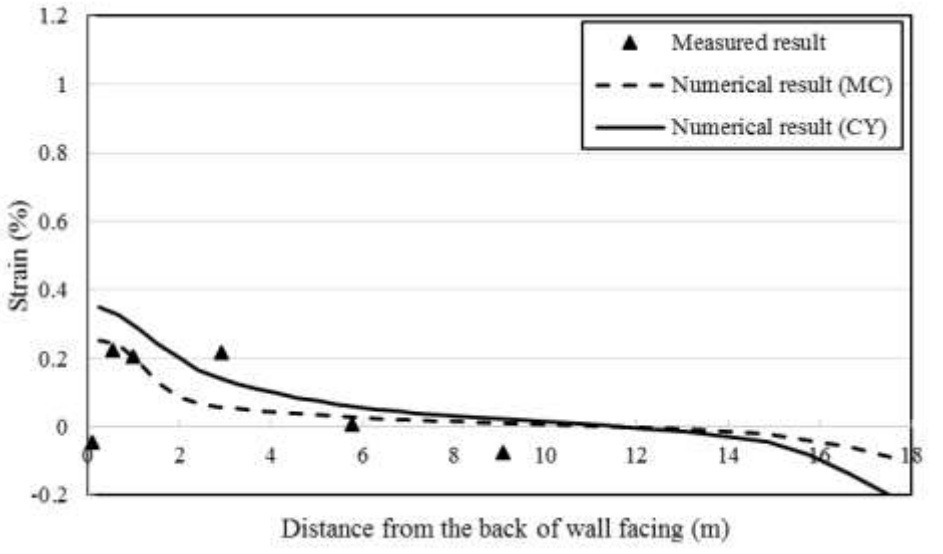

(b) Layer 2

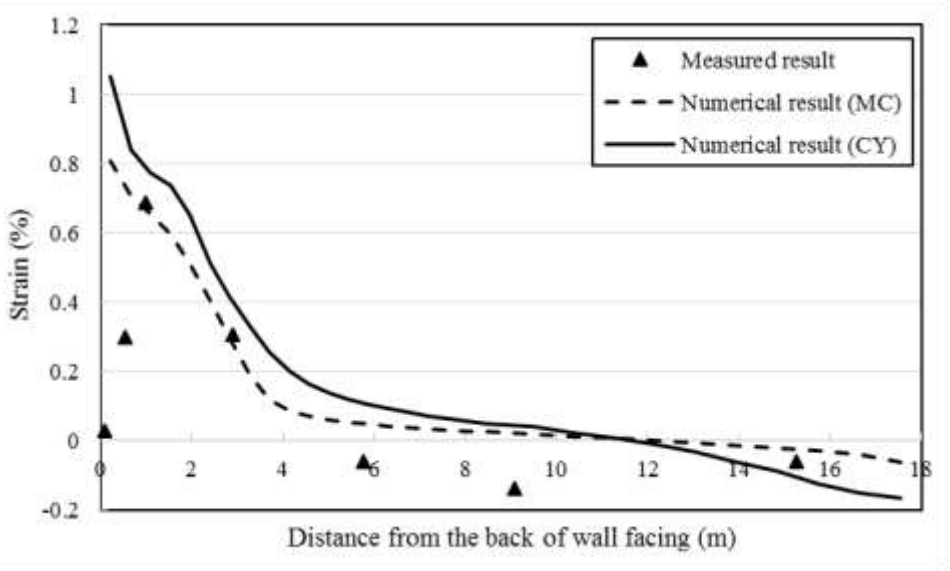

(c) Layer 3

Figure 6.6 Distribution of strains in the geogrid

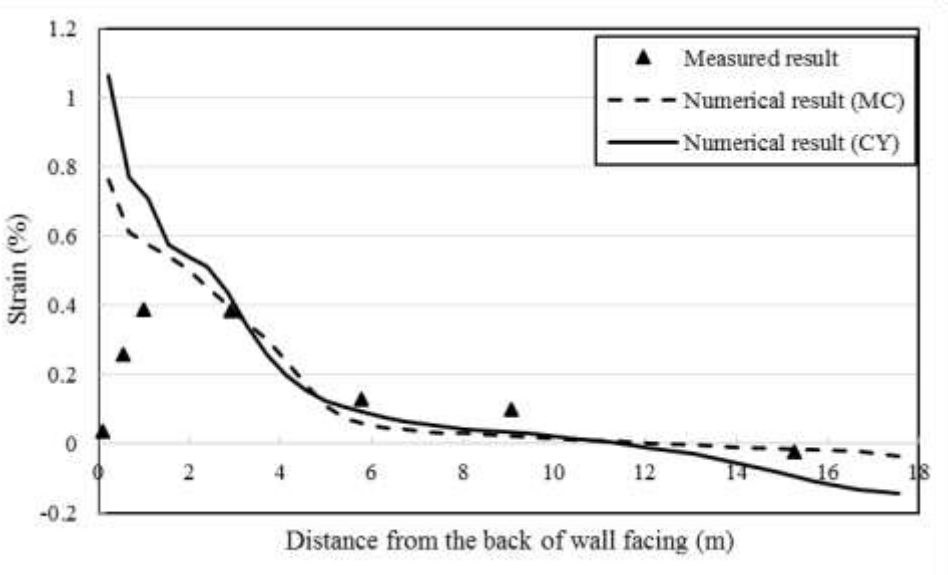

(d) Layer 4

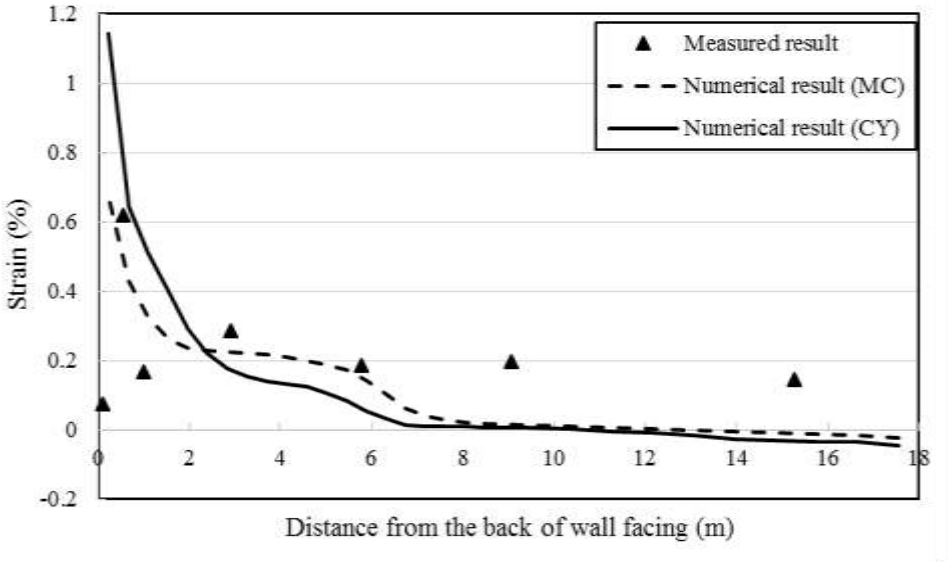

(e) Layer 5

Figure 6.6 Distribution of strains in the geogrid

The strains in the geogrid calculated by the numerical simulation using the MC model and the CY model are compared and shown in Figure 6.6. Overall, the strains

calculated by the numerical simulation using the CY model were larger than those using the MC model.

The maximum tensile stresses in the geogrid calculated by the numerical simulation at five instrumented layers are also compared with the measured ones as shown in Figure 6.7. It can be seen that the calculated maximum tensile stresses were overall slightly smaller than the measured ones.

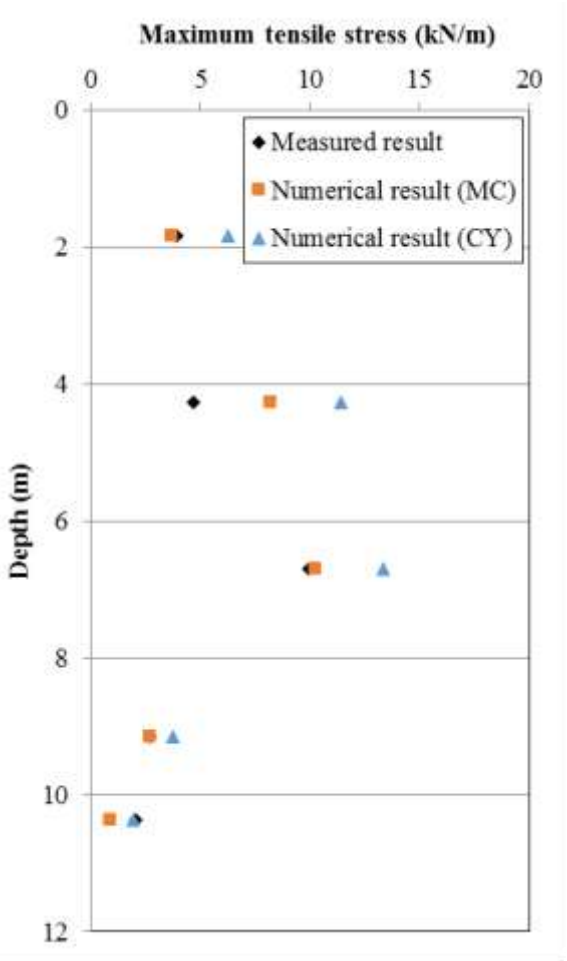

Figure 6.7 Distribution of the calculated maximum tensile stresses in the geogrids

6.5. Numerical results of hybrid GRR wall 1 (TS1)

6.5.1. Wall facing deflections

Wall facing deflections along the wall height before and after the construction of the backslope were calculated by the numerical simulation. Figure 6.8 shows the wall facing deflections calculated by the numerical simulation. For the comparison purpose, the wall facing deflections measured from the field tests are added in Figure 6.8 as well. Figure 6.8 (a) and (b) presents the wall facing deflections before and after the construction of the backslope, respectively. As shown in Figure 6.8, the wall facing deflections calculated by the numerical simulation increased to the maximum and then decreased along wall height. The wall facing deflections approached to the maximum value approximately in the middle of the wall height. The wall facing deflections calculated by the numerical simulation agreed well with those from the field test before the construction of the backslope while the wall facing deflections calculated by the numerical simulation were slightly larger than those from the field test after the construction of the backslope. After the construction of the backslope, the wall facing deflections increased both in the field tests and the numerical simulation. The maximum wall facing deflection calculated by the numerical simulation using the CY model increased from around 26 mm before the construction of the backslope to 40 mm after the construction of the backslope. The increase in the wall facing deflections resulted from the weight of the backslope and the lateral earth pressure induced by the backslope.

In addition, the wall facing deflection calculated by the numerical simulation using the MC model and the CY model are compared as shown in Figure 6.8. The wall facing deflections calculated by the numerical simulation using the CY model are slightly larger

than those using the MC model. This result is because the soil modulus in the CY model was lower than that in the MC model. The difference in the wall facing deflection became greater after the construction of the backslope because the soil modulus in the CY model decreased under shear loading while the soil modulus in the MC model was constant.

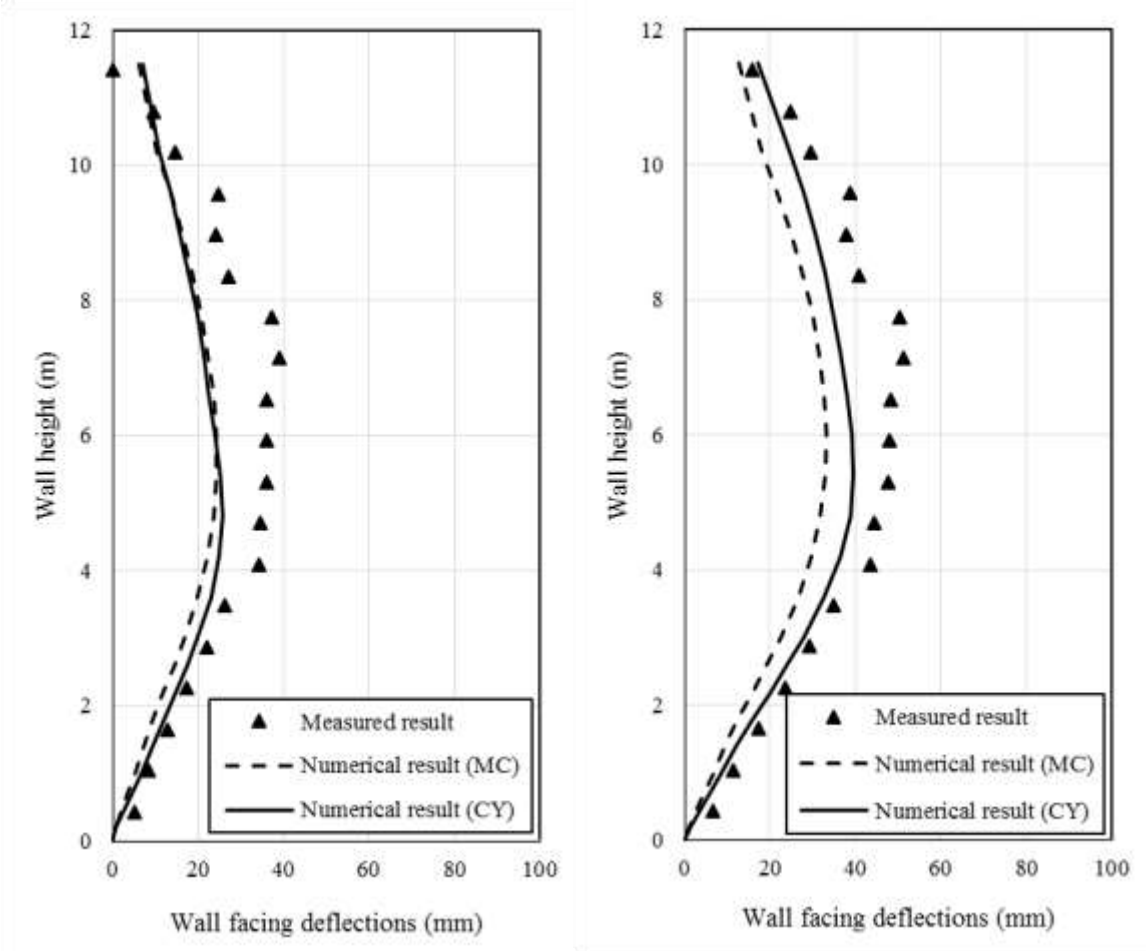

(a) Before the construction of the backslope (b) After the construction of the backslope

Figure 6.8 Wall facing deflections

6.5.2. Vertical earth pressures

The vertical earth pressures calculated by the numerical simulation are shown in Figure 6.9. Figure 6.9 (a) and (b) shows the distributions of vertical earth pressure

calculated by the numerical simulation before and after the construction of the backslope, respectively. For the comparison purpose, the vertical earth pressures measured from the field tests are presented in Figure 6.9 as well as the calculated vertical earth pressures using the simplified methods. As shown in Figure 6.9, the vertical pressures calculated by the numerical simulation quickly decreased within a distance around 1.5 m from the back of wall facing before and after the construction of the backslope. A similar decrease was also found in the results from the field tests. This phenomenon could be attributed to the effect of the interaction between the wall facing and the backfill soil. An upward friction due to the relative displacement between soil and wall facing was applied to the backfill soil behind the back of wall facing, which reduced the vertical earth pressure at the bottom of the wall. However, the effect of friction was not considered in the simplified methods to calculate the trapezoid stress and the overburden stress. After the rapid drop, the vertical earth pressure reached a constant value before the construction of the backslope and then gradually increased after the construction of the backslope. Although the vertical earth pressure calculated by the numerical simulation slightly underestimated the one measured in the field test, the calculated vertical pressures reasonably matched the measured ones as well as the calculated trapezoid stress.

The vertical earth pressures calculated by the numerical simulation using the MC model and the CY model are compared as well (see Figure 6.9). The numerical simulation using the CY model calculated slightly larger vertical earth pressures than those using the MC model. From practical viewpoint, there is not much difference between using the MC model and CY model in terms of the vertical earth pressures.

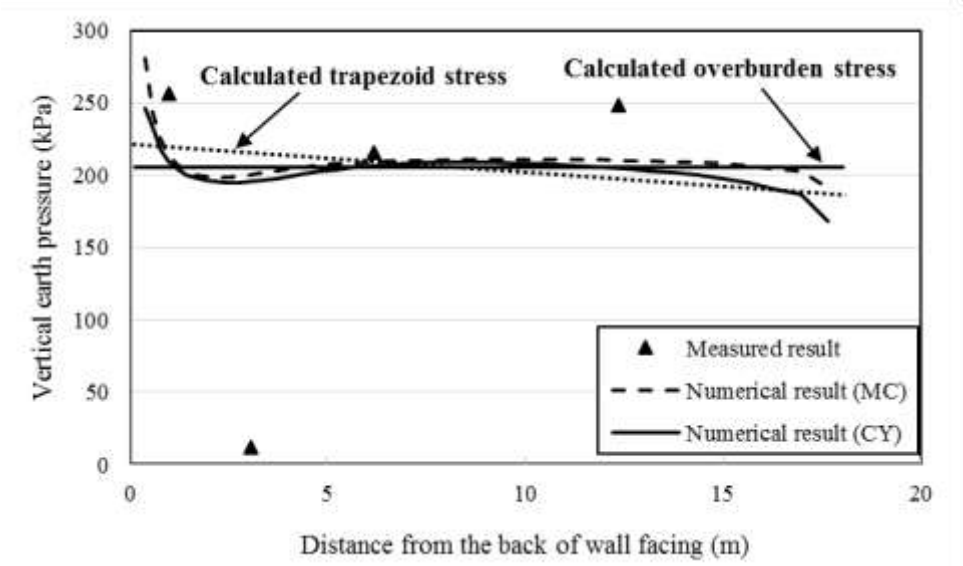

(a) Before the construction of the backslope

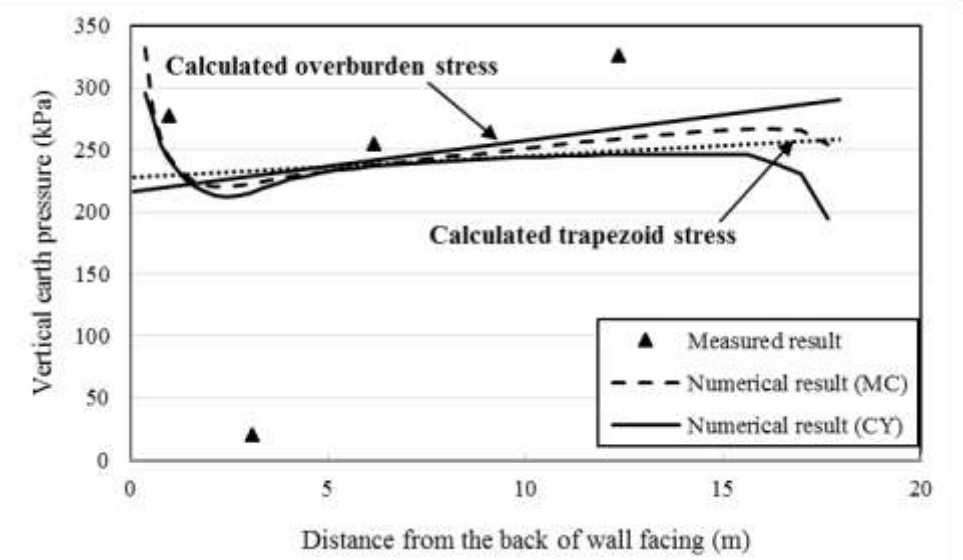

(b) After the construction of the backslope

Figure 6.9 Distribution of vertical earth pressures

6.5.3. Lateral earth pressures

Lateral earth pressures along depth before and after the construction of the backslope were calculated by the numerical simulation. Figure 6.10 shows the lateral earth pressures calculated by the numerical simulation. For the comparison purpose, the lateral

earth pressures measured in the field tests are shown in Figure 6.10 as well as the Rankine active earth pressure and the at-rest earth pressure. Figure 6.10 (a) and (b) presents the lateral earth pressure before and after the construction of the backslope, respectively. As shown in Figure 6.10, the lateral earth pressures calculated by the numerical simulation above the embedment zone approximately linearly increased with depth, which are close to the Rankine active earth pressures. The lateral earth pressure calculated by the numerical simulation below the top of the embedment zone rapidly increased till the bottom of the wall. The calculated lateral earth pressures were close to the at-rest earth pressure at the bottom of the wall. This result is because the lateral wall facing deflections below the top of the embedment zone were restricted so that the lateral earth pressure within the zone of embedment was close to the at-rest earth pressure. The lateral earth pressures calculated by the numerical simulation agreed well with those from the field tests. The lateral earth pressures from the field tests and the numerical simulation increased with the construction of the backslope. The increase in the lateral earth pressure resulted from the weight of the backslope.

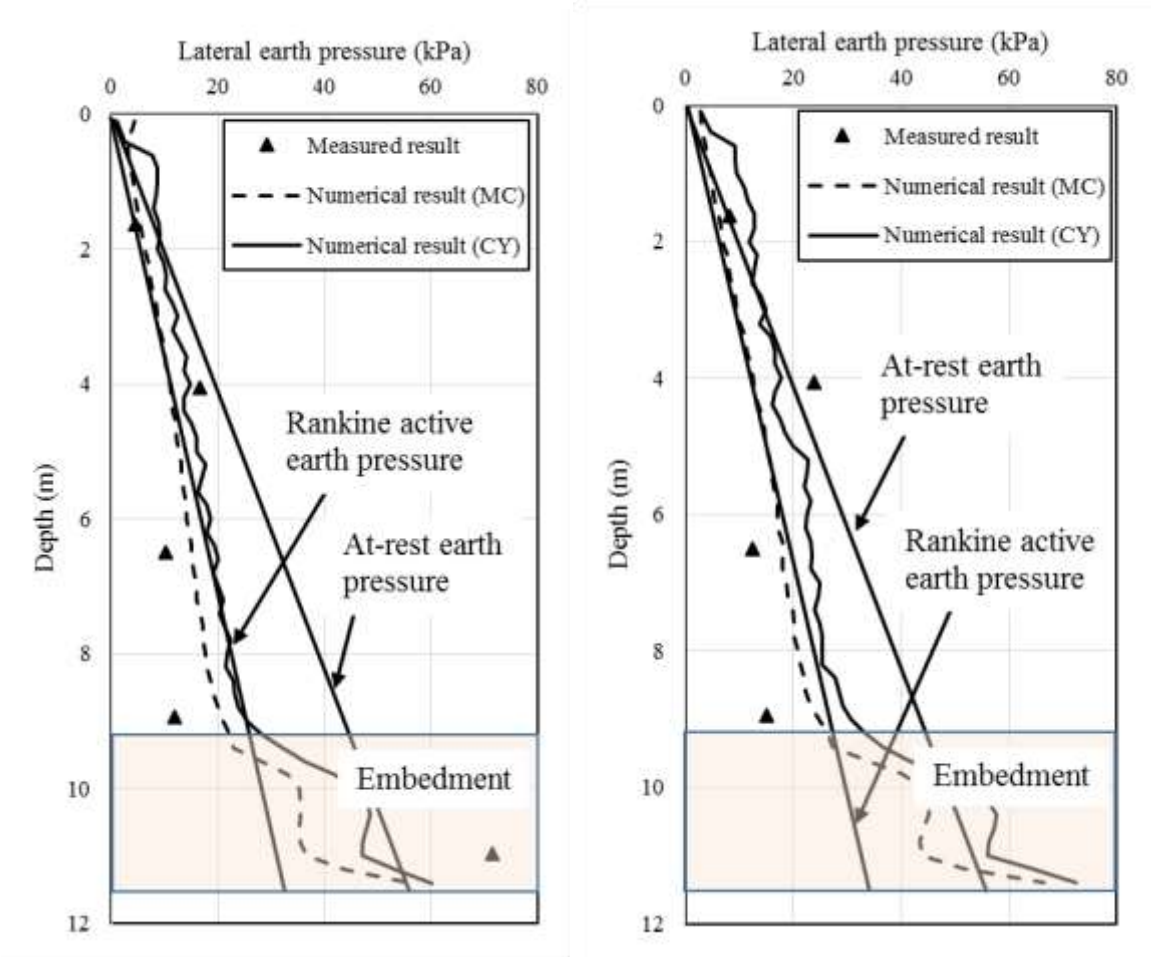

Figure 6.10 Distribution of lateral earth pressures

6.5.4. Strains in primary geogrid

Figure 6.11 presents the distribution of strains in the primary geogrids calculated by the numerical simulation at five instrumented layers after the construction of the backslope. For the comparison purpose, the measured strains in the primary geogrid at these instrumented layers are added in Figure 6.11 as well. The calculated strains at each instrumented layer decreased quickly behind the back of wall facing and gradually approached to zero. This rapid drcrease was found in the measured strains as well. The maximum strains in geogrid calculated by the numerical simulation did not always

happened at the connection. For example, the maximum tensile strains in Layer 3 occurred at the end of area reinforced with secondary reinforcement. For Layers 2, 4, and 5, the tensile strains within the area reinforced by the secondary reinforcement had approximately a uniform distribution. Overall, the strains calculated by the numerical simulation reasonably agreed with those measured in the field tests. The numerical simulation also had negative strains at the rear end of primary geogrids, which means that the primary geogrid was compressed at the rear end of the reinforced soil.

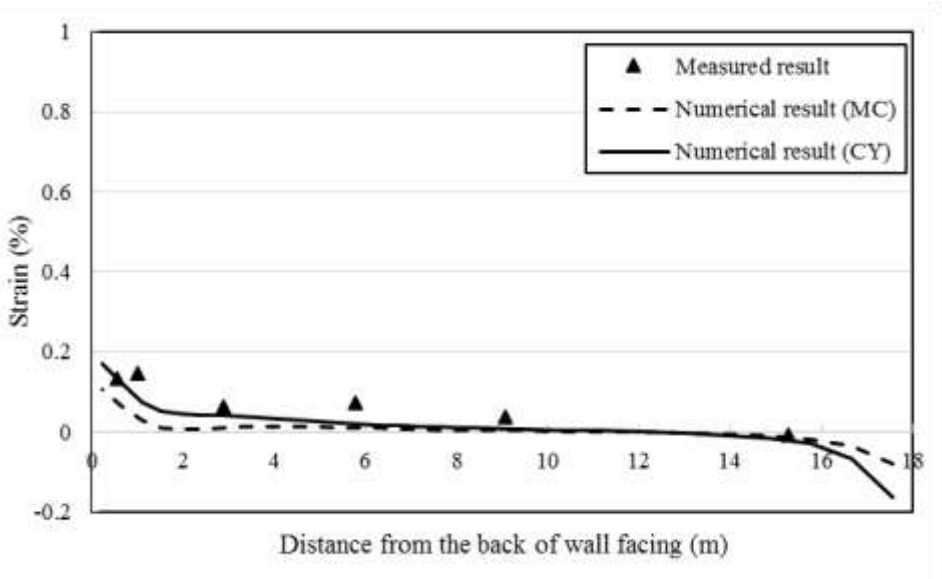

(a) Layer 1

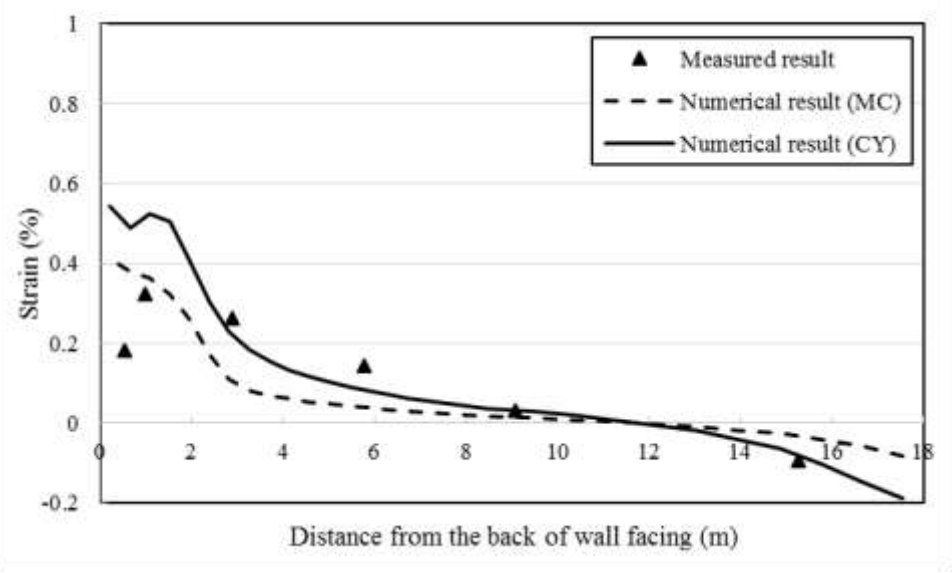

(b) Layer 2

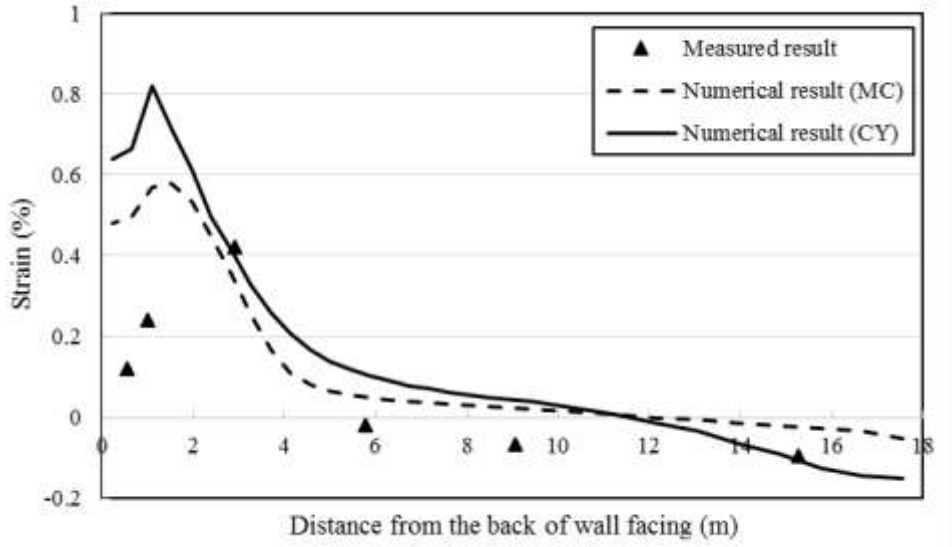

(c) Layer 3

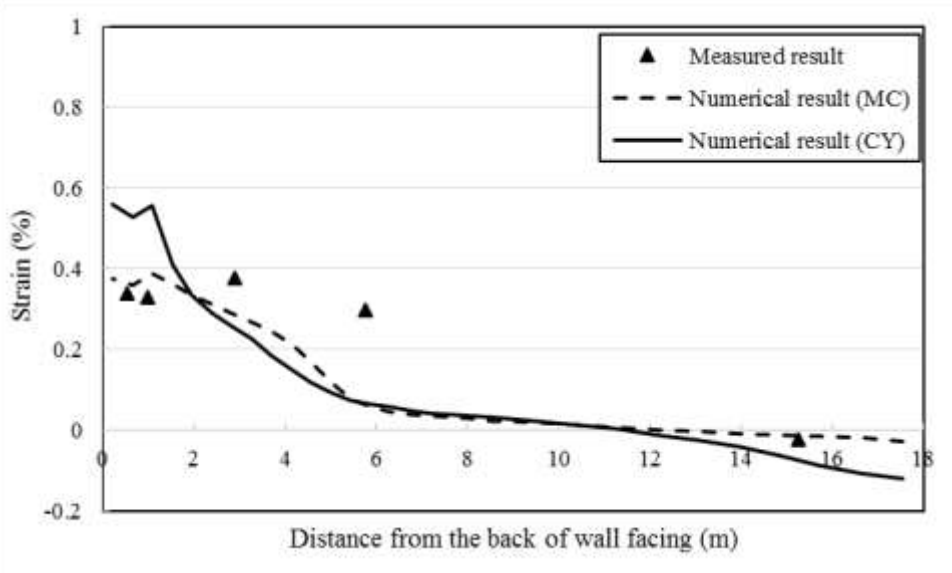

(d) Layer 4

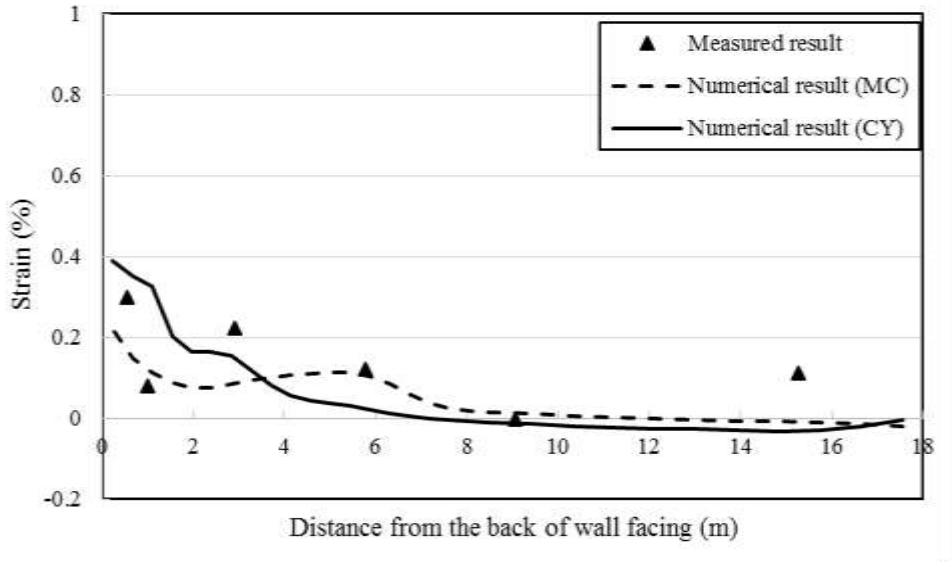

(e) Layer 5

Figure 6.11 Distribution of strains in geogrid

The strains in the primary geogrid calculated by the numerical simulation using the MC model and the CY model are compared and shown in Figure 6.11. Overall, the strains

calculated by the numerical simulation using the CY model were larger than those using the MC model.

The maximum tensile stresses in the primary geogrid calculated by the numerical simulation at five instrumented layers are also compared with the measured ones as shown in Figure 6.12. It can be seen that the calculated maximum tensile stresses were overall slightly smaller than the measured ones.

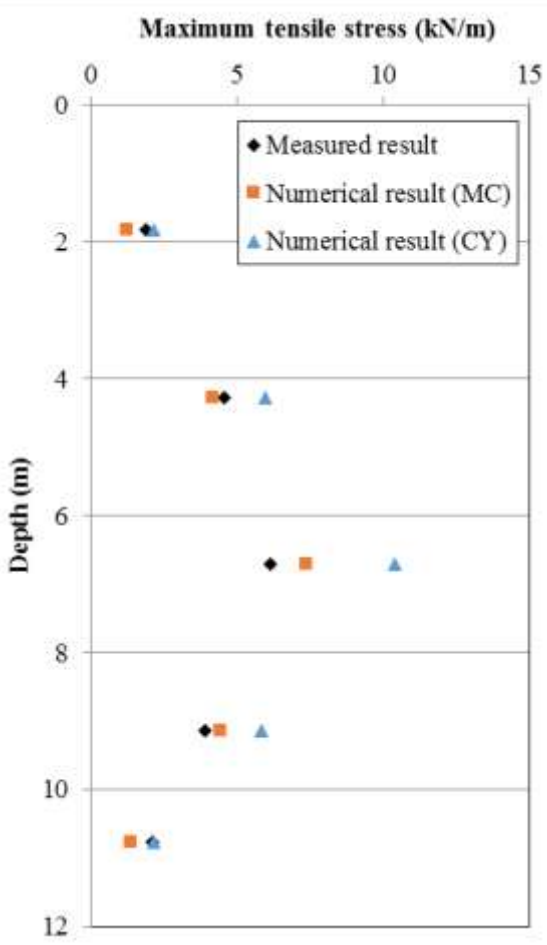

Figure 6.12 Maximum tensile stresses in primary geogrid

6.5.5. Strains in secondary geogrid

Figure 6.13 presents the distribution of strains in the secondary geogrid calculated by the numerical simulation at five instrumented layers after the construction of the backslope. For the comparison purpose, the measured strains in these secondary geogrid layers are added in Figure 6.13 as well. Overall, the calculated and measured strains at each instrumented layer decreased quickly behind the back of wall facing. The maximum strains in the secondary geogrid calculated by the numerical simulation happened at the connection. Overall, the strains calculated by the numerical simulation reasonably agreed with those measured in the field test.

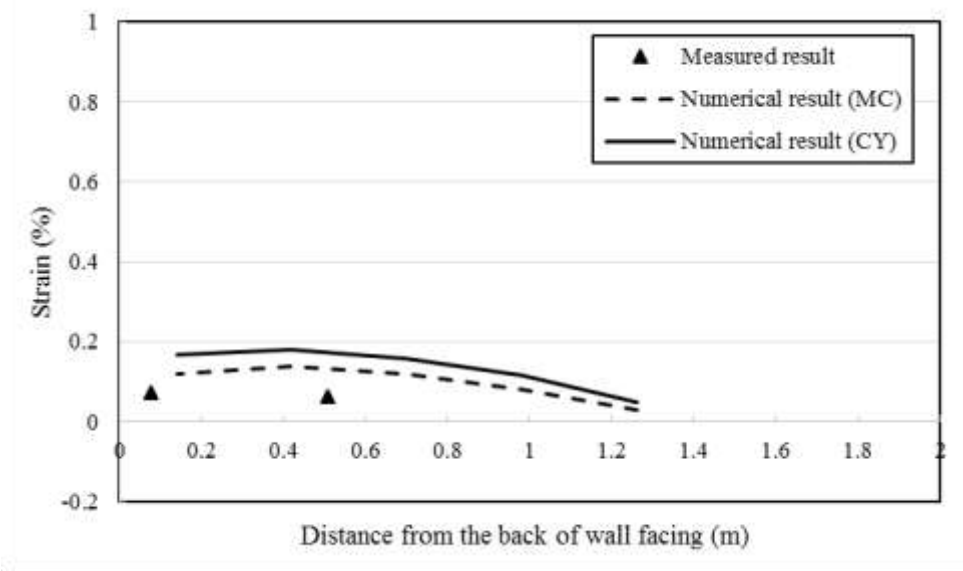

(a) Layer 1

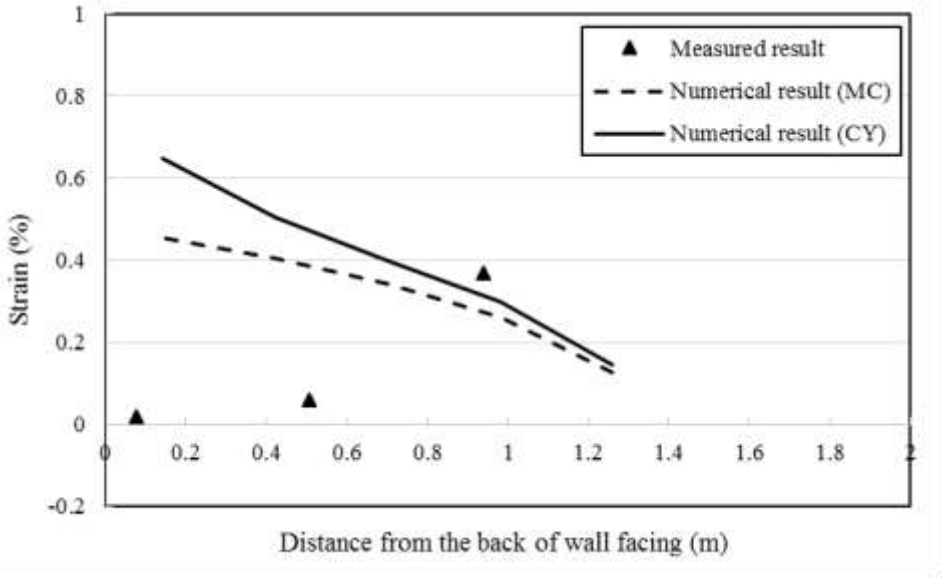

(b) Layer 2

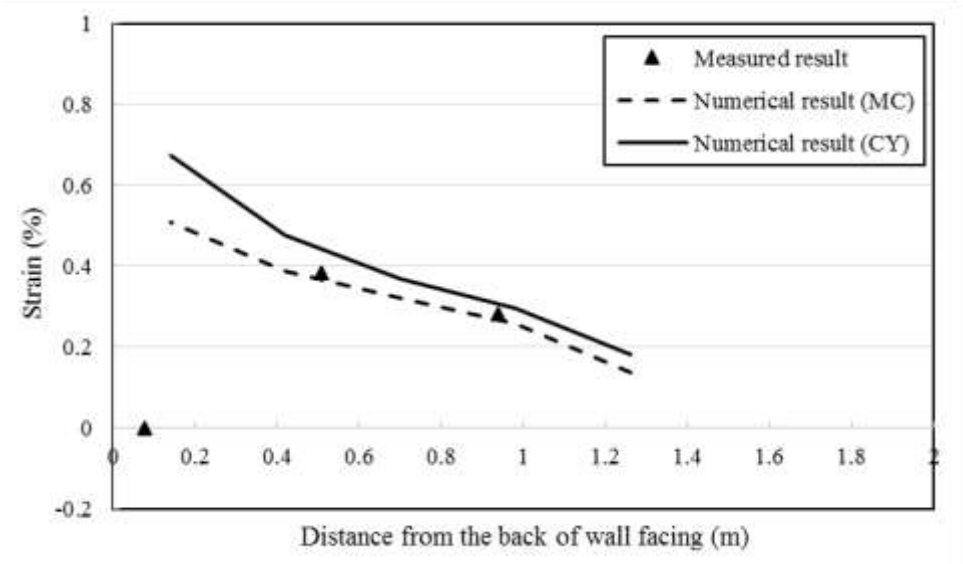

(c) Layer 3

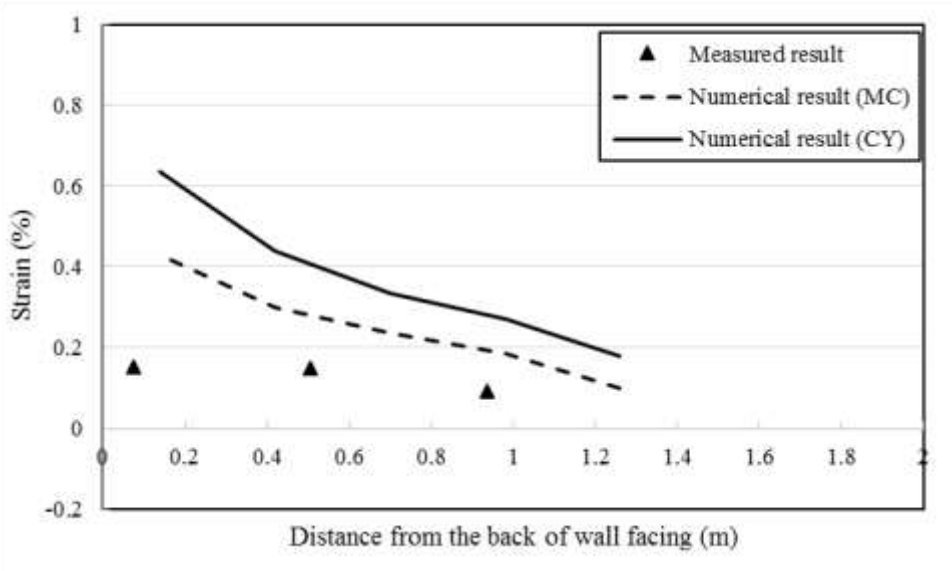

(d) Layer 4

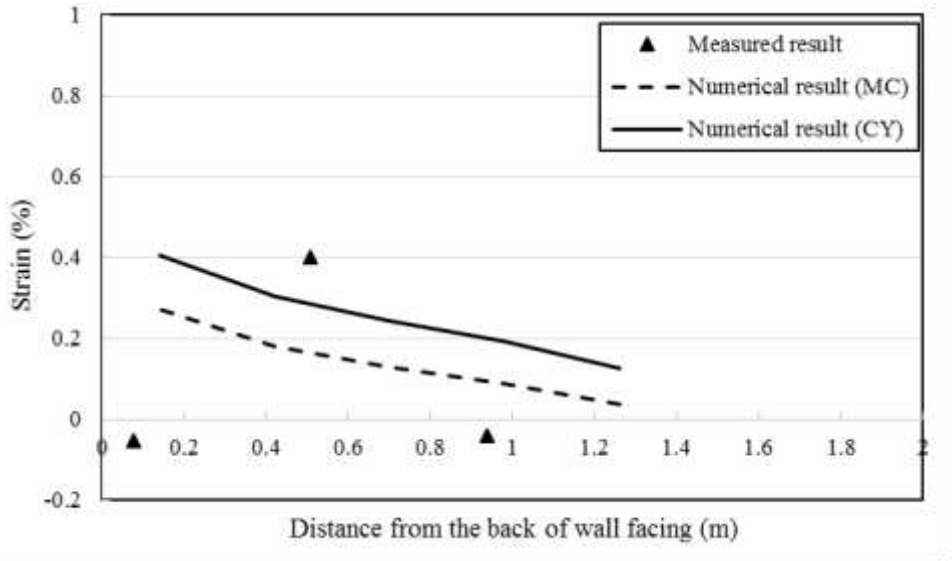

(e) Layer 5

Figure 6.13 Distribution of strains in secondary geogrid

6.6. Numerical results of hybrid GRR wall 2 (TS2)

6.6.1. Wall facing deflections

Wall facing deflections along the wall height before and after the construction of the backslope were calculated by the numerical simulation. Figure 6.14 shows the wall facing deflections calculated by the numerical simulation. For the comparison purpose, the wall facing deflections measured from the field tests are added in Figure 6.14 as well. Figure 6.14 (a) and (b) presents the wall facing deflections before and after the construction of the backslope, respectively. As shown in Figure 6.14, the wall facing deflections calculated by the numerical simulation increased to the maximum value and then decreased along the wall height. The wall facing deflections approached to the maximum value approximately in the middle of the wall height. The wall facing deflections calculated by the numerical simulation agreed well with those from the field test before the construction of the backslope while the wall facing deflections calculated by the numerical simulation were slightly larger than those from the field test after the construction of the backslope. After the construction of the backslope, the wall facing deflections increased both in the field tests and the numerical simulation. The maximum wall facing deflection calculated by the numerical simulation using the CY model increased from around 26 mm before the construction of the backslope to 40 mm after the construction of the backslope. The increase in the wall facing deflections resulted from the weight of the backslope and the lateral earth pressure induced by the backslope.

In addition, the wall facing deflection calculated by the numerical simulation using the MC model and the CY model are compared as shown in Figure 6.14. The wall facing deflections calculated by the numerical simulation using the CY model are slightly larger than those using the MC model. This result is because the soil modulus in the CY model

was lower than that in the MC model. The difference in the wall facing deflection became greater after the construction of the backslope because the soil modulus in the CY model decreased under shear loading while the soil modulus in the MC model was constant.

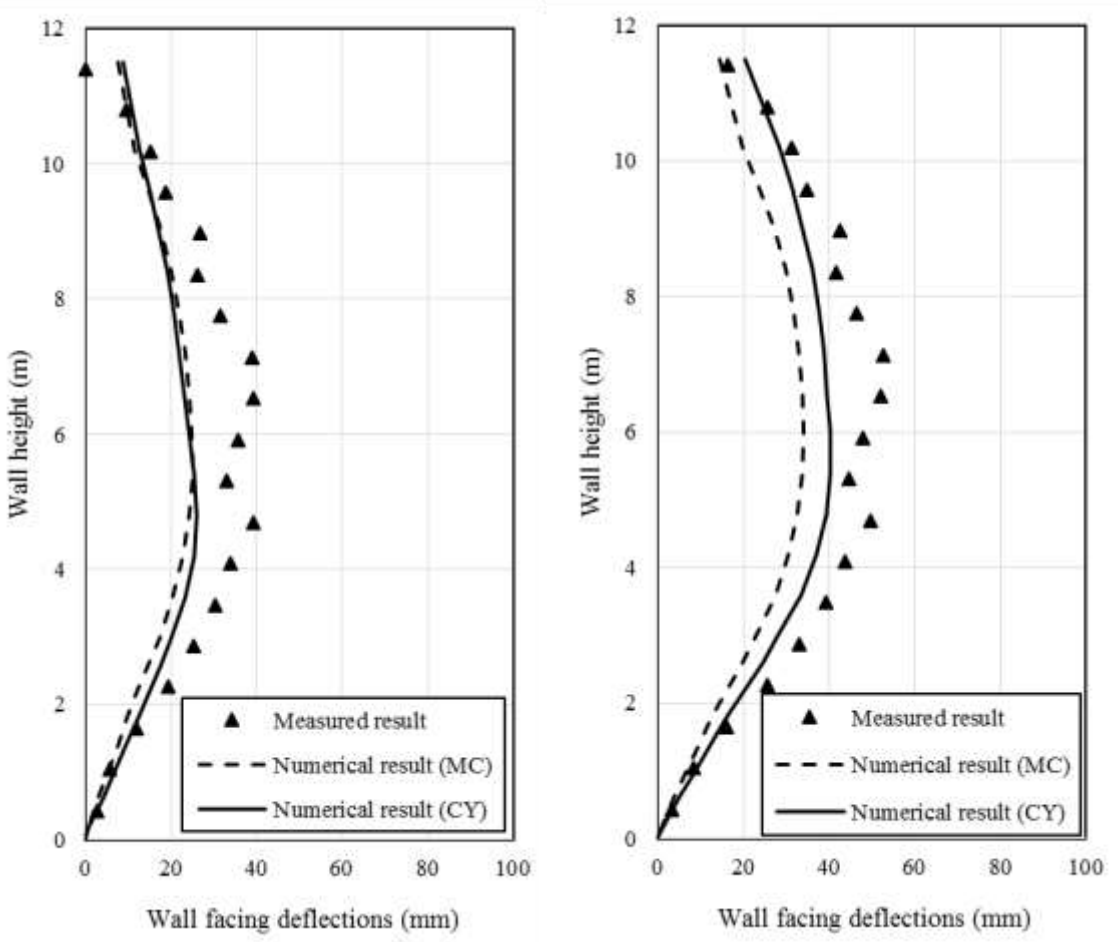

(a) Before the construction of the backslope (b) After the construction of the backslope

Figure 6.14 Wall facing deflections

6.6.2. Vertical earth pressures

The vertical earth pressures calculated by the numerical simulation are shown in Figure 6.15. Figure 6.15 (a) and (b) shows the distributions of vertical earth pressure calculated by the numerical simulation before and after the construction of the backslope,

respectively. For the comparison purpose, the vertical earth pressures measured from the field tests are presented in Figure 6.15 as well as the calculated vertical earth pressures using the simplified methods. As shown in Figure 6.15, the vertical pressures calculated by the numerical simulation quickly decreased within a distance around 1.5 m from the back of wall facing before and after the construction of the backslope. A similar decrease was also found in the results from the field tests. This phenomenon could be attributed to the effect of the interaction between the wall facing and the backfill soil. An upward friction due to the relative displacement between soil and wall facing was applied to the backfill soil behind the back of wall facing, which reduced the vertical earth pressure at the bottom of the wall. However, the effect of friction was not considered in the simplified methods to calculate the trapezoid stress and the overburden stress. After the rapid drop, the vertical earth pressure reached a constant value before the construction of the backslope and then gradually increased after the construction of the backslope. Although the vertical earth pressure calculated by the numerical simulation slightly underestimated the one measured in the field test, the calculated vertical pressures reasonably matched the measured ones as well as the calculated trapezoid stress.

The vertical earth pressures calculated by the numerical simulation using the MC model and the CY model are compared as well (see Figure 6.15). The numerical simulation using the CY model calculated the slightly larger vertical earth pressures than those using the MC model. From a practical viewpoint, there is not much difference between using the MC model and the CY model in terms of the vertical earth pressures.

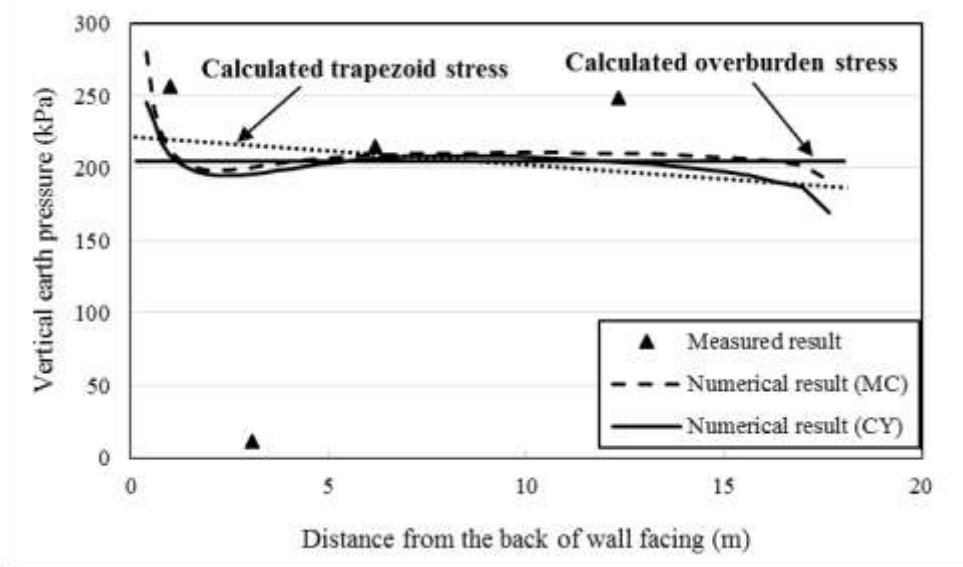

(a) Before the construction of the backslope

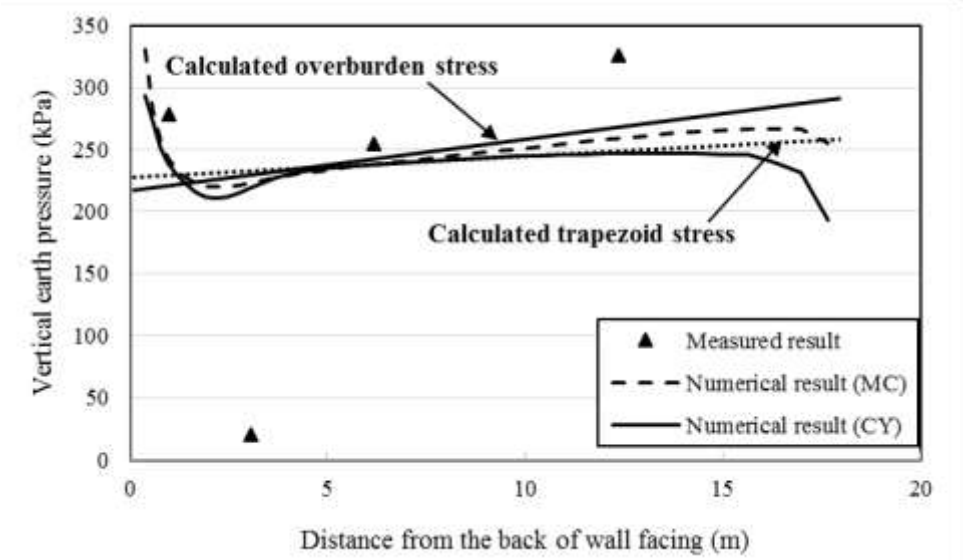

(b) After the construction of the backslope

Figure 6.15 Distribution of vertical earth pressures

6.6.3. Lateral earth pressures

Lateral earth pressures along depth before and after the construction of the backslope were calculated by the numerical simulation. Figure 6.16 shows the lateral earth pressures calculated by the numerical simulation. For the comparison purpose, the lateral

earth pressures measured in the field tests are shown in Figure 6.16 as well as the Rankine active earth pressure and the at-rest earth pressure. Figure 6.16 (a) and (b) presents the lateral earth pressure before and after the construction of the backslope, respectively. As shown in Figure 6.16, the lateral earth pressures calculated by the numerical simulation above the embedment zone approximately linearly increased with depth, which are close to the Rankine active earth pressures. The lateral earth pressure calculated by the numerical simulation below the top of the embedment zone rapidly increased till the bottom of the wall. The calculated lateral earth pressures were close to the at-rest earth pressure at the bottom of the wall. This result is because the lateral wall facing deflections below the top of the embedment zone were restricted so that the lateral earth pressure within the zone of embedment was close to the at-rest earth pressure. The lateral earth pressures calculated by the numerical simulation agreed well with those from the field tests. The lateral earth pressures from the field tests and the numerical simulation increased with the construction of the backslope. The increase in the lateral earth pressure resulted from the weight of the backslope.

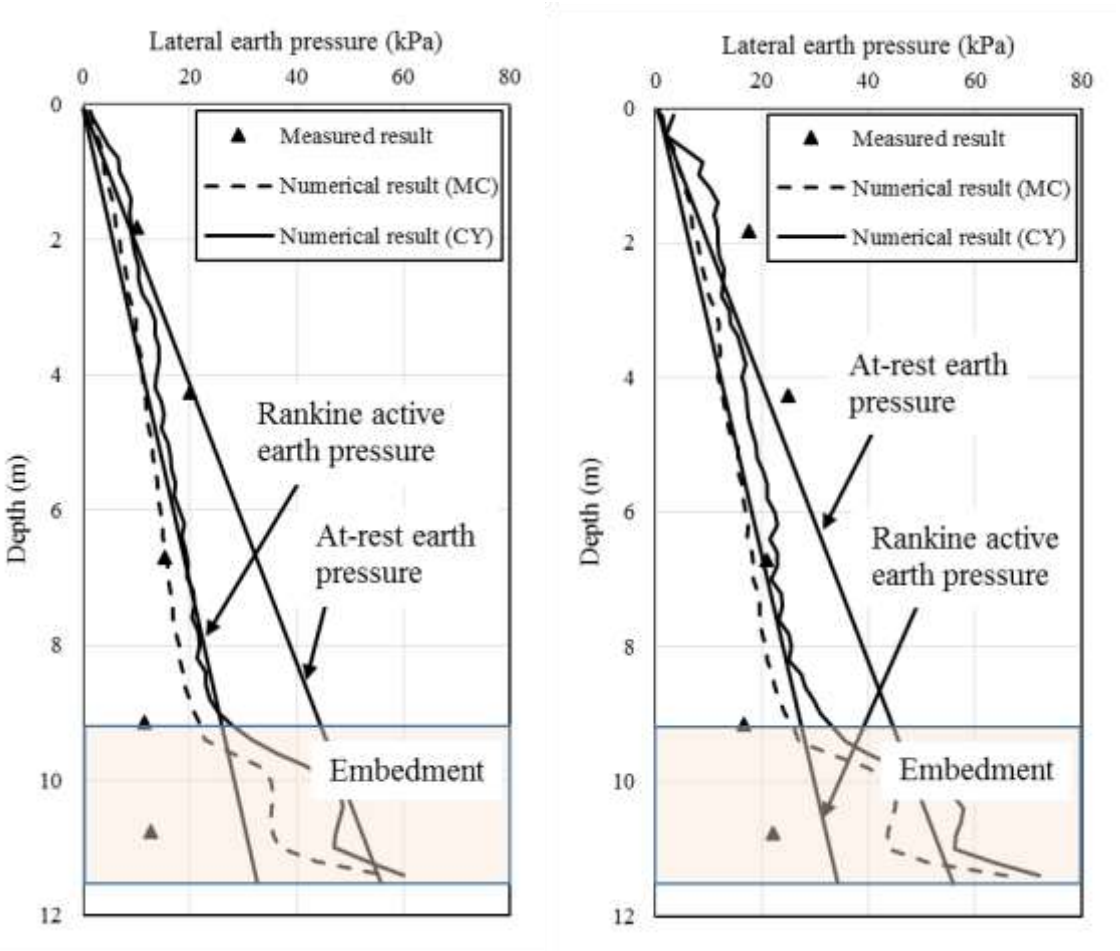

(a) Before the construction of the backslope (b) After the construction of the backslope

Figure 6.16 Distribution of lateral earth pressures

6.6.4. Strains in primary geogrid

Figure 6.17 presents the distribution of strains in the primary geogrids calculated by the numerical simulation at five instrumented layers after the construction of the backslope. For the comparison purpose, the measured strains in the primary geogrid at these instrumented layers are added in Figure 6.17 as well. The calculated strains at each instrumented layer decreased quickly behind the back of wall facing and gradually approached to zero. This rapid drcrease was found in the measured strains as well. The maximum strains in geogrid calculated by the numerical simulation did not always

happened at the connection. For example, the maximum tensile strains in Layer 3 occurred at the end of area reinforced with secondary reinforcement. Except for Layers 1, the tensile strains within the area reinforced by the secondary reinforcement had approximately a uniform distribution. Overall, the strains calculated by the numerical simulation reasonably agreed with those measured in the field tests. The numerical simulation also had negative strains at the rear end of primary geogrids, which means that the primary geogrid was compressed at the rear end of the reinforced soil.

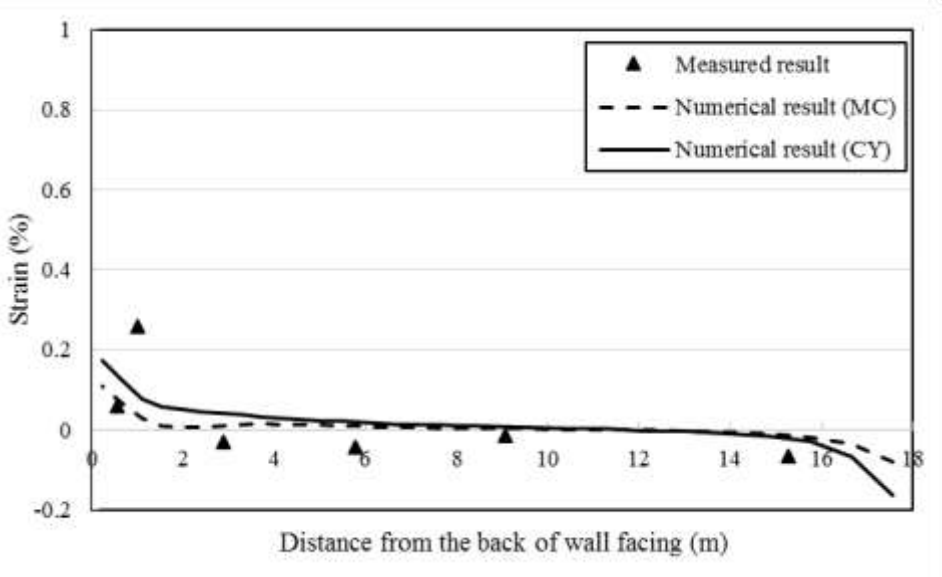

(a) Layer 1

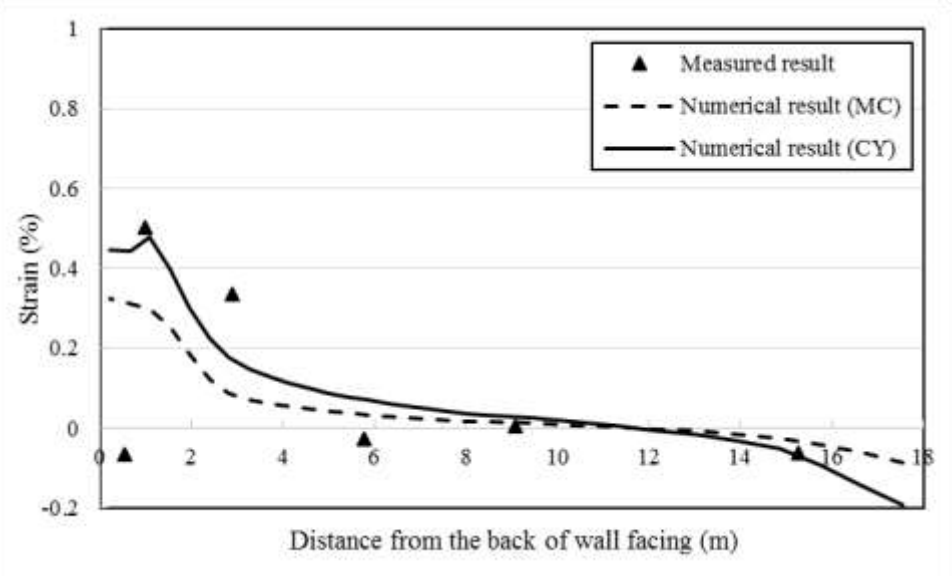

(b) Layer 2

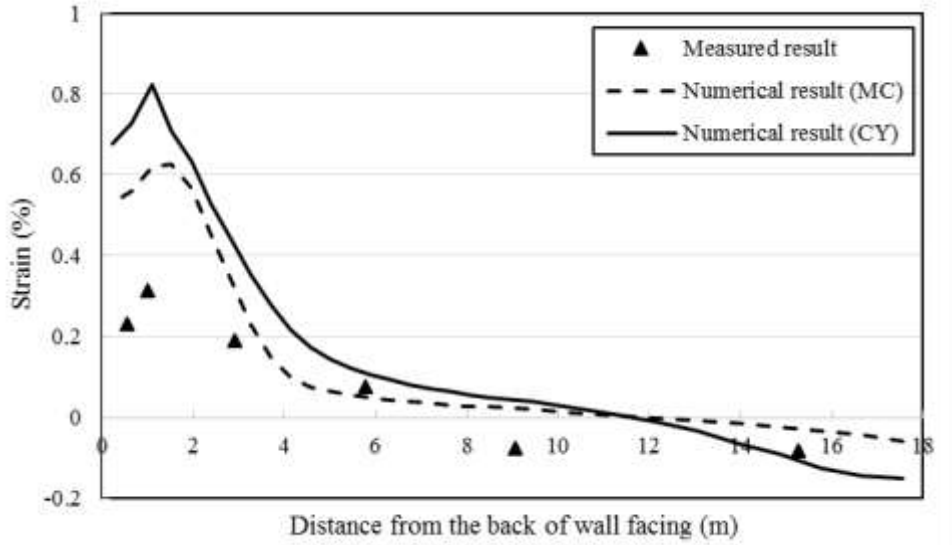

(c) Layer 3

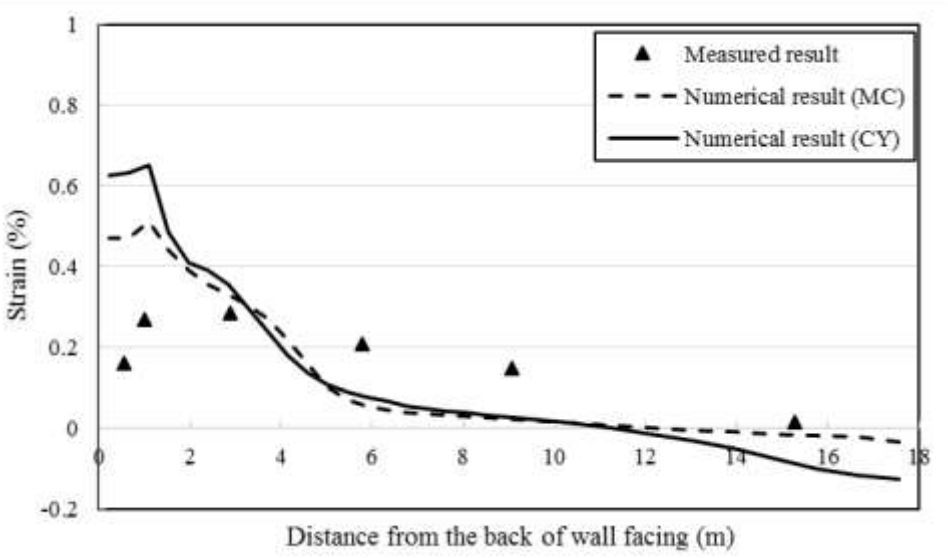

(d) Layer 4

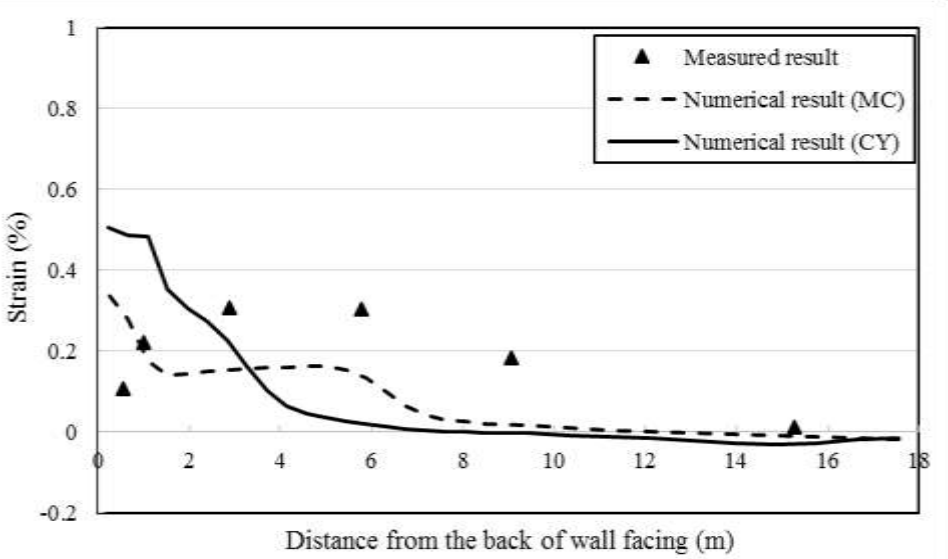

(e) Layer 5

Figure 6.17 Distribution of strains in primary geogrid

The strains in the primary geogrid calculated by the numerical simulation using the MC model and the CY model are compared and shown in Figure 6.17. Overall, the strains

calculated by the numerical simulation using the CY model were larger than those using the MC model.

The maximum tensile stresses in the primary geogrid calculated by the numerical simulation at five instrumented layers are also compared with the measured ones as shown in Figure 6.18. It can be seen that the calculated maximum tensile stresses were overall slightly smaller than the measured ones.

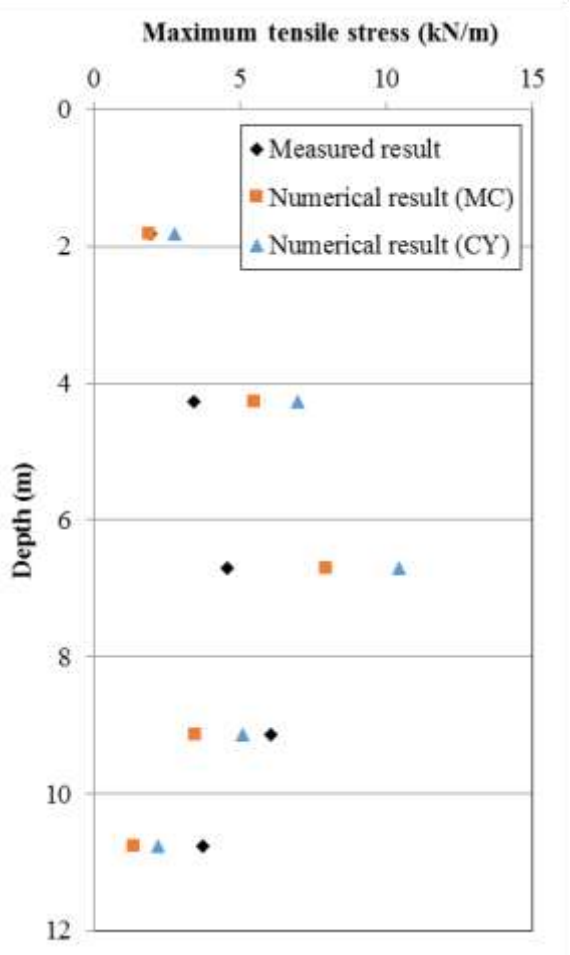

Figure 6.18 Maximum tensile stresses in primary geogrid

6.6.5. Strains in secondary geogrid

Figure 6.19 presents the distribution of strains in the secondary geogrid calculated by the numerical simulation at five instrumented layers after the construction of the backslope. For the comparison purpose, the measured strains in these secondary geogrid layers are added in Figure 6.19 as well. Overall, the calculated and measured strains at each instrumented layer decreased quickly behind the back of wall facing. The maximum strains in the secondary geogrid calculated by the numerical simulation happened at the connection. Overall, the strains calculated by the numerical simulation reasonably agreed with those measured in the field test.

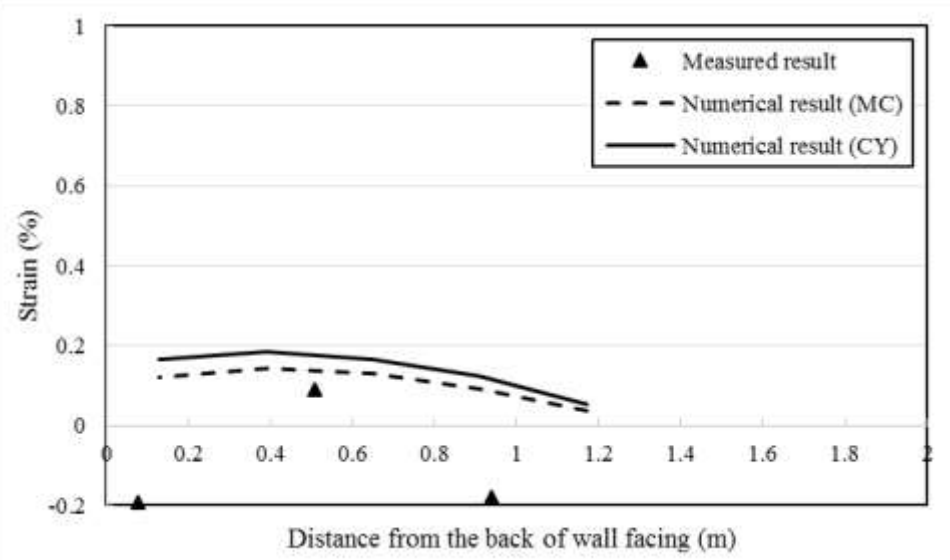

(a) Layer 1

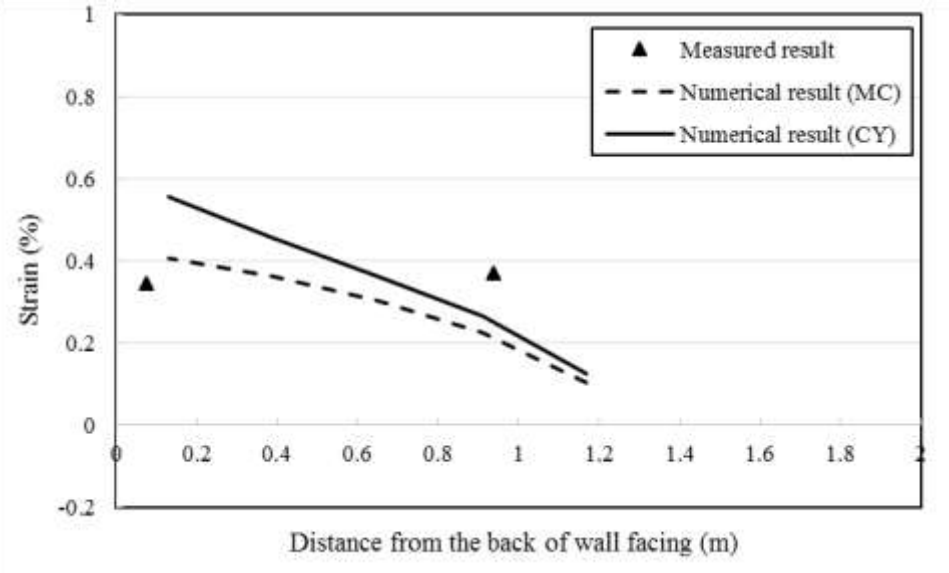

(b) Layer 2

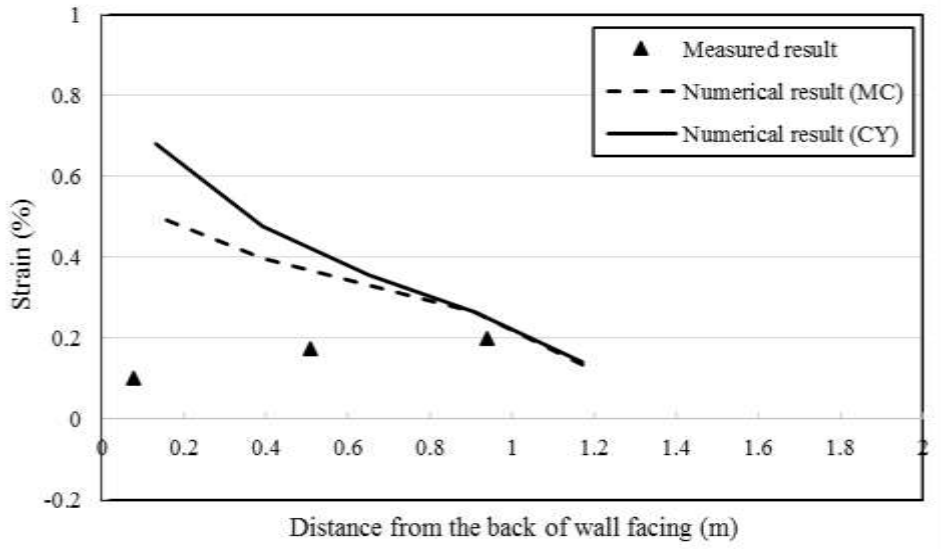

(c) Layer 3

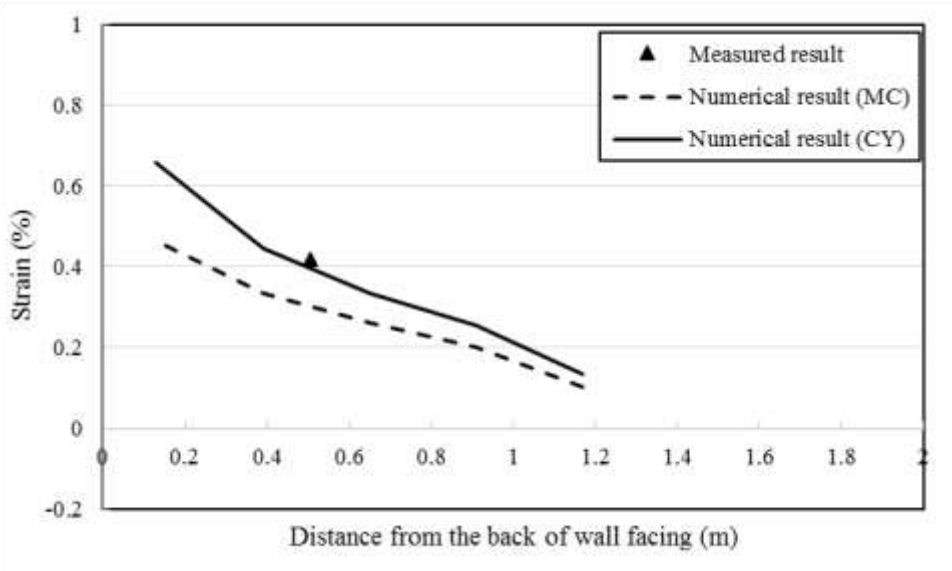

(d) Layer 4

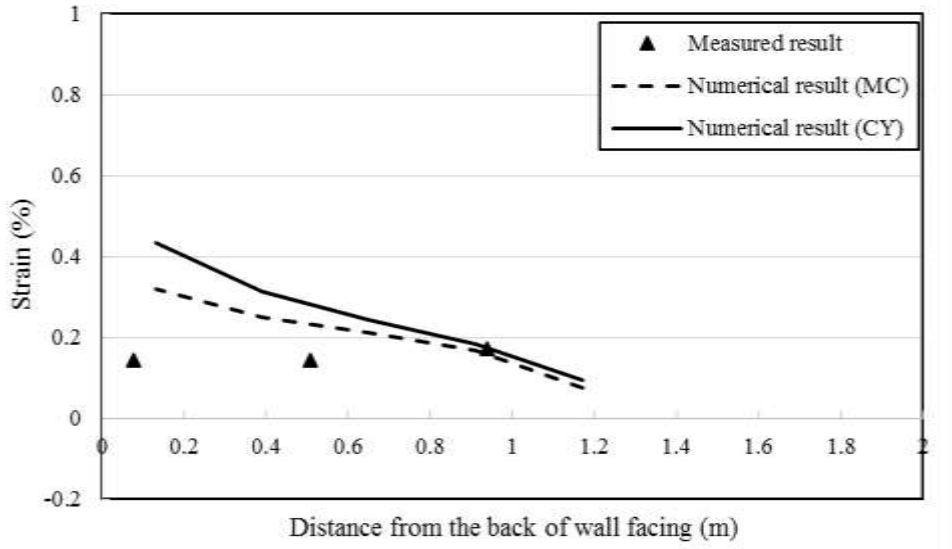

(e) Layer 5

Figure 6.19 Distribution of strains in secondary geogrid

Chapter 7 Parametric Study of Hybrid GRR Walls

7.1. Baseline model

A baseline model was developed based on the numerical models of the hybrid GRR walls in last chapter. Figure 7.1 shows the geometry and mesh of the baseline model. The baseline model contained a foundation soil zone, a wall facing zone, a reinforced soil zone, and a retained soil zone. A backslope soil zone and an embedment soil zone were not considered in the baseline model. The wall height of the baseline model was 11.6 m and the length of primary reinforcement was 0.7 times the wall height. In other words, the width of the reinforced soil zone was 8.1 m. The vertical spacing of primary reinforcement layers was 0.6 m, which is typical in design of MSE walls. The secondary reinforcement layers were installed between primary geogrid layers (i.e., connected on every block between the primary geogrids layers) with 0.2-m vertical spacing. The length of secondary geogrid was 1.8 m. Two types of reinforcement were used in the baseline case as the primary reinforcement and the secondary reinforcement. The behavior of the reinforcement was described by a strip element with a linearly elastic perfectly plastic behavior. The wall facing and the foundation soil were modelled as a linearly elastic material and the retained soil was modelled as a linearly elastic perfectly plastic material with the Mohr Coulomb (MC) failure criterion. The behavior of the backfill soil in the reinforced soil zone was modelled using the Cap Yield (CY) model. A compaction stress was not considered in the baseline model but its influence will be discussed in this chapter. The boundary conditions were the same as those used in numerical modeling of the hybrid GRR walls in the last chapter as well as the soil properties, the interface properties, and the construction stages.

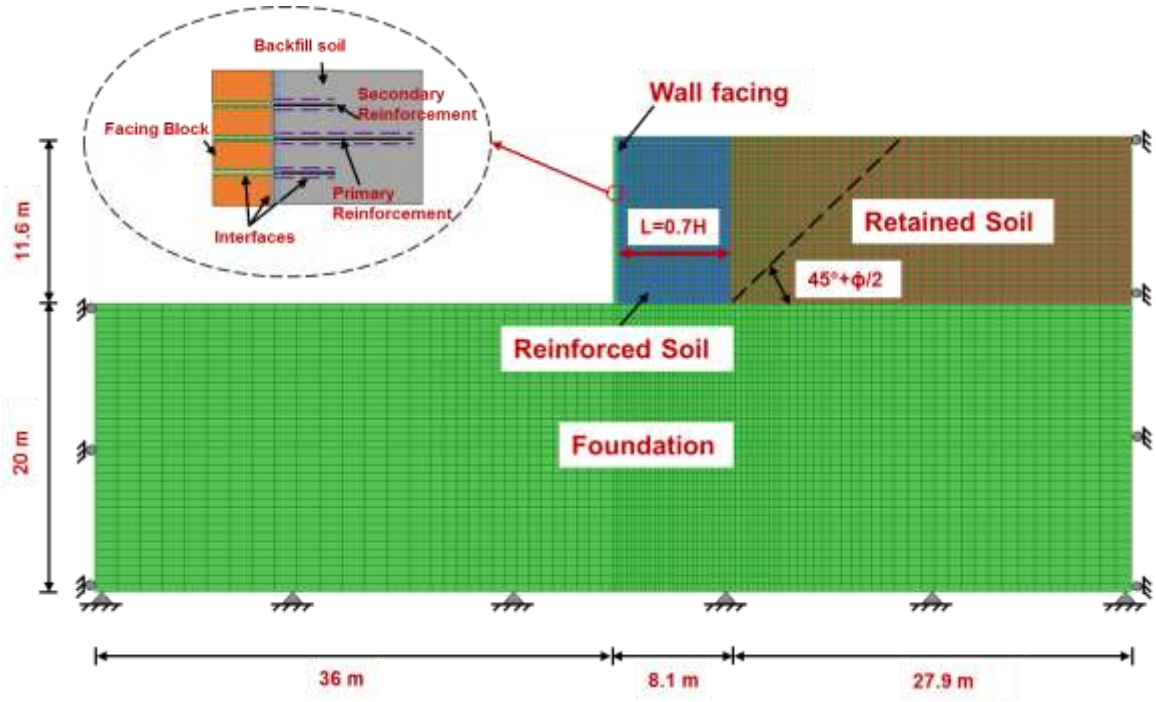

Figure 7.1 Geometry and mesh of baseline model

A parametric study was performed through varying one parameter in the baseline model to study its influence on the performance of the hybrid GRR wall, such as wall facing deflections, vertical earth pressures, lateral earth pressures, and stresses in reinforcement. The influence factors consisted of the length of primary reinforcement, the length of secondary reinforcement, the stiffness of primary reinforcement, the stiffness of secondary reinforcement, the soil friction, the soil dilation, the soil modulus, the compaction stress, and the foundation compressibility.

7.2. Effect of primary reinforcement length

The length of primary reinforcement was normalized by the wall height as the primary reinforcement length to wall height ratio, L/H. In the baseline model, L/H was 0.7,

which is commonly used in design of GRR walls. In this study, five cases including the baseline model were investigated. The primary reinforcement length to wall height ratio, L/H, ranged from 0.3 to 1.3.

7.2.1. Wall facing deflections

Figure 7.2 shows the profiles of wall facing deflections at different primary reinforcement length to wall height ratios. As shown in Figure 7.2, the wall facing deflections in all five cases were almost zero at the bottom of the wall. In the baseline model, the wall facing deflections increased with the wall height and reached the maximum value of 36 mm. The maximum wall facing deflections occurred approximately in the middle of the walls. Thereafter the wall facing deflection decreased with the height to 7 mm at the top of the wall. The profiles of the wall facing deflections in other four cases were similar to that in the baseline case.

In addition, the wall facing deflections decreased with an increase in the length of primary reinforcement. To clearly show the effect of the length of primary reinforcement on the maximum wall facing deflections, a relationship between the ratio of L/H and the maximum wall facing deflection is graphed in Figure 7.3. It can be seen that the maximum wall facing deflection increased with a decrease in the ratio of L/H. When the ratio of L/H was less than 0.5, the maximum wall facing deflection rapidly increased. This result indicated that the ratio of L/H had to be greater than 0.5 to prevent the excessive wall facing deflection in the hybrid GRR walls. On the other hand, when the ratio of L/H was greater than 1, the effect of an increase in the length of primary reinforcement to reduce the

maximum wall facing deflection was minimal. A similar finding was also reported by Rowe and Ho (1995).

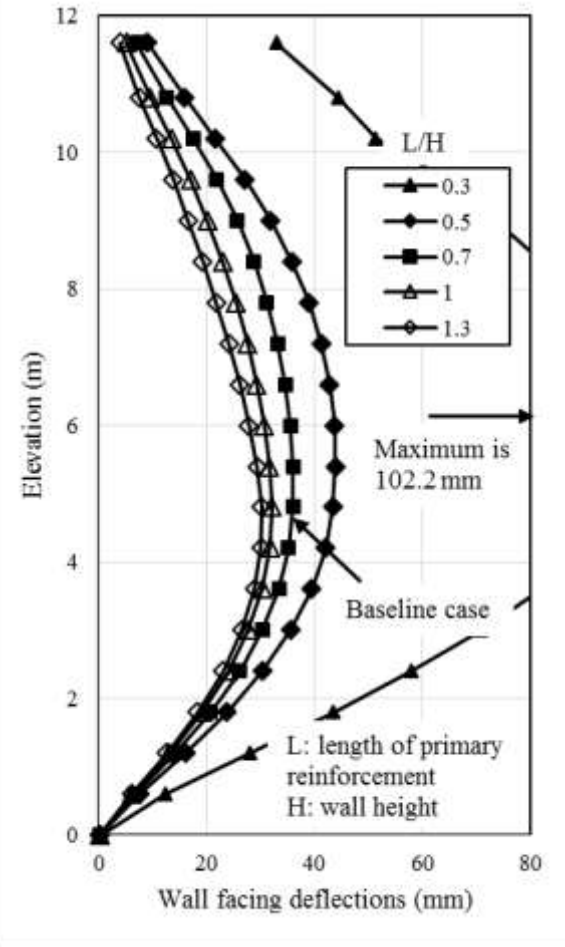

Figure 7.2 Effect of primary reinforcement length to wall height ratio (L/H) on wall facing deflections

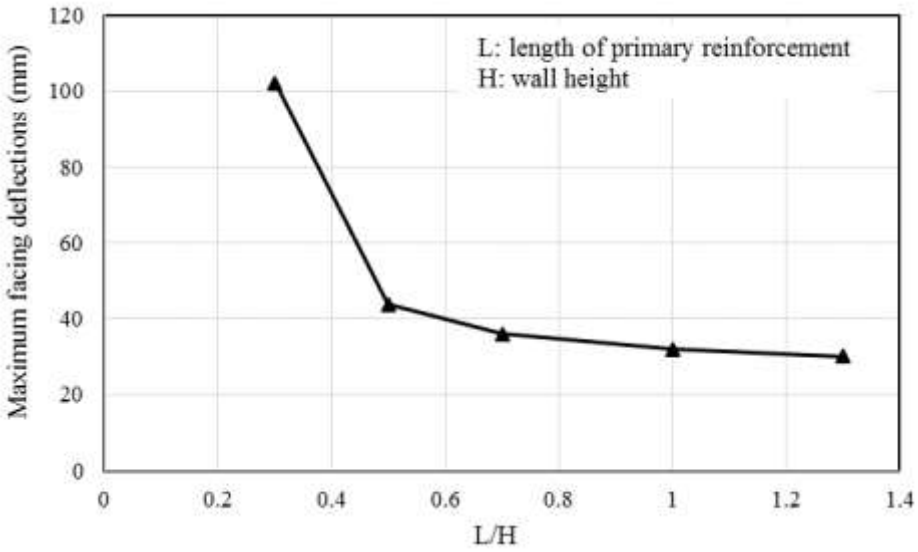

Figure 7.3 Relationship between primary reinforcement length to wall height ratio (L/H) and maximum wall facing deflections

7.2.2. Vertical earth pressures

Figure 7.4 shows the effect of the primary reinforcement length to wall height ratio (L/H) on the vertical earth pressure at the bottom of the reinforced soil zone. As shown in Figure 7.4, the vertical earth pressures quickly decreased within the area reinforced with the primary and secondary reinforcement and then gradually approached to the calculated overburden stress. The maximum vertical earth pressures occurred at the back of wall facing due to a potential overturning moment, which added an additional vertical earth pressure at the back of wall facing.

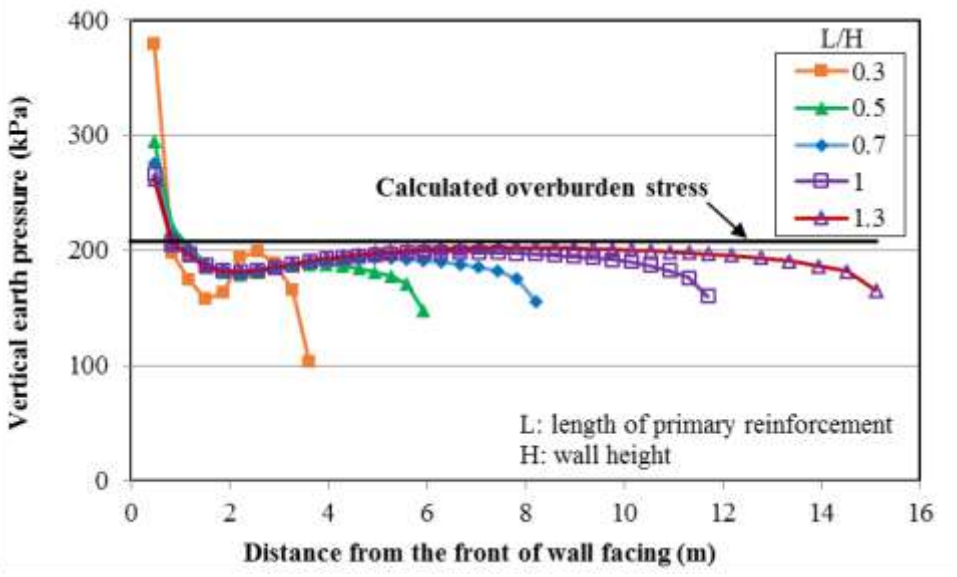

Figure 7.4 Effect of the primary reinforcement length to wall height ratio (L/H) on the vertical earth pressure at the bottom of reinforced soil

7.2.3. Lateral earth pressures

Figure 7.5 shows the effect of the primary reinforcement length to wall height ratio (L/H) on the lateral earth pressure at the back of wall facing. Two solid lines in Figure 7.5 represent the Rankine active earth pressure and the at-rest earth pressure using the friction angle of 52°. As shown in Figure 7.5, the lateral earth pressure increased with depth (a reduction of elevation). Near the top and bottom of the hybrid GRR walls, the lateral earth pressures were close to the at-rest earth pressures because the soil near the top and bottom of walls was not mobilized and had small horizontal deformations (shown in Figure 7.2) while the lateral earth pressures in the middle area of walls were close to the Rankine active earth pressures because the soil in this area was mobilized and had large deformations (shown in Figure 7.2). The effect of the primary reinforcement length to wall height ratio (L/H) was minimal when L/H was greater than 0.5.

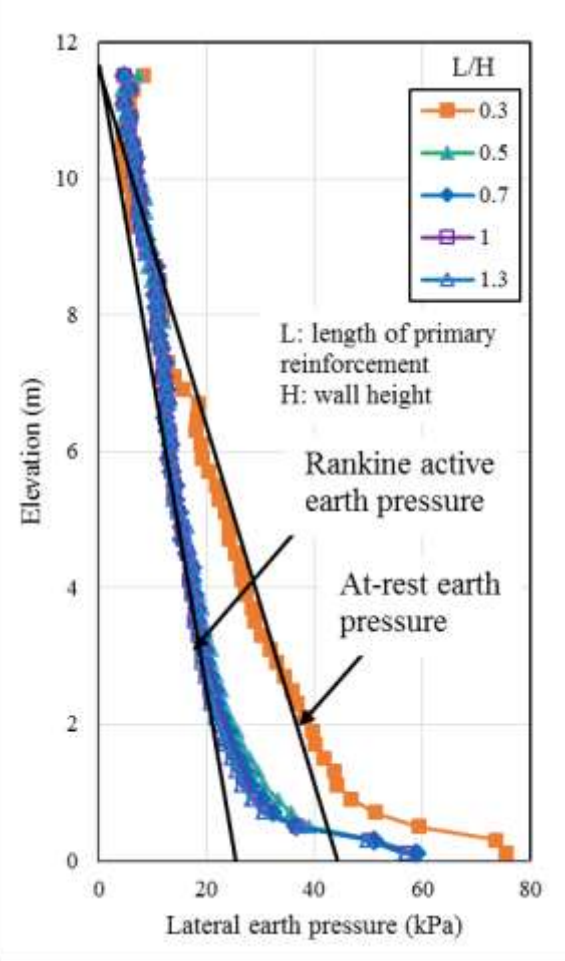

Figure 7.5 Effect of the primary reinforcement length to wall height ratio (L/H) on the lateral earth pressure at the back of wall facing

7.2.4. Tensile stress in reinforcement

Figure 7.6 shows the effect of the primary reinforcement length to wall height ratio (L/H) on the maximum tensile stresses in the primary reinforcement. For the comparison purpose, the AASHTO (2014) simplified method was used to calculate the maximum tensile stress with the friction angle of 52°. The calculated maximum tensile stress using the AASHTO simplified method was larger than those from the numerical simulation. The maximum tensile stress from the numerical simulation increased from the top of the walls to the elevation of 2.5 m and then slightly decreased toward the bottom of the walls; while

the maximum tensile stress calculated by the AASHTO simplified method increased linearly from the top of the wall to the bottom. The ratio of L/H also had an influence on the maximum tensile stresses. The maximum tensile stress increased with a decrease in the ratio of L/H. The influence on the maximum stress became less with an increase in the ratio of L/H.

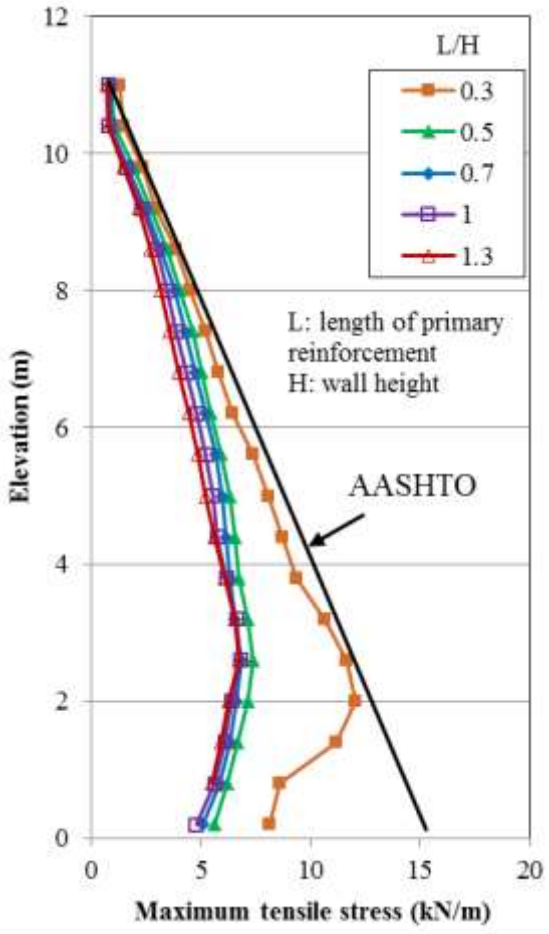

Figure 7.6 Effect of the primary reinforcement length to wall height ratio (L/H) on the maximum tensile stress in the primary reinforcement

Figure 7.7 shows the effect of the primary reinforcement length to wall height ratio (L/H) on the ratio of connection stress and the maximum tensile stress in the primary

reinforcement. When the maximum tensile stress occurred at the location of the connection between the reinforcement and the wall facing, the ratio of the connection stress and the maximum tensile stress in the primary reinforcement became 1.0. As shown in Figure 7.7, the ratio of the connection stress and the maximum tensile stress was equal to 1.0 when the elevation was greater than 5 m, which indicated that the ratio of L/H had no influence on the location of the maximum tensile stress in the primary reinforcement. When the elevation was lower than 5 m, the ratio of the connection stress to the maximum tensile stress became less than 1.0 and decreased with a decrease in the ratio of L/H. The smallest ratio of the connection stress and the maximum tensile stress was 0.8 when the ratio of L/H was 0.3.

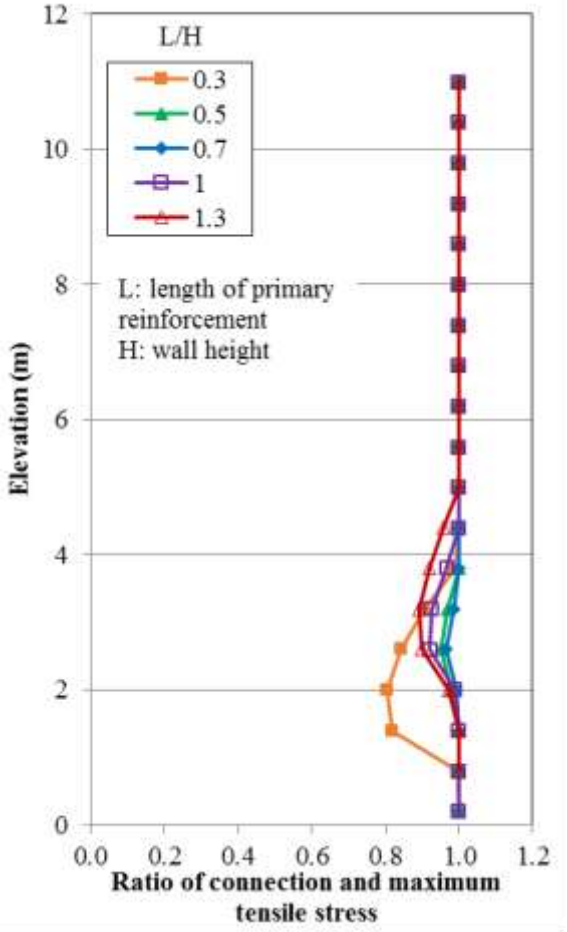

Figure 7.7 Effect of the primary reinforcement length to wall height ratio (L/H) on the ratio of connection stress and the maximum tensile stress in the primary reinforcement

Coefficient of lateral earth pressure behind the wall was estimated using the maximum tensile stress from the numerical simulation. The calculation of the coefficient can be seen in Eq. (7.1).

$$K_r = \frac{T_{max}}{S_v \cdot R_c \cdot \sigma_v} \tag{7.1}$$

where T_{max} = the maximum tensile stress in the reinforcement, S_v = the vertical spacing of the primary reinforcement, and R_c = the coverage ratio of geogrid. A normalized coefficient of lateral earth pressure is defined as K_r / K_a, where $K_a = tan^2\left(45^o - \phi/2\right)$. The method for calculating the coefficient of lateral earth pressure based on the maximum tensile stress in the primary reinforcement was adopted by AASHTO to develop the profile of K_r / K_a with depth included in AASHTO (2014).

Figure 7.8 presents the effect of the primary reinforcement length to wall height ratio (L/H) on the normalized coefficient of lateral earth pressure K_r/K_a. A constant normalized coefficient of lateral earth pressure suggested by AASHTO (2014) for geosynthetic reinforcement is also shown in Figure 7.8. It can be seen that the normalized coefficients of lateral earth pressure from the numerical simulation were approximately uniform along the elevation and the normalized coefficients were less than 1.0. With an increase of the ratio of L/H, the normalized coefficient decreased. The effect of the ratio of L/H on the normalized coefficient became less when the ratio of L/H was greater than 0.3.

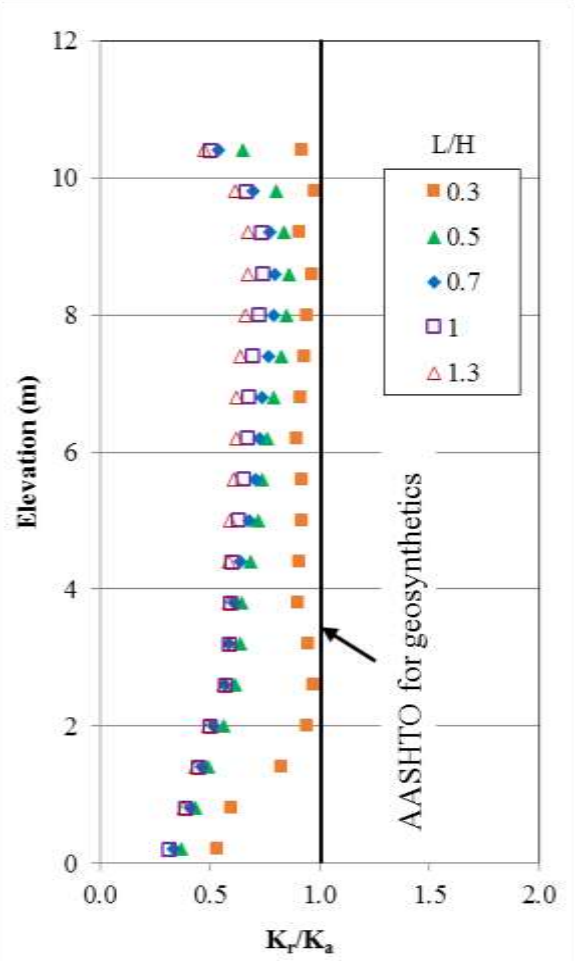

Figure 7.8 Effect of the primary reinforcement length to wall height ratio (L/H) on the ratio of K_r/K_a

Figure 7.9 shows the effect of the primary reinforcement length to wall height ratio (L/H) on the maximum tensile stresses in the secondary reinforcement. For the comparison purpose, the maximum tensile stresses were also calculated according to the Rankine active earth pressure and the at-rest earth pressure at the friction angle of 52°. The calculated maximum tensile stress using the Rankine active earth pressure was smaller than that from the numerical simulation when the elevation was greater than 3 m. On the other hand, the calculated maximum tensile stress using the at-rest earth pressure was almost same as that

from the numerical simulation when the elevation was greater than 7 m and then was greater than that from the numerical simulation when the elevation was lower than 7 m. The ratio of L/H also had an influence on the maximum tensile stresses in the secondary reinforcement. The maximum tensile stress in the secondary reinforcement increased with a decrease in the ratio of L/H. The influence of the ratio of L/H on the maximum stress in the secondary reinforcement became minimal when the ratio of L/H was greater than 0.5.

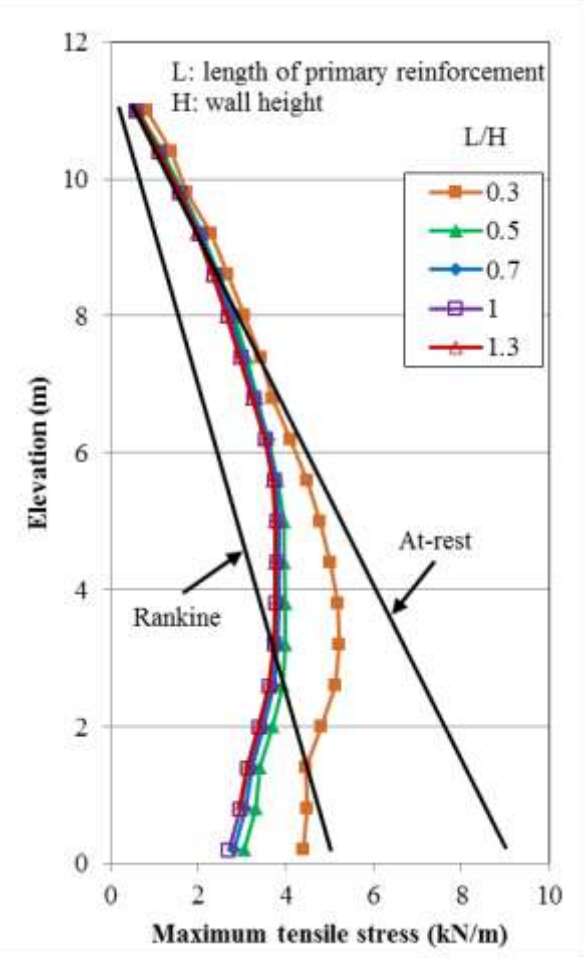

Figure 7.9 Effect of the primary reinforcement length to wall height ratio (L/H) on the maximum tensile stresses in the secondary reinforcement

7.3. Effect of secondary reinforcement length

The length of secondary reinforcement was also normalized by the wall height. A secondary reinforcement length to wall height ratio, l/H, was defined. In the baseline model, l/H was 0.13. In this section, five cases including the baseline model with different l/H ranging from 0.09 to 0.34 were investigated on the performance of the hybrid GRR walls.

7.3.1. Wall facing deflections

Figure 7.10 shows the profiles of wall facing deflections at different secondary reinforcement length to wall height ratios (l/H). As shown in Figure 7.10, the wall facing deflections in all the five cases were almost the same at the bottom and the top of walls. The wall facing deflection increased with the wall elevation to reach the maximum value approximately in the middle of the walls and then decreased with elevation toward the top of the wall. In addition, the wall facing deflections decreased with an increase in the length of the secondary reinforcement. To clearly show the effect of the length of the secondary reinforcement on the maximum wall facing deflections, a relationship between the ratio of l/H and the maximum wall facing deflections is graphed in Figure 7.11. It can be seen that the maximum wall facing deflection decreased linearly with a decrease in the ratio of l/H when the ratio of l/H was smaller than 0.26. When the ratio of l/H was greater than 0.26, the maximum wall facing deflections were almost constant, indicating that the ratio of l/H had an ignorable effect on the maximum wall facing deflections.

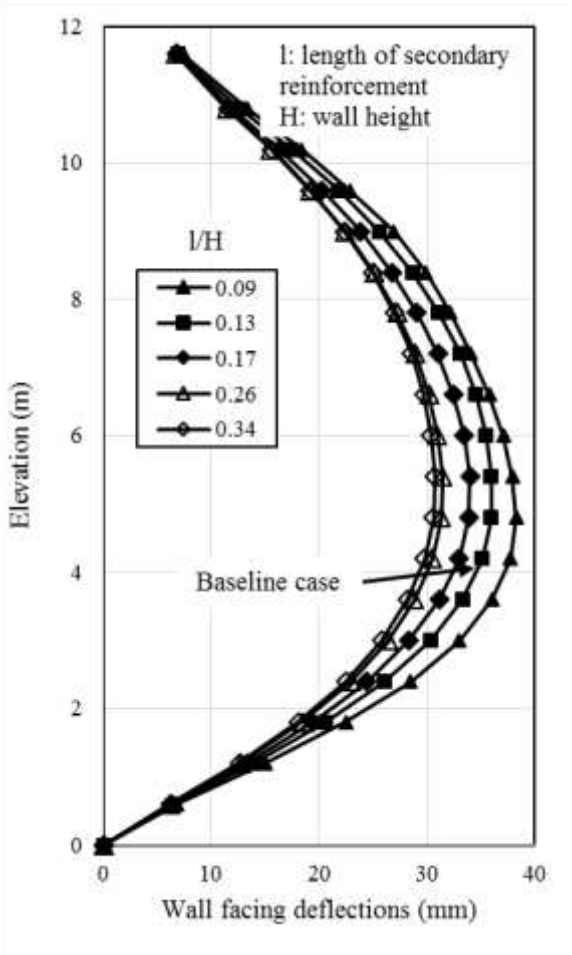

Figure 7.10 Effect of the secondary reinforcement length to wall height ratio (l/H) on the wall facing deflections

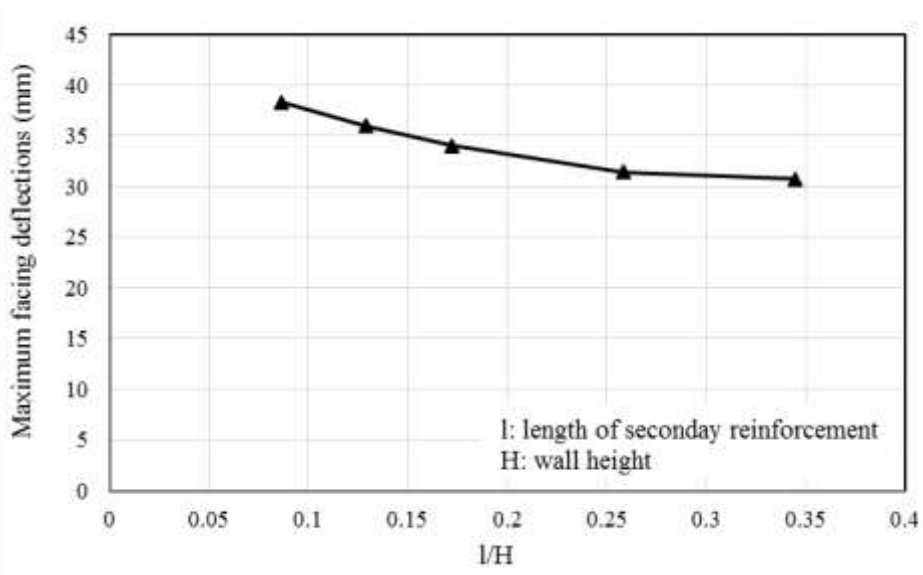

Figure 7.11 Effect of the secondary reinforcement length to wall height ratio (l/H) on the wall facing deflections

7.3.2. Vertical earth pressures

Figure 7.12 shows the effect of the secondary reinforcement length to wall height ratio (l/H) on the vertical earth pressure at the bottom of the reinforced soil. As shown in Figure 7.12, the vertical earth pressures quickly dropped within the area reinforced with the primary reinforcement and the secondary reinforcement and then gradually approached to the calculated overburden stress. The maximum vertical earth pressures occurred at the back of wall facing due to a potential overturning moment, which added an additional vertical earth pressure at the back of wall facing. The quick drop in the vertical earth pressure stopped at the end of the secondary reinforcement. Figure 7.13 shows the linear relationship between the locations where the end of the quick drop in the vertical earth pressure and the length of the secondary reinforcement.

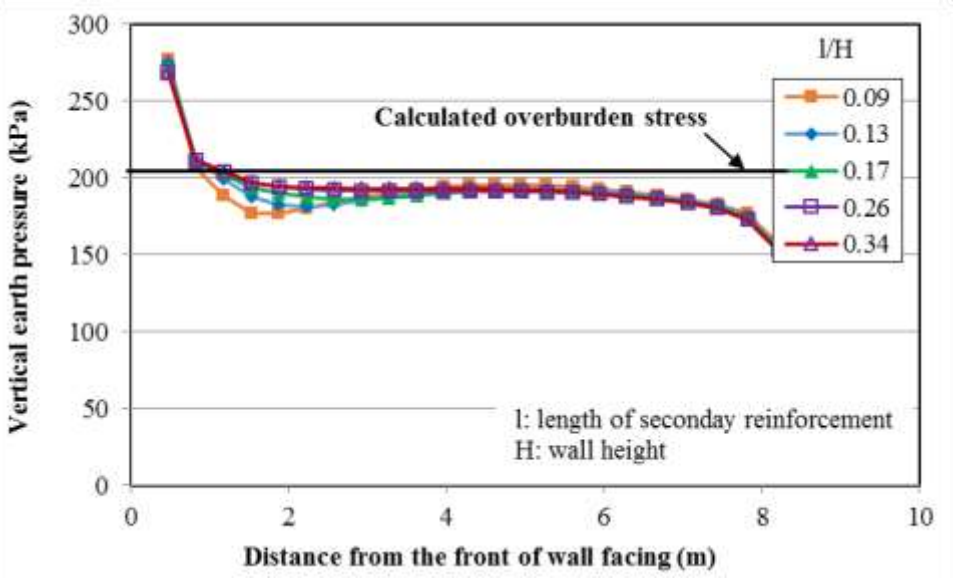

Figure 7.12 Effect of the secondary reinforcement length to wall height ratio (l/H) on the vertical earth pressure at the bottom of the reinforced soil zone

.

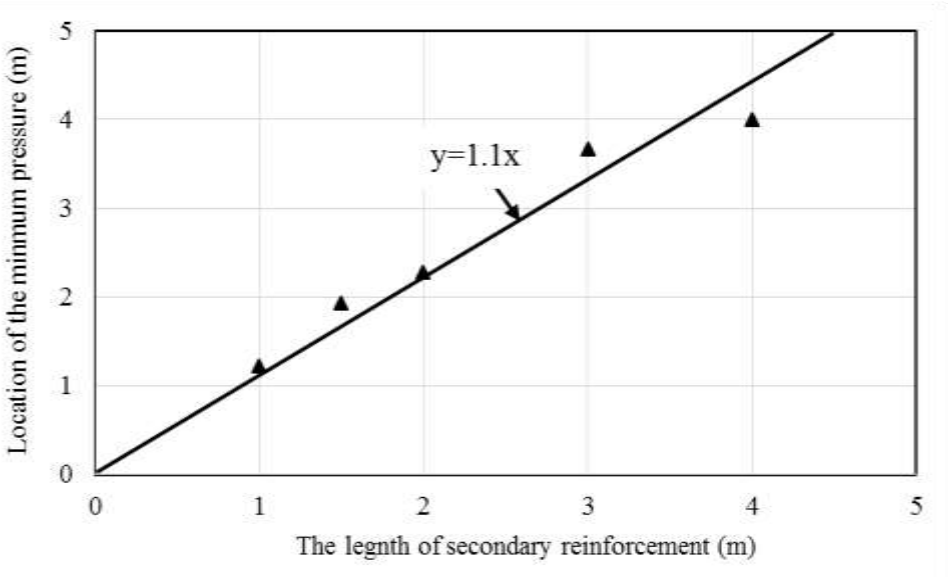

Figure 7.13 Relationship between the location of the end of the quick drop in the vertical earth pressure and the length of the secondary reinforcement

.

7.3.3. Lateral earth pressures

Figure 7.14 shows the effect of the secondary reinforcement length to wall height ratio (L/H) on the lateral earth pressure at the back of wall facing. Two solid lines in Figure 7.14 represent the Rankine active earth pressure and the at-rest earth pressure at the friction angle of 52°. As shown in Figure 7.14, the lateral earth pressure increased with depth (a reduction of elevation). Near the top and the bottom of the wall, the lateral earth pressures were close to the at-rest earth pressures because the soils near the top and bottom of the walls were not mobilized and had small horizontal deformations while the lateral earth pressure in the middle area of the walls was close to the Rankine active earth pressure because the soil in this area was mobilized and had large deformations. There is no effect of the secondary reinforcement length to wall height ratio (l/H) on the lateral earth pressure.

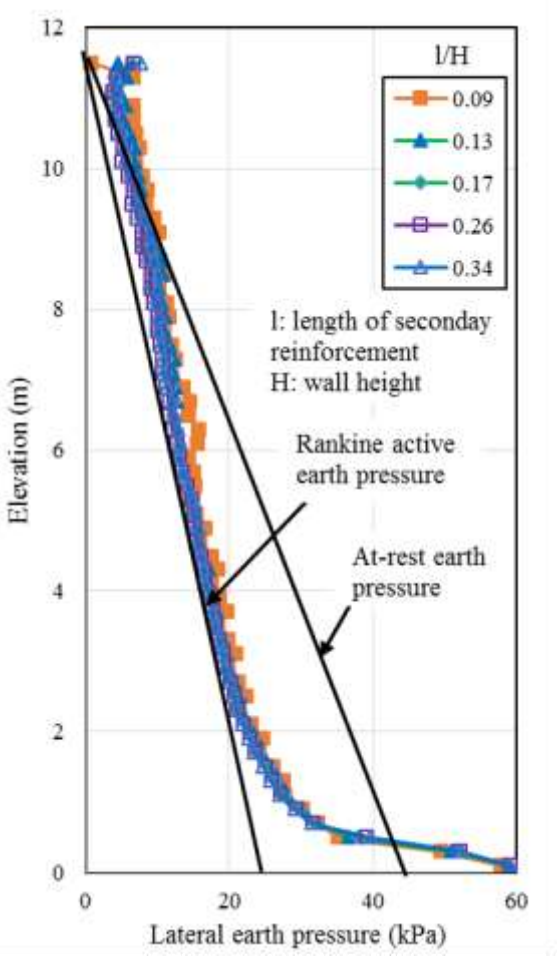

Figure 7.14 Effect of the secondary reinforcement length to wall height ratio (l/H) on the lateral earth pressure at the back of wall facing

7.3.4. Tensile stress in reinforcement

Figure 7.15 shows the effect of the secondary reinforcement length to wall height ratio (l/H) on the maximum tensile stresses in the primary reinforcement. For the comparison purpose, the AASHTO simplified method was used to calculate the maximum tensile stress at the friction angle of 52°. The calculated maximum tensile stress using the AASHTO simplified method was larger than that from the numerical simulation. The maximum tensile stress from the numerical simulation increased from the top of the walls to the elevation of 2.5 m and then slightly decreased until the bottom of the walls; while

the calculated maximum tensile stress using the AASHTO simplified method increased linearly from the top of the wall to the bottom. The ratio of l/H also had an influence on the maximum tensile stresses. The maximum tensile stress increased with a decrease in the ratio of l/H. The influence of the ratio of l/H on the maximum stress became little when the ratio of l/H was greater than 0.13.

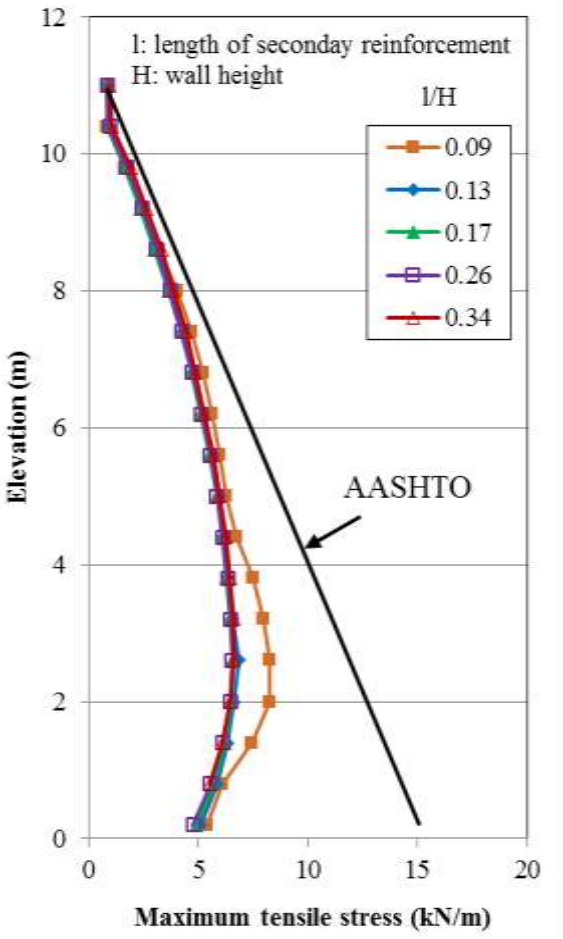

Figure 7.15 Effect of the secondary reinforcement length to wall height ratio (l/H) on the maximum tensile stress in the primary reinforcement

.

Figure 7.16 shows the effect of the secondary reinforcement length to wall height ratio (l/H) on the ratio of the connection stress and the maximum tensile stress in the primary reinforcement. When the ratio of the connection stress and the maximum tensile stress in the primary reinforcement was 1.0, it means that the maximum tensile stress occurred at the location of the connection between the reinforcement and the wall facing. The ratio of l/H had no influence on the ratio of the connection stress and the maximum tensile stress when the ratio of l/H was greater than 0.13. As shown in Figure 7.16, the ratio of the connection stress and the maximum tensile stress was equal to 1.0 when the ratio of l/H was greater than 0.13. When the ratio of l/H decreased to 0.09, the ratio of the connection stress to the maximum tensile stress was less than 1.0 when the elevation was less than 5 m. The smallest ratio of the connection stress and the maximum tensile stress was 0.8 when the ratio of l/H was 0.09.

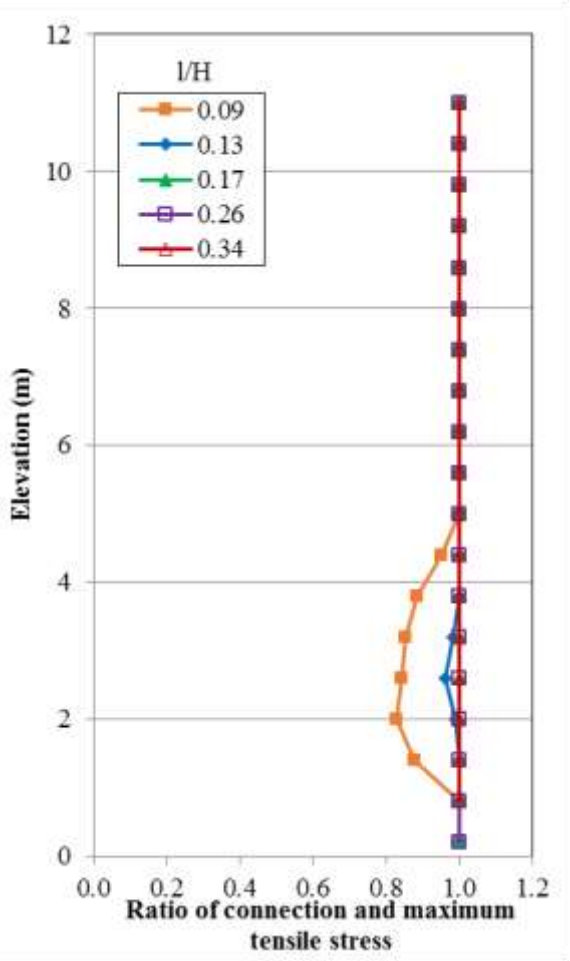

Figure 7.16 Effect of the secondary reinforcement length to wall height ratio (l/H) on the ratio of connection stress and maximum tensile stress in the primary reinforcement

.

Figure 7.17 presents the effect of the secondary reinforcement length to wall height ratio (l/H) on the normalized coefficient of lateral earth pressure K_r/K_a. AASHTO (2014) suggested the constant normalized coefficient of lateral earth pressure for geosynthetic reinforcement along elevation (see Figure 7.17). As shown in Figure 7.17, the normalized coefficient of the lateral earth pressure increased along the elevation and the normalized coefficients were less than 1.0. The normalized coefficient decreased with an increase of

the ratio of l/H. There is no effect of the ratio of l/H on the normalized coefficient when the ratio of l/H was greater than 0.13.

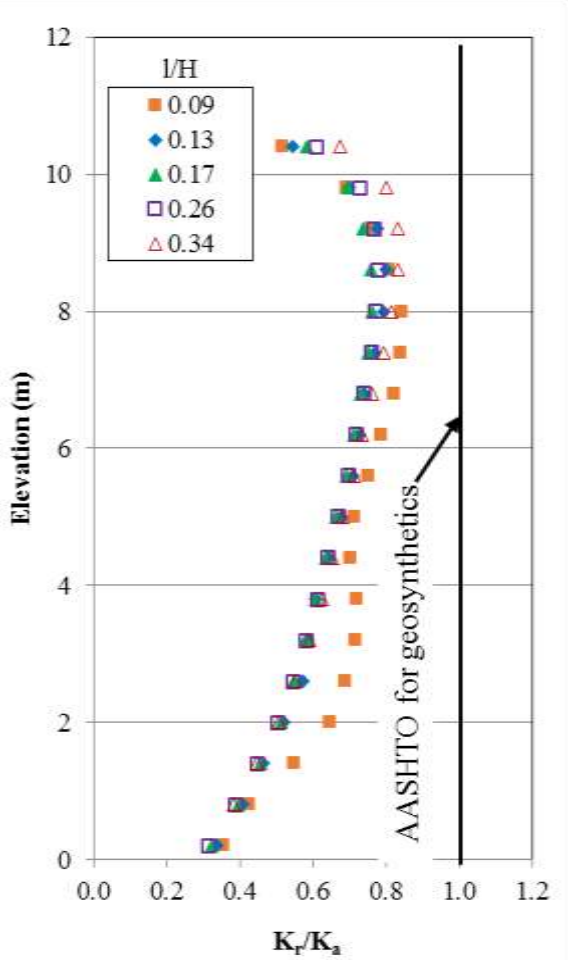

Figure 7.17 Effect of the secondary reinforcement length to wall height ratio (l/H) on the ratio of K_r/K_a

Figure 7.18 shows the effect of the secondary reinforcement length to wall height ratio (l/H) on the maximum tensile stresses in the secondary reinforcement. For the comparison purpose, the maximum tensile stresses were also calculated according to the Rankine active earth pressure and the at-rest earth pressure at the friction angle of 52°. The maximum tensile stress from the numerical simulation was greater than those using the

Rankine active earth pressure when the elevation was greater than 4 m. On the other hand, the calculated maximum tensile stress using the at-rest earth pressure was almost the same as that from the numerical simulation when the elevation was greater than 8 m and then was greater than that from the numerical simulation when the elevation was lower than 8 m. The ratio of l/H had a limited influence on the maximum tensile stresses.

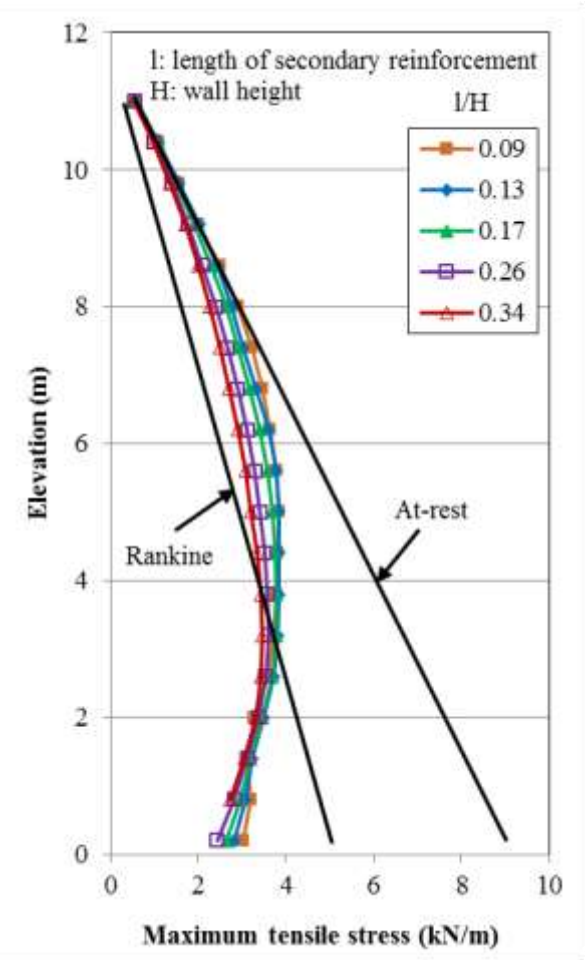

Figure 7.18 Effect of the secondary reinforcement length to wall height ratio (l/H) on the maximum tensile stresses in the secondary reinforcement

7.4. Effect of primary reinforcement stiffness

This section discusses the effect of the primary reinforcement stiffness. In the baseline model, the stiffness of the primary reinforcement was 1000 kN/m. Four additional cases with the stiffness of the primary reinforcement being 200, 500, 5000, and 10000 kN/m were studied.

7.4.1. Wall facing deflections

Figure 7.19 shows the profiles of the wall facing deflections at different stiffness of the primary reinforcement. As shown in Figure 7.19, the wall facing deflections in the five cases were almost the same at the bottom and the top of walls. The wall facing deflection increased with the elevation to reach the maximum value approximately in the middle of the wall and then decreased with the elevation until the top of the wall. In addition, the wall facing deflection decreased with an increase in the stiffness of the primary reinforcement. To clearly show the effect of the primary reinforcement stiffness on the maximum wall facing deflections, a relationship between the stiffness of the primary reinforcement and the maximum wall facing deflections is graphed in Figure 7.20. It can be seen that the maximum wall facing deflection rapidly decreased with an increase in the stiffness of the primary reinforcement. The stiffness of the primary reinforcement had a large influence on the maximum wall facing deflection when the stiffness of the primary reinforcement was lower than 5000 kN/m. When the stiffness of the primary reinforcement was higher than 5000 kN/m, the benefit of increasing the stiffness of the primary reinforcement became minimal.

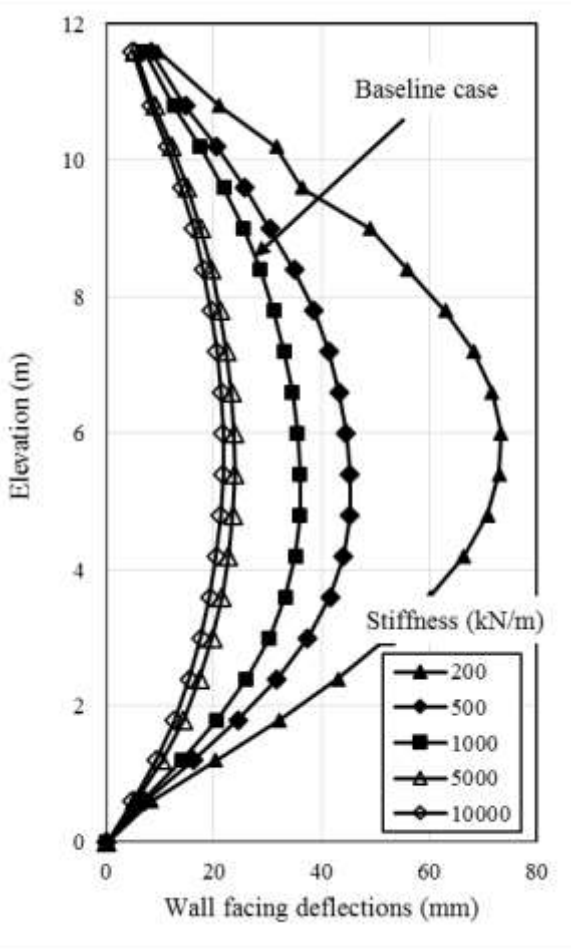

Figure 7.19 Effect of the primary reinforcement stiffness on the wall facing deflection

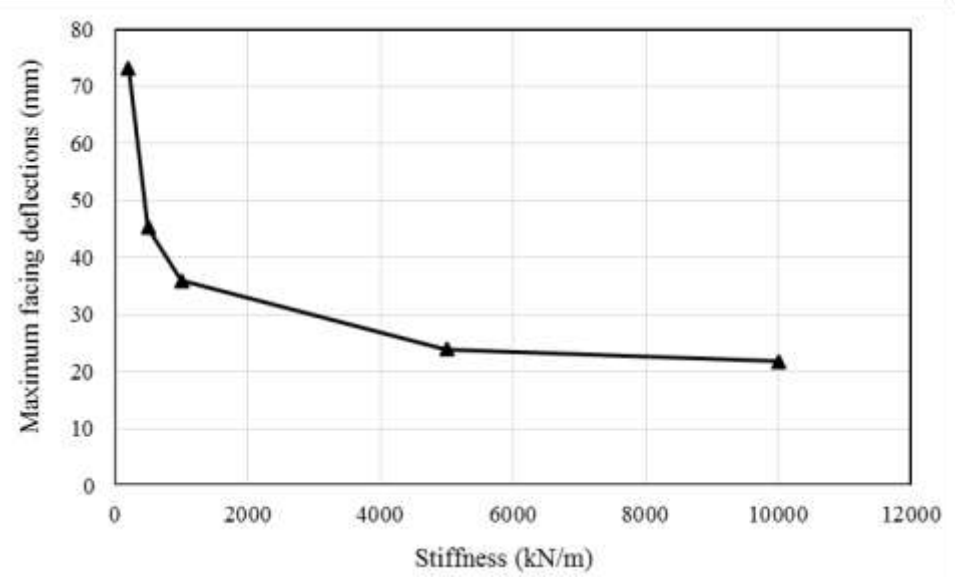

Figure 7.20 Relationship between the primary reinforcement stiffness and the maximum wall facing deflection

7.4.2. Vertical earth pressures

Figure 7.21 shows the effect of the primary reinforcement stiffness on the vertical earth pressure at the bottom of the reinforced soil zone. As shown in Figure 7.21, the vertical earth pressures quickly dropped within the area reinforced with the primary reinforcement and the secondary reinforcement and then gradually approached to the calculated overburden stress. The maximum vertical earth pressures occurred at the back of wall facing due to a potential overturning moment, which added an additional vertical earth pressure at the back of wall facing. The influence of the primary reinforcement stiffness on the vertical earth pressure mainly happened in an area behind the wall facing. The stiffer primary reinforcement resulted in a higher vertical earth pressure at a distance away from the back of the wall facing. In addition, this influence became minimal when the primary reinforcement stiffness was higher than 5000 kN/m.

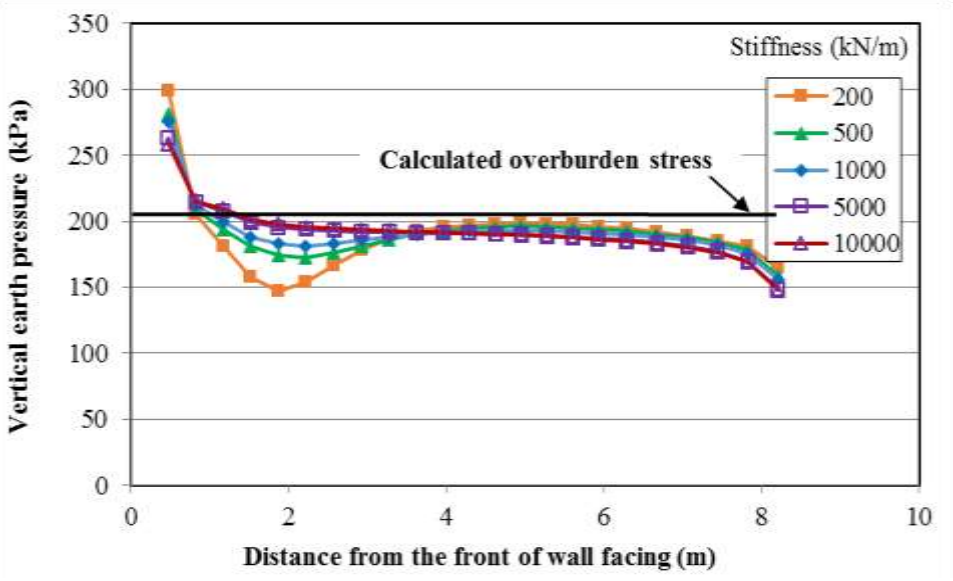

Figure 7.21 Effect of the primary reinforcement stiffness on the vertical earth pressure at the bottom of the reinforced soil zone

7.4.3. Lateral earth pressures

Figure 7.22 shows the effect of the primary reinforcement stiffness on the lateral earth pressure at the back of wall facing. Two solid lines in Figure 7.22 represent the Rankine active earth pressure and the at-rest earth pressure at the friction angle of 52°. As shown in Figure 7.22, the lateral earth pressure increased with depth (a reduction of elevation). Near the top and the bottom of the wall, the lateral earth pressures were close to the at-rest earth pressures because the soils near the top and bottom of the wall were not mobilized and had small horizontal deformations while the lateral earth pressures in the middle area of the wall were close to the Rankine active earth pressure because the soil in this area was mobilized and had large deformations. The primary reinforcement stiffness presents an effect on the lateral earth pressure when the elevation was lower than 7 m. The primary reinforcement with higher stiffness resulted in the larger lateral earth pressure close to the at-rest active earth pressure. This result is because the reinforced soil with higher primary reinforcement stiffness was not mobilized and had smaller horizontal deformation.

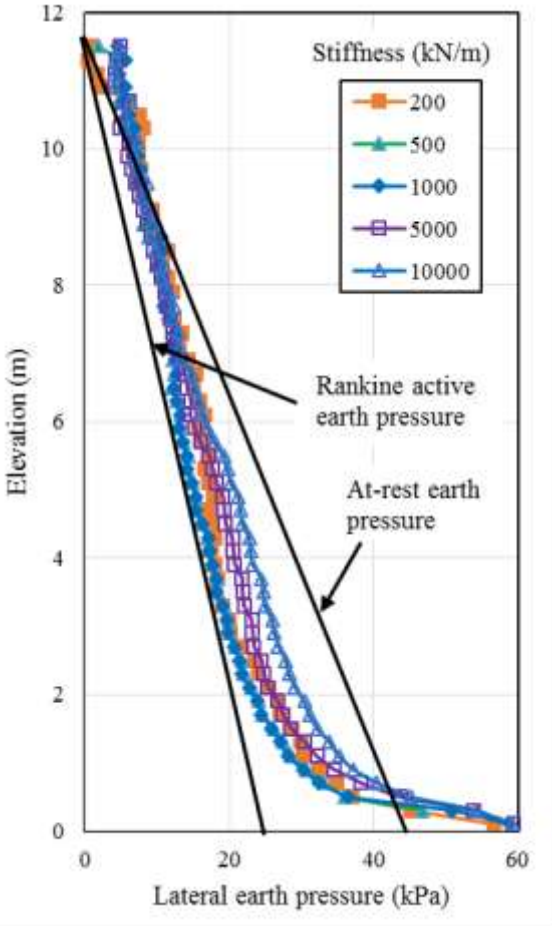

Figure 7.22 Effect of the primary reinforcement stiffness on the lateral earth pressure at the back of wall facing

7.4.4. Tensile stress in reinforcement

Figure 7.23 shows the effect of the primary reinforcement stiffness on the maximum tensile stress in the primary reinforcement. As shown in Figure 7.23, the maximum tensile stress from the numerical simulation increased from the top of the wall to the elevation of 2.5 m and then slightly decreased until the bottom of the wall. For the comparison purpose, the AASHTO simplified method for geosynthetics and steel strips was used to calculate the maximum tensile stress at the friction angle of 52°. When the primary reinforcement stiffness was lower than 1000 kN/m, the primary reinforcement was

regarded as geosynthetics and the calculated maximum tensile stress using the AASHTO simplified method for geosynthetics was higher than that from the numerical simulation. Similarly, when the primary reinforcement stiffness increased up to 10000 kN/m, the primary reinforcement behaved like the steel strip. The calculated maximum tensile stress using the AASHTO simplified method for the steel strip was close to that from the numerical simulation when the primary reinforcement stiffness was 10000 kN/m. The primary reinforcement stiffness had an influence on the maximum tensile stresses in the primary reinforcement. The maximum tensile stress increased with an increase in the primary reinforcement stiffness.

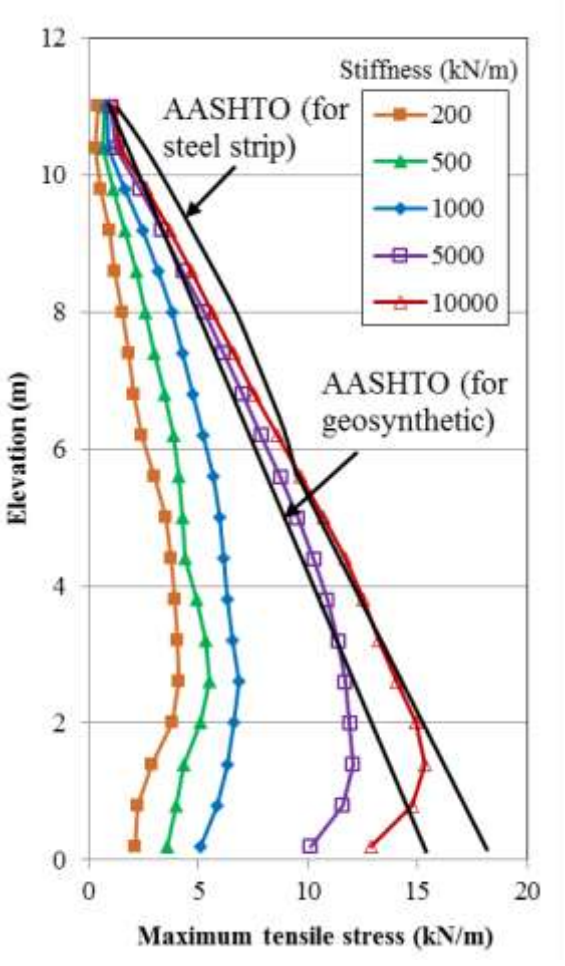

Figure 7.23 Effect of the primary reinforcement stiffness on the maximum tensile stress in the primary reinforcement

.

Figure 7.24 shows the effect of the primary reinforcement stiffness on the ratio of the connection stress and the maximum tensile stress in the primary reinforcement. When the ratio of the connection stress and the maximum tensile stress in the primary reinforcement was 1.0, it means that the maximum tensile stress occurred at the location of the connection between the primary reinforcement and the wall facing. The primary reinforcement stiffness had no influence on the ratio of the connection stress and the maximum tensile stress when the primary reinforcement stiffness was higher than 5000 kN/m. As shown in Figure 7.16, the ratio of the connection stress and the maximum tensile stress was equal to 1.0 when the primary reinforcement stiffness was higher than 5000 kN/m. The minimum ratio of the connection stress and the maximum tensile stress occurred within the lower part of the wall. The smallest ratio of the connection stress and the maximum tensile stress was 0.6 when the primary reinforcement stiffness was 200 kN/m.

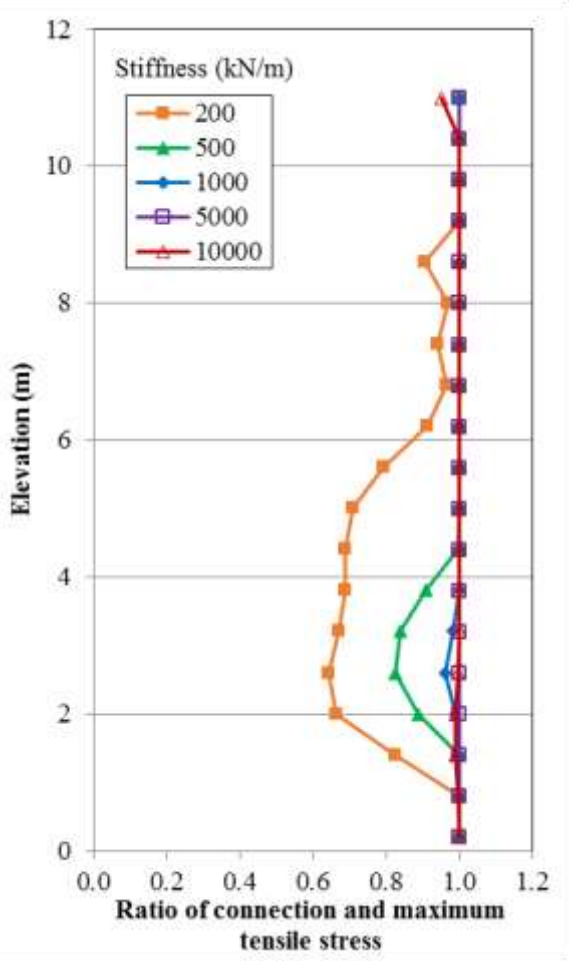

Figure 7.24 Effect of the primary reinforcement stiffness on the ratio of the connection stress and the maximum tensile stress in primary reinforcement

Figure 7.25 presents the effect of the primary reinforcement stiffness on the normalized coefficient of the lateral earth pressure K_r/K_a. AASHTO (2014) suggested the normalized coefficients of the lateral earth pressure for geosynthetic reinforcement and steel strips with the elevation (see Figure 7.25). As shown in Figure 7.25, the normalized coefficients of lateral earth pressure from the numerical simulation with the primary reinforcement stiffness lower than 1000 kN/m were less than the suggested normalized coefficient by AASHTO (2014) for geosynthetics. Similarly, the normalized coefficients of lateral earth pressure from the numerical simulation with the primary reinforcement

stiffness between 5000 and 10000 kN/m were less than the suggested normalized coefficient by AASHTO (2014) for steel strips. The normalized coefficient decreased with a decrease in the primary reinforcement stiffness.

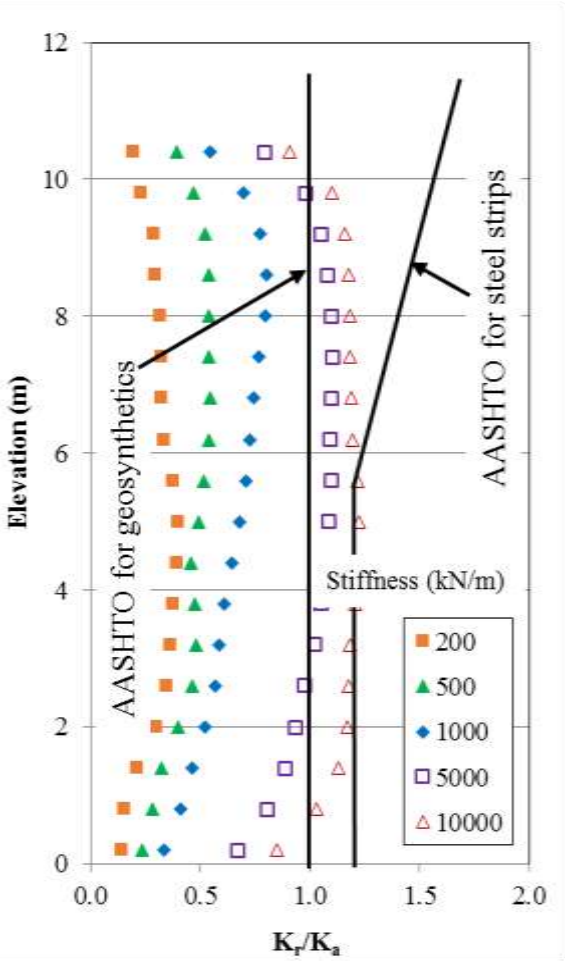

Figure 7.25 Effect of the primary reinforcement stiffness on the ratio of K_r/K_a

Figure 7.26 shows the effect of the primary reinforcement stiffness on the maximum tensile stresses in the secondary reinforcement. For the comparison purpose, the maximum tensile stresses were also calculated according to the Rankine active earth pressure and the at-rest earth pressure at the friction angle of 52°. The calculated maximum tensile stress using the at-rest earth pressure was almost the same as those from the

numerical simulation when the primary reinforcement stiffness was lower than 1000 kN/m. When the primary reinforcement stiffness increased up to 5000 kN/m, the maximum tensile stress from the numerical simulation was higher than that using the at-rest earth pressure within the upper half part of the wall; while the maximum tensile stress from the numerical simulation was lower within the lower part of the wall. The primary reinforcement stiffness had a great influence on the maximum tensile stress in the secondary reinforcement. The maximum tensile stress increased with a decrease in primary reinforcement stiffness.

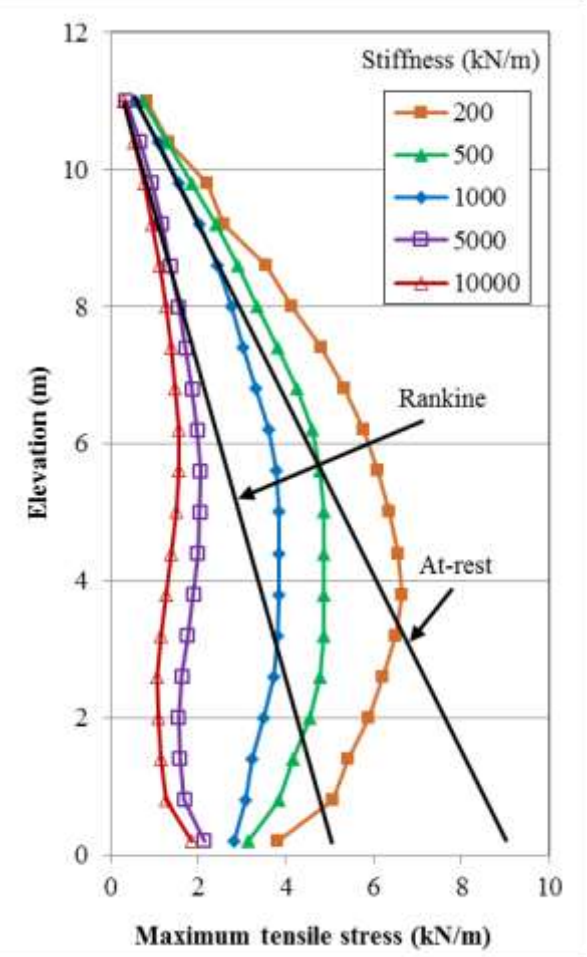

Figure 7.26 Effect of the primary reinforcement stiffness on the maximum tensile stresses in the secondary reinforcement

7.5. Effect of secondary reinforcement stiffness

This section discusses the effect of the secondary reinforcement stiffness. In the baseline model, the secondary reinforcement stiffness was 500 kN/m. Four additional cases with the secondary reinforcement stiffness at 100, 1000, 2000, and 5000 kN/m were studied.

7.5.1. Wall facing deflections

Figure 7.27 shows the profiles of the wall facing deflections at different secondary reinforcement stiffness. As shown in Figure 7.27, the wall facing deflections in the five cases were almost the same at the bottom and the top of walls. The wall facing deflection increased with the elevation to reach the maximum value approximately in the middle of the wall and then decreased with the elevation until the top of the wall. In addition, the wall facing deflection decreased with an increase in the secondary reinforcement stiffness. To clearly show the effect of the secondary reinforcement stiffness on the maximum wall facing deflection, a relationship between the secondary reinforcement stiffness and the maximum wall facing deflection is graphed in Figure 7.28. It can be seen that the maximum wall facing deflection rapidly decreased with an increase in the secondary reinforcement stiffness. The secondary reinforcement stiffness had a large influence on the maximum wall facing deflection when the secondary reinforcement stiffness was lower than 2000 kN/m. When the secondary reinforcement stiffness was higher than 2000 kN/m, the benefit of increasing the secondary reinforcement stiffness to reduce the maximum wall facing deflection became minimal.

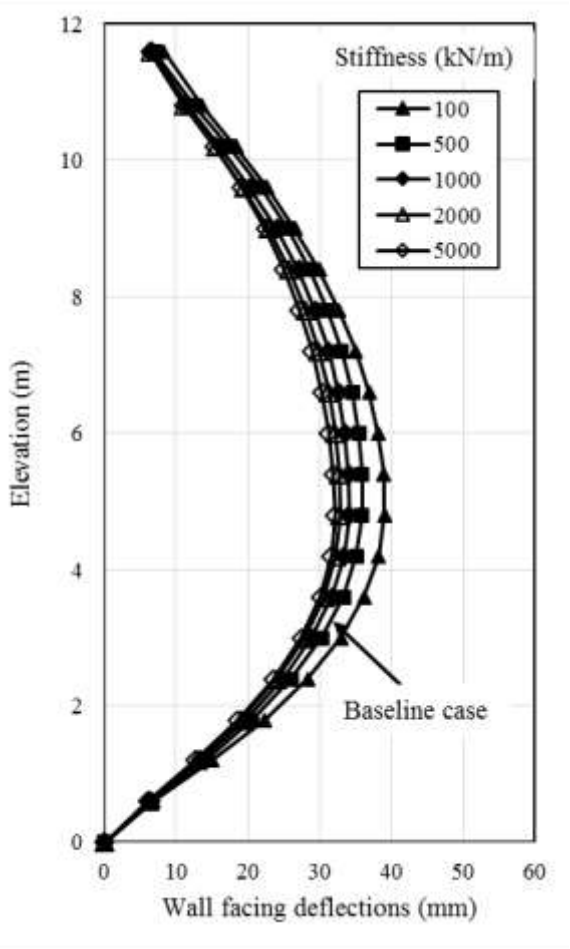

Figure 7.27 Effect of the secondary reinforcement stiffness on the wall facing deflections

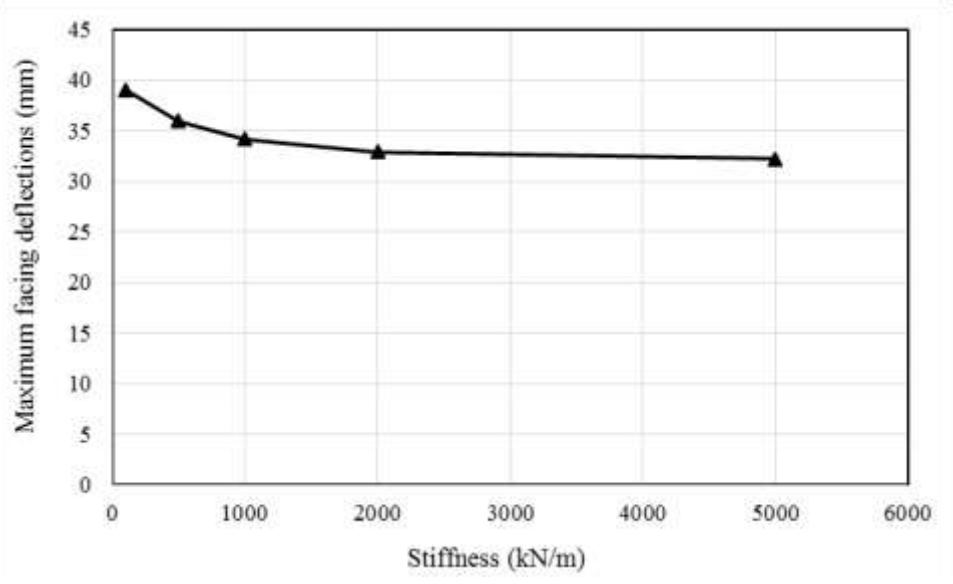

Figure 7.28 Relationship between the primary reinforcement stiffness and the maximum wall facing deflections

7.5.2. Vertical earth pressures

Figure 7.29 shows the effect of the secondary reinforcement stiffness on the vertical earth pressures at the bottom of the reinforced soil zone. As shown in Figure 7.29, the vertical earth pressures quickly dropped within the area reinforced with the primary reinforcement and the secondary reinforcement and then gradually approached to the calculated overburden stress. The maximum vertical earth pressures occurred at the back of wall facing due to a potential overturning moment resulting from the lateral earth pressure of the retaining soil, which added an additional vertical earth pressure at the back of wall facing. The influence of the secondary reinforcement stiffness on the vertical earth pressure was observed in the area behind the wall facing. The stiffer secondary reinforcement resulted in a lower vertical earth pressure at a distance away from the back of the wall facing.

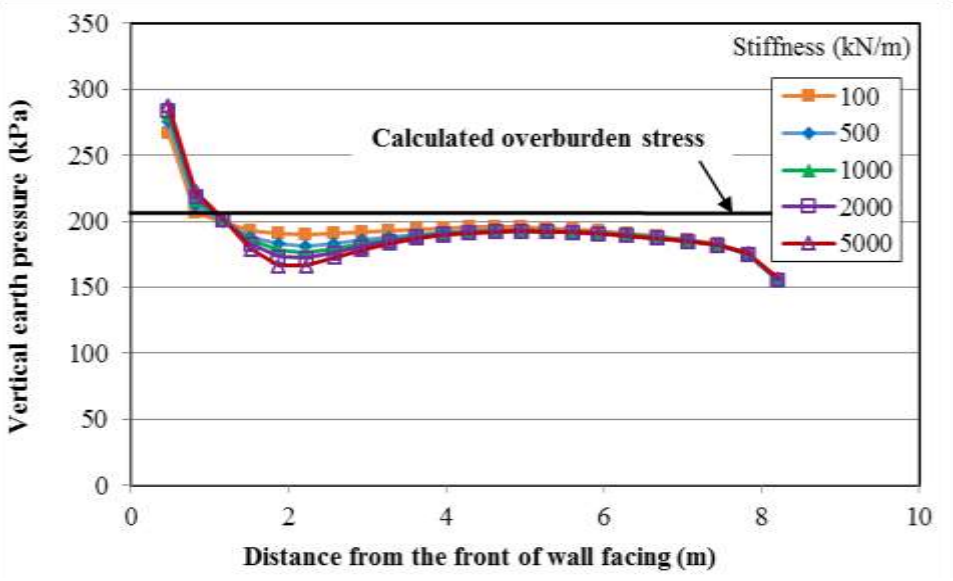

Figure 7.29 Effect of the secondary reinforcement stiffness on the vertical earth pressure at the bottom of the reinforced soil zone

7.5.3. Lateral earth pressures

Figure 7.30 shows the effect of the secondary reinforcement stiffness on the lateral earth pressure at the back of wall facing. Two solid lines in Figure 7.30 represent the Rankine active earth pressure and the at-rest earth pressure at the friction angle of 52°. As shown in Figure 7.30, the lateral earth pressure increased with the depth (a reduction of elevation). Near the top and the bottom of the wall, the lateral earth pressures were close to the at-rest earth pressures because the soils near the top and bottom of walls were not mobilized and had small horizontal deformations while the lateral earth pressure in the middle area of walls was close to the Rankine active earth pressure because the soil in this area was mobilized and had large deformation. The secondary reinforcement stiffness had an effect on the lateral earth pressure with the elevation. The secondary reinforcement with higher stiffness resulted in higher lateral earth pressure close to the at-rest active earth pressure. This result is because the reinforced soil with the higher secondary reinforcement stiffness was not mobilized and had smaller horizontal deformations.

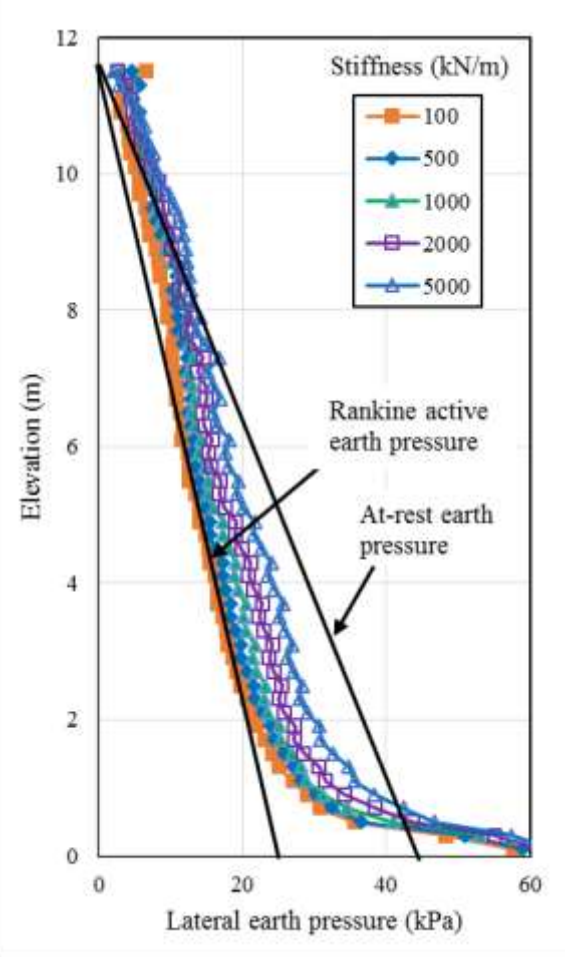

Figure 7.30 Effect of the secondary reinforcement stiffness on the lateral earth pressure at the back of wall facing

7.5.4. Tensile stress in reinforcement

Figure 7.31 shows the effect of the secondary reinforcement stiffness on the maximum tensile stresses in the primary reinforcement. As shown in Figure 7.31, the maximum tensile stress from the numerical simulation increased from the top of the wall to the elevation of 2.5 m and then slightly decreased until the bottommost layer of the primary reinforcement. For the comparison purpose, the AASHTO simplified method for geosynthetics was used to calculate the maximum tensile stress at the friction angle of 52°. Except the secondary reinforcement with the stiffness of 100 kN/m, the secondary

reinforcement with the stiffness higher than 500 kN/m produced the lower calculated maximum tensile stress in the primary reinforcement using the numerical simulation than that using the AASHTO simplified method. The secondary reinforcement stiffness had an influence on the maximum tensile stress in the primary reinforcement. The maximum tensile stress increased with an increase in secondary reinforcement stiffness but its influence become small when the secondary reinforcement stiffness higher than 1000 kN/m.

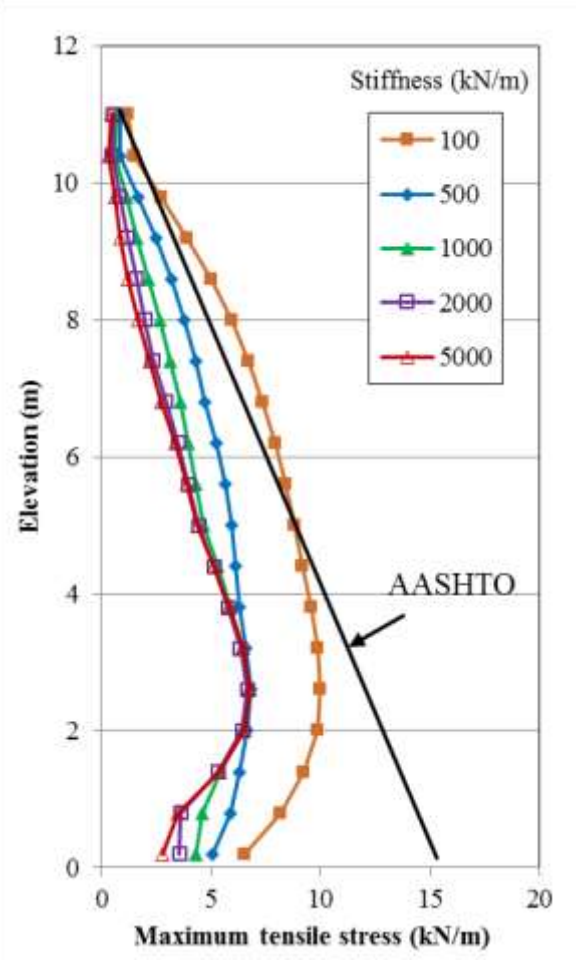

Figure 7.31 Effect of the secondary reinforcement stiffness on the maximum tensile stress in the primary reinforcement

Figure 7.32 shows the effect of the secondary reinforcement stiffness on the ratio of the connection stress and the maximum tensile stress in the primary reinforcement.

When the ratio of the connection stress and the maximum tensile stress in the primary reinforcement was 1.0, it means that the maximum tensile stress occurred at the location of the connection between the primary reinforcement and the wall facing. The connection stress was equal to the maximum tensile stress with the elevation when the secondary reinforcement stiffness was 100 kN/m. When the secondary reinforcement stiffness was higher than 500 kN/m, the ratio of the connection stress to the maximum tensile stress became less than 1.0, which occurred within the lower part of the wall. With an increase in the secondary reinforcement stiffness, the minimum ratio of the connection stress to the maximum tensile stress decreased and the area with the ratio less than 1.0 increased with the elevation. In other words, the stronger secondary reinforcement could reduce connection stress in the primary reinforcement. The smallest ratio of the connection stress and the maximum tensile stress was 0.4 when the secondary reinforcement stiffness was 5000 kN/m.

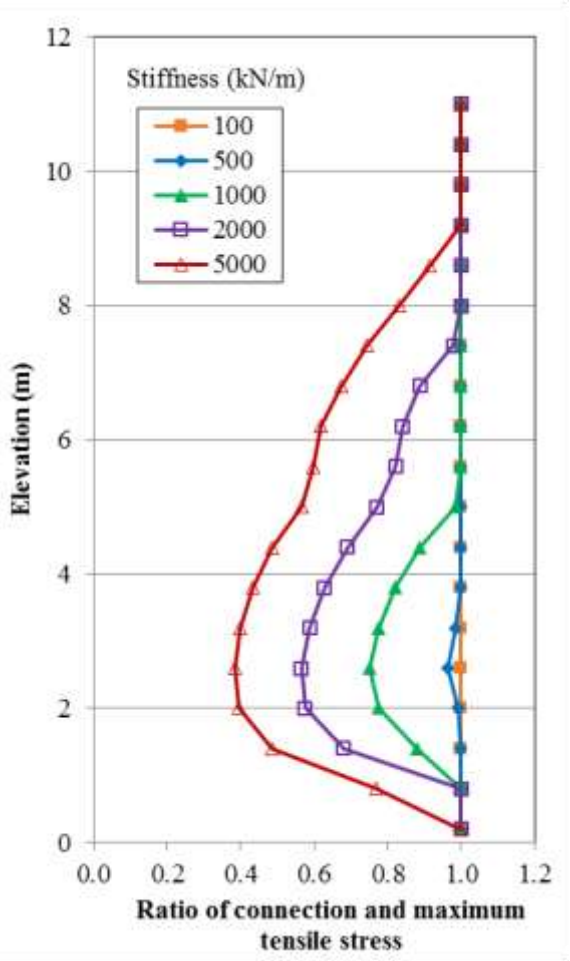

Figure 7.32 Effect of the secondary reinforcement stiffness on the ratio of the connection stress and the maximum tensile stress in the primary reinforcement

Figure 7.33 presents the effect of the secondary reinforcement stiffness on the normalized coefficient of lateral earth pressure K_r/K_a. AASHTO (2014) suggested the constant normalized coefficient of the lateral earth pressure for geosynthetic reinforcement (see Figure 7.33). As shown in Figure 7.33, the normalized coefficients were smaller than 1.0 except in the case with the secondary reinforcement being 100 kN/m. The secondary reinforcement stiffness had an influence on the normalized coefficient. The normalized coefficient decreased with a decrease in the primary reinforcement stiffness. When the secondary reinforcement stiffness was not lower than 500 kN/m, there was no obvious

influence of secondary reinforcement stiffness when the elevation was lower than 4 m; while there was a greater influence when the elevation was higher than 4 m.

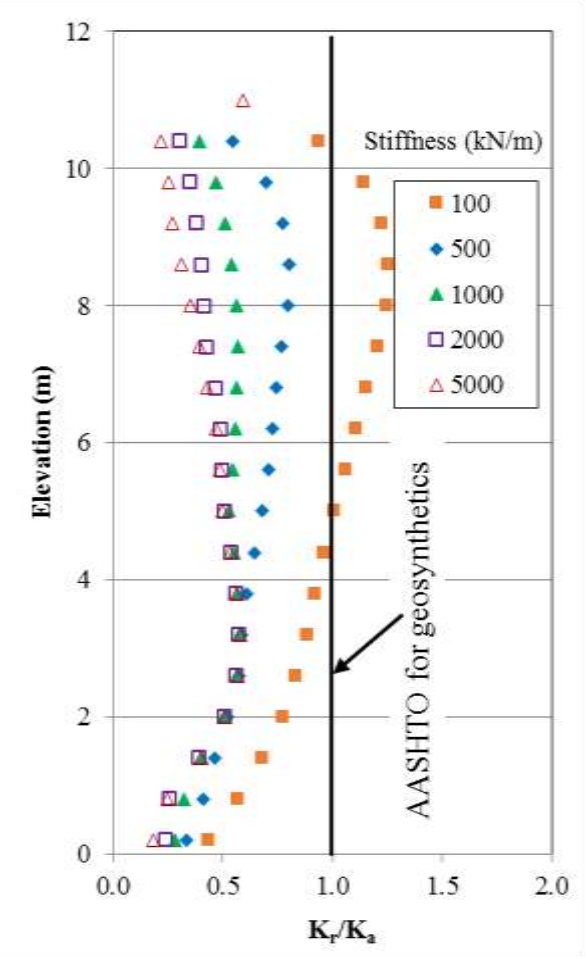

Figure 7.33 Effect of the secondary reinforcement stiffness on the ratio of K_r/K_a

Figure 7.34 shows the effect of the secondary reinforcement stiffness on the maximum tensile stress in the secondary reinforcement. For the comparison purpose, the maximum tensile stresses were also calculated according to the Rankine active earth pressure and the at-rest earth pressure at the friction angle of 52°. The calculated maximum tensile stress using the at-rest earth pressure was higher than that from the numerical simulation when the secondary reinforcement stiffness was lower than 500 kN/m. The

secondary reinforcement stiffness had a great influence on the maximum tensile stress in the secondary reinforcement. The maximum tensile stress increased with an increase in secondary reinforcement stiffness.

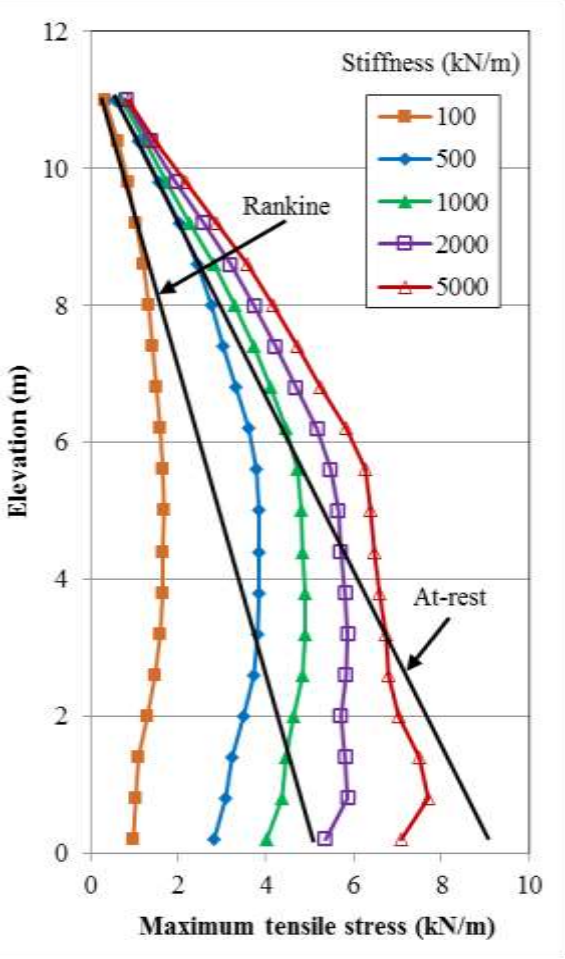

Figure 7.34 Effect of the secondary reinforcement stiffness on the maximum tensile stresses in the secondary reinforcement

7.6. Effect of soil friction angle

This section discusses the effect of the friction angle of the backfill soil. In the baseline model, the friction angle of the backfill soil was 52°. Additional four friction angles of the backfill soil were used in the parametric study, which were 34°, 38°, 40°, and

46°. The friction angle of 34° was the value suggested by AASHTO (2014) in the design of MSE walls when no triaxial tests were performed and the friction angle of 40° was the largest friction angle that can be used in the design of MSE walls according to AASHTO (2014). Adams et al. (2011) also pointed out that the friction angle of the backfill soil used for design of Geosynthetic Reinforced Soil (GRS) walls should be not lower than 38°.

7.6.1. Wall facing deflections

Figure 7.35 shows the profiles of the wall facing deflection with the backfill soil at different friction angles. As shown in Figure 7.35, the wall facing deflections for the five cases were almost the same at the bottom and the top of the walls. The wall facing deflection increased with the elevation to reach the maximum value approximately in the middle of the walls and then decreased with the elevation until the top of the wall. In addition, the wall facing deflection decreased with an increase in the friction angle of the backfill soil. To clearly show the effect of the friction angle of the backfill soil on the maximum wall facing deflection, a relationship between the friction angle of the backfill soil and the maximum wall facing deflection is graphed in Figure 7.36. It can be seen that the friction angle of the backfill soil had a great influence on the maximum wall facing deflection. The maximum wall facing deflection approximately linearly decreased with an increase in the friction angle of the backfill soil. This result could be explained by that the backfill soil with a lower friction angle had higher lateral earth pressure applied behind the wall facing, resulting in larger wall facing deflection.

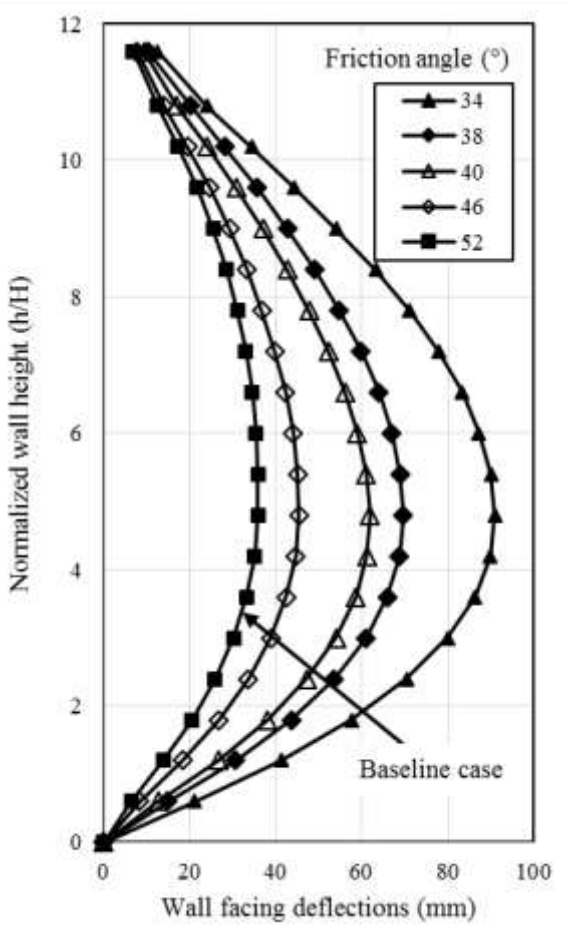

Figure 7.35 Effect of the friction angles of backfill soil on the wall facing deflections

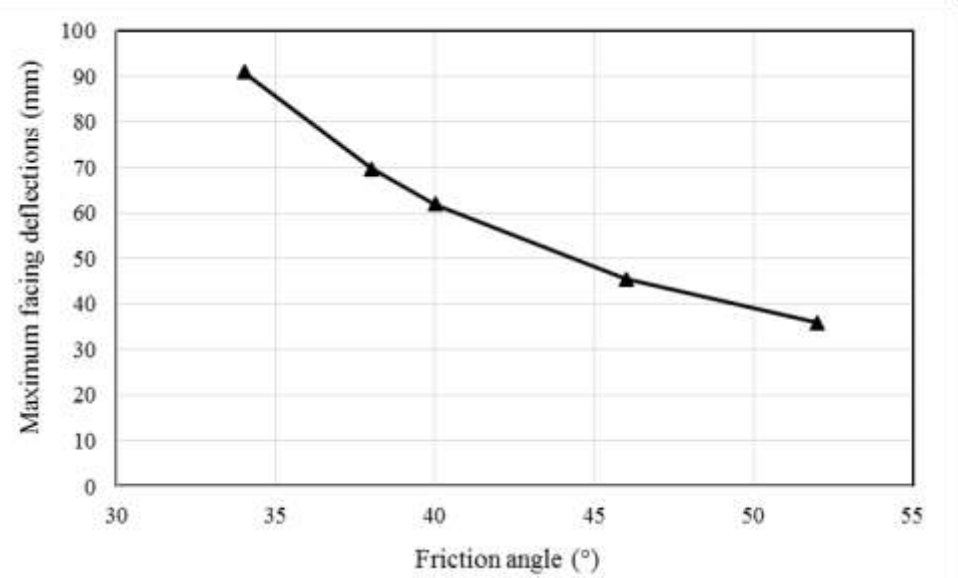

Figure 7.36 Relationship between the friction angle of backfill soil and the maximum wall facing deflections

7.6.2. Vertical earth pressures

Figure 7.37 shows the effect of the friction angle of the backfill soil on the vertical earth pressure at the bottom of the reinforced soil zone. As shown in Figure 7.37, the vertical earth pressures quickly dropped within the area reinforced with the primary reinforcement and the secondary reinforcement and then gradually approached to the calculated overburden stress. The maximum vertical earth pressures occurred at the back of wall facing due to a potential overturning moment, which added an additional vertical earth pressure at the back of wall facing. The influence of the friction angle of the backfill soil on the vertical earth pressure happened in an area behind the wall facing. The lower friction angle of the backfill soil resulted in a larger drop of the vertical earth pressure at the back of the wall facing. In other words, the backfill soil with a higher friction angle could reduce the difference in vertical earth pressure in an area near the wall facing. In addition, this influence became minimal when the friction angle of the backfill soil was lower than 40°.

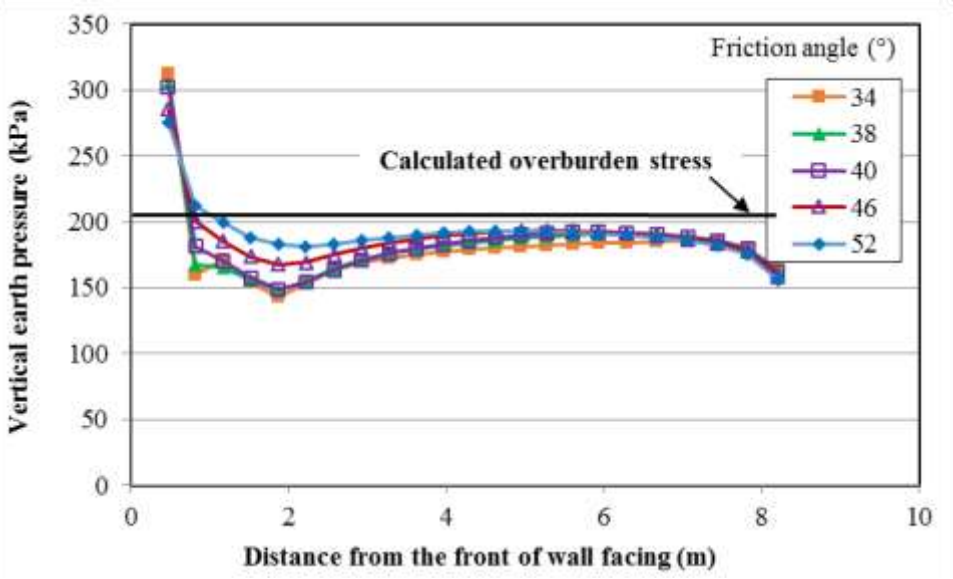

Figure 7.37 Effect of the friction angle of the backfill soil on the vertical earth pressure at the bottom of the reinforced soil zone

7.6.3. Lateral earth pressures

Figure 7.38 shows the effect of the friction angle of the backfill soil on the lateral earth pressure at the back of wall facing. Figure 7.38 also presents the Rankine active earth pressures and the at-rest earth pressure with the friction angle of 34° and 52°, respectively. As shown in Figure 7.38, the lateral earth pressure increased with the depth (a reduction of the elevation) and fell between the Rankine active earth pressure and the at-rest earth pressure. Near the top and the bottom of the wall, the lateral earth pressures were close to the at-rest earth pressure because the soils near the top and bottom of walls were not mobilized and had small horizontal deformations while the lateral earth pressure in the middle area of walls was close to the Rankine active earth pressure because the soil in this area was fully mobilized and had large deformations. The friction angle of the backfill soil presents an effect on the lateral earth pressure with the elevation. The backfill soil with a

higher friction angle resulted in a lower lateral earth pressure. This result is also consistent with the theories of the Rankine earth pressure and the Coulomb earth pressure.

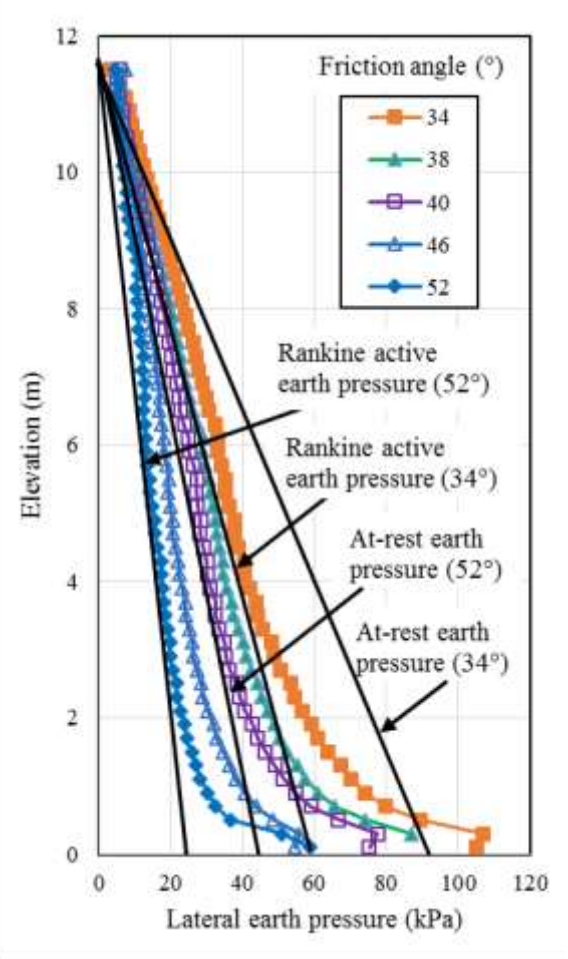

Figure 7.38 Effect of the friction angle of the backfill soil on the lateral earth pressure at the back of wall facing

7.6.4. Tensile stress in reinforcement

Figure 7.39 shows the effect of the friction angle of the backfill soil on the maximum tensile stresses in the primary reinforcement. As shown in Figure 7.39, the maximum tensile stress from the numerical simulation increased from the top of the walls to the elevation of 2.5 m and then slightly decreased until the bottommost layer of the primary reinforcement. For the comparison purpose, the AASHTO simplified method for

geosynthetics was used to calculate the maximum tensile stress with the friction angle of 52°. The calculated maximum tensile stress in the primary reinforcement in the numerical simulation was lower than the one using the AASHTO simplified method when the friction angle of the backfill soil was 52°. The friction angle of the backfill soil had an influence on the maximum tensile stress in the primary reinforcement. The maximum tensile stress decreased with an increase in the friction angle of the backfill material because the backfill soil with a lower friction angle resulted in a higher lateral earth pressure at the back of the wall facing.

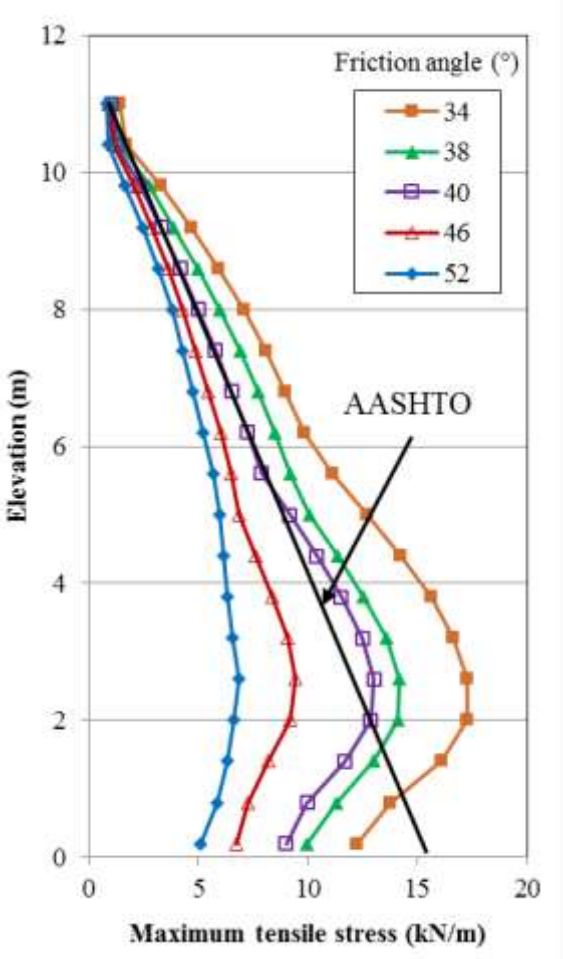

Figure 7.39 Effect of the friction angle of the backfill soil on the maximum tensile stress in the primary reinforcement

Figure 7.40 shows the effect of the friction angle of the backfill soil on the ratio of the connection stress to the maximum tensile stress in the primary reinforcement. When the ratio of the connection stress to the maximum tensile stress in the primary reinforcement was 1.0, it means that the maximum tensile stress occurred at the location of the connection between the reinforcement and the wall facing. With an increase in the friction angle of the backfill soil, the minimum ratio of the connection stress to the maximum tensile stress decreased but the area with the ratio less than 1.0 increased with the elevation. This result means that the secondary reinforcement exhibited more benefit on the reduction of the connection stress with the backfill soil having lower friction angles. The smallest ratio of the connection stress to the maximum tensile stress was 0.75 when the friction angle of the backfill soil decreased to 34°.

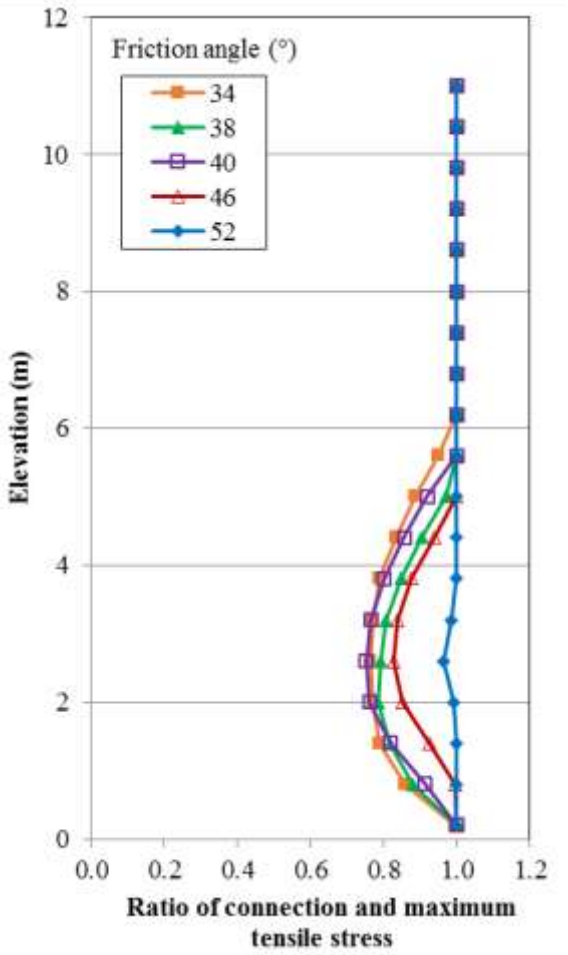

Figure 7.40 Effect of the friction angle of the backfill soil on the ratio of the connection stress to the maximum tensile stress in the primary reinforcement

Figure 7.41 presents the effect of the friction angle of the backfill material on the normalized coefficient of lateral earth pressure K_r/K_a. AASHTO (2014) suggested a constant normalized coefficient of the lateral earth pressure for geosynthetic reinforcement (see Figure 7.41). As shown in Figure 7.41, the normalized coefficients with different friction angles of the backfill soil were less than 1.0. The normalized coefficient increased with the elevation until the elevation reached 3 m and then the normalized coefficient was almost constant with the elevation. The friction angle of the backfill soil had a little

influence on the normalized coefficient. The normalized coefficient decreased with a decrease in the friction angle of the backfill soil when the elevation was greater than 2.5 m.

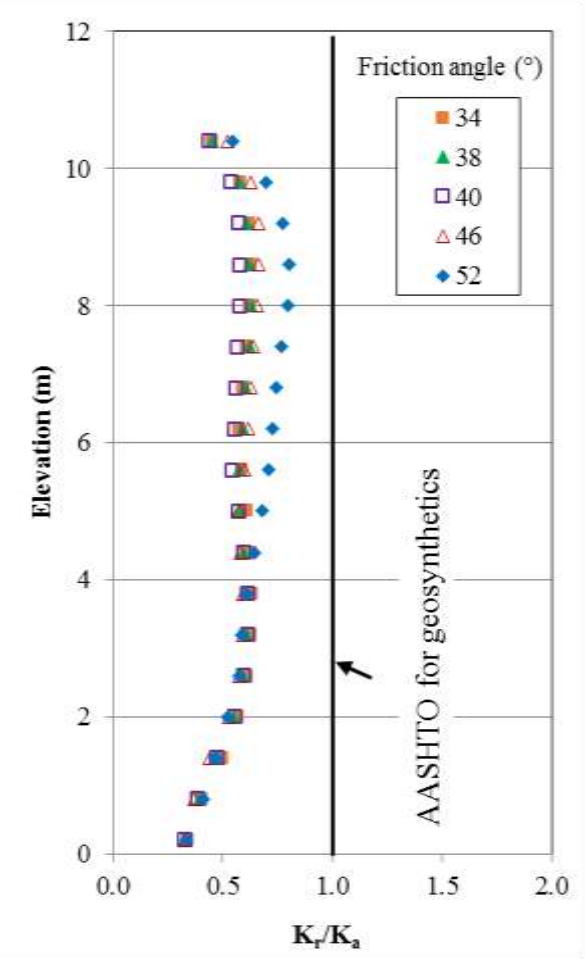

Figure 7.41 Effect of the friction angle of the backfill soil on the ratio of K_r/K_a

Figure 7.42 shows the effect of the friction angle of the backfill soil on the maximum tensile stresses in the secondary reinforcement. For the comparison purpose, the maximum tensile stresses were also calculated according to the Rankine active earth pressure and the at-rest earth pressure with the friction angle of 52°. The calculated maximum tensile stresses using the at-rest earth pressure were higher than those from the numerical simulation. However, the calculated maximum tensile stresses using the Rankine

active earth pressure were lower than those from the numerical simulation when the elevation was greater than 3 m. The friction angle of the backfill soil had an influence on the maximum tensile stress in the secondary reinforcement. The maximum tensile stress decreased with an increase in the friction angle of the backfill soil.

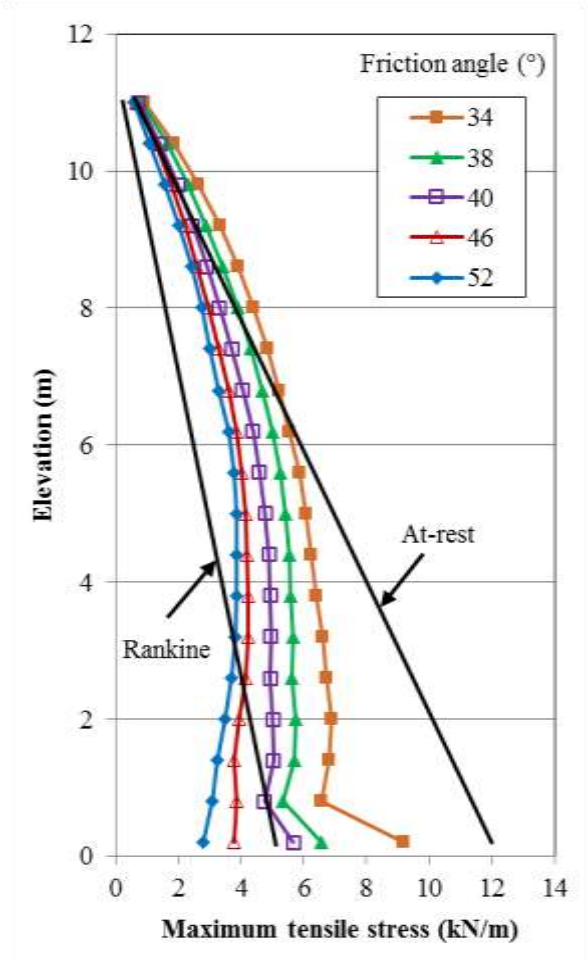

Figure 7.42 Effect of the friction angle of the backfill soil on the maximum tensile stresses in the secondary reinforcement

7.7. Effect of soil dilation

This section discusses the effect of the dilation angle of the backfill soil. In the baseline model, the dilation angle of backfill soil was 8°. Additional four dilation angles

of the backfill soil were investigated in the parametric study, which were 0°, 16°, 24°, and 32°.

7.7.1. Wall facing deflections

Figure 7.43 shows the profiles of wall facing deflections at different dilation angles of the backfill material. As shown in Figure 7.43, the wall facing deflections in the five cases were almost the same at the bottom and the top of the walls. The wall facing deflection increased with the elevation to reach the maximum value approximately in the middle of the wall and then decreased with the elevation until the top of the wall. In addition, the wall facing deflection decreased with an increase in the dilation angle of the backfill soil. To clearly show the effect of the dilation angle of the backfill soil on the maximum wall facing deflections, a relationship between the dilation angle of the backfill soil and the maximum wall facing deflection is graphed in Figure 7.44. It can be seen that the dilation angle of the backfill soil had a limited influence on the maximum wall facing deflection. The benefit of increasing the dilation angle of the backfill soil on the reduction of the maximum wall facing deflection became ignorable when the dilation angle of the backfill soil was higher than 8°.

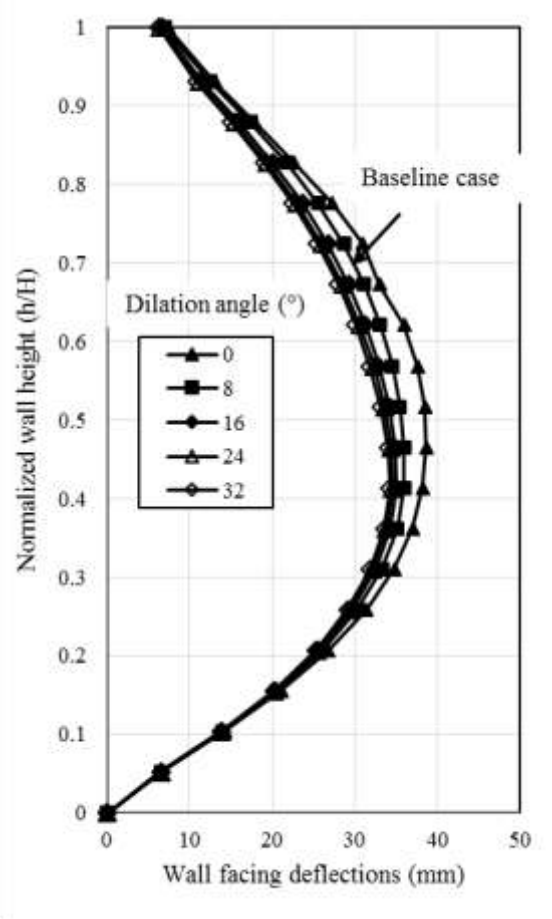

Figure 7.43 Effect of the dilation angle of the backfill soil on the wall facing deflection

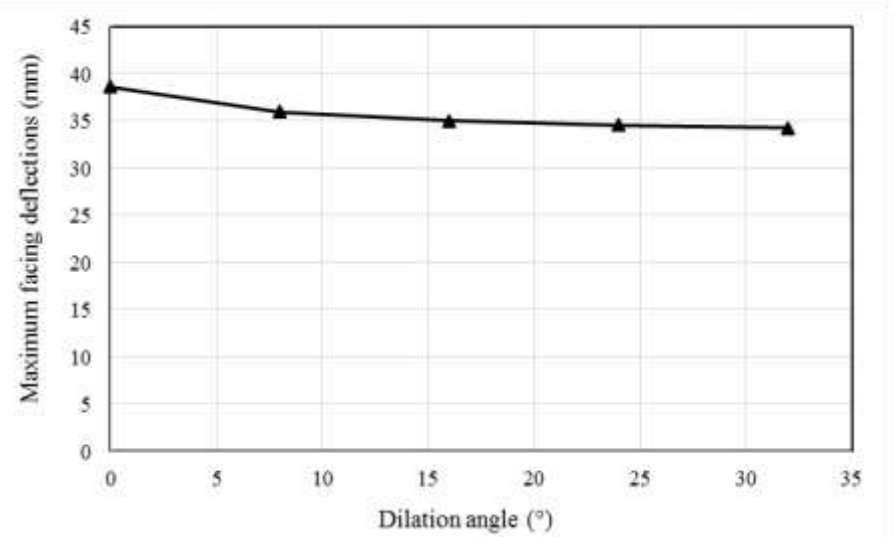

Figure 7.44 Relationship between the dilation angle of backfill soil and the maximum wall facing deflection

7.7.2. Vertical earth pressures

Figure 7.45 shows the effect of the dilation angle of the backfill soil on the vertical earth pressure at the bottom of reinforced soil. As shown in Figure 7.45, the vertical earth pressures quickly dropped within the area reinforced with the primary reinforcement and the secondary reinforcement and then gradually approached to the calculated overburden stress. The maximum vertical earth pressures occurred at the back of wall facing due to a potential overturning moment, which added an additional vertical earth pressure at the back of wall facing. The influence of the dilation angle of the backfill soil on the vertical earth pressure was ignorable.

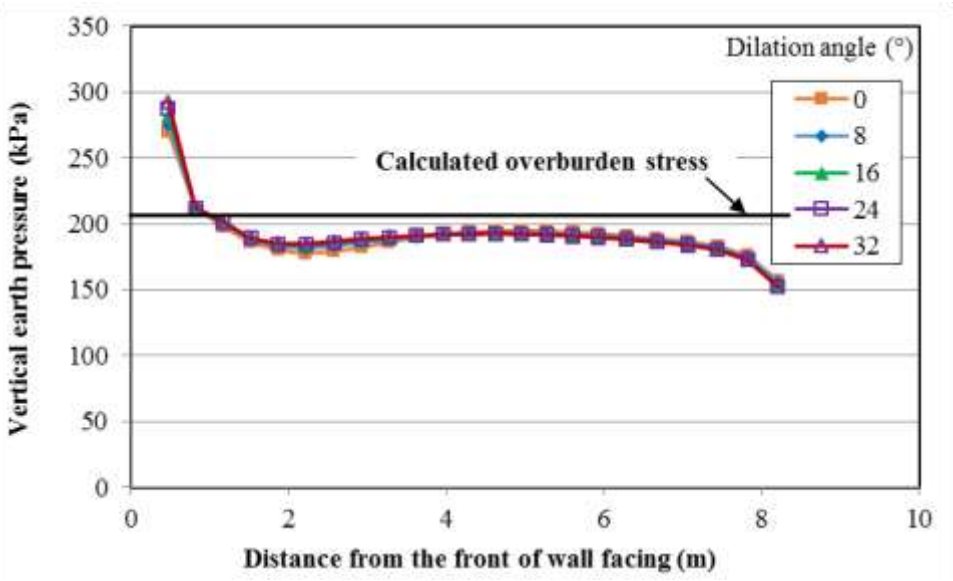

Figure 7.45 Effect of the dilation angle of the backfill soil on the vertical earth pressure at the bottom of the reinforced soil zone

7.7.3. Lateral earth pressures

Figure 7.46 shows the effect of the dilation angle of the backfill soil on the lateral earth pressure at the back of wall facing. Two solid lines in Figure 7.46 represent the

Rankine active earth pressure and the at-rest earth pressure at the friction angle of 52°. As shown in Figure 7.46, the lateral earth pressure increased with the depth (a reduction of the elevation). Near the top and the bottom of the wall, the lateral earth pressures were close to the at-rest earth pressure because the soils near the top and bottom of walls were not mobilized and had small horizontal deformations while the lateral earth pressures in the middle area of walls was close to the Rankine active earth pressure because the soil in this area was fully mobilized and had large deformations. The dilation angle of the backfill soil presents a little effect on the lateral earth pressure with the elevation.

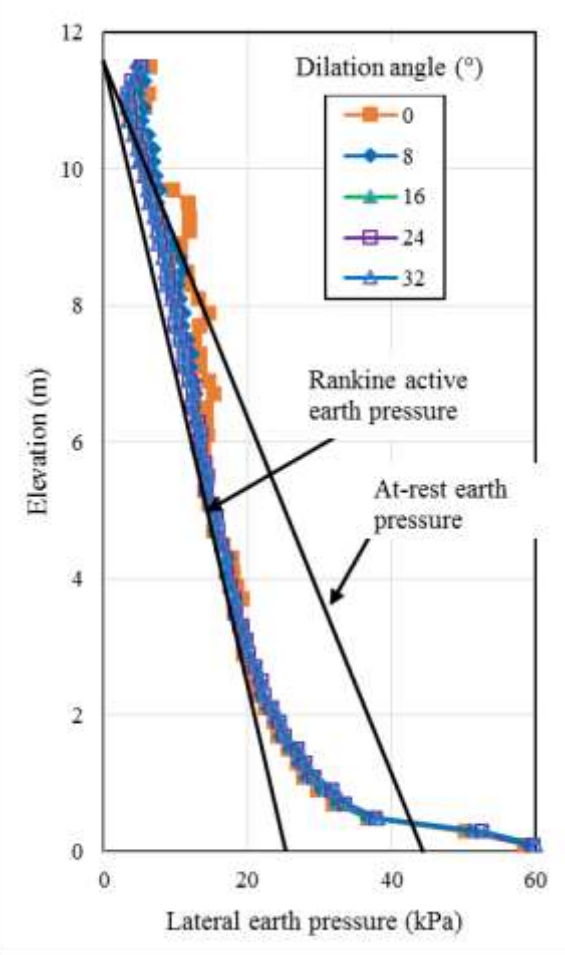

Figure 7.46 Effect of the dilation angle of the backfill soil on the lateral earth pressure at the back of wall facing

7.7.4. Tensile stress in reinforcement

Figure 7.47 shows the effect of the dilation angle of the backfill soil on the maximum tensile stresses in the primary reinforcement. As shown in Figure 7.47, the maximum tensile stress from the numerical simulation increased from the top of the walls to the elevation of 2.5 m and then slightly decreased until the bottommost layer of the primary reinforcement. For the comparison purpose, the AASHTO simplified method for geosynthetic reinforcement was used to calculate the maximum tensile stress at the friction angle of 52°. The calculated maximum tensile stress in the primary reinforcement in the numerical simulation was lower than the one using the AASHTO simplified method. The dilation angle of the backfill material had a little influence on the maximum tensile stresses in the primary reinforcement.

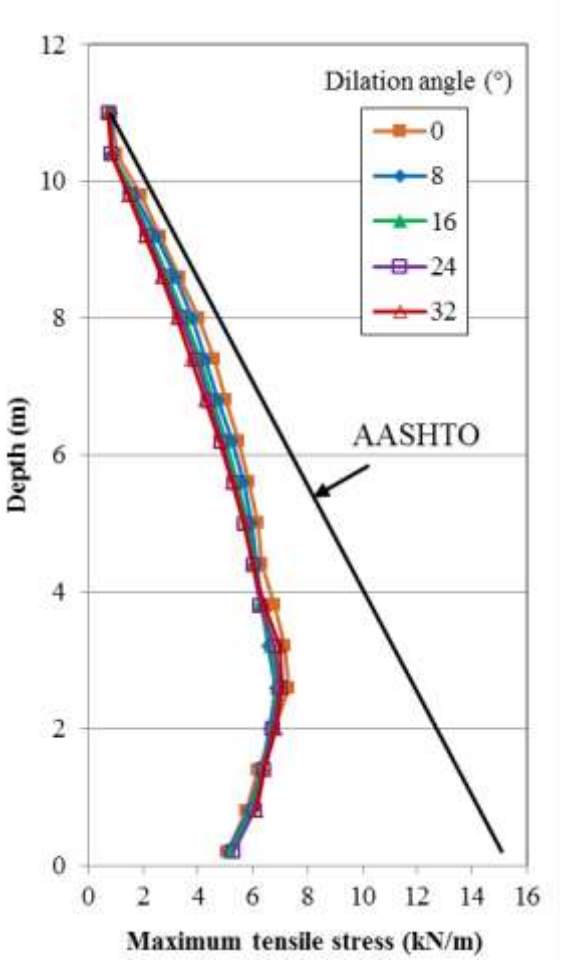

Figure 7.47 Effect of the dilation angle of the backfill soil on the maximum tensile stress in the primary reinforcement

Figure 7.48 shows the effect of the dilation angle of the backfill soil on the ratio of the connection stress to the maximum tensile stress in the primary reinforcement. When the ratio of the connection stress to the maximum tensile stress in the primary reinforcement was 1.0, it means that the maximum tensile stress occurred at the location of the connection between the primary reinforcement and the wall facing. The dilation angle of the backfill soil had a little influence on the ratio of the connection stress to the maximum tensile stress. The smallest ratio of the connection stress to the maximum tensile stress was 0.9 when the dilation angle of the backfill material decreased to 0°.

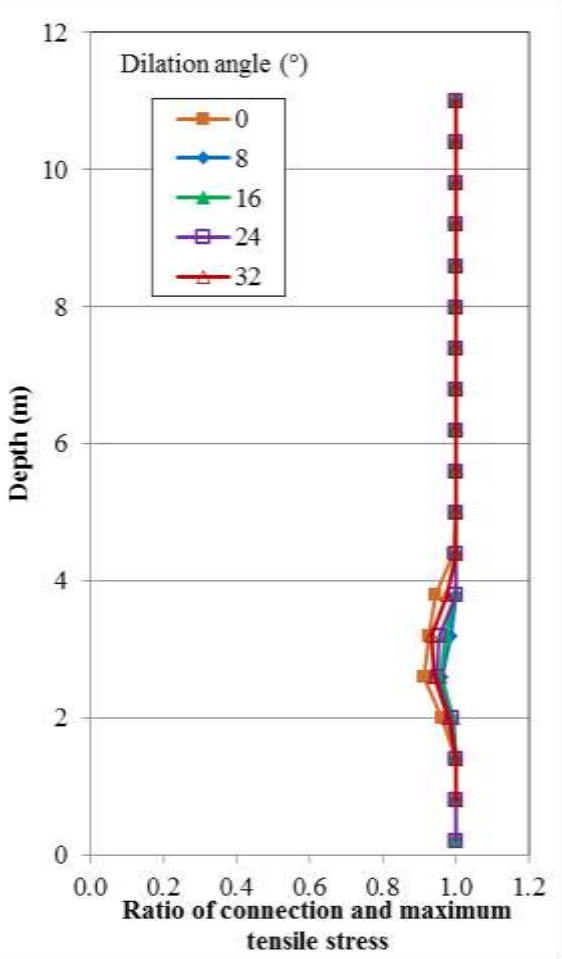

Figure 7.48 Effect of the dilation angle of the backfill soil on the ratio of the connection stress and the maximum tensile stress in the primary reinforcement

Figure 7.49 presents the effect of the dilation angle of the backfill soil on the normalized coefficient of lateral earth pressure K_r/K_a. AASHTO (2014) suggested a constant normalized coefficient of the lateral earth pressure for geosynthetic reinforcement (see Figure 7.41). As shown in Figure 7.49, the normalized coefficients with the backfill soil at different dilation angles were less than 1.0. The dilation angle of the backfill soil had an influence on the normalized coefficient when the elevation was greater than 2.5 m.

The normalized coefficient decreased with a decrease in the dilation angle of the backfill soil.

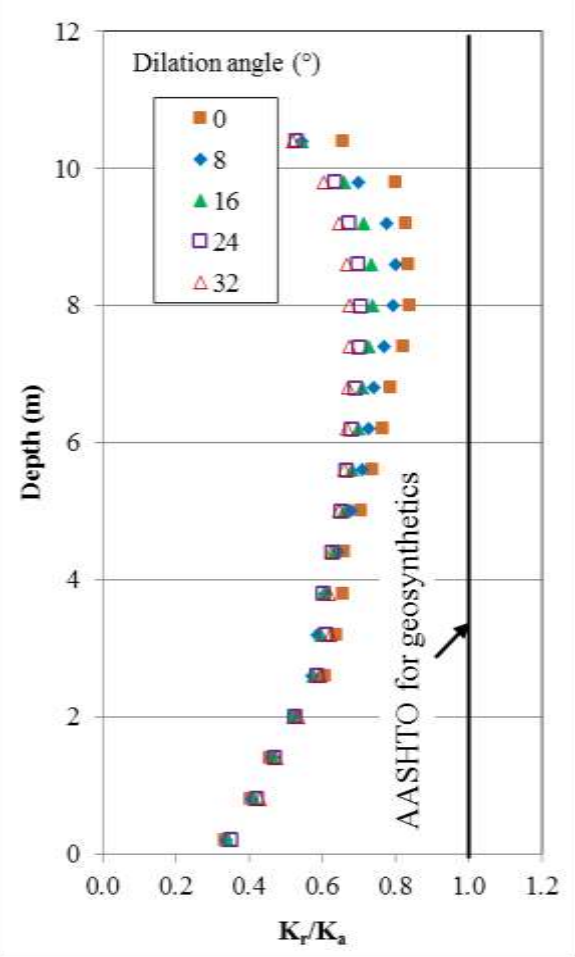

Figure 7.49 Effect of the dilation angle of the backfill soil on the ratio of K_r/K_a

Figure 7.50 shows the effect of the dilation angle of the backfill soil on the maximum tensile stresses in the secondary reinforcement. For the comparison purpose, the maximum tensile stresses were also calculated according to the Rankine active earth pressure and the at-rest earth pressure at the friction angle of 52°. The calculated maximum tensile stresses using the at-rest earth pressure were higher than those from the numerical simulation. However, the calculated maximum tensile stresses using the Rankine active

earth pressure were lower than those from the numerical simulation when the elevation was greater than 3 m. The dilation angle of the backfill soil had a little influence on the maximum tensile stresses in the secondary reinforcement.

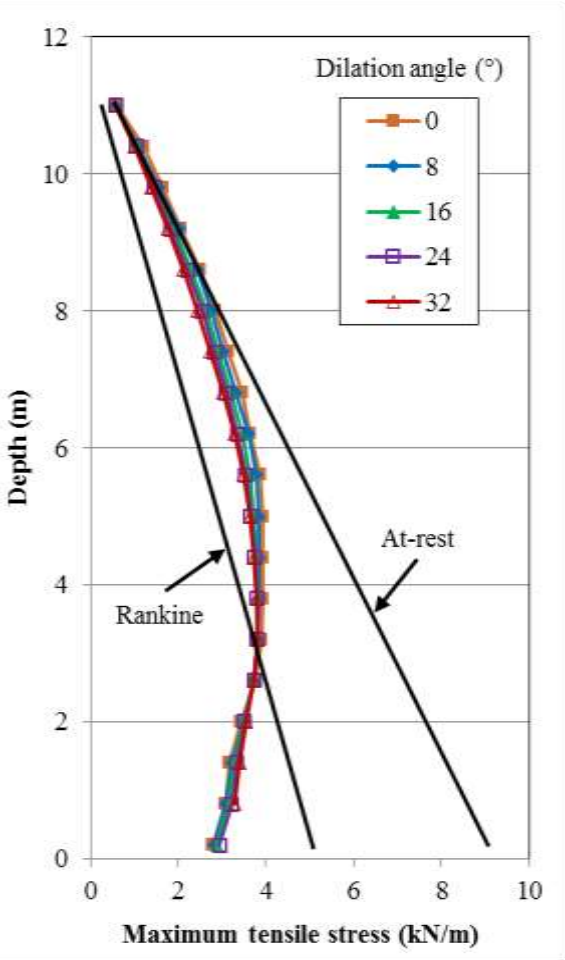

Figure 7.50 Effect of the dilation angle of the backfill soil on the maximum tensile stresses in the secondary reinforcement

7.8. Effect of soil modulus

This section discusses the effect of the modulus of the backfill soil. Since the numerical simulation using the CY model and the MC model calculated close results as shown in last chapter, the elastic modulus of the backfill soil in the CY model in the

baseline case was approximately equivalent to 20-MPa in the MC model. Two additional cases with the modulus of the backfill soil being two times and four times the modulus in the baseline model (i.e., approximately equivalent to the moduli of 40 and 80 MPa in the MC model) were studied.

7.8.1. Wall facing deflections

Figure 7.51 shows the profiles of the wall facing deflections at different moduli of the backfill soil. As shown in Figure 7.51, the wall facing deflections for the three cases were almost the same at the bottom of walls. The wall facing deflection increased with the elevation to reach the maximum value approximately in the middle of the wall and then decreased with the elevation until the top of the wall. In addition, the wall facing deflection decreased with an increase in the modulus of the backfill soil. To clearly show the effect of the modulus of the backfill soil on the maximum wall facing deflection, a relationship between the modulus of the backfill soil and the maximum wall facing deflection is graphed in Figure 7.52. It can be seen that the modulus of the backfill soil had an influence on the maximum wall facing deflection. The benefit of increasing the modulus of the backfill material to reduce the maximum wall facing deflection became minimal when the modulus of the backfill soil was higher than 40 MPa.

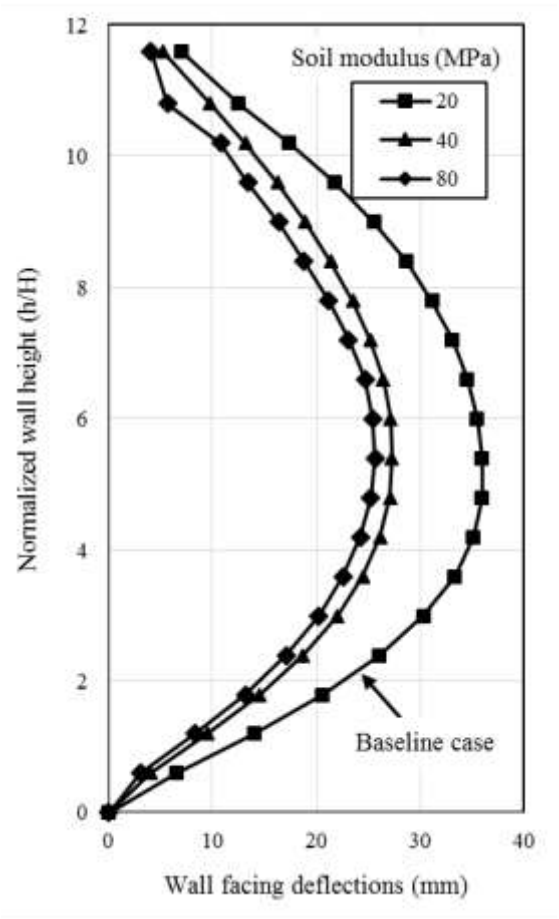

Figure 7.51 Effect of the modulus of the backfill soil on the wall facing deflection

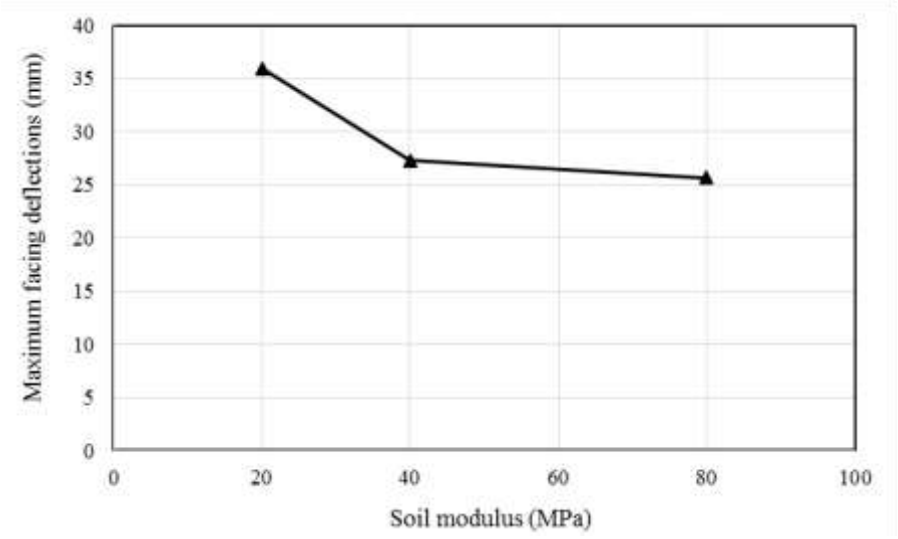

Figure 7.52 Relationship between the modulus of the backfill soil and the maximum wall facing deflection

7.8.2. Vertical earth pressures

Figure 7.53 shows the effect of the modulus of the backfill soil on the vertical earth pressure at the bottom of the reinforced soil zone. As shown in Figure 7.53, the vertical earth pressures quickly decreased within the area reinforced with the primary reinforcement and the secondary reinforcement and then gradually approached to the calculated overburden stress. The maximum vertical earth pressures occurred at the back of wall facing due to a potential overturning moment, which added an additional vertical earth pressure at the back of the wall facing. The higher modulus of the backfill soil resulted in a higher vertical earth pressure at the bottom of the reinforced soil zone. However, the modulus of the backfill soil had a limited effect on the vertical earth pressure at the bottom of the reinforced soil zone.

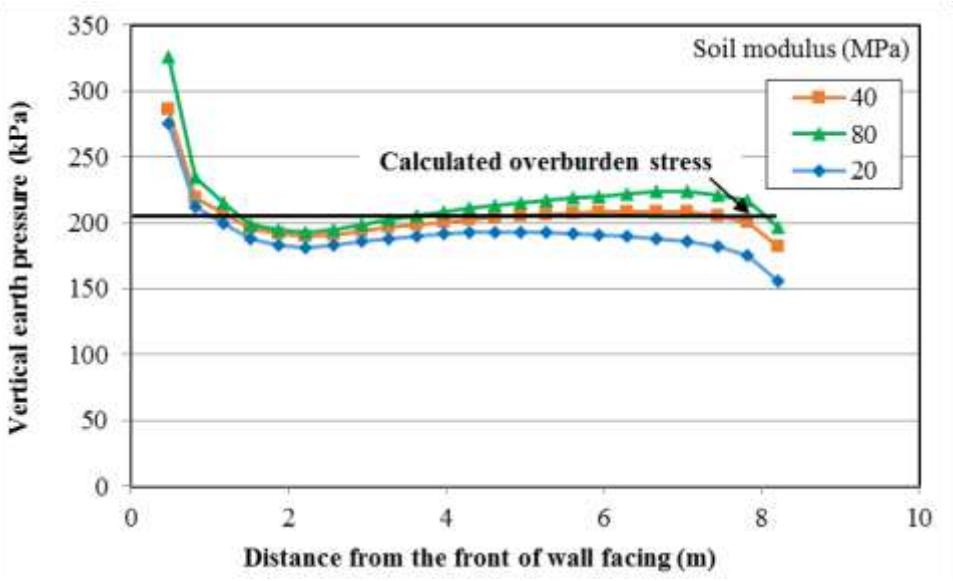

Figure 7.53 Effect of the modulus of the backfill soil on the vertical earth pressure at the bottom of the reinforced soil zone

7.8.3. Lateral earth pressures

Figure 7.54 shows the effect of the modulus of the backfill soil on the lateral earth pressure at the back of the wall facing. Two solid lines in Figure 7.54 represent the Rankine active earth pressure and the at-rest earth pressure at the friction angle of 52°. As shown in Figure 7.54, the lateral earth pressure increased with the depth (a reduction of the elevation). Near the top and the bottom of the wall, the lateral earth pressures were close to the at-rest earth pressure because the soils near the top and bottom of walls were not mobilized and had small horizontal deformations while the lateral earth pressures in the middle area of walls was close to the Rankine active earth pressure because the soil in this area was mobilized and had large deformations. The modulus of the backfill material presents a little effect on the lateral earth pressure with the elevation.

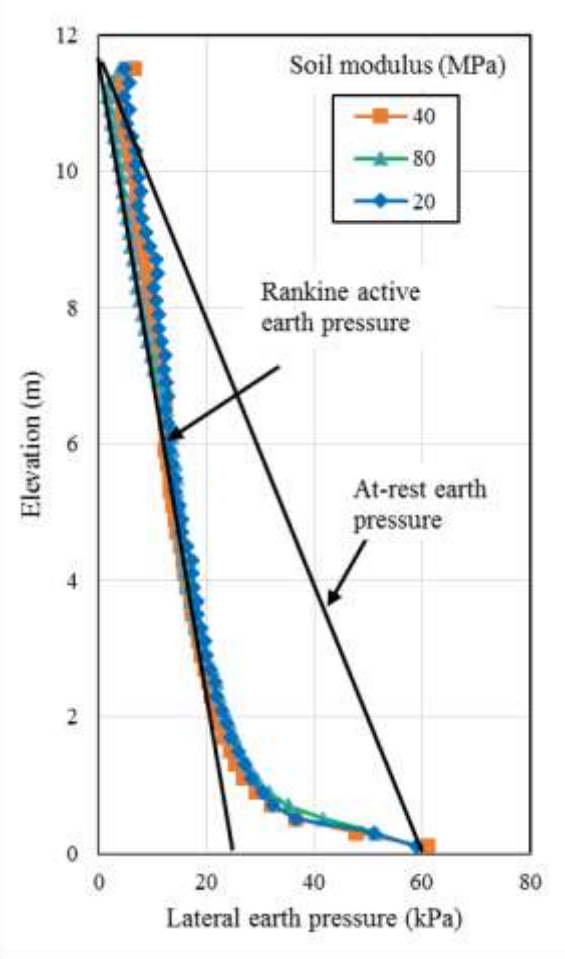

Figure 7.54 Effect of the modulus of the backfill soil on the lateral earth pressure at the back of the wall facing

7.8.4. Tensile stress in reinforcement

Figure 7.55 shows the effect of the modulus of the backfill soil on the maximum tensile stresses in the primary reinforcement. As shown in Figure 7.55, the maximum tensile stresses from the numerical simulation increased from the top of the walls to the elevation of 2.5 m and then slightly decreased until the bottommost layer of the primary reinforcement. For the comparison purpose, the AASHTO simplified method for geosynthetic reinforcement was used to calculate the maximum tensile stress at the friction angle of 52°. The calculated maximum tensile stress in the primary reinforcement in the

numerical simulation was lower than the one using the AASHTO simplified method. The maximum tensile stress in the primary reinforcement decreased with an increase in the modulus of the backfill material. However, the modulus of the backfill soil had a limited influence on the maximum tensile stresses in the primary reinforcement.

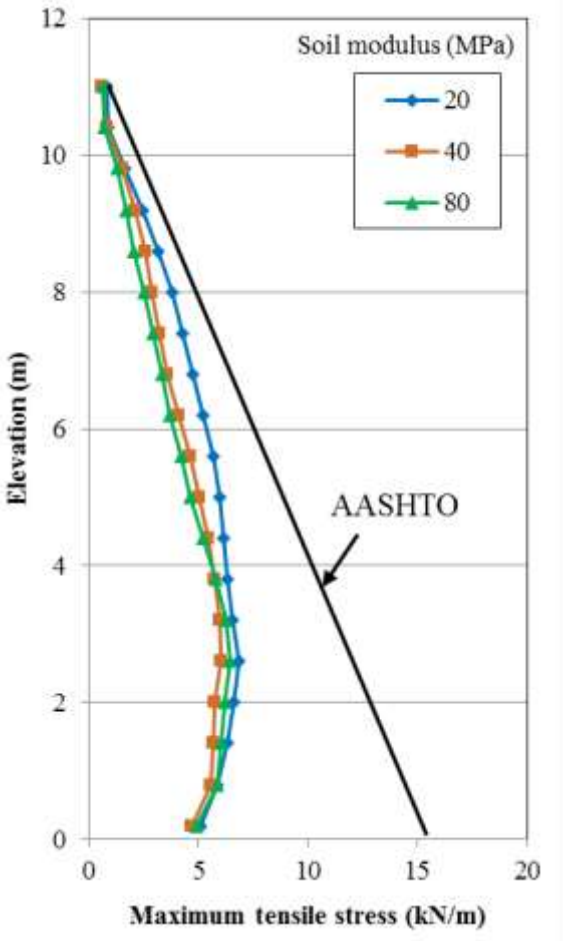

Figure 7.55 Effect of the modulus of the backfill soil on the maximum tensile stress in the primary reinforcement

Figure 7.56 shows the effect of the modulus of the backfill soil on the ratio of the connection stress to the maximum tensile stress in the primary reinforcement. When the ratio of the connection stress and the maximum tensile stress in the primary reinforcement

was 1.0, it means that the maximum tensile stress occurred at the location of the connection between the primary reinforcement and the wall facing. The connection stress was almost equal to the maximum tensile stress when the modulus of the backfill soil was 20 MPa. When the modulus of the backfill soil was 40 MPa, the minimum ratio of the connection stress to the maximum tensile stress occurred within the lower part of the wall. When the modulus of the backfill soil increased up to 80 MPa, the minimum ratio of the connection stress to the maximum tensile stress continued to decrease but the area with the ratio less than 1.0 increased with the elevation. In addition, the location of the smallest ratio occurred at the top part of the wall. The secondary reinforcement presents more benefit on the reduction of the connection stress with an increase in the modulus of the backfill soil.

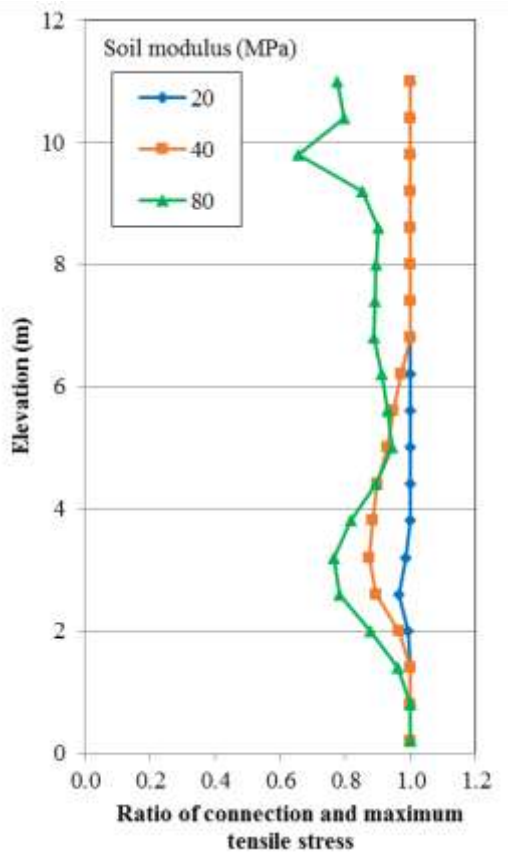

Figure 7.56 Effect of the modulus of the backfill soil on the ratio of the connection stress and the maximum tensile stress in the primary reinforcement

Figure 7.57 presents the effect of the modulus of the backfill soil on the normalized coefficient of lateral earth pressure K_r/K_a. AASHTO (2014) suggested the constant normalized coefficient of the lateral earth pressure for geosynthetic reinforcement (see Figure 7.57). As shown in Figure 7.57, the normalized coefficients with the backfill soil at different moduli were smaller than 1.0. The modulus of the backfill soil had an influence on the normalized coefficient. The normalized coefficient decreased with an increase in the modulus of the backfill soil but the influence became little when the modulus of the backfill soil was higher than 40 MPa. The benefit of reducing the normalized coefficient of lateral earth pressure became ignorable when the modulus of the backfill soil was higher than 40 MPa.

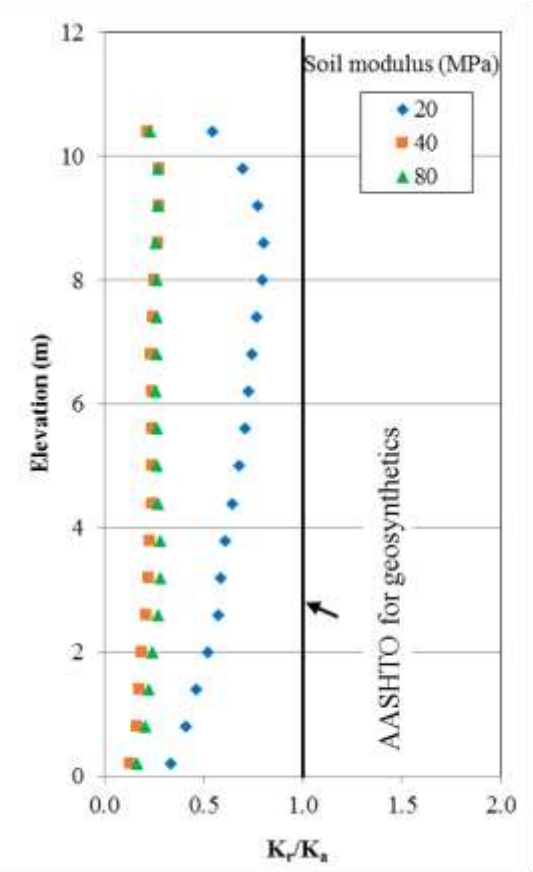

Figure 7.57 Effect of the modulus of the backfill soil on the ratio of K_r/K_a

Figure 7.58 shows the effect of the modulus of the backfill soil on the maximum tensile stress in the secondary reinforcement. For the comparison purpose, the maximum tensile stress was also calculated according to the Rankine active earth pressure and the at-rest earth pressure at the friction angle of 52°. The calculated maximum tensile stress using the at-rest earth pressure was higher than that from the numerical simulation. The modulus of the backfill soil had an influence on the maximum tensile stress in the secondary reinforcement. The maximum stress in the secondary reinforcement decreased with an increase in the modulus of the backfill soil. The benefit of reducing the maximum stress in the secondary reinforcement became ignorable when the modulus of the backfill soil was higher than 40 MPa.

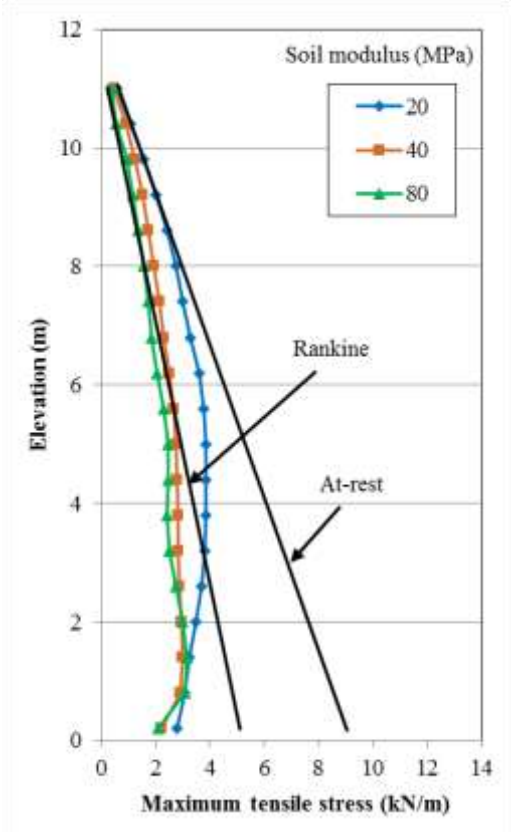

Figure 7.58 Effect of the modulus of the backfill soil on the maximum tensile stress in the secondary reinforcement

7.9. Effect of compaction stress

Compaction stress plays an important role in the performance of GRR walls during the construction. Hatami and Bathurst (2006) applied an 8-kPa vertical stress on the top of backfill soil at each lift during the construction to simulate the compaction stress in the numerical model of a GRR wall. In addition to the 8-kPa vertical earth pressure, Huang and Bahturst (2009) used 16-kPa vertical stress to simulate the compaction stress. The amount of compaction stress seems to be arbitrarily used in numerical modeling. Therefore it is necessary to investigate the effect of the compaction stress on the performance of the GRR walls. In the baseline model, the compaction stress was zero. Three additional cases with the compaction stress being 8, 16, and 32 kPa were studied.

7.9.1. Wall facing deflections

Figure 7.59 shows the profiles of wall facing deflections at four different compaction stresses. As shown in Figure 7.59, the wall facing deflections for the four cases were almost the same at the bottom and the top of the wall. The wall facing deflection increased with the elevation to reach the maximum value approximately in the middle of the wall and then decreased with the elevation until the top of the wall. In addition, the wall facing deflection increased with an increase in the compaction stress. To clearly show the effect of the compaction stress on the maximum wall facing deflection, a relationship between the compaction stress and the maximum wall facing deflection is graphed in Figure 7.60. It can be seen that the compaction stress had an influence on the maximum wall facing deflection. The maximum wall facing deflection linearly increased with an increase in the compaction stress.

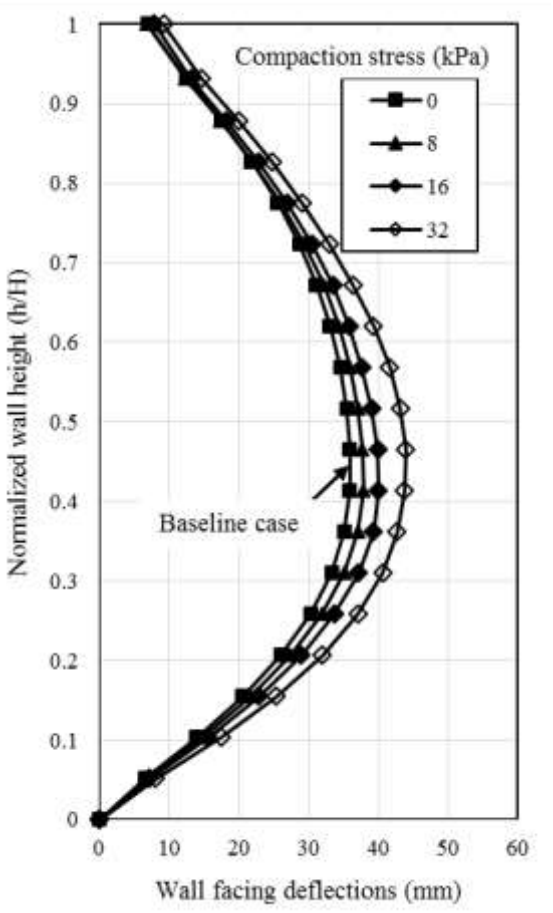

Figure 7.59 Effect of the compaction stress on the wall facing deflections

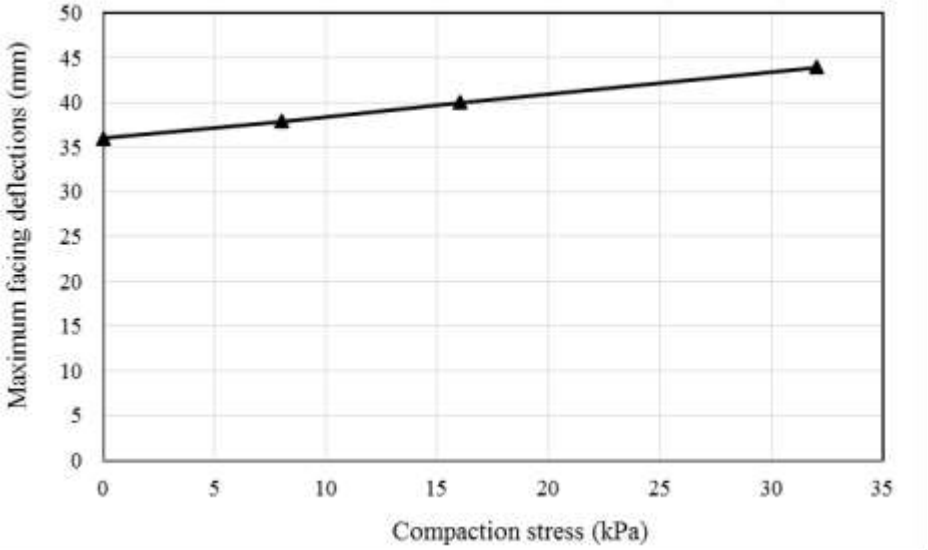

Figure 7.60 Relationship between the compaction stress and the maximum wall facing deflection

7.9.2. Vertical earth pressures

Figure 7.61 shows the effect of the compaction stress on the vertical earth pressure at the bottom of the reinforced soil zone. As shown in Figure 7.61, the vertical earth pressures quickly dropped within the area reinforced with the primary reinforcement and the secondary reinforcement and then gradually approached to the calculated overburden stress. The maximum vertical earth pressures occurred at the back of wall facing due to a potential overturning moment, which added an additional vertical earth pressure at the back of wall facing. The higher compaction stress resulted in the higher vertical earth pressure at the bottom of the reinforced soil zone. However, the compaction stress had a limited effect on the vertical earth pressure at the bottom of the reinforced soil zone.

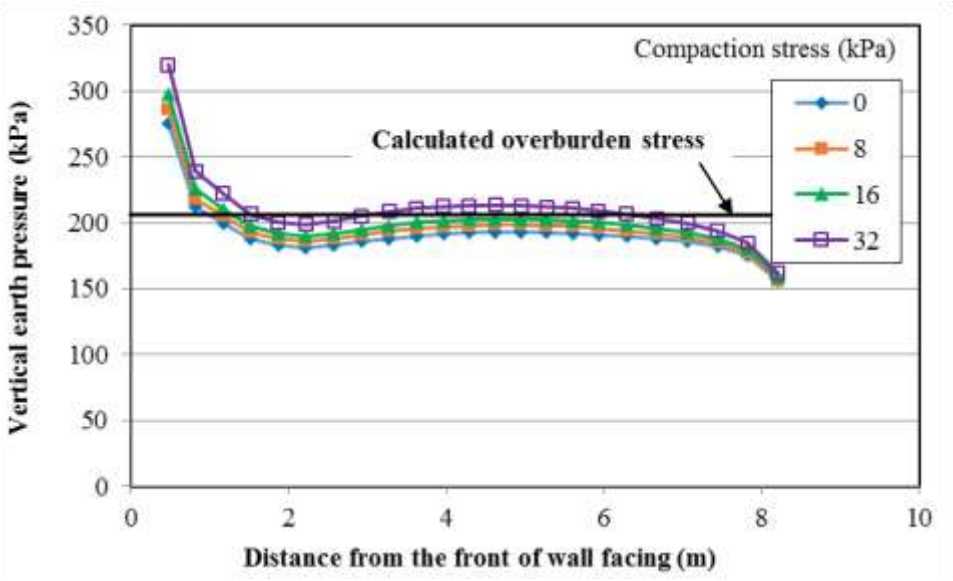

Figure 7.61 Effect of the compaction stress on the vertical earth pressure at the bottom of the reinforced soil zone

7.9.3. Lateral earth pressures

Figure 7.62 shows the effect of the compaction stress on the lateral earth pressure at the back of the wall facing. Two solid lines in Figure 7.62 represent the Rankine active earth pressure and the at-rest earth pressure with the friction angle of 52°. As shown in Figure 7.62, the lateral earth pressure increased with the depth (a reduction of the elevation). Near the top and the bottom of the wall, the lateral earth pressures were close to the at-rest earth pressures because the soils near the top and bottom of walls were not mobilized and had small horizontal deformations while the lateral earth pressures in the middle area of walls was close to the Rankine active earth pressure because the soil in this area was mobilized and had large deformations. The lateral earth pressure increased with an increase in the compaction stress. However, the effect of the compaction stress on the lateral earth pressure with the elevation was limited.

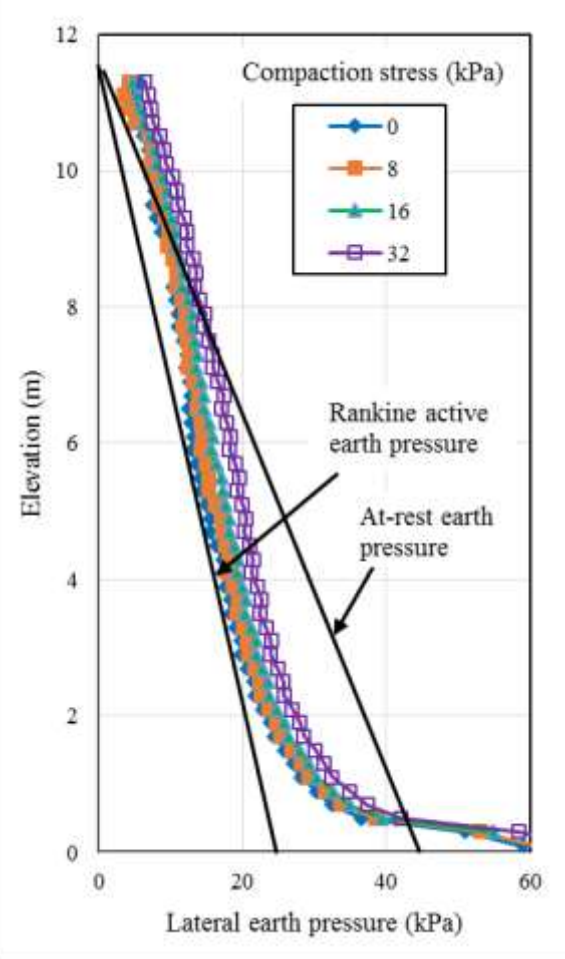

Figure 7.62 Effect of the compaction stress on the lateral earth pressure at the back of the wall facing

7.9.4. Tensile stress in reinforcement

Figure 7.63 shows the effect of the compaction stress on the maximum tensile stresses in the primary reinforcement. As shown in Figure 7.63, the maximum tensile stress from the numerical simulation increased from the top of the walls to the elevation of 2.5 m and then slightly decreased until the bottommost layer of the primary reinforcement. For the comparison purpose, the AASHTO simplified method for geosynthetic reinforcement was used to calculate the maximum tensile stress at the friction angle of 52°. The calculated maximum tensile stress in the primary reinforcement in the numerical simulation was

almost lower than the one using the AASHTO simplified method. The compaction had an influence on the maximum tensile stress in the primary reinforcement. The maximum tensile stress in the primary reinforcement increased with an increase in the compaction stress.

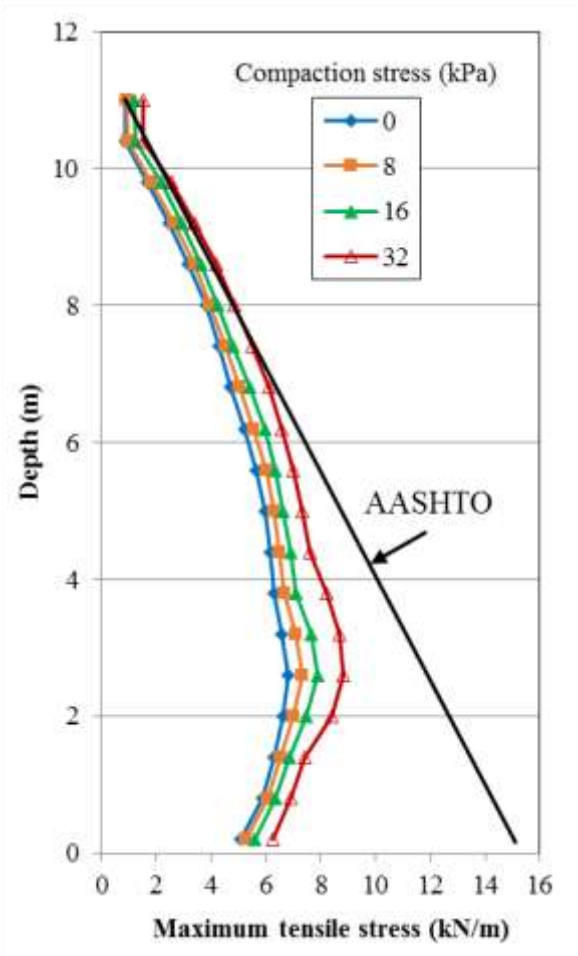

Figure 7.63 Effect of the compaction stress on the maximum tensile stress in the primary reinforcement

Figure 7.64 shows the effect of the compaction stress on the ratio of the connection stress to the maximum tensile stress in the primary reinforcement. When the ratio of the connection stress to the maximum tensile stress in the primary reinforcement was 1.0, it

means that the maximum tensile stress occurred at the location of the connection between the primary reinforcement and the wall facing. The minimum ratio of the connection stress to the maximum tensile stress occurred within the lower part of the wall. With an increase in the compaction stress, the minimum ratio of the connection stress to the maximum tensile stress decreased and the area with the ratio less than 1.0 expanded with the elevation.

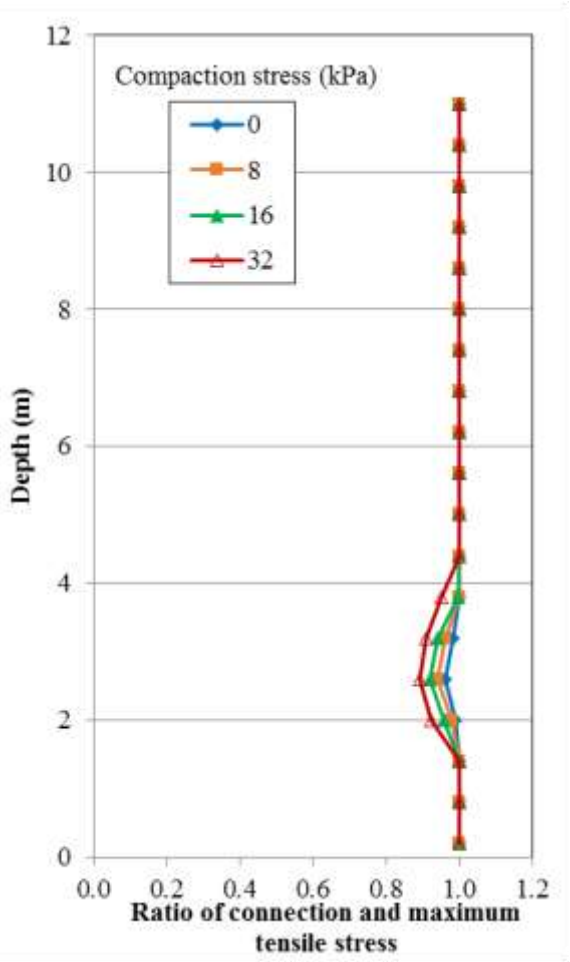

Figure 7.64 Effect of the compaction stress on the ratio of the connection stress and the maximum tensile stress in the primary reinforcement

Figure 7.65 presents the effect of the compaction stress on the normalized coefficient of lateral earth pressure K_r/K_a. AASHTO (2014) suggested the constant

normalized coefficient of the lateral earth pressure for geosynthetic reinforcement (see Figure 7.65). As shown in Figure 7.65, the normalized coefficients with different compaction stresses were less than 1.0 when the compaction stress was lower than 16 kPa. The compaction stress had an influence on the normalized coefficient. The normalized coefficient increased with an increase in the compaction stress.

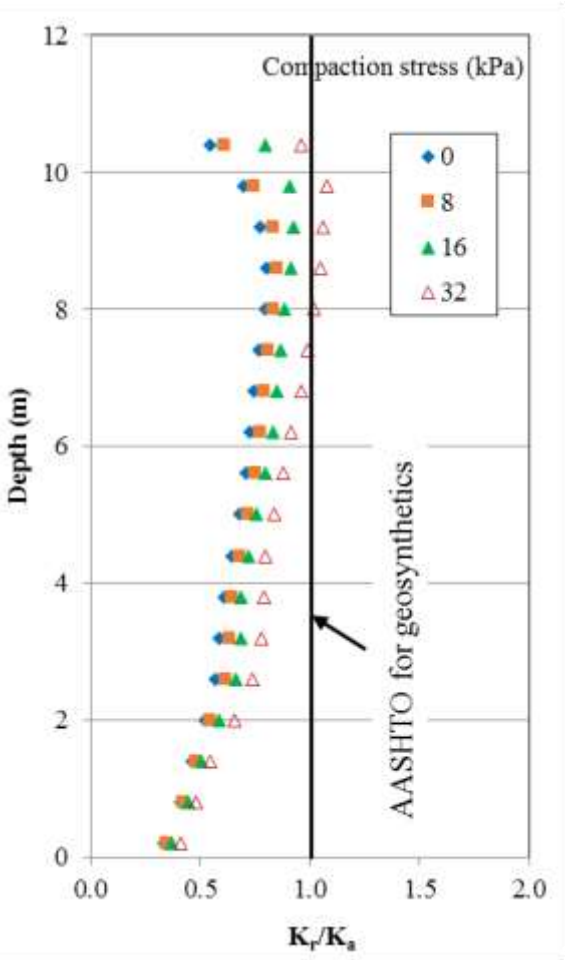

Figure 7.65 Effect of the compaction stress on the ratio of K_r/K_a

Figure 7.66 shows the effect of the compaction stress on the maximum tensile stress in the secondary reinforcement. For the comparison purpose, the maximum tensile stress was also calculated according to the Rankine active earth pressure and the at-rest earth

pressure at the friction angle of 52°. The calculated maximum tensile stresses using the at-rest earth pressure agreed well with those from the numerical simulation when the elevation was greater than 6 m. When the elevation was smaller than 6 m, the calculated maximum tensile stresses using the at-rest earth pressure were larger than those from the numerical simulation. The compaction stress had an influence on the maximum tensile stress in the secondary reinforcement. An increase in the compaction stress increased the maximum tensile stress in the secondary reinforcement.

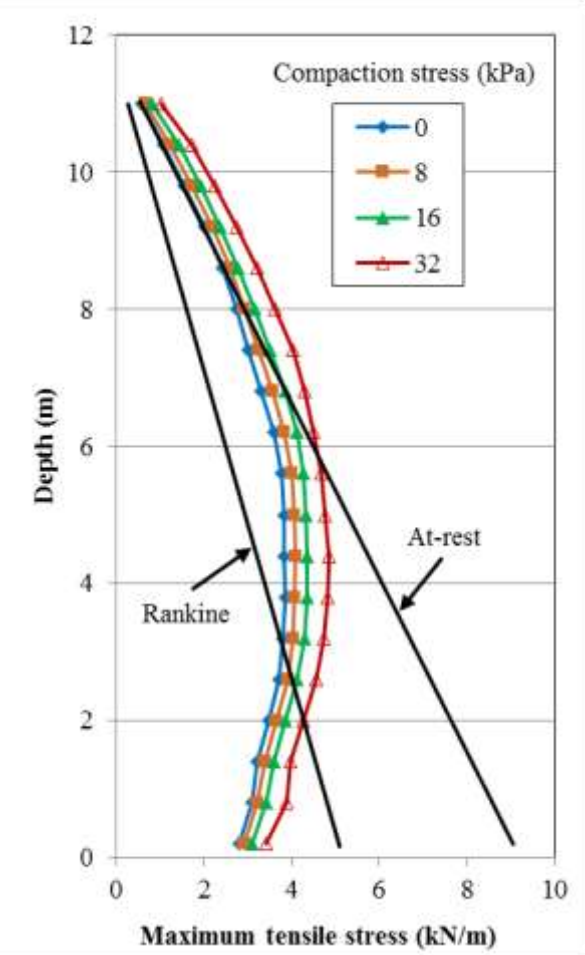

Figure 7.66 Effect of the compaction stress on the maximum tensile stresses in the secondary reinforcement

7.10. Effect of foundation compressibility

In the design of a GRR wall, its foundation soil is typically assumed to be rigid. Foundation compressibility is not considered. However, the influence of the foundation compressibility cannot be neglected on the performance of the GRR wall. This section discusses the effect of the foundation compressibility. In the baseline model, the elastic modulus of the foundation soil was 2000 MPa, which was considered to be rigid. Two additional cases considering the foundation soil with the elastic modulus of 40 and 80 MPa were studied.

7.10.1. Wall facing deflections

Figure 7.67 shows the profiles of wall facing deflections at different moduli of the foundation soil. As shown in Figure 7.67, the wall facing deflections in the cases with the elastic modulus larger than 200 MPa were around 0 and 7 mm at the bottom and the top of walls, respectively; while the wall facing deflection in the GRR wall with the 20-MPa elastic modulus increased to 47 and 23 mm at the bottom and the top of the wall, respectively. The wall facing deflection increased with the elevation to reach the maximum value approximately in the middle of the wall and then decreased with the elevation until the top of the wall. In addition, the wall facing deflection increased with an increase in the elastic modulus of the foundation soil. To clearly show the effect of the foundation compressibility on the maximum wall facing deflection, a relationship between the elastic modulus of the foundation soil and the maximum wall facing deflection is graphed in Figure 7.68. It can be seen that the elastic modulus of the foundation soil had a great

influence on the maximum wall facing deflection when the elastic modulus of the foundation soil was less than 200 MPa.

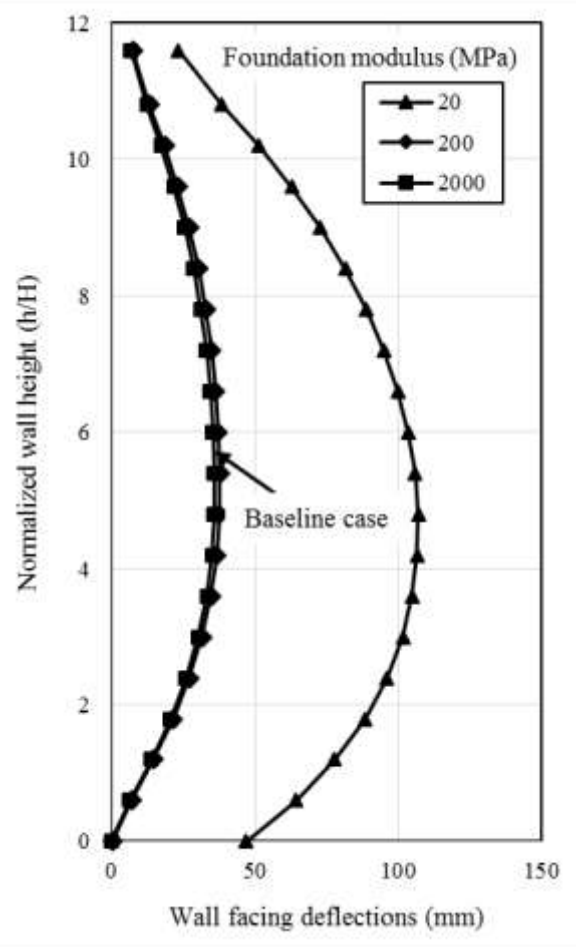

Figure 7.67 Effect of the elastic modulus of the foundation soil on the wall facing deflections

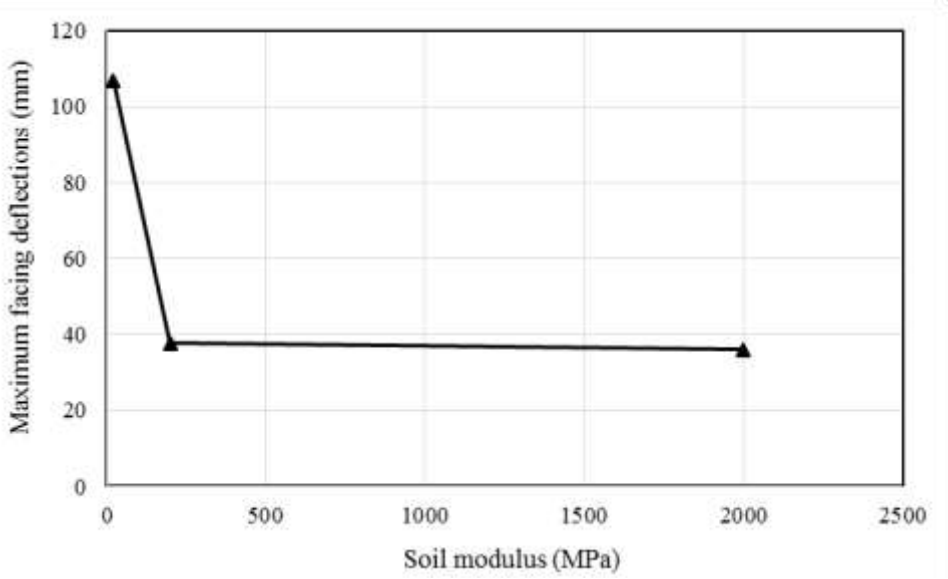

Figure 7.68 Relationship between the elastic modulus of the foundation soil and the maximum wall facing deflection

7.10.2. Vertical earth pressures

Figure 7.69 shows the effect of the elastic modulus of the foundation soil on the vertical earth pressure at the bottom of the reinforced soil zone. As shown in Figure 7.69, the vertical earth pressures quickly dropped within the area reinforced with the primary reinforcement and the secondary reinforcement and then gradually approached to the calculated overburden stress. The maximum vertical earth pressures occurred at the back of wall facing due to a potential overturning moment, which added an additional vertical earth pressure at the back of wall facing. The lower elastic modulus of the foundation soil resulted in the higher vertical earth pressure at the bottom of the reinforced soil zone.

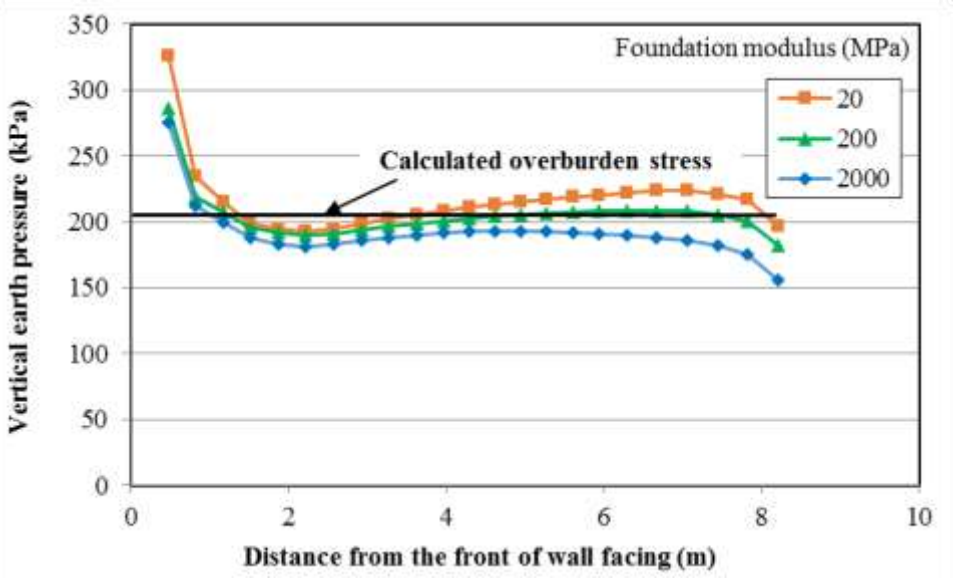

Figure 7.69 Effect of the elastic modulus of the foundation soil on the vertical earth pressure at the bottom of the reinforced soil zone

7.10.3. Lateral earth pressures

Figure 7.70 shows the effect of the elastic modulus of the foundation soil on the lateral earth pressure at the back of wall facing. Two solid lines in Figure 7.70 represent the Rankine active earth pressure and the at-rest earth pressure at the friction angle of 52°. As shown in Figure 7.70, the lateral earth pressure increased with the depth (a reduction of the elevation). Near the top and the bottom of the wall, the lateral earth pressures were close to the at-rest earth pressures because the backfill soils near the top and bottom of the wall were not mobilized and had small horizontal deformations while the lateral earth pressures in the middle area of the wall were close to the Rankine active earth pressure because the backfill soil in this area was mobilized and had large deformations. The lateral earth pressure increased with an increase in the elastic modulus of the foundation but the effect of the elastic modulus of the foundation soil on the lateral earth pressure with the elevation was little when the elastic modulus of the foundation was higher than 200 MPa.

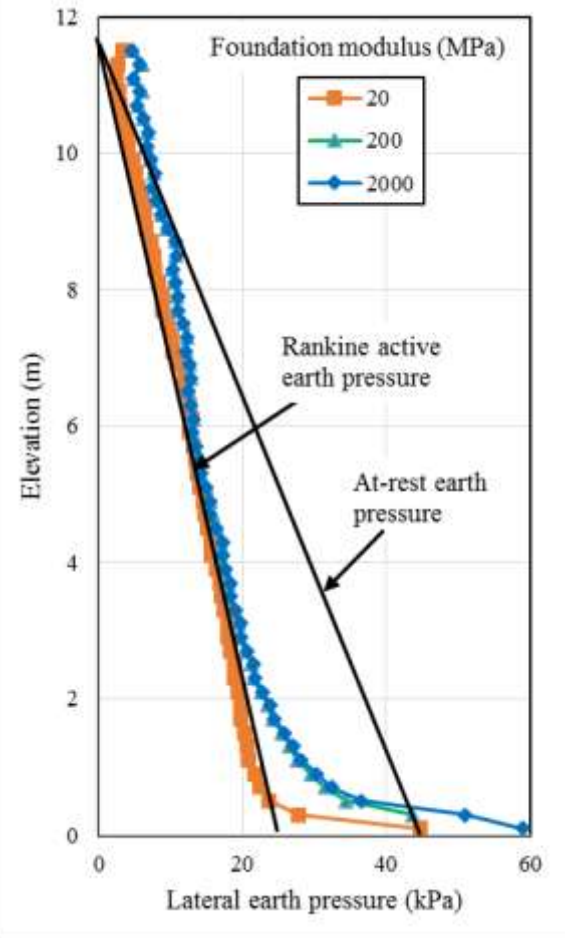

Figure 7.70 Effect of the elastic modulus of the foundation soil on lateral earth pressure at the back of wall facing

7.10.4. Tensile stress in reinforcement

Figure 7.71 shows the effect of the elastic modulus of the foundation soil in the primary reinforcement. As shown in Figure 7.71, the maximum tensile stress from the numerical simulation increased from the top of the walls to the elevation of 2.5 m and then slightly decreased until the bottommost layer of the primary reinforcement. For the comparison purpose, the AASHTO simplified method for geosynthetics was used to calculate the maximum tensile stress at the friction angle of 52°. The calculated maximum

tensile stress in the primary reinforcement in the numerical simulation was almost lower than the one using the AASHTO simplified method. When the elastic modulus of the foundation decreased from 2000 to 200 MPa, the elastic modulus of the foundation soil had no influence on the maximum tensile stress in the primary reinforcement. However, the elastic modulus of the foundation soil had a great influence on the distribution of the maximum tensile stress in the primary reinforcement with the elevation when the elastic modulus of the foundation decreased from 200 to 20 MPa. At the lower part of the wall, the maximum tensile stress in the primary reinforcement with the foundation elastic modulus of 20 MPa was higher than that with the foundation elastic modulus of 200 MPa. This result is because the foundation with a lower elastic modulus had larger differential settlements resulting in additional down-drag stress in the primary reinforcement. However, this influence disappeared approximately at the elevation of 4.2 m.

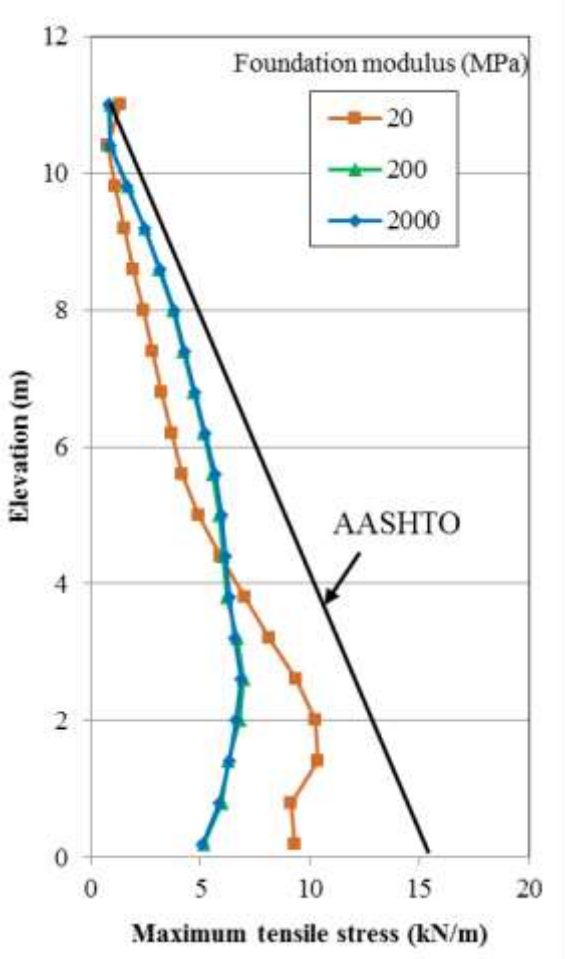

Figure 7.71 Effect of the elastic modulus of the foundation soil on the maximum stresses in the primary reinforcement

Figure 7.72 shows the effect of the elastic modulus of the foundation soil on the ratio of the connection stress to the maximum tensile stress in the primary reinforcement. When the ratio of the connection stress to the maximum tensile stress in the primary reinforcement was 1.0, it means that the maximum tensile stress occurred at the location of the connection between the reinforcement and the wall facing. The minimum ratio of the connection stress to the maximum tensile stress occurred within the lower part of the wall when the elastic modulus of the foundation soil was higher than 200 MPa. With a decrease in the elastic modulus of the foundation soil, the minimum ratio of the connection stress to

the maximum tensile stress decreased and the area with the ratio less than 1.0 expanded with the elevation. In the case with the elastic modulus of the foundation soil being 20 MPa, the secondary reinforcement not only reduced the connection stress within the lower part of the wall but also reduced the connection stress near the upper part of the wall.

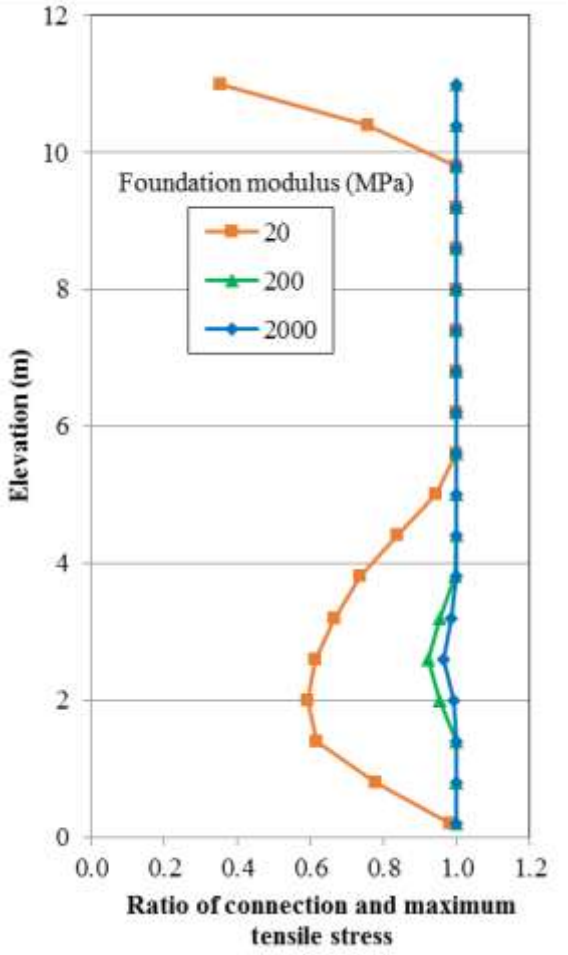

Figure 7.72 Effect of the elastic modulus of the foundation soil on the ratio of the connection stress and the maximum tensile stress in the primary reinforcement

Figure 7.73 presents the effect of the elastic modulus of the foundation soil on the normalized coefficient of lateral earth pressure K_r/K_a. AASHTO (2014) suggested the constant normalized coefficient of the lateral earth pressure for geosynthetic reinforcement

(see Figure 7.73). As shown in Figure 7.73, the normalized coefficients with different elastic moduli of the foundation soil were less than 1.0. The elastic modulus of the foundation soil had an influence on the distribution of the normalized coefficient with the elevation. The normalized coefficient decreased with an increase in the elastic modulus of the foundation soil when the elevation was higher than 4.2 m. However, when the elastic modulus of the foundation soil was lower than 200 MPa, the normalized coefficient increased with an increase in the elastic modulus of the foundation soil at the elevation lower than 4.2 m.

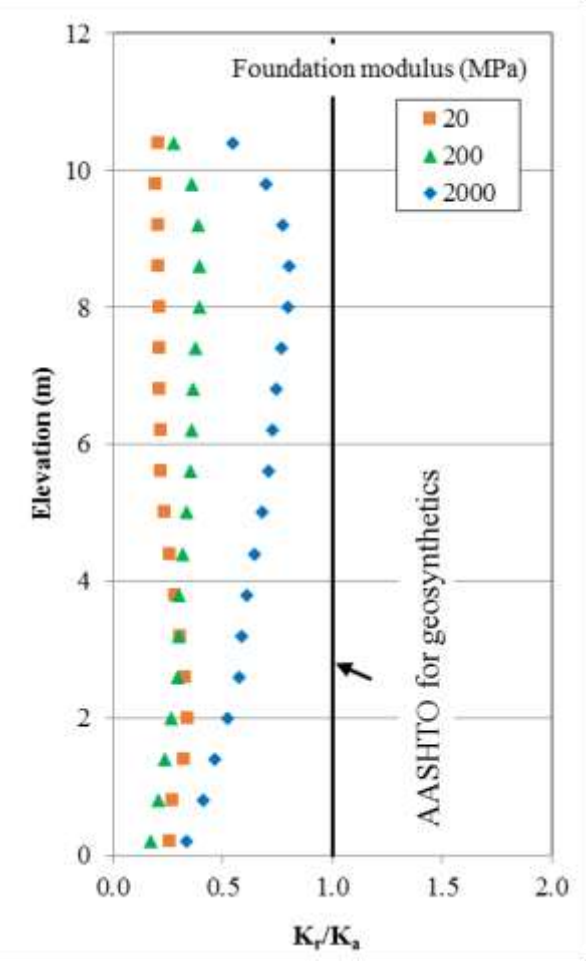

Figure 7.73 Effect of the elastic modulus of the foundation soil on the ratio of K_r/K_a

Figure 7.74 shows the effect of the elastic modulus of the foundation soil on the maximum tensile stress in the secondary reinforcement. For the comparison purpose, the calculated maximum tensile stresses using the Rankine active earth pressure and the at-rest earth pressure at the friction angle of 52° are added in Figure 7.74 as well. The calculated maximum tensile stress in the secondary reinforcement from the numerical simulation was smaller than the one using the at-rest earth pressure. When the elastic modulus of the foundation soil decreased from 2000 to 200 MPa, the elastic modulus of the foundation soil had no influence on the maximum tensile stress in the secondary reinforcement. However, the elastic modulus of the foundation soil had a great influence on the distribution of the maximum tensile stress in the secondary reinforcement with the elevation when the elastic modulus of the foundation soil decreased from 200 to 20 MPa. Within the lower part of the wall, the maximum tensile stress in the secondary reinforcement with the foundation elastic modulus of 20 MPa was higher than that with the foundation elastic modulus of 200 MPa. This result is because the foundation soil with the lower elastic modulus had larger differential settlements resulting in additional down-drag stress in the secondary reinforcement. This influence disappeared approximately at the elevation of 1.8 m.

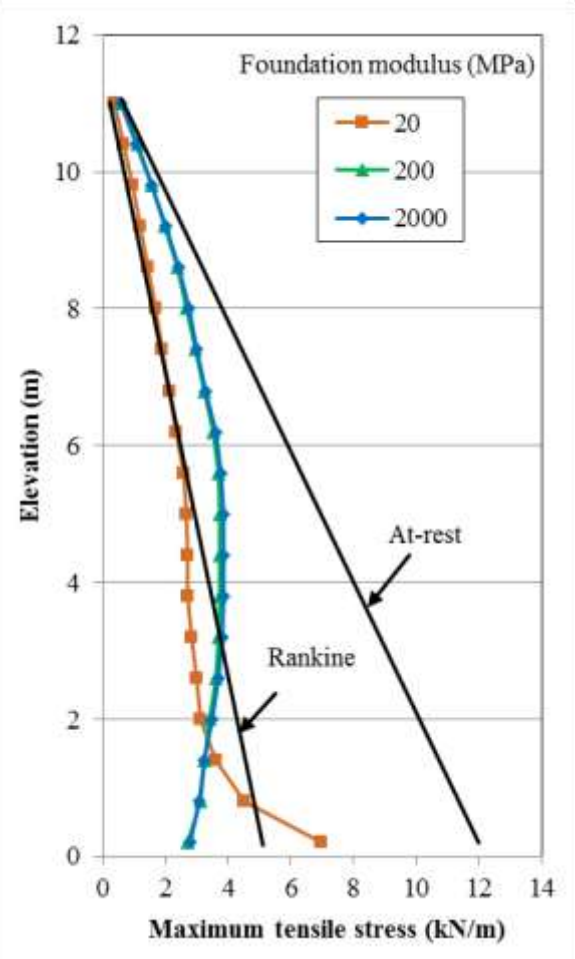

Figure 7.74 Effect of the compaction stress on maximum tensile stresses in the secondary reinforcement

Chapter 8 Conclusions and Recommendations

8.1. Conclusions

In this study, field tests and numerical simulation were performed on one geosyntehtic-reinforced retaining (GRR) wall and two hybrid GRR walls. Three test sections including one test section with primary uniaxial geogrid layers and secondary uniaxial geogrid layers (TS1), one test section with primary uniaxial geogrid layers and secondary biaxial geogrid layers (TS2), and one test section with primary geogrid layers only (TS3) were instrumented and monitored. The wall facing deflections, the vertical earth pressures, the lateral earth pressures, and the strains in the reinforcement in the field tests and the numerical simulation were analyzed and discussed. A parametric study was also conducted to investigate the performance of the hybrid GRR wall. The following conclusions can be drawn in this study:

(1) The measured accumulated wall facing deflections increased with the wall height. The maximum deflections happened at the top of the wall. The maximum accumulated wall facing deflections in TS1 and TS2 were smaller than that in TS3, indicating that the inclusion of secondary geogrid reduced the accumulated wall facing deflections. The accumulated wall facing deflections at the top of the wall in three test sections (TS1, TS2, and TS3) during construction were small.

(2) The measured vertical earth pressures increased with the construction of the wall. The measured vertical stress close to the wall facing was higher than those away from the wall facing before the construction of the backslope because the lateral earth pressure from the retained soil increased the eccentricity of the reinforced soil and increased the bearing stress close to the wall facing. The measured vertical

earth pressures close to the wall facing were lower than those away from the wall facing after the construction of the backslope because, as an eccentric load, the backslope led to potential rotation away from the toe of the wall.

(3) In the test wall section without secondary geogrid layers, the measured lateral earth pressure at the back of the wall increased approximately linearly with depth and was between the calculated active earth pressure and the at-rest earth pressure using the actual friction angle of the aggregate. The measured earth pressures within the lower portion of the wall were close to the at-rest earth pressures because the existence of the embedment limited the wall deflection. However, the measured earth pressures within the upper portion of the wall were close to the active earth pressure because the wall deflection was sufficient to allow the reinforced soil to be in an active state.

(4) The measured lateral earth pressures at the back of the wall in the test wall sections with secondary geogrid layers were approximately uniform with depth. The measured lateral earth pressures within the upper portion of the wall were close to the at-rest earth pressures because the existence of secondary reinforcement reduced the wall deflection.

(5) The average normalized earth pressure coefficient ratio at the top three layers of the instrumented geogrid in TS3 was greater than those in TS1 and TS2. This result can be explained that the secondary reinforcement shared part of the required tension and reduced the maximum tension in the primary reinforcement. The normalized earth pressure coefficient ratios back-calculated using the measured lateral earth pressures behind the wall facing were greater than those back-

calculated using the measured maximum tension in the reinforcement because the toe resistance of the wall due to embedment and the shear resistance of the block facing reduced the maximum tension in the reinforcement.

(6) The strains of primary geogrid layers increased along the geogrid layers to reach a maximum value and then decreased to zero at a distance away from the wall facing, which implied the distance of tension mobilization in the geogrid from the wall facing. This tension mobilization distance increased with the height of the wall.

(7) The secondary reinforcement carried a portion of the tension force from lateral earth pressures and reduced the tension force in the primary geogrid layers.

(8) The results from the pullout tests and the numerical simulation agree well. The numerical simulation using the Cap-Yield (CY) model for the backfill soil calculated a better result than the one using the Mohr-Coulomb (MC) model.

(9) In one GRR wall and two hybrid GRR walls, the wall facing deflections from numerical simulation increased to the maximum value and then decreased with the wall height. The wall facing deflections approached to the maximum value approximately in the middle of wall height. The wall facing deflections calculated by the numerical simulation were slightly smaller than those from the field tests, but the wall facing deflections from the numerical simulation overall agreed well with those from the field tests before and after the construction of the backslope. After the construction of the backslope, the wall facing deflections increased in the field tests and the numerical simulation. The increase in the wall facing deflections resulted from the weight of the backslope.

(10) The wall facing deflections from the numerical simulation using the CY model was slightly larger than those using the MC model. This result is because the soil modulus in the CY model was lower than that in the MC model. The difference in the wall facing deflection became larger after the construction of the backslope because the soil modulus in the CY model decreased under shear loading while the modulus in MC model was constant.

(11) Vertical earth pressures calculated by the numerical simulation quickly decreased within a distance around 1.5 m from the back of wall facing before and after the construction of the backslope. A similar drop was also found in the results from the field tests. This phenomenon could be attributed to the effect of the interaction between the wall facing and the backfill soil. An upward friction due to the relative displacement between soil and the wall facing was applied to the backfill soil behind the back of the wall facing, which reduced the vertical earth pressure at the wall bottom. After the fast drop, the vertical earth pressure reached a constant value before the construction of the backslope but gradually increased after the construction of the backslope. The vertical pressures from the numerical simulation reasonably matched the measured ones as well as the calculated trapezoid stress.

(12) Lateral earth pressures from the numerical simulation above the embedment zone approximately linearly increased with the depth, which were close to the Rankine active earth pressure. The lateral earth pressure calculated by the numerical simulation below the top of the embedment zone increased at a greater rate until the bottom of the wall. The lateral earth pressure from the numerical simulation was close to the at-rest earth pressure at the bottom of the wall. This result is because the

lateral wall facing deflections below the top of the embedment zone was restricted so that the lateral earth pressure within the zone of the embedment was close to the at-rest earth pressure.

(13) The lateral earth pressures calculated by the numerical simulation agreed well with those from the field tests. The lateral earth pressures from the field tests and the numerical simulation increased with the construction of the backslope. The increase in the lateral earth pressure resulted from the weight of the backslope.

(14) The calculated strains in the primary reinforcement layer dropped quickly behind the back of wall facing and gradually approached to zero. This fast drop was found in the measured strains as well. In the GRR walls, the maximum strains in the primary reinforcement calculated by the numerical simulation happened at the connection. However, this phenomenon is not always true in the hybrid GRR walls. The maximum strains in the primary reinforcement in the middle area of the hybrid walls occurred at the end of the area reinforced with the primary reinforcement and the secondary reinforcement. The tensile strains within the area had an approximately uniform distribution.

(15) The calculated and measured strains in the secondary reinforcement dropped quickly behind the back of wall facing. The maximum strains in the secondary reinforcement calculated by the numerical simulation happened at the connection. Overall, the strains calculated by the numerical simulation reasonably agreed with those measured in the field tests.

(16) The maximum wall facing deflection decreased with an increase in the primary reinforcement length, the secondary reinforcement length, the primary

reinforcement stiffness, the secondary reinforcement stiffness, the backfill soil friction angle, the backfill soil dilation angle, the backfill soil modulus, and the foundation compressibility while increased with an increase in the compaction stress.

(17) The effect of reducing the maximum wall facing deflections became minimal when the primary reinforcement length to wall height ratio was higher than 1.0, the secondary reinforcement length to wall height ratio was higher than 0.25, the primary reinforcement stiffness was higher than 5000 kN/m, the secondary reinforcement stiffness was higher than 2000 kN/m, the backfill soil dilation angle was higher than 8°, the backfill soil modulus was higher than 40 MPa, and the foundation modulus was higher than 200 MPa.

(18) The primary reinforcement length, the secondary reinforcement length, the primary reinforcement stiffness, the secondary reinforcement stiffness, the backfill soil friction angle had an influence on the vertical earth pressure within the area reinforced with primary reinforcement and secondary reinforcement. The vertical earth pressure increased with an increase in the backfill soil modulus and the compaction stress while decreased with an increase in the foundation compressibility.

(19) The lateral earth pressure increased with an increase in the primary reinforcement stiffness, the secondary reinforcement stiffness, and the backfill soil friction angle because the wall facing deflections decreased with an increase in the primary reinforcement stiffness, the secondary reinforcement stiffness, and the backfill soil friction angle.

(20) The maximum tensile stress in the primary reinforcement increased with an increase in the primary reinforcement stiffness and the compaction stress while decreased with an increase in the primary reinforcement length, the secondary reinforcement stiffness, and the backfill soil friction angle.

(21) The foundation compressibility had a great influence on the distribution of the maximum tensile stresses in the primary reinforcement and the secondary reinforcement with the elevation when the elastic modulus of the foundation decreased from 200 to 20 MPa. Within the lower part of the wall, the maximum tensile stresses in the primary reinforcement and the secondary reinforcement with the foundation elastic modulus of 20 MPa were higher than those with the foundation elastic modulus of 200 MPa. This result is because the foundation with a lower elastic modulus had larger differential settlements resulting in additional down-drag stresses in the primary reinforcement and the secondary reinforcement.

8.2. Recommendations for the future study

(1) This study has evaluated the behavior of the hybrid GRR walls without a footing on the top of the wall. The study on the behavior of the hybrid GRR walls subjected to footing loading to support a superstructure such as a bridge is recommended.

(2) The performance of the hybrid GRR walls during the construction has been evaluated in this study. The study on the performance of the hybrid GRR walls considering seismic loading is recommended.

(3) The field tests and the comprehensive numerical study have been performed in this study to evaluate the performance of hybrid GRR walls. A development of a simplified design method is recommended.

References

AASHTO. (2007). LRFD bridge design specifications. 4th ed., Washington, DC.

AASHTO. (2014). LRFD bridge design specifications. 7th ed., Washington, DC.

Adams, M.T., and Saunders, S.A. (2007). "Upper Ouachita National Wildlife Refuge GRS Abutments for Replacement Bridges." Presentation by Adams, M., and Saunders, S.A., FHWA.

Adams, M.T., Nicks, J.E., Stabile, T., Wu, J.T.H., Schlatter, W., and Hartmann, J. (2011). "Geosynthetic Reinforced Soil Integrated Bridge System, Synthesis Report." Report No. FHWA-HRT-11-027, Federal Highway Administration, McLean, VA.

Adib, M., Mitchell, J.K., and Christopher, B. (1990). "Finite Element Modeling of Reinforced Soil Walls and Embankments." *Geotechnical Special Publication (GSP)*, 25, 409-423.

Allen, T.M., Christopher, B.R., and Holtz, R.D. (1992). "Performance of a 41-Foot High Geotextile Wall." Report No. WA-RD 257.1, Washington Department of Transportation, Washington, 1992.

Allen, T.M., and Bathurst, R.J. (2002). "Soil reinforcement loads in geosynthetic walls at working stress conditions." *Geosynthetic International*, 9(5-6), 525-566.

Allen, T.M. and Bathurst, R.J. (2014a). "Performance of a 11 m High Block-Faced Geogrid Wall Designed Using The K-Stiffness Method." *Canadian Geotechnical Journal*, 51(1): 16-29 (http://dx.doi.org/10.1139/cgj-2013-0261).

Allen, T.M. and Bathurst, R.J. (2014b). "Design and Performance of a 6.3 m High Block-Faced Geogrid Wall Designed Using the K-Stiffness Method." *Journal of Geotechnical and Geoenvironmental Engineering*, 142(2): 1-12.

Allen, T.M. and Bathurst, R.J. (2015). “An improved simplified method for prediction of loads in reinforced soil walls.” *Journal of Geotechnical and Geoenvironmental Engineering*, 141(11): 04015049 (http://10.1061/(ASCE)GT.1943-5606.0001355).

Alzamora, D. (2013). "Massachusetts Every Day Counts Showcase on GRS-IBS." Presentation by Alzamora, D., FHWA.

American Society for Testing and Materials (ASTM C136). 2006. Standard Test Method for Sieve Analysis of Fine and Coarse Aggregates.

American Society for Testing and Materials (ASTM D698). 2014. Standard Test Method for Laboratory Compaction Characteristics of Soil Using Standard Effort (12 400 ft-lbf/ft3 (600 kN-m/m3)).

American Society for Testing and Materials (ASTM D1556). 2007. Standard Test Method for Density and Unit Weight of Soil in Place by Sand-Cone Method.

American Society for Testing and Materials (ASTM D1196). 2012. Standard Test Method for Nonrepetitive Static Plate Load Tests of Soils and Flexible Pavement Components, for Use in Evaluation and Design of Airport and Highway Pavements.

American Society for Testing and Materials (ASTM D7181). 2011. Standard Test Method for Consolidated Drained Triaxial Compression Test for Soils.

American Society for Testing and Materials (ASTM D4318). 2010. Standard Test Methods for Liquid Limit, Plastic Limit, and Plasticity Index of Soils.

American Society for Testing and Materials (ASTM D4595). 2011. Standard Test Method for Tensile Properties of Geotextiles by the Wide-Width Strip Method.

American Society for Testing and Materials (ASTM D2487). 2011. Standard Practice for Classification of Soils for Engineering Purposes (Unified Soil Classification System).

Bathurst, R.J., Allen, T.M. and Walters, D.L. (2002). "Short-term strain and deformation behavior of geosynthetic wall at working stress conditions." *Geosynthetic International*, 9(5-6), 451-482.

Bathurst, R. J., Nernheim, A., Walters, D. L., Allen, T.M., Burgess, P., and Saunders, D. D. (2009). "Influence of Reinforcement Stiffness and Compaction on the Performance of Four Geosynthetic-Reinforced Soil Walls." *Geosynthetics International*, 16(1): 43-59

Bathurst, R.J., Vlachopoulos, N., Walters, D. L., Burgess, P.G. and Allen, T. M. (2006). "The Influence of Facing Stiffness on the Performance of Two Geosynthetic Reinforced Soil Retaining Walls." *Canadian Geotechnical Journal*, 43(12):1225-1237

Bathurst, R.J., Walters, D., Vlachopoulos, N., Burgess, P., and Allen, T.M. (2000). "Full Scale Testing of Geosynthetic Reinforced Walls." *ASCE Special Publication, Proceedings of GeoDenver 2000*.

Benjamim, C.V.S., Bueno, B.S., and Zornberg, J.G. (2007). "Field Monitoring Evaluation of Geotextile-Reinforced Soil-Retaining Walls." *Geosynthetics International*, 14(2): 100-118.

Berg, R.R. (1993). Guidelines for Design, Specification, and Contracting of Geosynthetic Mechanically Stabilized Earth Slopes on Firm Foundations, Federal Highway Administration, Publication No. FHWA-SA-93-025.

Bloser, S., Shearer, D., Corradini, K., and Scheetz, B. (2012). "Geosynthetically Reinforced Soil-Integrated Bridge Systems (GRS-IBS) Specification Development for PennDOT Publication 447." Publication No. 447 (10-14), Pennsylvania Department of Transportation.

Budge, A., Dasenbrock, D., Mattison, D., Bryant, G., Grosser, A., Adams, M., and Nicks, J. (2014). "Instrumentation and Early Performance of a Large Grade GRS-IBS Wall." Geo-Congress 2014 Technical Papers @ Geo-characterization and Modeling for Sustainability, ASCE.

Chen, J.F., Liu, J.X., Xue, J.F., and Shi, Z.M. (2014). "Stability Analyses of a Reinforced Soil Wall on Soft Soils Using Strength Reduction Method." *Engineering Geology*, 177: 83-92.

Christopher, B.R., Gill, S.A., Giroud, J.P., Juran, I. Scholsser, F., Mitchell, J.K., and Dunnicliff, J. (1989). "Reinforced Soil Structures, Volume I. Design and Construction Guidelines and Volume II. Summary of Research and Systems Information." Report No. FHWA-RD-89-043, Federal Highway Administration, Washington DC, November 1989, 287 p.

Correia, A.A.S., Pinto, M.I.M., and Lopes, M.L.C. (2012). "Design of Brick-Faced Retaining Walls Reinforced with Geotextiles: Face Deformation." *Journal of Geotechnical and Geoenvironmental Engineering*, 138(5): 629-632.

Desai, C.S., and Hoseiny, K.E.E. (2005). "Prediction of Field Behavior of Reinforced Soil Wall Using Advanced Constitutive Model." *Journal of Geotechnical and Geoenvironmental Engineering*, 131(6): 729-739.

Elias, V., Christopher, B.R., and Berg, R.R. (1997). Mechanically Stabilized Earth Walls and Reinforced Soil Slopes, Design and Construction Guidelines, Federal Highway Administration, Demonstration Project 82, Publication No. FHWA-SA-96-071, Washington, D.C., August.

Fakharian, K. and Attar, I.H. (2007). "Static and seismic numerical modeling of geosynthetic-reinforced soil segmental bridge abutments." *Geosynthetics International*, 14(4): 228-243.

Guler, E., Hamderi, M., and Demirkan, M. M. (2007). "Numerical Analysis of Reinforced Soil-Retaining Wall Structures with Cohesive and Granular Backfills." *Geosynthetics International*, 14(6): 330-345.

Han, J. and Leshchinsky, D. (2006). "General Analytical Framework for Design of Flexible Reinforced Earth Structures." *Journal of Geotechnical and Geoenvironmental Engineering*, 132(11): 1427-1435.

Hatami, K. and Bathurst, R.J. (2005). "Development and Verification of a Numerical Model for the Analysis of Geosynthetic-Reinforced Soil Segmental Walls under Working Stress Conditions." *Canadian Geotechnical Journal*, 42(4): 1066-1085.

Hatami, K. and Bathurst, R.J. (2006). "Numerical Model for Reinforced Soil Segmental Walls under Surcharge Loading." *Journal of Geotechnical and Geoenvironmental Engineering*, 32(6): 673-684.

Helwany, S.M.B., Wu, J.T.H., and Froessl, B. (2003). "GRS Bridge Abutments-an Effective Means to Alleviate Bridge Approach Settlement." *Geotextiles and Geomembranes*, 21: 177-196.

Helwany, S.M.B., Wu, J.T.H., and Kitsabunnarat, A. (2007). "Simulating the Behavior of GRS Bridge Abutments." *Journal of Geotechnical and Geoenvironmental Engineering*, 133(10), 1229-1240.

Herold, A. (2006). "Kurzfassung: Brückenwiderlager aus Kbe-Kunststoff-Bewehrter Erde." Bautex 2006, Chemnitz, Germany.

Ho, S.K. and Rowe, R.K. (1996). "Effect of Wall Geometry on the Behaviour of Reinforced Soil Walls." *Geotextiles and Geomembranes*, 14: 521-541.

Holtz, R.D. and Lee, W.F. (2002). "Internal Stability Analyses of Geosynthetic Reinforced Retaining Walls." Report No. WA-RD 532.1, Washington State Department of Transportation, January, 379 p.

Huang, B.Q., Bathurst, R.J., and Hatami, K. (2009). "Numerical Study of Reinforced Soil Segmental Walls Using Three Different Constitutive Soil Models." *Journal of Geotechnical and Geoenvironmental Engineering*, 135(10): 1486-1498.

Huang, J., Parsons, R.L., Han, J., and Pierson, M.C. (2011). "Numerical Analysis of a Laterally Loaded Shaft Constructed Within an MSE Wall." *Geotextiles and Geomembranes*, 29: 233-241.

Huang, J., Han, J., Parsons, R.L., and Pierson, M.C. (2013). "Refined Numerical Modeling of a Laterally-Loaded Drilled Shaft in an MSE Wall." *Geotextiles and Geomembranes*, 37: 61-73.

Huang, J., Bin-Shafique, S., Han, J., and Rahman, M.S. (2014). "Modelling of Laterally Loaded Drilled Shaft Group in Mechanically Stabilised Earth Wall." *Proceedings of the ICE-Geotechnical Engineering*, 167(4): 402-414.

Jaky, J. (1948). "Pressure in silos." *2nd ICSMFE*, London, 1, 103-107.

Jiang, Y., Han, J., Parsons, R.L., and Cai, H. (2015). "Field Monitoring of MSE Walls to Investigate Secondary Reinforcement Effects." KTran Report, Kansas Department of Transportation.

Kansas Department of Transportation (KDOT) (2007). Standard Specifications for State Road and Bridge Construction, Section 1107 - Aggregates for Backfill.

Karpurapu, R. and Bathurst, R.J. (1995). "Behaviour of Geosynthetic Reinforced Soil Retaining Walls Using the Finite Element Method." *Computers and Geotechnics,* 17: 279-299.

Kasozi, A.M., Siddharthan, R.V., and Mahamud, R. (2013). "MSE Wall Geogrid Tensile Strength at High Temperature Sites." *Environmental Geotechnics,* http://dx.doi.org/10.1680/envgeo.13.00073

Kniss, K.T., Wright, S.G., Zornberg, J.G., and Yang, K.H. (2007). "Design Considerations for MSE Retaining Walls Constructed in Confined Spaces." Report No. 0-5506-1, Center for Transportation Research (CTR), Austin, Texas, October 2007.

Koerner G.R. and Koerner G.R. (2011). "The Importance of Drainage Control for Geosynthetic Reinforced Mechanically Stabilized Earth Walls." *Journal of GeoEngineering*, 6(1), 3-13.

Kongkitkul, W., Tatsuoka, F., Hirakawa, D., Sugimoto, T., Kawahata, S., and Ito, M. (2010). "Time Histories of Tensile Force in Geogrid Arranged in Two Full-Scale High Walls." *Geosynthetics International*, 17(1) 12-32.

Leshchinsky, D. (2000). "Alleviating connection load." Geotechnical Fabrics Report, 34-39.

Leshchinsky, D., Zhu, F., and Meehan, C. (2010). "Required unfactored strength of geosynthetic in reinforced earth structures." *Journal of Geotechnical and Geoenvironmental Engineering*, 136(2), 281–289.

Leshchinsky, D. and Vahedifard, F. (2012). "Impact of toe resistance in reinforced masonry block walls: design dilemma." *Journal of Geotechnical and Geoenvironmental Engineering*, 138(2), 236–240.

Leshchinsky, D., Kang, B.J., Han, J., Ling, H.I. (2014). “Framework for Limit State Design of Geosynthetic-Reinforced Walls and Slopes,” *Transportation Infrastructure Geotechnology*, 1(2), 129-164.

Leshchinsky, D. and Vulova, C. (2001). "Numerical Investigation of the Effects of Geosynthetic Spacing on Failure Mechanisms of MSE Block Walls." *Geosynthetics International*, 8(4): 343-365.

Leshchinsky, D. and Vulova, C. (2002). "Effects of Geosynthetic Reinforcement Spacing on The Behavior of Mechanically Stabilized Earth Walls." Delaware Center of Transportation

Ling, P. and Leshchinsky, D. (1996). "Mesa Walls: Field Data Reduction, Finite Element Analysis, and Preliminary Design Recommendations." Report to Tensar Earth Technologies, Inc., Atlanta, GA, February 1.

Ling, H.I. and Leshchinsky, D. (2003). "Finite Element Parametric Study of the Behavior of Segmental Block Reinforced-Soil Retaining Walls." *Geosynthetics International*, 10(3): 77-94.

Ling, H.I., Tatsuoka, F., and Tateyama, M. (1995). "Simulating Performance of GRS-RW by Finite-Element Procedure." *Journal of Geotechnical Engineering*, 121(4): 330-340.

Liu, H.B. (2012). "Long-Term Lateral Displacement of Geosynthetic-Reinforced Soil Segmental Retaining Walls." *Geotextiles and Geomembranes*, 32: 18-27.

Liu, H.B. and Won, M.S. (2009). "Long-Term Reinforcement Load of Geosynthetic-Reinforced Soil Retaining Walls." *Journal of Geotechnical and Geoenvironmental Engineering*, 137(5): 875-889.

Liu, H.B., Wang, X., and Song, E. (2009). "Long-term behavior of GRS retaining walls with marginal backfill soils." *Geotextiles and Geomembranes*, 27(4): 295-307.

Luo, Y., Leshchinsky, D., Rimoldi, P., Lugli, G., and Xu, C. (2015). "Instrumented mechanically stabilized earth wall reinforced with polyester straps." *Transportation Research Record: Journal of the Transportation Research Board*, No. 2511, Transportation Research Board, Washington, D.C., 9–17.

Michalowski, R. (2000). "Secondary Reinforcement for Slopes." *Journal of Geotechnical and Geoenvironmental Engineering*, 126(12): 1166–1173.

Mirmoradi, S.H., and Ehrlich, M. (2014). "Numerical Evaluation of the Behavior of GRS Walls with Segmental Block Facing under Working Stress Conditions." *Journal of Geotechnical and Geoenvironmental Engineering*, 141(3): 1-8.

Morrison, K. F., Harrison, F. E., Collin J. G., Dodds A., and Arndt B. (2006). "Shored Mechanically Stabilized Earth (SMSE) Wall Systems Design Guidelines." Report No. FHWA-CFL/TD-06-001, Federal Highway Administration.

Perkins, S.W., Schulz, J.L and Lapeyre, J.A., (1997). "Local versus Global Strain Measurement of a Polymeric Geogrid." *Journal of Testing and Evaluation*, 25(6), 576-583.

Pham, T.Q. (2009). "Investigating Composite Behavior of Geosynthetic Reinforced Soil (GRS) Mass." Ph.D. Thesis, The University of Colorado at Denver, 358 p.

Pierson, M.C., Parsons, R.L., Han, J., and Brennan, J.J. (2009). "Load-deflection responses of laterally loaded shafts in an MSE wall." *Transportation Research Record: Journal of the Transportation Research Board,* Transportation Research Board of the National Academics, Washington, D.C., 2116, 62-69.

Pierson, M.C., Parsons, R.L., Han, J., and Brennan, J.J. (2011). "Laterally loaded shaft group capacities and deflections behind an MSE wall." *Journal of Geotechnical and Geoenvironmental Engineering*, 137(10), 882-889.

Portelinha, F.H.M., Bueno, B.S., and Zornberg, J.G. (2013). "Performance of Nonwoven Geotextile-Reinforced Walls Under Wetting Conditions: Laboratory and Field Investigations." *Geosynthetics International*, 20(2): 90-104.

Portelinha, F.H.M., Zornberg, J.G., and Pimentel, V. (2014). "Field Performance of Retaining Walls Reinforced with Woven and Nonwoven Geotextiles." *Geosynthetics International*, 21(4): 270-284.

Riccio, M., Ehrlich, M., and Dias D. (2014). "Field Monitoring and Analyses of the Response of a Block-Faced Geogrid Wall Using Fine-Grained Tropical Soils." *Geotextiles and Geomembranes*, 42(2): 127–138.

Rowe, R.K., and Ho, S.K. (1998). "Horizontal Deformation in Reinforced Soil Walls." *Canadian Geotechnical Journal*, 35: 312-327.

Rowe, R.K., and Skinner, G.D. (2001). "Numerical Analysis of Geosynthetic Reinforced Retaining Wall Constructed on a Layered Soil Foundation." *Geotextiles and Geomembranes*, 19(7): 387-412.

Ruiken, A., Ziegler, M., Vollmert, L., Höhny, S. (2011). "Investigation of the compound behavior of geogrid reinforced soil." *Proceedings of the 15th European Conference on Soil Mechanics and Geotechnical Engineering*, 138(3): 345-356.

Santos, E. C. G., Palmeira, E. M., and Bathurst R. J. (2014). "Performance of Two Geosynthetic Reinforced Walls with Recycled Construction Waste Backfill and Constructed on Collapsible Ground." *Geosynthetics International*, 21(4): 256-269.

Schlosser, F. (1978). “Experience on reinforced earth in france.” *Proc., Symp. Reinforced Earth and Other Composite Soil Techniques,* Heriot-Watt University, TRRL Sup. 457.

Skinner, G.D., and Rowe, R.K. (2005b). "Design and Behaviour of a Geosynthetic Reinforced Retaining Wall and Bridge Abutment on a Yielding Foundation." *Geotextiles and Geomembranes*, Vol. 23, pp. 234-260.

Soong, T.Y., and Koerner, R.M. (1998). "On the Required Connection Strength of Geosynthetically Reinforced Walls." *Geotextiles and Geomembranes*, 15(4-6): 377-393.

Stuedlein, A.W., Allen, T.M., Holtz, R.D., and Christopher, B.R. (2012). "Assessment of Reinforcement Strains in Very Tall Mechanically Stabilized Earth Walls." *Journal of Geotechnical and Geoenvironmental Engineering*, 138(3): 345-356

Stuedlein, A.W., Bailey, M., Lindquist D., Sankey, J., and Neely, W. J. (2010). "Design and Performance of a 46-m-High MSE Wall." *Journal of Geotechnical and Geoenvironmental Engineering*, 136(6): 786–796.

Thielen, D.L., and Collin, J.G. (1993) "Geogrid Reinforcement for Surficial Stability of Slopes", *Geosynthetics '93 Conference Proceedings*, pp. 229-241, Vancouver, Canada.

Vulova, C. and Leshchinsky, D. (2003). "Effects of Geosynthetic Reinforcement Spacing on The Behavior of Mechanically Stabilized Earth Walls." Report No. FHWA-RD-03-048, Federal Highway Administration, McLean, VA.

Vennapusa, P., White, D. J., Klaiber, F.W., Wang, S., and Gieselman, H. (2012). "Geosynthetic Reinforced Soil for Low-Volume Bridge Abutments." Report No. IHRB Project TR-621, Iowa Department of Transportation, Ames, IA, January 2012.

Warren, K.A., Whelan, M.J., Hite J., and Adams M. (2014). "Three Year Evaluation of Thermally Induced Strain and Corresponding Lateral End Pressures for a GRS IBS in

Ohio." *Geo-Congress 2014 Technical Papers @ Geo-characterization and Modeling for Sustainability*, ASCE.

Wu, J.T.H. (2001). "Revising the AASHTO Guidelines for Design and Construction of GRS Walls." Report No. CDOT-DTD-R-2001-16, Colorado Department of Transportation, 148 p.

Wu, J.T.H., Lee, K.Z.Z., Helwany, S.B., and Ketchart, K. (2006). "Design and Construction Guidelines for Geosynthetic-Reinforced Soil Bridge Abutments with a Flexible Facing." Report No. 556, National Cooperative Highway Research Program, Washington, DC.

Wu, J.T.H. and Pham, T.Q. (2013). "Load-Carrying Capacity and Required Reinforcement Strengthof Closely Spaced Soil-Geosynthetic Composites." *Journal of Geotechnical and Geoenvironmental Engineering*, 139(9), 1468–1476.

Xiao, C., Han, J., and Zhang, Z. (2016). "Experimental study on performance of geosynthetic-reinforced soil model walls subjected to static footing loading." *Geotextiles and Geomembranes*, 44, 81-94.

Xue, J.F., Chen, J.F., Liu, J.X., and Shi, Z.M. (2014). "Instability of a Geogrid Reinforced Soil Wall on Thick Soft Shanghai Clay with Prefabricated Vertical Drains: a Case Study." *Geotextiles and Geomembranes*, 42: 302-311.

Yang, G., Liu, H., Lv P., and Zhang, B. (2012). "Geogrid-Reinforced Lime-Treated Cohesive Soil Retaining Wall: Case Study and Implications." *Geotextiles and Geomembranes*, 35: 112-118.

Yang, G., Liu, H., Zhou Y., and Xiong, B. (2014). "Post-Construction Performance of a Two-Tiered Geogrid Reinforced Soil Wall Backfilled with Soil-Rock Mixture." *Geotextiles and Geomembranes*, 42(2): 91-97.

Yang, G., Zhang B., Lv P., and Zhou Q. (2009). "Behaviour of Geogrid Reinforced Soil Retaining Wall with Concrete-Rigid Facing." *Geotextiles and Geomembranes*, 27(5): 350-356.

Yoo, C. (2004). "Performance of a 6-Year-Old Geosynthetic Reinforced Segmental Retaining Wall." *Geotextiles and Geomembranes*, 22: 377-397.

Yoo, C., and Jung, H. (2003). "Measured Behavior of a Geosynthetic-Reinforced Segmental Retaining Wall in a Tiered Configuration." *Geotextiles and Geomembranes*, 22(5): 359-376

Yoo, C., and Jung, H. (2006). "Case History of Geosynthetic Reinforced Segmental Retaining Wall Failure." *Journal of Geotechnical and Geoenvironmental Engineering*, 132(12): 1538-1548.

Yoo, C., and Kim, S.B. (2008). "Performance of a Two-Tier Geosynthetic Reinforced Segmental Retaining Wall under a Surcharge Load: Full-Scale Load Test and 3D Finite Element Analysis." *Geotextiles and Geomembranes*, 26: 460-472.

Yu, Y., Bathurst, R.J. and Allen, T.M. 2015. "Numerical modelling of the SR-18 geogrid reinforced modular block retaining walls." *Journal of Geotechnical and Geoenvironmental Engineering* (http://dx.doi.org/10.1061/(ASCE)GT.1943-5606.0001438).

Ziegler, M. (2014). "Application of Geosynthetics in the Construction of Roads and Railways: Yesterday-Today-Tomorrow." Keynote Lecture. XV Danube-*European Conference on Geotechnical Engineering (DECGE 2014)*, Vienna, Austria.